Effet Hall Quantiques de spin dans les matériaux III-V

Colin Avogadri

To cite this version:

Colin Avogadri. Effet Hall Quantiques de spin dans les matériaux III-V. Astrophysique [astro-ph]. Université de Montpellier, 2023. Français. NNT : 2023UMONS004 . tel-04486230

HAL Id: tel-04486230
https://theses.hal.science/tel-04486230

Submitted on 1 Mar 2024

THÈSE POUR OBTENIR LE GRADE DE DOCTEUR
DE L'UNIVERSITÉ DE MONTPELLIER

En Physique

Ecole Doctorale Information, Structures et Systèmes

Unité de recherche : Laboratoire Charles Coulomb

Effet Hall Quantique de spin dans les matériaux III-V

Présentée par Colin AVOGADRI
le 13/04/2023

Sous la direction de Benoit JOUAULT
et Frederic TEPPE

Devant le jury composé de

Eric TOURNIÉ, Professeur HDR, IES - Université de Montpellier	Président
Michel GOIRAN, Professeur HDR, LNCMI - CNRS	Rapporteur
Wilfrid POIRIER, Directeur de Recherche, LNE - Université Paris-Sud	Rapporteur
Fabian HARTMAN, Professeur, Affiliation	Examinateur
Sébastien NANOT, Maître de Conférence, L2C - Université de Montpellier	Co-Encadrant
Isabelle SAGNES, Directrice de Recherche, C2N - CNRS	Examinateur
Benoit JOUAULT, Directeur de Recherche, L2C - CNRS	Directeur
Frédéric TEPPE, Directeur de Recherche, L2C - CNRS	Codirecteur

UNIVERSITÉ
DE MONTPELLIER

Acknowledgements

Je tiens tout d'abord à exprimer ma profonde gratitude envers Benoit Jouault et Frédéric Teppe, mes directeurs de thèse, ainsi que Sébastien Nanot qui a co-encadré ce projet. Je souhaite remercier sincèrement les trois pour m'avoir inspiré à poursuivre dans cette voie.

Benoit, je te remercie d'avoir été présent quotidiennement au L2C. Merci pour ton aide et de m'avoir toujours poussé à aller plus loin, même lorsque je ne voyais pas clairement la direction à suivre. Je me souviens encore clairement de nos mesures sur ma première barre de Hall avec un effet de grille, des plateaux de Hall et des oscillations Shubnikov-de Haas, ainsi que de l'enthousiasme que cela a suscité chez toi. À la veille des vacances de Noël 2019, cet engouement et vos félicitations, à toi et Frédéric, ont été un cadeau merveilleux auquel je me suis accroché maintes fois lors des moments plus difficiles. La quantité de connaissances acquise à tes côtés est vertigineuse, et j'espère que nous aurons à nouveau l'occasion de travailler ensemble.

Frédéric, je te remercie sincèrement pour ton soutien permanent et ton humanité, non seulement tout au long de ma thèse, mais aussi pour ma carrière future. Ton regard extérieur a été d'une valeur inestimable pour apprécier les progrès accomplis lorsque j'avais l'impression de stagner, ainsi que pour envisager le chemin qui reste à parcourir. Merci pour toutes les leçons, scientifiques et autres, que tu m'as enseignées et qui ont fait de moi un meilleur chercheur.

Sébastien, je te suis reconnaissant pour ton encadrement, tant sur le plan scientifique que personnel, et pour m'avoir ouvert d'autres perspectives dans mon travail de doctorat, notamment avec Annealsys et l'enseignement. Nos discussions m'ont souvent permis de prioriser mes activités lorsque je me dispersais dans trop de directions, sans jamais me brider pour autant.

Ensuite, je souhaite exprimer ma gratitude à l'ensemble des membres du jury : Eric Tournié, Michel Goiran, Wilfrid Poirier, Fabian Hartman et Isabelle Sagnes, d'avoir accepté d'évaluer mon travail. Merci infiniment pour vos précieux commentaires et les échanges lors de la soutenance. J'espère que nous aurons encore de nombreuses discussions scientifiques à l'avenir.

Je tiens à remercier toutes les personnes avec lesquelles j'ai eu la chance d'interagir au cours de cette thèse. Tout d'abord, les équipes du L2C et de l'IES. Merci aux Christophes : Roblin, pour ton aide constante en salle blanche, Consejo, sans qui peu d'expériences auraient pu être réalisées, et Coillot, pour ta présence, nos discussions et tes précieux conseils en laboratoire. Merci à Sandra Ruffenach pour ton énergie et tes encouragements.

Un grand merci à toutes les personnes de la CTM. Pour son bon fonctionnement, je remercie Frédéric Pichot, Renaud Félix et Jean-Marie Peiris. Merci à Dilek Cakiroglu, ma mentore en microfabrication, ainsi qu'à Daniel Diaz et Zeineb Loghmari, d'avoir toujours répondu présents lorsque j'ai sollicité votre aide.

Merci à Ivan Castillo et Haitham Hrich, mes "jumeaux" de thèse, d'avoir partagé cette expérience et ces pauses café avec moi. Pour prolonger l'analogie familiale, merci à mon grand frère Sebastian Gebert de m'avoir si chaleureusement accueilli, et merci à mon "Benjamin", Benhamou-Bui, d'avoir été une présence rafraîchissante lors de ma dernière année. Je vous souhaite, à toi et à Juliette, de vous épanouir pendant vos propres thèses. Merci à Tristan Beranger pour ces soirées, enfin, peut-être pas toutes, et merci à Maria Szola d'apporter autant de gentillesse depuis la Pologne au sein de notre groupe de doctorants.

Enfin, pour conclure, j'aimerais remercier ma famille et mes amis qui ont toujours cru en moi et m'ont soutenu. Merci à Théophile, Martin, Mathilde et bien sûr Andréa, d'avoir créé un foyer si merveilleux et d'avoir partagé tant d'aventures avec moi. Merci pour tous ces moments que nous avons vécus ensemble.

Abstract

The quantum spin Hall effect is a unique phase of matter in which the bulk of a two-dimensional material is an insulator, but its edges are perfect conductors, composed of special quantum states generated by the non-trivial topology of the band structure. These edge states, composed of massless Dirac fermions propagating in opposite directions according to their spin polarization, are protected from backscattering by time-reversal symmetry. The conductance of these edge states is quantized, similar to that of edge states in the quantum Hall effect regime, but without application of an external magnetic field. These exotic edge states are one of the remarkable consequences of the inverted band structure of materials called topological insulators.

However, the quantum spin Hall effect has been rarely observed until now. Indeed, this quantum phase was first expected theoretically in graphene in 2005 [KM05]. However, the spin-orbit coupling, which is one of the essential effects at the origin of this topological phase, is too weak for the quantum spin Hall effect to be observed there [BMC+22]. Soon, another two-dimensional system was proposed, namely, HgTe/HgCdTe based quantum wells [BHZ06] in which the quantum Hall effect was observed for the first time in 2007 [KWB+07]. In parallel, another system, composed of composite quantum wells formed from Sb-based III-V semiconductors, was proposed in 2008 [LHQ+08]. These topological insulators have the advantage of being designed on mature growth and process technologies available in a large number of laboratories. Finally, another more recent work has demonstrated the spin quantum Hall effect in a two-dimensional material, WTe2 [WFG+18], at much higher temperatures. These last results have motivated a large part of the scientific community for the search of new semiconductor structures, in which the topological energy gap could be increased and the QSHE observed at room temperature. Unfortunately, the band structure of II-VI semiconductors is very temperature dependent, which limits the observation of the desired effect to ultra-low temperatures only. By constrast, unlike HgTe/HgCdTe wells, the band structure of III-V semiconductor-based wells varies very weakly with temperature. Therefore, in 2017, it was proposed in the Charles Coulomb Laboratory (L2C) to significantly increase the gap of these topological insulators by adding a third layer in the Sb-based composite quantum well [KIM+17]. Indeed, the inversion asymmetry of the InAs/GaSb bilayer structure brings the gap opening at non-zero k value by Rashba effect, while higher energies are expected at the Γ point due to quantum confinement for symmetric structures.

In this thesis work, the objectives are not only to show the significant energy gap increase for these original heterostructures, but also to highlight the existence of edge states.

To carry out this study, we first characterized the different III-V based growths provided by our partner team led by E.Tournié from the Institut Electronique et Systèmes (IES). Processes for the fabrication of Hall bar devices with an top dielectric gate in order to be able to move the Fermi level in the band structure have been developed in the clean room of the Centrale de Technologie de Montpellier (CTM). This was made possible by the interaction with the group of S. Höfling (Technische Physik) of the University of Würzburg. This device fabrication investigations allowed the fabrication of a base of devices which could be measured by magneto-transport measurements from 300 mK to 300 K and under a magnetic field up to 13 T. We also took advantage of a collaboration with the Laboratoire National des Champs Magnétiques Intenses de Toulouse (LNCMI) to probe the evolution of Landau levels under pulsed fields up to 55 T.

This manuscript is therefore organized as follows: in the first chapter, I present a review of a recent work on topological insulators, from the emergence of this subject with graphene to the beginning of this work. I also develop the theoretical concepts behind the experiments

presented in this thesis. In chapter 2, I develop the experimental details and present the different InAs/GaSb based growths studied. I also detail the fabrication processes of the devices made from these same growths. Chapter 3 is devoted to the magneto-transport measurements for the different devices. I demonstrate the validity of the theoretical calculations of the band structure by showing a clear increase of the band gap size for the InAs/GaSb based structures, as well as the existence of an edge conduction whose properties are compatible with the topological character expected for these structures.

Abstract-Français

L'effet Hall quantique de spin est une phase unique de la matière dans laquelle le cœur d'un matériau bi-dimensionnel est un isolant, mais ses bords sont de parfaits conducteurs, composés d'états quantiques particuliers générés par la topologie non-triviale de la structure de bandes. Ces états de bords, composés de fermions de Dirac sans masse se propageant dans des directions opposées selon leur polarisation de spin, sont protégés de la rétro-diffusion par la symétrie par renversement du temps. La conductance de ces états de bords est quantifiée, de manière similaire à celle des états de bords en régime d'effet Hall quantique, mais sans application d'un champ magnétique extérieur. Ces états de bords exotiques sont l'une des conséquences remarquables de la structure de bandes inversée des matériaux appelés isolants topologiques.

Pourtant, l'effet Hall quantique de spin n'a été que rarement observé jusqu'à présent. En effet, cette phase quantique a tout d'abord été attendue théoriquement dans le graphène en 2005 [KM05]. Cependant, le couplage spin-orbite, qui se trouve être l'un des effets essentiels à l'origine de cette phase topologique, y est trop faible pour que l'effet Hall quantique de spin n'y soit observé [BMC+22]. Rapidement, un autre système bi-dimensionnel a été proposé, à savoir, des puits quantiques à base de HgTe/HgCdTe [BHZ06] et l'effet Hall quantique y a été observé pour la première fois en 2007 [KWB+07]. En parallèle, un autre système, composé de puits quantiques composites formés à partir de semi-conducteurs III-V à base d'antimoine, a été proposé en 2008 [LHQ+08]. Ces isolants topologiques ont l'avantage d'être conçus sur une technologie de croissance et de process mature et disponible dans un grand nombre de laboratoires. Enfin, un autre travail plus récent a mis en évidence l'effet Hall quantique de spin dans un matériau bi-dimensionnel, le WTe2 [WFG+18], à des températures bien plus élevée. Ce résultat a motivé une partie de la communauté pour augmenter l'énergie du gap topologique dans les semi-conducteurs pour espérer observer l'effet Hall quantique de spin à hautes températures. Or, la structure de bandes de semi-conducteurs II-VI est très dépendante de la température, ce qui limite malheureusement l'observation de l'effet recherché aux ultra-basses températures [TMK+16]. Cependant, contrairement aux puits de HgTe/HgCdTe, la structure de bandes des puits à base de semi-conducteurs III-V varie très peu en fonction de la température. En 2017, il a donc été proposé dans l'équipe du Laboratoire Charles Coulomb (L2C) d'augmenter de manière significative le gap de ces isolants topologiques en ajoutant une troisième couche de semi-conducteur dans le puits quantique composite à base d'antimoine pour supprimer l'asymétrie d'inversion de la structure [KIM+17]. En effet, l'asymétrie d'inversion de la structure bicouche InAs/GaSb amène l'ouverture du gap à une valeur k non nulle par effet Rashba, alors que des énergies plus élevées sont attendues au point Γ en raison du confinement quantique pour des structures symétriques.

Dans ce travail de thèse, les objectifs sont de non seulement montrer l'augmentation significative de la taille du gap pour ces heterostructures originales, mais aussi mettre en évidence l'existence des états de bord.

Pour mener à bien cette étude, nous avons tout d'abord caractérisé les différentes croissances à base de III-V fournie par notre équipe partenaire dirigée par E.Tournié de l'Institut Electronique et Systèmes (IES). Des procédés de fabrication de dispositifs de barre de Hall, disposant d'une grille diélectrique supérieure afin de pouvoir déplacer le niveau de Fermi dans la structure de bande, ont été mis au point dans la salle blanche de la Centrale de Technologie de Montpellier (CTM). Cela a été rendu possible notamment grace à l'interaction avec le groupe de S.Höfling (Technische Physik) de l'université of Würzburg. Cette mise au point des procédés de fabrication a permis de fournir une base de dispositifs permettant des mesures de magnéto-transport de 300 mK à 300 K et sous un champ magnétique allant jusqu'à 13 T. Nous avons aussi profité d'une collaboration avec le Laboratoire National des Champs Magnétiques

Intenses de Toulouse (LNCMI) pour sonder l'évolution des niveaux de Landau sous des champ pulsés jusqu'à 55 T.

Ce manuscrit est de ce fait organisé de la manière suivante: dans le premier chapitre, je présente une revue des travaux récents autour des isolants topologiques, depuis l'émergence de ce sujet avec le graphène jusqu'au début de ce travail. Je développe également les concepts théoriques à la base des expériences présentées dans cette thèse. Dans le chapitre 2, je développe les détails expérimentaux et présente les différentes croissances à base d'InAs/GaSb étudiées. Je détaille également les procédés de fabrication des dispositifs réalisés à partir de ces mêmes croissances. Le chapitre 3 est consacré aux mesures de magnéto-transport pour les différents dispositifs. Je démontre la validité des calculs théoriques de la structure de bande en montrant une nette augmentation de la taille de la bande interdite pour les structures à base d'InAs/GaSb, ainsi que l'existence d'une conduction de bord dont les propriétés sont compatibles avec le caractère topologique attendu pour ces structures.

Contents

CHAPTER 1

InAs/GaSb: 2D topological insulators

1.1 Band theory and topology

Band theory

In the field of solid state physics, the set of approximations used in band theory distinguishes two categories of materials: metals and (band) insulators. This theory models the energy states accessible by electrons in the bulk of the material by bands of accessible energies and others forbidden. The determination of this band structure is done solving the Schrödinger equation from the Hamiltonian describing the system. The electrons obey the Fermi-Dirac distribution (see Eq. 1.1) and fill the energy bands. The last band completely filled is the valence band and the one above, in increasing order of energy, is the conduction band.

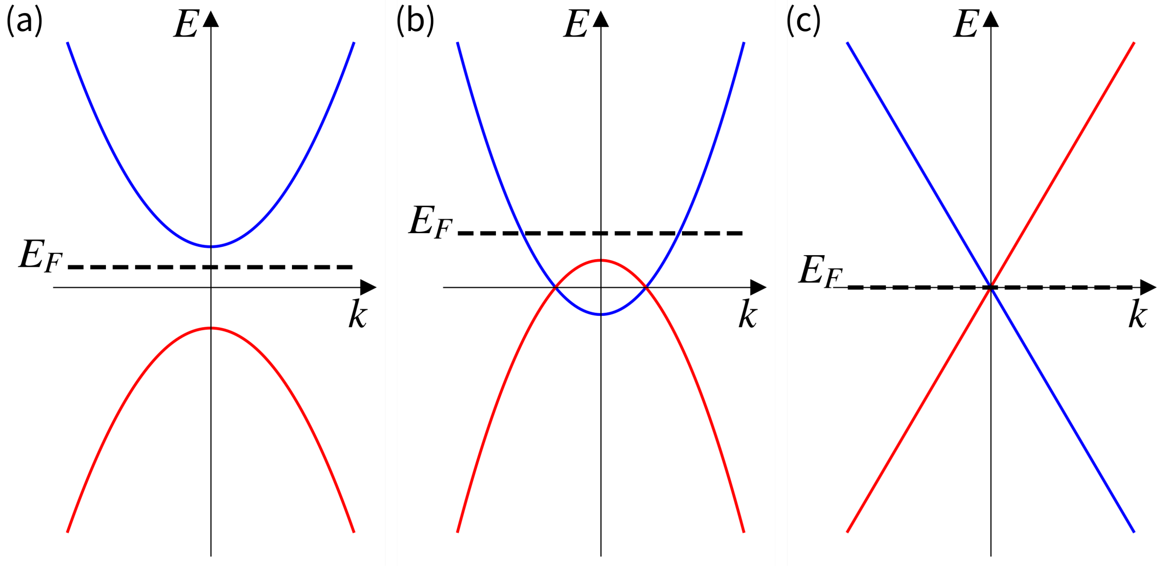

Figure 1.1: Schematic band structure of (a) an insulator, (b) a metal, (c) a Dirac cone. The blue lines represent the conduction band and the red lines correspond to the valence band. The dashed lines correspond to the Fermi energy E_F.

At low temperature ($T \to 0\,\mathrm{K}$), the distinction between insulators and metals is then made as follows:

- In an insulator, the Fermi level E_F (*i.e.* the maximum accessible energy state) is in the band gap separating the valence and conduction band. No unpopulated states are available so the Pauli exclusion principle leads the electrons to be frozen in the valence band. If the gap is small enough to be thermally activated then we speak of a semiconductor.
- In a metal, the valence and conduction bands overlap as shown in Fig. 1.1(b). In the extreme case, the gap is zero as for the Dirac cone shown in Fig. 1.1(c). The electrons can then access unpopulated states, and conduct the current.

Note that one can tune a semiconductor from an insulating state to a metallic state by changing the position of the Fermi level. In addition, for a semiconductor of small gap value, the insulating state can be thermally activated. It means that the thermal broadening of the Fermi-Dirac distribution is large enough to overlap both valence and conduction bands. Figure 1.2 shows the Fermi-Dirac distribution as a function of the energy E, for different temperatures T where the probability of occupation is defined as:

$$f(E) = \frac{1}{1 + e^{\frac{E-E_F}{k_B T}}}, \tag{1.1}$$

where E_F is the Fermi energy and k_B is the Boltzmann constant. In the extreme case $T = 0\,\mathrm{K}$, all allowed states are full for energies below the Fermi energy and empty for energies above. Figure 1.2 shows that for $k_B T = \frac{E_F}{10}$, states in a range depending of $k_B T$ have a non-negligible probability of occupation, even for energies above the Fermi level.

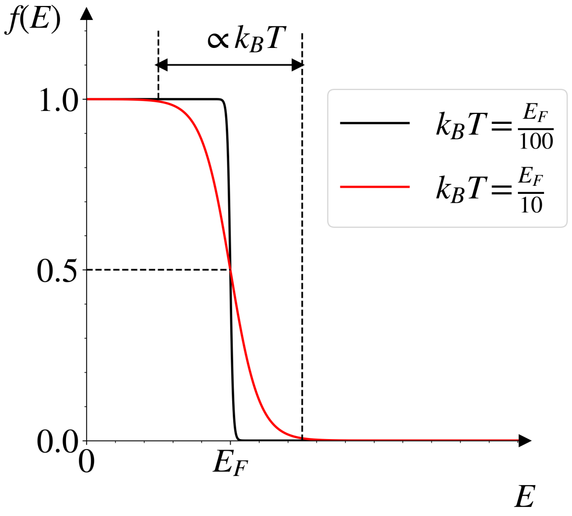

Figure 1.2: Fermi-Dirac distribution for different temperatures.

Topological band theory

Topology is a field of mathematics that classifies geometric objects according to robust properties. By robust properties, we adress their conservation despite continuous deformations of these objects. In the context of solid state physics, the application of topology concerns in particular the study of the continuous deformation of the band structure, *i.e.* of the Hamiltonian that describes the system, in particular of insulators. We can then define that two insulators are topologically equivalent if it is possible to continuously deform their Hamiltonians into each other without closing the gap. the topological object has topological properties which allow to classify it. This is notably the case of the geometric phase (or Berry phase), which is the time-independent phase, accumulated during the evolution of a state (*e.g.* described by a wave function) on a closed circuit in a parameter space. The berry phase associated with a trivial system is zero. Moreover, these topological classifications can also be conditioned by the conservation of a certain number of symmetries of the system (time reversal, particle-hole, inversion, translation, rotation, etc.). A first class of equivalence that we can consider is the one to which the vacuum belongs and is called trivial. It can be shown that when the crystal has an inversion symmetry, the Berry phase reduces to the parity of the Bloch wave function. If the product of the parity of the wave function on all points of high symmetry is even, then the system is trivial. If this product is odd, the system is non-trivial. Now there is only one way to obtain a system in which the parity is different in a precise point of the Brillouin zone, it is to have an inverted band structure. As soon as the structure is inverted, the system is non-trivial.

The determination of equivalence classes through the identification of topological invariants, and respecting the prescribed symmetries, may seem a very conceptual work in addition to being tedious. The Royal Swedish Academy of Sciences has nevertheless awarded the Nobel Prize in Physics in 2016 to D. J. Thouless, D. M. Haldane and J. M. Kosterlitz '*for theoretical discoveries of topological phase transitions and topological phases of matter.*' These discoveries have notably contributed to explain the Quantum Hall effect which is one of those phases whose topology is non-trivial.

Bulk-edge correspondence

The particular interest in topological (*i.e.* non-trivial) insulators comes from the existence of metallic edge states at the interface between two different topological phases. And so, at the edge of any topological insulator, *i.e.* at the interface between it and vacuum. As an illustration of this principle, one can interpret the appearance of edge states as follows: the value of a topological invariant cannot change without gap closure. Thus the difference between a topological invariant at the interface between vacuum (trivial insulator) and a topological insulator can only be made by having a gap closure at the edge of the TI. This principle is called the bulk-edge equivalence. Figure 1.3 illustrates the bulk-edge correspondence principle for a Quantum Spin Hall Insulator (QSHI) in contact with a trivial one. Because of the inversion symmetry, this topological insulator differs from the trivial case by the inversion of the respective parity (s-type or p-type) of the valence and conduction bands. These topological gaps are sometimes referred to as inverted gaps. The emergence of this topological phase is developed in Section 1.2.

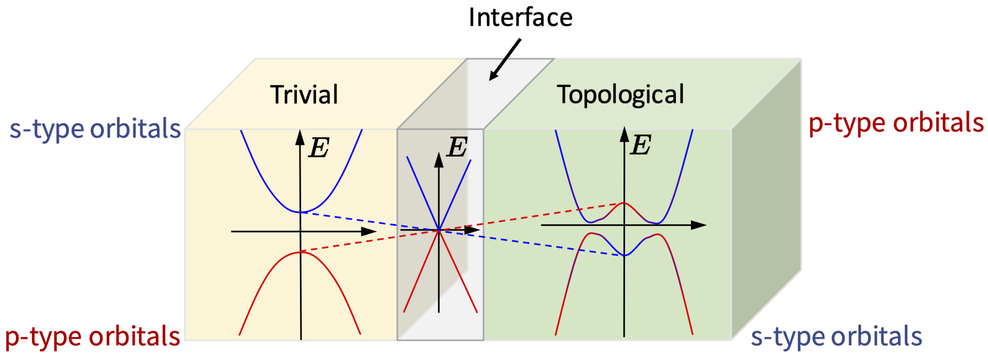

Figure 1.3: Schematic illustration of the bulk-edge correspondence. The respective band structures are directly superimposed on each associated region. Note that here not only the insulators but also the interface are shown in volume for clarity. The interface should be a 2D plane for 3D insulators, or a 1D edge channel for a 2D topological insulator. In addition, here, the topological phase transition occurs in the real space, but the bulk-edge correspondence is expected for any topological phase transition in the full parameter space.

Topological protection of edge states

We have just seen that the bulk-edge correspondence allows us to understand the existence of these topological edge states. To understand even more the interest in these insulators is the topological protection of these edge states which makes them immune to impurities, and whose conduction does not depend on the material. In the following, we take up the simple argument presented by X-L. Qi and S-C. Zhang in two papers [QZ10, QZ11]. The first of the necessary conditions for the topological protection of these edge states is the spatial separation of the counter-propagating states, illustrated for a 2-terminal device in Fig. 1.4 (a, b). Let us take the case of the quantum Hall effect to begin with: the strong magnetic field applied to reach the QHE forces the electrons to travel around the edge of the material in a single direction. If the spatial separation between the two counter-propagating channels is large enough, then it is impossible for an electron to be backscattered. Even when it encounters an impurity, as shown in Fig. 1.4(a), the edge state electron simply takes a detour and continues to move in the same direction.

The situation is similar for the QSHE In the case of QHE, a strong magnetic field is applied, and breaks the time reversal symmetry. Conversely, in a QSHE, the magnetic field is zero and the time-reversal symmetry is preserved. In the absence of a magnetic field, we then consider a system with spin, which leads to 4 edge states, as shown in Fig. 1.4(b) (2 directions $\times$ 2 spins). The spatial separation for a 2D system implies the existence of 2 counter-propagating states for each edges. Nevertheless, it is precisely the reversal symmetry that protects the electrons from backscattering from one state to the other. Indeed, spatial separation imposes a spin-flip for a back-scattered electron. Either the spin rotates clockwise (*i.e.* by π) or counterclockwise (*i.e.* by $-\pi$). That difference of 2π is associated to a -1 factor for the wave function of a spin-1/2 particle and leads to destructive interference of the two paths. Therefore, the backscattering of electrons is suppressed.

In both QHE and QSHE, the topological protection of edge states from backscattering leads to quantized value of conductance, as shown in Section 1.3.3.

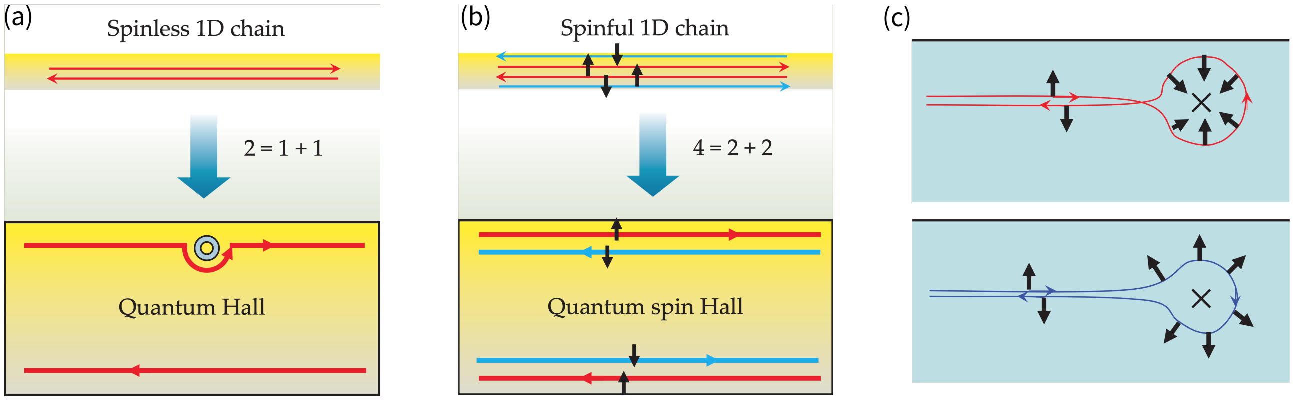

Figure 1.4: (a) Schematic representation of a spinless one-dimensional system has both a forward and a backward channel. Those two basic degrees of freedom are spatially separated in a 2D system. The upper edge contains only a forward mover and the lower edge has only a backward mover. The states are robust: They will go around an impurity without scattering. (b) A spinful 1D system has four basic channels, which are spatially separated in a 2D system: The upper edge contains a forward mover with up spin and a backward mover with down spin, and conversely for the lower edge. (c) Schematic representation of a quantum spin Hall edge state scattered by a nonmagnetic impurity. The spin-flip is counterclockwise along the red curve and clockwise along the blue curve (figure and caption from [QZ10]).

1.2 The emergence of topological insulators

1.2.1 Graphene

In 2005, Kane and Mele used the case of graphene to propose a new electronic state of matter, topologically distinct from a band insulator [KM05]. Indeed, graphene, a monolayer of carbon atoms organized in a honeycomb structure, presents a low-energy electronic state at very low temperature, which is sensitive to perturbative terms, and in particular that of the spin-orbit (SO) coupling. The unit cell of the associated Bravais lattice, shown in Fig. 1.5, contains 2 atoms located at δ_1 and δ_2 with respect to the lattice origin. Graphene is described by a tight-binding Hamiltonian which takes into account only the nearest-neighbor hopping term:

$$\mathcal{H} = \sum_{\langle i,j \rangle \alpha} t c^{\dagger}_{i,\alpha} c_{j,\alpha}, \tag{1.2}$$

where $c^{\dagger}_{i,\alpha}(c_{i,\alpha})$ is the fermionic operator that creates (annihilates) an electron at the $\alpha = A, B$ site whose position is $\mathbf{r_i}$, and t the hopping constant.

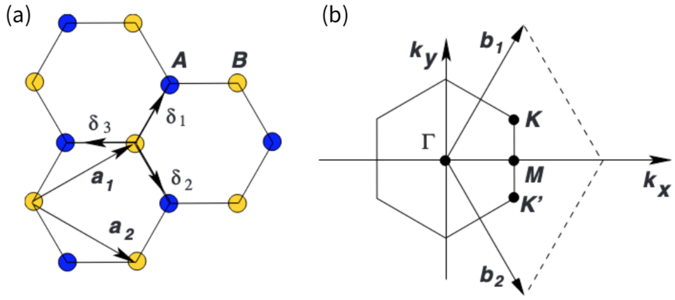

Figure 1.5: Honeycomb lattice and its Brillouin zone. Left: lattice structure of graphene, consisting of two interpenetrating triangular lattices. The unit vectors of the lattice are $\mathbf{a_1}$ and $\mathbf{a_2}$, and the nearest neighbor vectors are $\delta_i, i = 1, 2, 3$. Right: corresponding Brillouin zone. The Dirac cones are located at points K and K' (figure and caption after Ref. [NGP$^+$09])

Introducing SO coupling, Kane and Mele also considered a second neighbor tight-binding term, which depends on the spin. Equation 1.2 becomes :

$$\mathcal{H} = \sum_{\langle ij \rangle \alpha} t c^{\dagger}_{i,\alpha} c_{j,\alpha} + \sum_{\langle\langle ij \rangle\rangle \alpha\beta} i t_2 \nu_{i,j} s^z_{\alpha\beta}, c^{\dagger}_{i,\alpha} c_{j,\beta}, \tag{1.3}$$

where $s^z_{\alpha,\beta}$ is a Pauli matrix representing the electron spin, and ν_{ij} is a spin-dependent amplitude. $\nu_{ij} = -\nu_{ji} = \pm 1$, depending on the orientation of the two closest bonds that the electron crosses on its way from the j site to the i site. $\nu_{ij} = +1(-1)$ if the electron makes a left turn (right turn) to reach the second bond. At low energies, it can be shown by solving Eq. 1.3 that SO coupling opens gaps of opposite signs at the K and K' points $\Delta_{SO} = 3\sqrt{3}t_2$.

Fig. 1.6 shows the one dimensional energy bands for a strip where the edges are along the zig-zag direction in the graphene plane. The bulk band gaps at the one dimensional projections of the K and K' points are clearly seen. Two edge states traverse the gap, connecting the K and K' points. These edge states are called helical because the direction of propagation is related to the orientation of the associated spin. In doing so, they are protected from back-scattering.

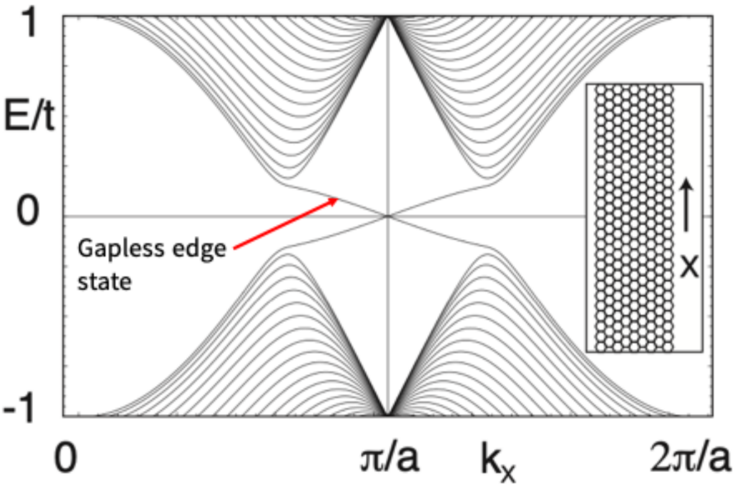

Figure 1.6: Calculated band structure for a strip of monolayer graphene with edges along the zig-zag direction (x-axis) as shown in the inset. The parameters are $t_2/t = 0.03$ (figure and caption from Ref. [KM05]).

As the authors point out, the particular interest in graphene in this article is also related to the technical progress in the realization of graphene monolayers at that time. Unfortunately, experimental observations of these edge states are hampered by the small gap size $\Delta = 45\,\mu\mathrm{eV}$ [BMC+22], created by the SO coupling. Yet, as Kane and Mele (2005) themselves state in their paper, their work on graphene ”*may provide a starting point for the search for other spin-Hall insulators in two dimensional or in layered materials with stronger SO interaction.*”.

1.2.2 HgCdTe and the Bernevig–Hughes–Zhang (BHZ) model

Indeed, in the following year a paper by Bernevig, Hughes and Zhang (BHZ) was published, proposing another candidate material for the observation of insulating QSH [BHZ06]. They calculated the band structure in HgTe quantum well (QW) confined between CdTe barriers. Although this structure is not the focus of this thesis, the calculation of the band structure of this topological insulator is briefly developed. A first point concerns the respective band structures for the two respective bulk materials, HgTe and CdTe. As Hg and Te are heavy atoms, relativistic corrective terms in the fine structure model have to be taken into account. We are particularly interested in these corrections for the bands related to the $6s$ electrons from Hg atoms (Cd respectively) and the $5p$ electrons of Te atoms. The first correction is the Darwin term $\mathcal{H}_D$, related to the effect of the mean electric field of the nucleus [JC07]. As shown in Fig. 1.7, it shifts the energy level of the s states. The second correction is the mass velocity of the electron $\mathcal{H}_{mv}$. Due the greater mass and core charge in Hg, the drop in energy is very significative for the s state in HgTe. The last correction is the term induced by the spin-orbit coupling $\mathcal{H}_{SO}$, which splits the p states into two bands. In HgTe, as the s and p states were close enough in energy due to the mass velocity correction, the spin-orbit splitting shifts the Γ_8 states above the Γ_6 states. These two bands are inverted compared to the usual situation, as in CdTe.

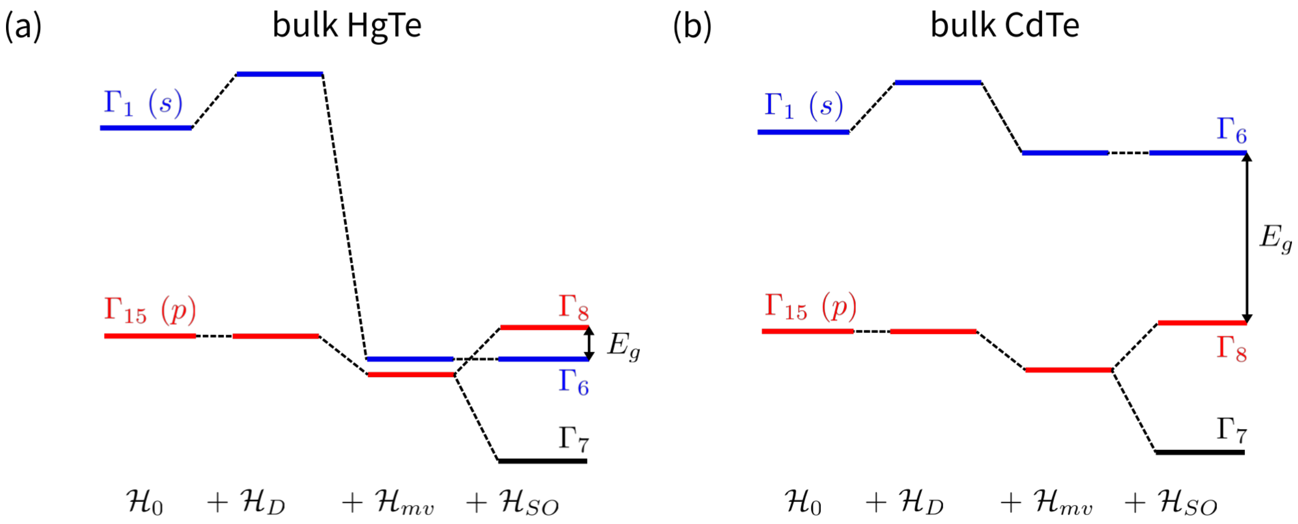

Figure 1.7: Fine structure corrections to the band energies at the Γ point applied to the unperturbed Hamiltonian $\mathcal{H}_0$ for (a) HgTe and (b) CdTe. The correction terms are the Darwin term $\mathcal{H}_D$, the velocity mass term $\mathcal{H}_{mv}$ and the spin-orbit interaction $\mathcal{H}_{SO}$ (figure adapted from Ref. [JC07]).

From the two bulk band structures near the Γ point shown in Fig. 1.8(a), BHZ established the Hamiltonian corresponding to a HgTe layer confined between CdTe barriers. They neglected the effect of the Γ_7 band, and proposed a 4 QW subbands model where the $|E1, m_J\rangle$ QW subband state is a linear combination of the $\left|\Gamma_6, m_J = \pm\frac{1}{2}\right\rangle$ and $\left|\Gamma_8, m_J = \pm\frac{1}{2}\right\rangle$ states, while the $|H1, m_J\rangle$ QW subband state is a linear combination of $\left|\Gamma_8, m_J = \pm\frac{3}{2}\right\rangle$.

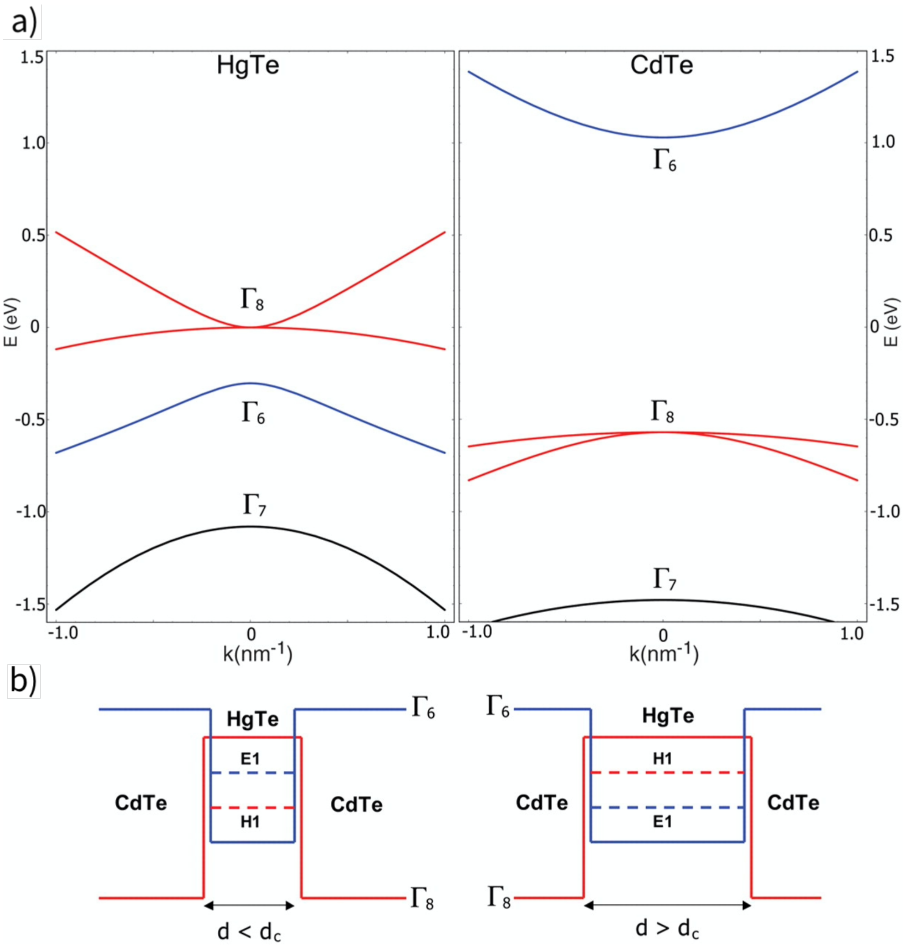

Figure 1.8: (a) Bulk energy bands of HgTe and CdTe near the G point. (b) The CdTe-HgTe-CdTe quantum well in the normal regime E1 > H1 with $d < d_c$ and in the inverted regime H1 > E1 with $d > d_c$. In this and other figures, Γ_8/H1 symmetry is indicated in red and Γ_6/E1 symmetry is indicated in blue (figure and caption from Ref. [BHZ06]).

They deduced from parity arguments that the effective Hamiltonian takes the form:

$$\begin{aligned} \mathcal{H}_{eff}(k) &= \begin{pmatrix} \mathcal{H}(k) & 0 \\ 0 & \mathcal{H}^{\star}(-k) \end{pmatrix}, \\ \mathcal{H}(k) &= \varepsilon(k) + d_i(k)\sigma_i, \end{aligned} \tag{1.4}$$

where σ_i are the Pauli matrices and

$$\begin{aligned} \varepsilon(k) &= \mathcal{C} - \mathcal{D}(k_x^2 + k_y^2), \\ d_1 + id_2 &= \mathcal{A}(k_x + ik_y), \\ d_3 &= \mathcal{M} - \mathcal{B}(k_x^2 + k_y^2), \end{aligned} \tag{1.5}$$

with $\mathcal{A}$, $\mathcal{B}$, $\mathcal{C}$, $\mathcal{D}$ and $\mathcal{M}$ parameters depending of the QW geometry. By changing the sign of the mass $\mathcal{M}$ from negative to positive, one gets a gap closing at $k = 0$. Indeed, based on the thickness d of the HgTe quantum well, one can engineer the energy of the H1 and E1 band. Under a critical thickness d_c the H1 band is higher in energy than the E1 band as shown in Fig. 1.8(b). Figure 1.9 shows the energy spectra of a HgTe layer confined between CdTe barriers. A stricking result of these tight binding calculations is that when the HgTe has a thickness exceeding 6.8 nm, the system is a QSHI

The simplified model given in Eqs. 1.4, 1.5 is known as the BHZ model. It is basically two copies of the massive Dirac Hamiltonian $\mathcal{H}(k)$

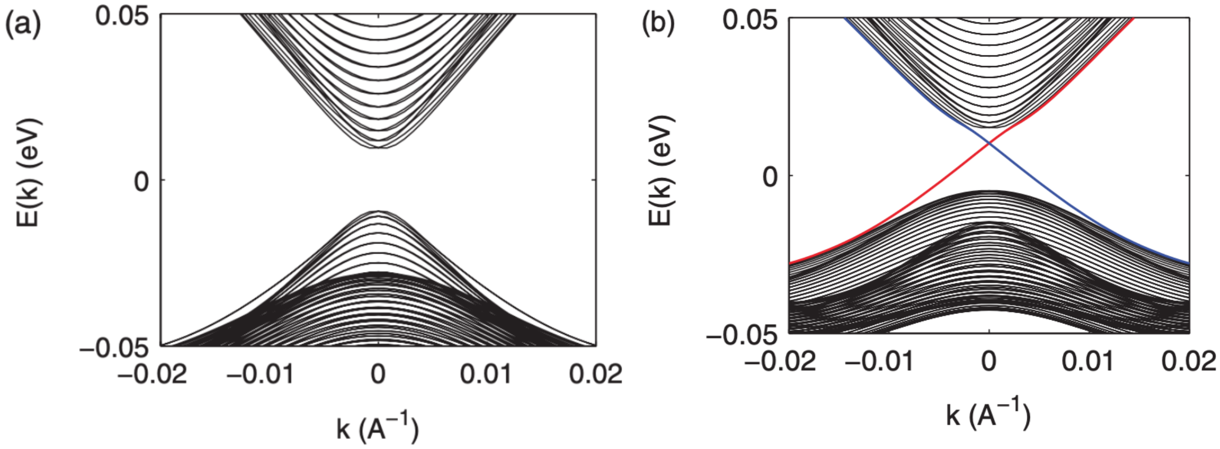

Figure 1.9: The energy spectra of the quantum wells for a thin ($d < d_c$) HgTe layer (a) and a thick ($d > d_c$) HgTe layer. The thin quantum well has an insulating energy gap, but inside the gap in the thick quantum well are edge states, shown by red and blue lines. (from Ref. [QZ10, QZ11]).

This simplified Hamiltonian allows us to generalize some properties necessary for any material candidate to be a topological insulator:

- an electron-like band (s-type parity),
- a hole-like band (p-type parity),
- a k-linear coupling between these two bands,
- an inverted gap separating these two bands.

In semiconductors with strong spin-orbit coupling, the first three properties are verified. It is then sufficient that the band structure is inverted, *i.e.* that the hole-like band is higher in energy than the electron-like band.

This theoretical work is very quickly followed by an experimental verification and in particular transport measurements at low temperature [KWB+07]. In 2007, the group of L. W. Molenkamp has demonstrated the existence of helical edge states in HgCdTe quantum wells. Figure 1.10 shows the longitudinal resistance in both normal and topological insulator based on HgCdTe. The $V_g - V_{thr} = 0\,\mathrm{V}$ position corresponds to the gap regime. It is clear that the resistance diverges in the gap for a normal insulator (black line) while finite plateaus of resistance are observed for inverted gap regime (blue, green and red lines). For devices small enough compared to the inelastic mean free path $\lambda \approx 3$ µm, the edge states are protected from backscattering. According to the Landauer–Büttiker formalism (see Section 1.3.3), the expected quantized value of conductance $G = 2e^2/h$ is observed for various small devices. This was the first experimental observation of this new electronic state of matter. This achievement is all the more remarkable since few research groups are able to grow HgCdTe layers and to fabricate devices from it. Nevertheless, these same technological difficulties have motivated the search for other candidates as topological insulators. In addition, a relatively small inverted band gap (typically lower than 15 meV) in HgTe QWs grown on CdTe buffer makes it difficult to observe the quantized edge conductance at elevated temperatures. Note that strain engineering using virtual substrate increases the band-gap up to 55 meV in compressively strained QWs [LLB+16]. Such high values, however, occur at low temperatures only, whereas increasing temperature yields the band-gap vanishing and topological phase transition into trivial state [TMK+16, KYB+16, IKD+16, MRK+17, KKJ+18]. Hence, the observation of the QSHI state in HgTe Qws is so far limited to 15 K [BSH+18].

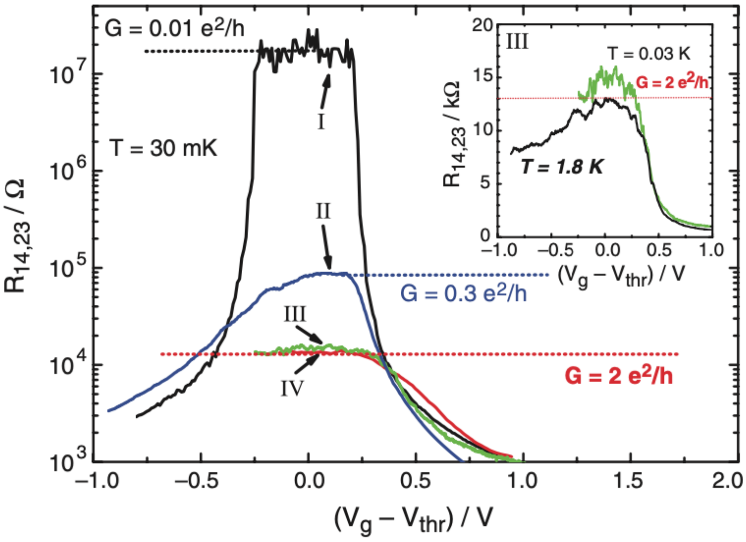

Figure 1.10: (a) The longitudinal four-terminal resistance, $R_{14,23}$, of various normal ($d = 5.5\,\mathrm{nm}$) (I) and inverted ($d = 7.3\,\mathrm{nm}$) (II, III, and IV) QW structures as a function of the gate voltage measured for $B = 0\,\mathrm{T}$ at $T = 30\,\mathrm{mK}$. The device sizes are $(20.0 \times 13.3)\mathrm{µm}^2$ for devices I and II, $(1.0 \times 1.0)\mathrm{µm}^2$ for device III, and $(1.0 \times 0.5)\mathrm{µm}^2$ for device IV. The inset shows $R_{14,23}(V_g)$ of two samples from the same wafer, having the same device size (III) at 30 mK (green) and 1.8 K (black) on a linear scale. (figure and caption from Ref. [LHQ+08]).

1.2.3 InAs/GaSb quantum wells

As early as 1977, Sasaki *et al.* investigated the band inversion at the interface between InAs/-GaSb. This inverted regime was believed to be a semi-metallic state but an hybridization gap appears at finite k, which can be modelled by the BHZ model. As early as 2008, Liu *et al.* proposed a new candidate based on InAs/GaSb quantum wells, confined between AlSb barriers [LHQ+08]. QSHIs based on bilayers of InAs/GaSb QWs are attracting considerable interest compared to HgTe QWs due to their ease of fabrication. However this system has no structural inversion symmetry, unlike the previous case. Note that in the case of InAs/GaSb bilayers, the hole band and the electron band do not lie in the same layer. The $H1$ band corresponds to the valence band of the GaSb layer and is 150 meV higher than the $E1$ band in the conduction band of the InAs layer. As a consequence of this inverted band sequence, the two bands cross at finite k. However, a small hybridization gap is opened at the crossing points due to the mixing between $E1$ and $H1$, as shown in Fig. 1.11.

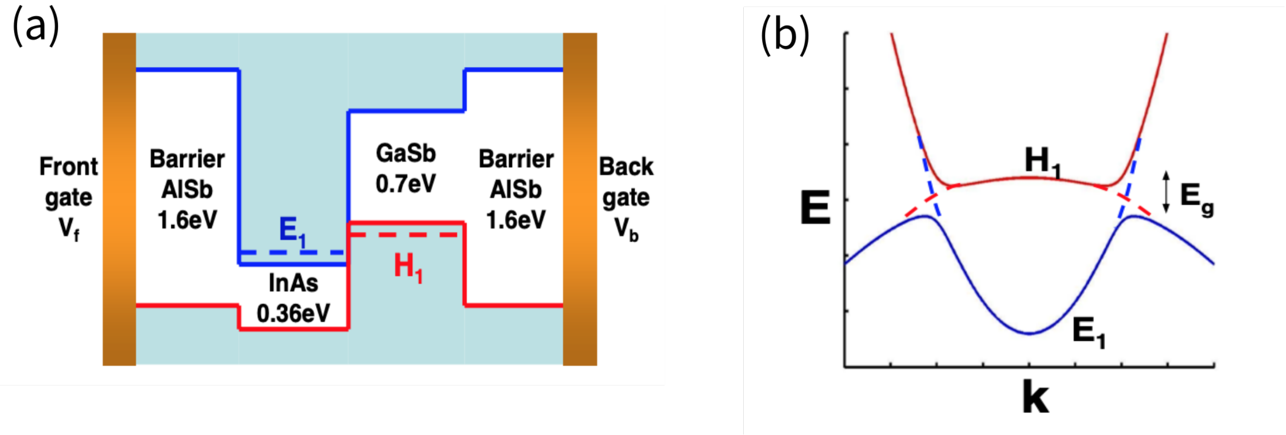

Figure 1.11: (a) Bandgap and band offset diagram for an asymmetric AlSb/InAs/GaSb/AlSb structure. The left AlSb barrier layer is connected to a front gate while the right barrier is connected to a back gate. The $E1$ subband is localized in the InAs layer and $H1$ is localized in the GaSb layer. The outer AlSb barriers provide an overall confining potential for electron and hole states. (b) Schematic band structure diagram. The dashed line shows the crossing of the edge states in the inverted regime. Due to the hybridization between $E1$ and $H1$, the gap E_g appears (figure and caption from Ref. [LHQ+08]).

The calculation of the band structure is performed using the BHZ Hamiltonian $\mathcal{H}_0$, considering 4 states in the "*spin basis*": $\{|E_1, {}^1\!/_2\rangle, |H_1, {}^1\!/_2\rangle, |E_1, -{}^1\!/_2\rangle, |H_1, -{}^1\!/_2\rangle\}$. Only the terms up to quadratic powers of k are considered:

$$\mathcal{H}_0 = \varepsilon(k)\mathbb{I}_{4x4} + \begin{pmatrix} \mathcal{M}(k) & Ak_+ & 0 & 0 \\ Ak_- & -\mathcal{M}(k) & 0 & 0 \\ 0 & 0 & \mathcal{M}(k) & -Ak_- \\ 0 & 0 & -Ak_+ & -\mathcal{M}(k) \end{pmatrix}, \tag{1.6}$$

where $\varepsilon(k) = C_0 + C_2k^2$, $\mathbb{I}_{4x4}$ is the 4×4 identity matrix, and $\mathcal{M}(k) = M_0 + M_2k^2$. The total Hamiltonian $\mathcal{H}$ takes into account two other terms. The first term is due to the zinc-blende structure which has two different atoms per unit cell, leading to bulk inversion asymmetry (BIA). The second term is due to the asymmetric structure of the quantum well (SIA), and results in a k-linear Rashba term for electrons. The k-cubic term for holes is neglected. The additional terms are expressed in the previous basis as:

$$\mathcal{H}_{BIA} = \begin{pmatrix} 0 & 0 & \Delta_e k_+ & -\Delta_0 \\ 0 & 0 & \Delta_0 & \Delta_h k_- \\ \Delta_e k_- & \Delta_0 & 0 & 0 \\ -\Delta_0 & \Delta_h k_+ & 0 & 0 \end{pmatrix}, \quad \mathcal{H}_{SIA} = \begin{pmatrix} 0 & 0 & i\xi_e k_- & 0 \\ 0 & 0 & 0 & 0 \\ -i\xi_e^\star k_+ & 0 & 0 & 0 \\ 0 & 0 & 0 & 0 \end{pmatrix}. \tag{1.7}$$

The parameters $\Delta_h, \Delta_e, \Delta_0$ and ξ_e depend on the quantum well geometry. From the pure BHZ Hamiltonian, there is a topological phase transition when the gap is closing (*i.e.* $M_0 = 0$), and quantum spin Hall phase corresponds to the region $M_0/M_2 < 0$. Liu *et al.* verified that there is an adiabatic connection between the BHZ Hamiltonian $\mathcal{H}_0$ and the full Hamiltonian $\mathcal{H}$, meaning that the QSH state is preserved as long as the energy gap between $E1$ and $H1$ remains finite. However both terms modify the quantum phase transition between QSH phase and trivial insulator (TI). Figure 1.11(b) shows that the gap-closing occurs at finite-k, rather than at the Γ point.

In addition, Liu *et al.* also demonstrated that the QSH-TI phase transition can be tuned with reasonable gate voltages. A dual-gate geometry is required to independently tune the relative position between the E_1 and H_1 band edges and the Fermi level. Figure 1.12 shows the phase diagram in the (V_f, V_b) plane, where V_f and V_g correspond to the gate voltages applied on the front and back gate respectively. The calculation of the phase diagram is performed by a self-consistent Poisson-Schrödinger type calculation with realistic parameters for InAs/GaSb quantum wells. The respective thicknesses of InAs and GaSb layer is $d_1 = d_2 = 10\,\text{nm}$.

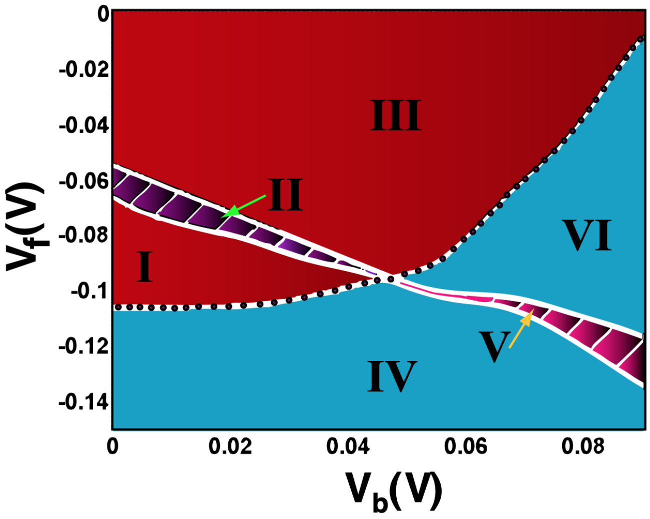

Figure 1.12: The phase diagram for different front (V_f) and back (V_b) gate voltages. Regions I, II, III are in the inverted regime, in which the striped region II is the QSH phase with Fermi- level in the bulk gap, and I, III are the p-doped and n-doped inverted system. Regions IV, V, VI are in the normal regime, in which the striped region V is the NI phase with Fermi level in the bulk gap, and IV, VI are the p-doped and n-doped normal semiconductors. The well configuration is set as $d_1 = d_2 = 10\,\text{nm}$, and the AlSb barrier thickness is taken 30 nm on each side in the self-consistent calculation. V_f and V_b are defined with respect to the Fermi level in the quantum well (figure and caption from Ref. [LHQ+08]).

However, the small inverted band-gap of about 3 meV to 4 meV induces a large residual bulk conductance [NL01]. This limits the observation of quantized edge conductance values. Experimentally, the residual bulk conductance can be reduced by means of various techniques such as the use of low-purity Ga source for MBE growth [CFR+13]. Nevertheless, the observation of quantized edge conductance in the QSH regime was made possible for temperature below $T \approx 4\,\mathrm{K}$ by the addition of Si dopants at the InAs/GaSb interface [KRY+14, DKSD15]. These dopants serve as donors in InAs and acceptors in GaSb, creating a localization gap of $\Delta_{loc} \approx 2\,\mathrm{meV}$. By definition, the conductance in the ballistic regime of the topological edge states is not affected by disorder. Figure 1.13(a) exhibits the conductance plateaus obtained for two different devices [DKSD15]. As shown in Section 1.3.3, the quantized value is dependent of the device geometry *i.e.* whether it is a π-bar (red) or a Hall bar (blue) device. Du *et al.* also shows that the conductance is independent of the temperature below 4 K (see Fig. 1.13(b)). However a surprising behavior is observed considering magnetic field. Figure 1.13(c) shows that the conductance plateaus are independent of the in-plane magnetic field. When a magnetic field B is applied, the time-reversal symmetry is broken and it is generally accepted that the quantized conductance will be affected. For instance, in semiconductor-based QSH systems, the counter-propagating edge modes are coupled by the magnetic field, leading to the opening of a Zeeman gap in the edge spectrum. Skolasinski *et al.* have identified three mechanisms that could explain this robustness [SPAW18]:

- the effective g-factor of the edge states is suppressed due to the heavy-hole contribution of the edge-state wave function,
- the Dirac point of the edge states is hidden in the bulk band, making the Zeeman gap opened by the magnetic field invisible to transport,
- the backscattering is strongly suppressed away from the Dirac point due to the nearly anti-aligned spins of the counter-propagating edge states.

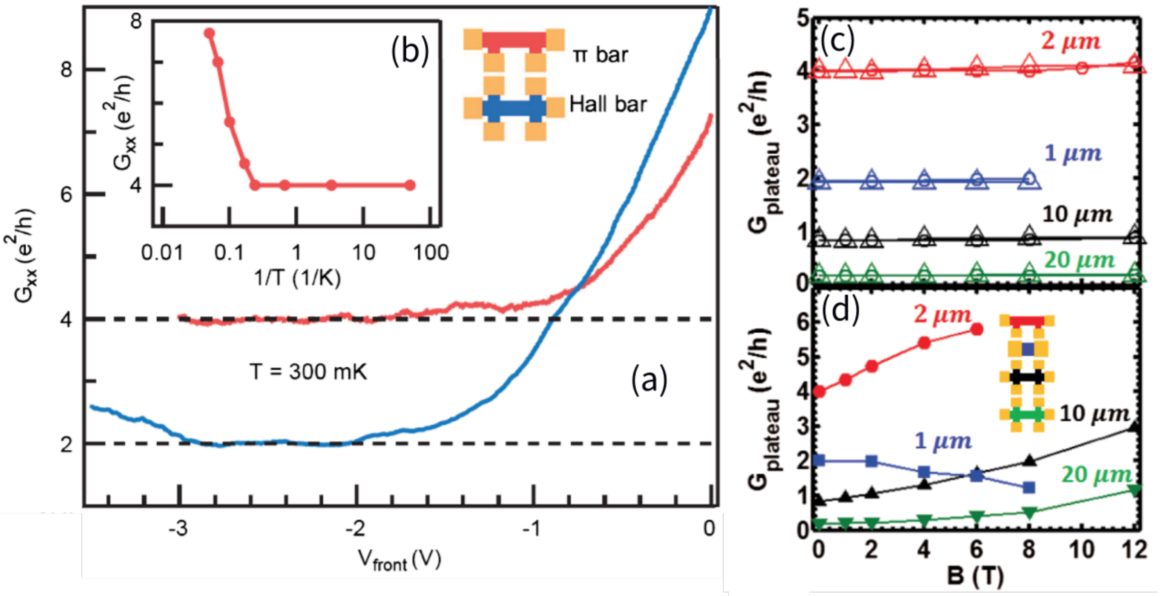

Figure 1.13: (a) Wide conductance plateaus quantized to $2e^2/h$ and $4e^2/h$, respectively, for two device configurations shown in inset, both have length 2 µm and width 1 µm. (b) Plateau persists to 4 K, and conductance increases at higher temperature due to delocalized 2D bulk carriers. (c) Plateau values measured for four different devices with in-plane magnetic field applied parallel (open circles) or perpendicular (open triangles) to the edge axis. (d) The same four samples were measured ($T = 300\,\mathrm{mK}$) in a field applied perpendicular to the 2D plane, with the 4-terminal signal of the Hall bar devices showing increasing conductance, and the 2-terminal device (blue squares) showing decreasing conductance (figure and caption adapted from Ref. [DKSD15]).

1.2.4 Strained InAs/GaInSb quantum wells

Although the residual bulk conductance can be indeed reduced by means of various techniques such as implantation of Si impurities at the InAs/GaSb interface, as previously mentioned, the quantized values of edge conductance at higher temperature than 4 K have not yet been observed even in strained InAs/GaSb QW bilayers. In order to observe the QSH phase at higher temperature, one must increase the band-gap. In 2016, Akiho *et al.* proposed a strained InAs/In$_x$Ga$_{1-x}$Sb QW structure as shown in Fig. 1.14(a) and demonstrate by 8-band $k \cdot p$ calculations that the strain increases the energy gap. In$_{0.25}$Ga$_{0.75}$Sb has a 0.82% lattice mismatch with respect to AlSb, which induces compressive strain in the InGaSb layer.

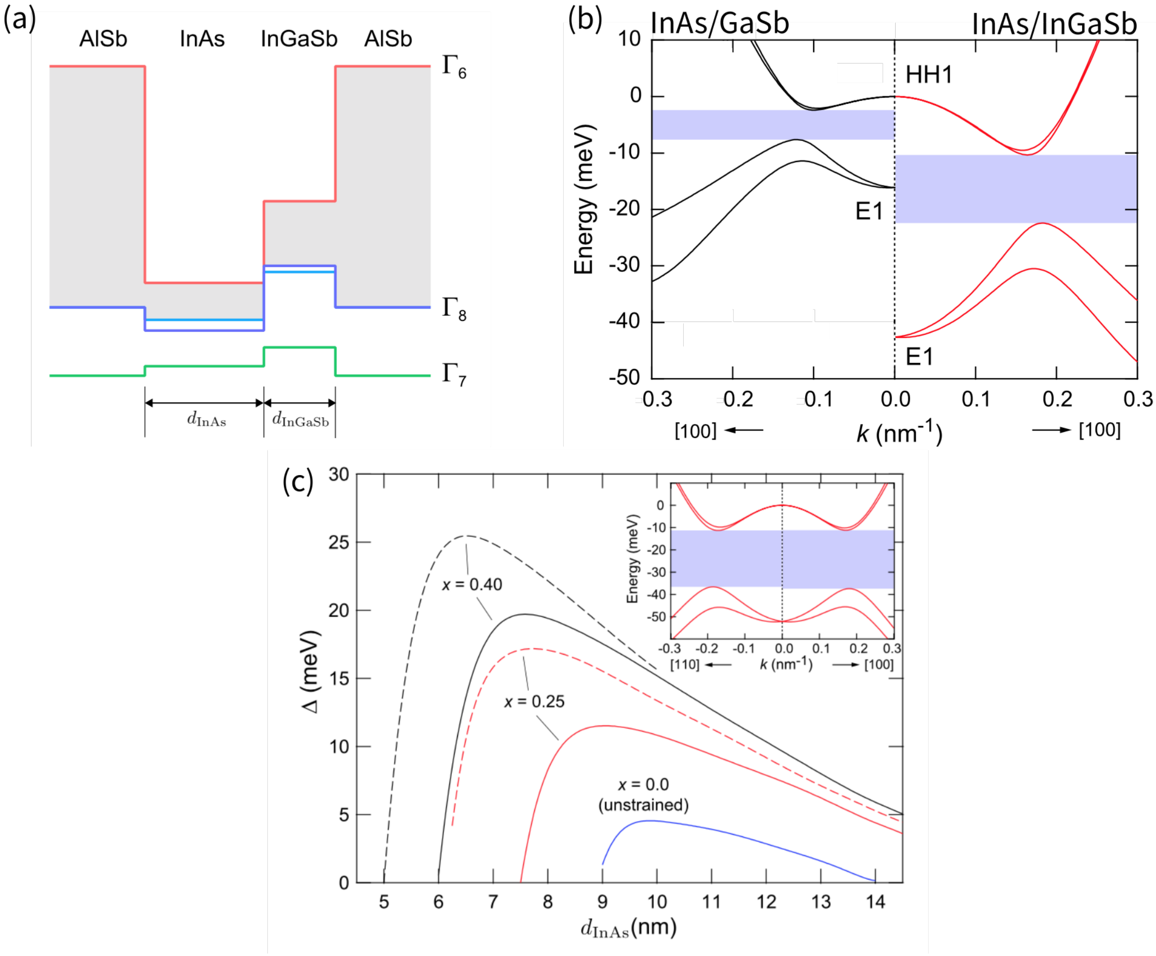

Figure 1.14: (a) The band edge profile of InAs/In$_{0.25}$Ga$_{0.75}$Sb quantum wells (QWs) with AlSb barriers, assuming pseudomorphic growth on AlSb. (b) In-plane energy dispersions along the [100] direction of unstrained InAs/GaSb QWs and strained InAs/In$_{0.25}$Ga$_{0.75}$Sb QWs. The shaded region represents the energy gap. (c) Hybridization gap Δ of InAs/In$_x$Ga$_{1-x}$Sb QWs ($x = 0$, 0.25, and 0.40) calculated as a function of InAs layer thickness d_{InAs}. In$_x$Ga$_{1-x}$Sb layer thickness is 6 nm. The blue solid line shows the calculation for unstrained QW with $x = 0$. Red and black solid (dashed) lines show calculations assuming pseudomorphic growth on AlSb (GaSb). The inset shows the energy dispersion for a QW with $x = 0.40$, $d_{\mathrm{InAs}} = 6.5$ nm, and $d_{\mathrm{InGaSb}} = 6$ nm, pseudomorphic on GaSb, where Δ reaches 25 meV (≈ 290 K) (figure and caption adapted from Ref. [ACI+16]).

The strain strengthens the $\Gamma_8 - \Gamma_6$ band inversion. Figure 1.14(b) shows the comparison of the energy dispersion between unstrained and strained QW in the [100] direction for an heterostructure with respective thicknesses $d_{\mathrm{InAs}} = 10$ nm and $d_{\mathrm{InGaSb}} = 6$ nm. Akiho *et al.* have calculated that one can engineer the energy gap as shown in Fig. 1.14(c) to a maximum

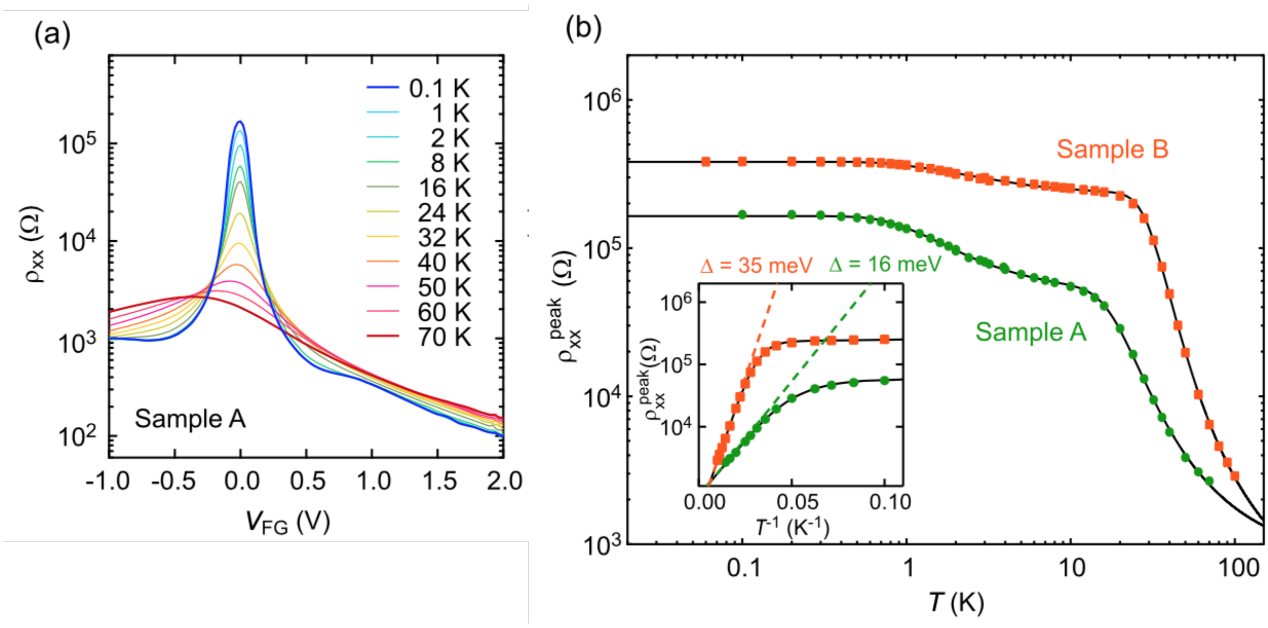

Figure 1.15: (a) Front gate voltage (V_{FG}) dependence of ρ_{xx} at different temperatures for a CQW with $x = 0.25$, $d_{\text{InAs}} = 8.5\,\text{nm}$ and $d_{\text{InGaSb}} = 5.9\,\text{nm}$. (b) Temperature dependence of the peak resistivity ρ_{xx}^{peak}. The solid lines are fits with a double-exponential function. The inset is an Arrhenius plot of the data in the high-temperature regime. The solid (dashed) lines are fits with a double- (single-) exponential function (figure and caption adapted from Ref. [IAC+20]).

of 25 meV. These theoretical predictions were demonstrated experimentally in the following years in the same group by activation energy measurements [IAC+20]. Figure 1.15(a) shows the temperature evolution of the resistance peak associated with the topological gap and panel (b) display the fitting of the peak value of resistivity. This work experimentally demonstrated the possibility to increase the energy gap up to 35 meV.

1.2.5 Three layer InAs/GaSb quantum wells

Krishtopenko *et al.* [KT18b] proposed a triple-layered InAs/Ga(In)Sb/InAsS QW (TQW), shown in Fig 1.16(a) which is distinct from the bilayer in that its band gap is located at the center of the Brillouin zone. To remove the inversion asymmetry in the growth direction, an additional layer of InAs is added to the InAs/GaSb bilayer. In the bilayers, the inverted gap opens at finite k due to the mixing of E1 and H1 levels. However, the inverted band gap in the three-layer InAs/GaSb QWs arises at $k = 0$ due to quantum confinement, while the $E1$-$H1$ mixing vanishes at $k = 0$. Since the confinement effect is much stronger than the $E1 - H1$ interaction at non-zero k, higher energies of the inverted band gap were expected in these novel structures, with respect to the InAs/GaSb bilayers.

Band structure calculations have been performed on the basis of the full 8-band Kane model with material parameters taken from [VMRM01] to investigate the band ordering. Figure 1.16(b) shows the positions of electron-like and hole-like subbands at zero quasimomentum k in the TQW as a function of InAs-layer thickness d_1, and with a fixed GaSb-layer thickness $d_2 = 4\,\text{nm}$. The QWs are supposed to be grown on GaSb buffer along (001) crystallographic direction. Krishtopenko *et al.* have explored the phase diagram, shown in Fig. 1.16(c), of the three-layer structure. The solid curve, describing the crossing between E1 and H1 subbands, divides the d_1-d_2 plane into white region, corresponding to the trivial insulator phase with direct band ordering, and grey region with inverted band structure. The grey region is split

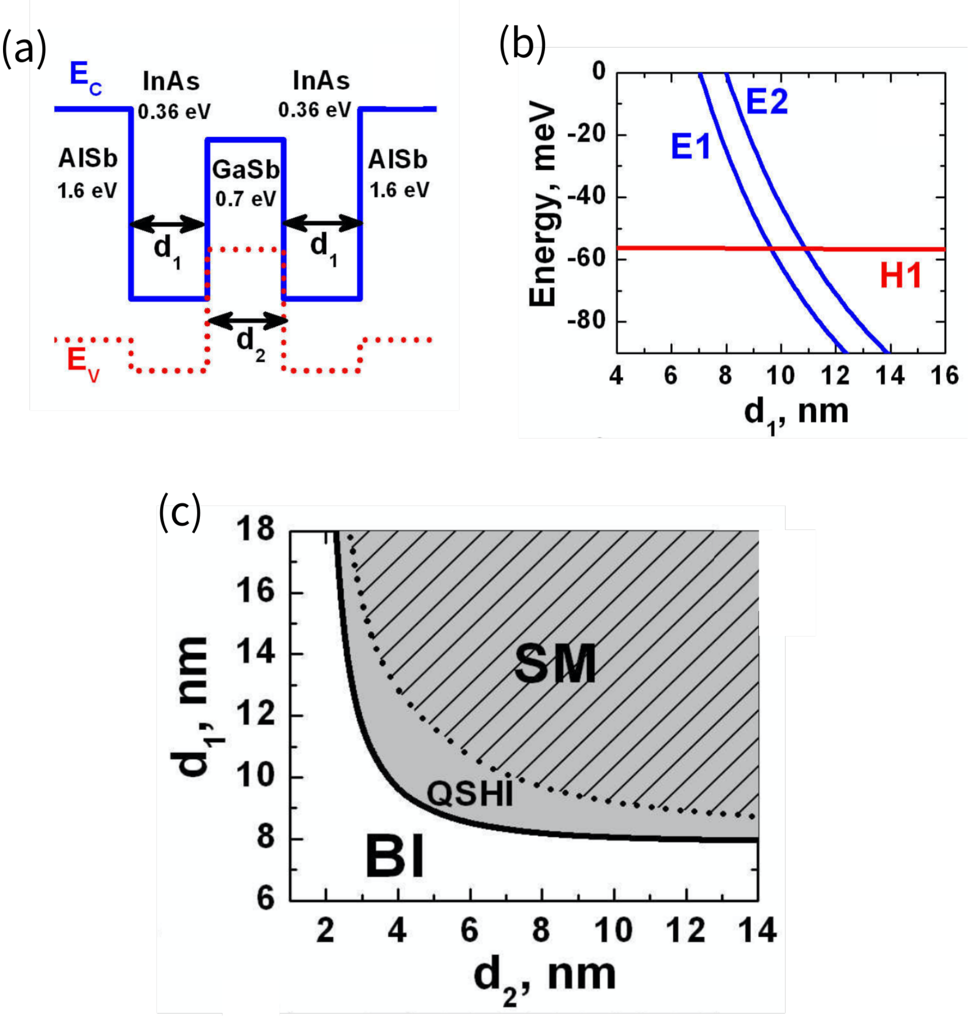

Figure 1.16: Schematic representation of a symmetrical three-layer InAs/GaSb QW. (b) Energy of electron-like (blue curves) and heavy-hole like (red curve) subbands at k = 0, as a function of the InAs-layer thickness d_1, and with GaSb-layer thickness $d_2 = 4\,\text{nm}$. (c) Phase diagram for different d_1 and d_2 in InAs/GaSB TQW (figure and caption from Ref. [KT18b]).

into open and striped areas, corresponding to QSHI and semimetal (SM) phase, respectively. The SM phase is characterized by a vanishing indirect band gap, when the side maxima of the valence subband exceed in energy the bottom of the conduction band.

The $k \cdot p$ band structure can be fitted by a 2-dimensional BHZ model:

$$\begin{aligned} \mathcal{H}_{eff}(k_x,k_y) &= \begin{pmatrix} \mathcal{H}_1(k_x,k_y) & 0 \\ 0 & \mathcal{H}_1^{\star}(-k_x,-k_y) \end{pmatrix}, \\ \mathcal{H}_1(k_x,k_y) &= \begin{pmatrix} \varepsilon_{\text{E1}}(k) & -Ak_+ & Sk_- \\ -Ak_- & \epsilon_{\text{H1}}(k) & Rk_-^2 \\ Sk_+ & Rk_+^2 & \epsilon_{\text{E2}}(k) \end{pmatrix}, \end{aligned} \tag{1.8}$$

where $k\pm = k_x \pm ik_y$ are the momentum k component in the 2D plane, $k^2 = k_+k_-$ and $\varepsilon_{\text{E1}}(k) = C + M + B_{\text{E1}}k^2$, $\varepsilon_{\text{H1}}(k) = C - M + B_{\text{H1}}k^2$ and $\varepsilon_{\text{E2}}(k) = C + M + \Delta_{\text{E1E2}} + B_{\text{E2}}k^2$. Here, C, M, A, B_{E1}, B_{H1}, B_{E2}, R and S are structure parameters, which depend on d_1 and d_2. As in HgCdTe, the sign of the mass parameter M defines the inversion of the $E1$ and $H1$ bands. As 3 bands are considered, an additional term Δ_{E1E2} describes the gap between the $E1$ and $E2$ subbands $k = 0$. The predicted phase diagram (see Fig. 1.16(c)) was also confirmed by evidencing the existence of massless Dirac fermions in gapless band structures by cyclotron resonance measurement [KIM+17, RKB+17], but the inverted band structure (QSHI) was also investigated by Landau levels (LLs) spectroscopy [KRGP+18].

A specific feature of inverted-band ordering under a quantizing magnetic field is the emergence of a specific pair of LLs, also known as zero-mode LLs. The zero-mode LLS cross at a critical magnetic field as the lowest zero-mode LL (at $B = 0\,\mathrm{T}$) arises from the valence band and has an electron-like character, while the second level arises from the conduction band and has a heavy-hole-like character. At lower magnetic field, the band ordering is inverted in a TI and is driven into the trivial band ordering for higher magnetic field $B > B_c$. This typical signature is shown in Fig. 1.17(a). Finally, Fig. 1.17(b) is the case of a QWs with trivial band ordering, in which the electron- and heavy-hole-like levels arise at $B = 0\,\mathrm{T}$ in the conduction and valence band, respectively, and the zero-mode LLs do not cross.

Figure 1.17(c) shows the energy of the optical transition obtained by magneto-absorption. The principle of the LL spectroscopy is more detailed in 2.3.1. At higher magnetic field, it is clear that the higher energy transition observed has a non-zero energy at $B = 0\,\mathrm{T}$. Considering the inverted ordering of zero-modes LLs between topological and trivial insulator, this optical transition could be either the α_1 (black arrow) or the β_1 (grey arrow) transition, respectively. However, by calculating the oscillator strength of these 2 transitions, Krishtopenko *et al.* have shown that the β_1 transition should not be observed. Therefore this transition can only be attributed to the α_1 transition which has a non-zero energy at zero magnetic field only for the inverted band structure. In addition, one can see that the energies of these optical transitions are independent of the temperature, as the experimental data at 100 K (green symbols) coincide with the observed transitions at 2 K (orange symbols).

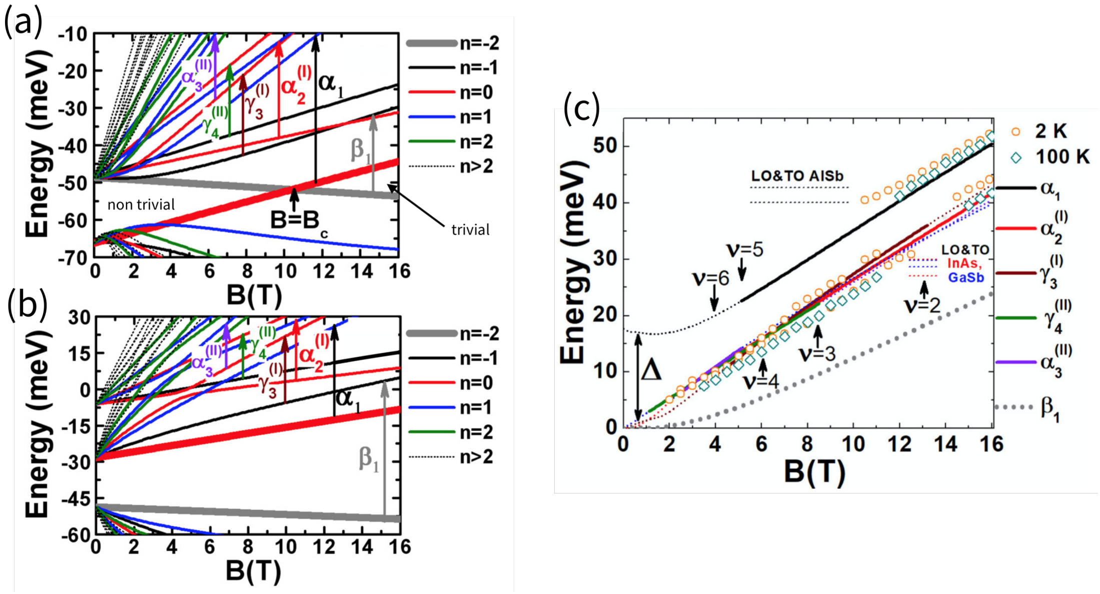

Figure 1.17: Landau-level fan chart for the three layer InAs/GaSb/InAs QW with (a) inverted-band structure, $d_1 = 34$ ML and $d_2 = 14$ ML, and (b) trivial band ordering, $d_1 = 27$ ML and $d_2 = 14$ ML. The numbers in the right side correspond to the LL indices. The expected dominant absorption transitions are denoted by arrows and Greek letters. A pair of zero-mode LLs with indices -2 and 0 is shown by bold curves. (c) Fan chart of the most intense LL transitions. The arrows indicate the magnetic fields, corresponding to integer LL filling factors ν at 2 K (figure and caption from Ref. [KRGP+18]).

1.3 Magnetotransport

1.3.1 Classical Drude model

A 2DEG under electrical and magnetic field is usually described by the Drude model where charge carriers are described as classical independent particles. The probability of collision for a carrier during the infinitesimal amount of time dt is dt/τ where τ is the mean free time. In the case where carriers from independent subbands are involved in the conduction, we assume they conduct as channels in parallel each described by a density of carrier n_i, a charge q being e or $-e$ for electrons and holes respectively and of mobility $\mu_i = q\tau_i/m_i^*$ where m_i^* is the effective mass of the carriers. We detail here the relation between the carrier properties and the physical quantities experimentally measured ρ_{xx} and ρ_{xy}.

Under electric and magnetic field the mean momentum $\langle \mathbf{p} \rangle$ of each carrier channel verifies:

$$\frac{d\langle \mathbf{p} \rangle}{dt} = -\frac{\langle \mathbf{p} \rangle}{\tau} - q\left[\mathbf{E} + \frac{\langle \mathbf{p} \rangle}{m^*} \times \mathbf{B}\right]. \tag{1.9a}$$

One can derive Eq. 1.9a to the trivial case where $\mathbf{B} = \mathbf{0}, \mathbf{E} \neq \mathbf{0}$ and obtain:

$$\langle \mathbf{p} \rangle = -q\tau\mathbf{E}. \tag{1.9b}$$

Using the definition of current density $\mathbf{j} = -nq\dfrac{\langle \mathbf{p} \rangle}{m^*}$ we obtain the Ohm's law:

$$\mathbf{j} = \frac{nq^2\tau}{m^*}\mathbf{E},$$

with a conductivity given by $\sigma_0 = \dfrac{nq^2\tau}{m^*}$.

An other trivial case is the one where $\mathbf{B} \neq \mathbf{0}, \mathbf{E} = \mathbf{0}$. Equation 1.9a describes a cyclotron motion:

$$\frac{d\langle \mathbf{p} \rangle}{dt} = -\frac{\langle \mathbf{p} \rangle}{\tau} - \frac{qB}{m^*}\langle \mathbf{p} \rangle \times \frac{\mathbf{B}}{B} \tag{1.9c}$$

We can easily identify the cyclotron frequency $\omega_c = eB/m^*$. With Hall bar devices, the equation of motion 1.9a is also simplified as we only consider an in-plane magnetic field equal to 0, and a perpendicular magnetic field $\mathbf{B} = B\mathbf{z}$, the Ohm's law becomes:

$$\begin{pmatrix} j_x \\ j_y \end{pmatrix} = \frac{\sigma_0}{1 + (\omega_c\tau)^2}\begin{pmatrix} 1 & \omega_c\tau \\ -\omega_c\tau & 1 \end{pmatrix}\begin{pmatrix} E_x \\ E_y \end{pmatrix}. \tag{1.10}$$

The conductance for a specific carrier type is now described by a symmetric 2 x 2 tensor $\hat{\sigma}$ with:

$$\sigma_{xx}(B) = \frac{\sigma_0}{1 + (\omega_c\tau)^2}, \qquad \sigma_{xy}(B) = \frac{\omega_c\tau}{1 + (\omega_c\tau)^2}\sigma_0. \tag{1.11}$$

In the case of carrier channels in parallel, the respective conductivity tensors can be directly summed such as $\hat{\sigma} = \sum_i \hat{\sigma}_i$. The resistivity tensor $\hat{\rho}$ is directly related to the conductivity tensor $\hat{\sigma}$ by tensor inversion:

$$\rho_{xx} = \frac{\sigma_{xx}}{\sigma_{xx}^2 + \sigma_{xy}^2}, \qquad \rho_{xy} = -\frac{\sigma_{xy}}{\sigma_{xx}^2 + \sigma_{xy}^2}. \tag{1.12}$$

We derive Eq. 1.12 in the case of a single carrier channel:

$$\rho_{xx} = \frac{1}{en\mu}, \qquad \rho_{xy} = \frac{B}{en}. \tag{1.13}$$

In the case of electrons (n) and holes (p) conducting in parallel, Eq. 1.12 becomes:

$$\rho_{xx} = \frac{1}{e}\frac{(n\mu_n + p\mu_p) + (n\mu_n\mu_p^2 + p\mu_p\mu_n^2)B^2}{(n\mu_n + p\mu_p)^2 + \mu_n^2\mu_p^2B^2(n-p)^2}, \tag{1.14a}$$

$$\rho_{xy} = \frac{B}{e}\frac{(n\mu_n^2 - p\mu_p^2) + \mu_n^2\mu_p^2B^2(n-p)}{(n\mu_n + p\mu_p)^2 + \mu_n^2\mu_p^2B^2(n-p)^2}. \tag{1.14b}$$

1.3.2 Shubnikov–de Haas oscillations

The energy levels of a 2D electron gas with a parabolic band ($\propto k^2$) placed in a perpendicular magnetic field, are called Landau levels:

$$E_N = \hbar\omega_c(N + \frac{1}{2}), \tag{1.15}$$

with $\hbar\omega_c = eB/m$ the cyclotron energy. A magneto-transport signature of these LLs are oscillations of the longitudinal resistivity ρ_{xx}, called Shubnikov-de Haas Oscillations (SdHO), and expressed according to the Liftshitz-Kosterlitz formula:

$$\begin{aligned} \rho_{xx}^{\mathrm{LK}}(B,T) &= \rho_0\left[1 - F^{\mathrm{LK}}(B,T)\cos\left(2\pi\frac{hn}{2eB}\right)\right], \\ F^{\mathrm{LK}}(B,T) &= 2e^{-\pi/\omega_c\tau_q}\frac{2\pi^2k_BT/\hbar\omega_c}{\sinh\left(2\pi^2k_BT/\hbar\omega_c\right)}, \end{aligned} \tag{1.16}$$

where ρ_0 is the zero-magnetic field resistivity, τ_q the quantum lifetime, and n the carrier density. We will refer to $F_{\mathrm{LK}}(B,T)$ as the envelope of the oscillations. The study of SdHO allows us to extract many properties of the electron gas, such as the carrier concentration n, the effective mass m^*, the quantum lifetime τ_q and consequently the Landau level broadening Γ:

- the carrier concentration n is extracted from the frequency of the oscillations $f = hn\,/\,2eB$. This extraction is often done by Fourier analysis, which usually requires a special treatment of the experimental data to minimize numerical errors. A large number of periods is also required for such an analysis. In our case, only a few periods are observed (< 10) in the best case, so we extract "manually" the periodicity of these oscillations. (see Chapter 3)

- the effective mass of carriers is extracted from the temperature dependence of the SdHO enveloppe $F^{\mathrm{LK}}(B,T)$. The amplitude (*i.e.* the difference between the maximum (at $B = B_{\mathrm{max}}$) and minimum (at $B = B_{\mathrm{min}}$) of the same period) is:

  $$\Delta\rho_{xx}^{\mathrm{LK}}(T) = 2\rho_0\left[F^{\mathrm{LK}}(B_{\mathrm{max}},T) + F^{\mathrm{LK}}(B_{\mathrm{min}},T)\right]. \tag{1.17}$$

  It is assumed that the variation in magnetic field of the envelope function is negligible over the same period:

  $$\begin{aligned} \Delta\rho_{xx}^{\mathrm{LK}}(T) &\approx 4\rho_0F^{\mathrm{LK}}(B_n,T), \\ &\approx 4\rho_0e^{-\pi/\omega_c\tau_q}\frac{2\pi^2k_BT/\hbar\omega_c}{\sinh\left(2\pi^2k_BT/\hbar\omega_c\right)}, \end{aligned} \tag{1.18}$$

where $\omega_c = \frac{eB_n}{m^*}$, B_n being the magnetic field at which a temperature-independent ρ_{xx} node between the two chosen extremas appears. Then,

$$\begin{aligned} \frac{\Delta\rho_{xx}^{\mathrm{LK}}(T_{\mathrm{ref}})}{\Delta\rho_{xx}^{\mathrm{LK}}(T)} &= \frac{X(T_{\mathrm{ref}})}{X(T)}\frac{\sinh(X(T))}{\sinh(X(T_{\mathrm{ref}}))}, \\ X(T) &= \frac{2\pi^2 k_B T}{\hbar\omega_c}. \end{aligned} \tag{1.19}$$

The effective mass of carriers is extracted in the regime of thermal activation of the LLs: $2\pi^2 k_B T \gg \hbar\omega_c$:

$$\sinh\left(X(T)\right) \sim e^{X(T)}/2$$
$$\Rightarrow \frac{\Delta\rho_{xx}^{\mathrm{LK}}(T_{\mathrm{ref}})}{\Delta\rho_{xx}^{\mathrm{LK}}(T)}\frac{X(T)}{X(T_{\mathrm{ref}})} \sim \frac{e^{X(T)}}{2\sinh X(T_{\mathrm{ref}})}$$

$$\Rightarrow \ln\left(\frac{\Delta\rho_{xx}^{\mathrm{LK}}(T_{\mathrm{ref}})}{\Delta\rho_{xx}^{\mathrm{LK}}(T)}\frac{X(T)}{X(T_{\mathrm{ref}})}\right) \sim \frac{2\pi^2 k_B}{e\hbar B_n} m^* T - \ln\left(2\sinh\left(X(T_{\mathrm{ref}})\right)\right). \tag{1.20}$$

- the influence of scattering on the potential fluctuations limits the lifetime τ_q of an electron in a certain quantum state. We consider a Lorentzian DoS for each LLs with a half-width $\Gamma = h/(2\tau_q)$. Γ can be extracted by the magnetic field dependence of the resistivity ρ_{xx}. If we consider the difference between a resistivity maximum and minimum on the same oscillation, we get from Eq. 1.18

$$\frac{\Delta\rho_{xx}^{\mathrm{LK}}(T)}{4\rho_0} \approx e^{-\pi/\omega_c\tau_q}\frac{2\pi^2 k_B T/\hbar\omega_c}{\sinh\left(2\pi^2 k_B T/\hbar\omega_c\right)}. \tag{1.21}$$

The quantum lifetime can be extracted at low temperature from the magnetic field dependence of the SdHO amplitude.

1.3.3 Landauer–Büttiker formalism

In 1957, Landauer proposed to model the electric transport in materials with localized scatterers [Lan57, Lan70]. Instead of computing currents from homogeneous distribution of the electrons in the momentum space in the whole medium, Landauer considered the electric field as the consequence of a continuous flow of charges between the scattering centers. He thus showed that the average electric field obtained is identical in both cases, but locally non uniform and concentrated around the scattering centers in his approach. Büttiker then took up this approach to model the electric transport in quantum Hall insulators [Büt86, Büt88] where the electron transport is carried by the chiral edge states between the different terminals. The current is then defined by the matrix of transmission coefficients between the device probes and their associated chemical potentials.

We model the electronic system by leads connected to the contacts, as shown in Fig. 1.18. We imagine these contacts as large electron reservoirs that are in thermal equilibrium and perfectly absorb all incident electrons. We can summarize the behavior of the system by a transmission matrix where the element T_{ij} describes the transmission probability (adjusted to the number of channels) from probe i to probe j. The current flowing between the probe i and the probe j is then defined as:

$$\begin{aligned} I_{ij} &= \frac{e}{2\pi}\int_0^\infty t_{ij}(k) f_{\mu_i}(k) v_k dk - \frac{e}{2\pi}\int_0^\infty t_{ji}(k) f_{\mu_j}(k) v_k dk \\ &= \frac{e}{2\pi\hbar}\int_0^\infty t_{ij}(E) f(E-\mu_i) dE - \frac{2e}{2\pi\hbar}\int_0^\infty t_{ji}(E) f(E-\mu_j) dE, \end{aligned} \tag{1.22}$$

where $t_{ij}(k)$ the probability of transmission from the contact i to contact j for an electron of wave vector k , f the Fermi distribution function, $v_k = (1/\hbar)(dE/dk)$ the velocity for an electron of wave vector k and μ_i is the chemical potential at the reservoir i. Note that experimentally, we often consider the voltage of the probes $V_i = \mu_i/e$. As $\int_0^\infty t_{ij}(E) f(E-\mu_i) dE = T_{ij}\mu_i$, we obtain:

$$I_{ij} = \frac{e}{h}(T_{ij}\mu_i - T_{ji}\mu_j). \tag{1.23}$$

The net current at the probe i is then the sum of the currents between the probe i and all the other probes:

$$\begin{aligned} I_i &= \frac{e}{h}\sum_{j\neq i} T_{ij}\mu_i - T_{ji}\mu_j = \frac{e}{h}\left(\sum_{j\neq i} T_{ij}\mu_i - \sum_{j\neq i} T_{ji}\mu_j\right) \\ &= \frac{Ne}{h}\mu_i - \frac{e}{h}\sum_{j\neq i} T_{ji}\mu_j, \end{aligned} \tag{1.24}$$

where N is the number of channels in the leads.

In the next paragraph we apply the Landauer-Büttiker formalism in the case of chiral edge states (QHE) and then in the case of helical edge states (QSHE).

Chiral edge states (QHE)

We consider a standard Hall bar with 6 contacts in the quantum Hall regime and calculate the four-probe longitudinal resistance $R_{14,23}$ and transverse resistance $R_{14,35}$. The current is imposed between the probe 1 ($\mu_1 = \mu$) and the probe 4 ($\mu_4 = 0$). The other contacts are perfect voltage probes with zero net current. In the case of chiral edge states, the matrix of transmission is simplified as the quantum Hall edge channels are protected from back-scattering (T = 1) and connect only nearest neighbors contacts. If the magnetic field is strong enough such that ν LLs are filled, then $N = \nu$ chiral edge states traverse the perimeter of the device and we obtain as system of equations from Eq. 1.24:

$$\begin{bmatrix} I_1 \\ 0 \\ 0 \\ I_4 = -I_1 \\ 0 \\ 0 \end{bmatrix} = \frac{e}{h}\begin{bmatrix} N & 0 & 0 & 0 & 0 & -N \\ -N & N & 0 & 0 & 0 & 0 \\ 0 & -N & N & 0 & 0 & 0 \\ 0 & 0 & -N & N & 0 & 0 \\ 0 & 0 & 0 & -N & N & 0 \\ 0 & 0 & 0 & 0 & -N & N \end{bmatrix}\begin{bmatrix} \mu \\ \mu_2 \\ \mu_3 \\ 0 \\ \mu_5 \\ \mu_6 \end{bmatrix} \tag{1.25}$$

The four-probe measurement of the longitudinal and transverse resistance is then derived from Eq. 1.25:

$$R_{14,23} = \frac{V_{23}}{I_{14}} = 0, \tag{1.26}$$

$$R_{14,35} = \frac{V_{35}}{I_{14}} = \frac{1}{N}\frac{h}{e^2}, \tag{1.27}$$

where (h/e^2) is the quantum of resistance, also known as the von Klitzing constant [vKDP80]. An important consequence of the chirality of the edge channels is that the longitudinal resistance is vanished, regardless of the number of voltage probes placed along the perimeter.

Helical edge states (QSHE)

The helical edge states can be considered as the coexistence of two chiral edge states with opposite propagation directions. We calculate the four-probe longitudinal resistance $R_{14,23}$ and transverse resistance $R_{14,35}$ in the quantum spin Hall regime. The system of equations 1.24 is:

$$\begin{bmatrix} I_1 \\ 0 \\ 0 \\ I_4 = -I_1 \\ 0 \\ 0 \end{bmatrix} = \begin{bmatrix} 2 & -1 & 0 & 0 & 0 & -1 \\ -1 & 2 & -1 & 0 & 0 & 0 \\ 0 & -1 & 2 & -1 & 0 & 0 \\ 0 & 0 & -1 & 2 & -1 & 0 \\ 0 & 0 & 0 & -1 & 2 & -1 \\ -1 & 0 & 0 & 0 & -1 & 2 \end{bmatrix} \begin{bmatrix} \mu \\ \mu_2 \\ \mu_3 \\ 0 \\ \mu_5 \\ \mu_6 \end{bmatrix}. \tag{1.28}$$

In contrast to the chiral edge states, the resistance that is measured depends on the number of contacts between source and drain of the current flow. We now have $R_{14,23} = (1/2)(h/e^2)$ and $R_{14,35} = 0$. In this work, we often consider the non-local resistance as $R_{26,35}$. In the QSH regime, the non-local resistance is calculated from the system of equations:

$$\begin{bmatrix} 0 \\ I_2 \\ 0 \\ 0 \\ 0 \\ I_6 = -I_2 \end{bmatrix} = \begin{bmatrix} 2 & -1 & 0 & 0 & 0 & -1 \\ -1 & 2 & -1 & 0 & 0 & 0 \\ 0 & -1 & 2 & -1 & 0 & 0 \\ 0 & 0 & -1 & 2 & -1 & 0 \\ 0 & 0 & 0 & -1 & 2 & -1 \\ -1 & 0 & 0 & 0 & -1 & 2 \end{bmatrix} \begin{bmatrix} \mu_1 \\ \mu \\ \mu_3 \\ \mu_4 \\ \mu_5 \\ 0 \end{bmatrix}. \tag{1.29}$$

One then obtain $R_{26,35} = (2/3)(h/e^2)$.

In both cases, we have assumed that edge states are protected from back-scattering. Although helical edge states cannot be backscattered by elastic scatterers, inelastic scatterers can. We now consider the case of QSH regime in a device where the edge length exceeds the inelastic mean free path λ. In the QSH state, the Hall bar device is modelled as the resistor network presented in Fig. 1.18(c) where each edge can be replaced by a resistor of $R_0 = (h/e^2)$. However if the length of the edge $L_{\text{edge}} > \lambda$ then, following Abanin [ANZ+07], one has $R_{\text{edge}} = (h/e^2)(1 + L_{\text{edge}}/\lambda)$, which we often approximate by $R_{\text{edge}} = (h/e^2)(L_{\text{edge}}/\lambda)$ in the following. For a device with the dimensions shown in Fig. 1.18(c) where $l_p > \lambda$ and $l_1 > \lambda$, the four-probe measurements no longer lead to quantized value of resistances. Instead, one can show that:

$$R_{14,23} = \frac{h}{e^2}\frac{1}{\lambda}\frac{l_p}{2} \text{ and } R_{26,35} = \frac{h}{e^2}\frac{1}{\lambda}\frac{(2l_1)^2}{4l_1 + 2l_p}.$$

1.3.4 Square lattice model

In the Landauer-Büttiker formalism presented above, it is assumed that the bulk does not participate to the conduction. Nevertheless, in topological structures based on InAs/GaSb, a residual contribution of the bulk has often been observed leading to measured resistance values not corresponding to the expected quantization [KDS10, NPP+14, Beu16]. We propose a more complete model where both the edge and the bulk are modeled by a 2D square lattice network

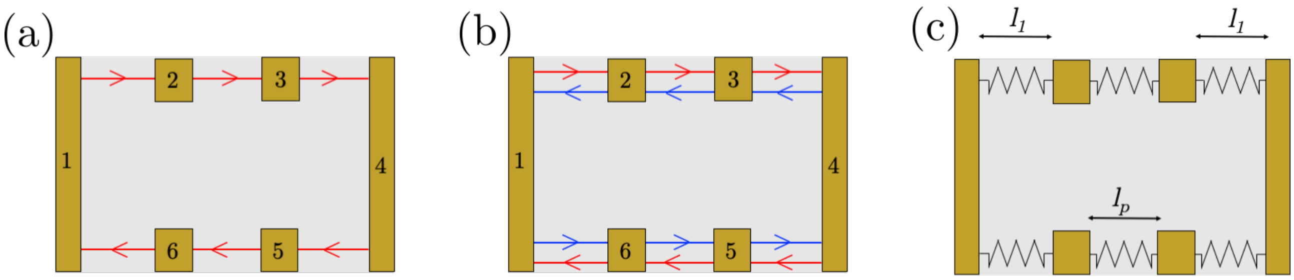

Figure 1.18: (a) Hall bar scheme with chiral edge states. (b) Hall bar scheme with helical edge states. Potentials for each probes are provided in the case where $\mu_1 = 1$ and $\mu_4 = 0$ are imposed. (c) Network of resistor equivalent of the QSH edge states of panel (b). In the ballistic regime, each resistor is independent of the edge length and is $R_0 = (h/e^2)$. In the diffusive regime, resistors are dependent of the Hall bar dimensions and $R_{\text{edge}} = (h/e^2)(L_{\text{edge}}/\lambda)$ where L_{edge} is the length of the corresponding edge.

of resistors, as shown in Fig. 1.19, where the square lattice array is purposely shown with a low number of resistors for the readability of the figure. In practice, we try to have a sufficiently large number of resistors to discretize the space with a mesh length of the order of 1 µm. We call n_W, n_L and n_p the number of nodes along the Hall bar width, along the Hall bar length, and between the lateral probes, respectively.

In the bulk, the conductance of one of the resistors (in red in Fig. 1.19) corresponds simply to the bulk conductivity (in $\Omega/\Box$). Thus, the conductance of one of the inner resistor is given by $G_b = \sigma_{\text{bulk}}$. On the Hall bar edges, the 1D conductance is given by σ_{edge} (in unit of length per Ohm). Thus, the conductance of a single edge resistor (in blue in Fig. 1.19) is given by $G_e = \sigma_{\text{edge}}/l_c$, where l_c is the length of the mesh size (the length of one resistor). At each i node of the network, the potential V_i obeys the equation of current conservation:

$$\sum_{(i,j)=CN} G_{i,j}(V_j - V_i) = I_i, \tag{1.30}$$

where (i,j) are the pairs of connected nodes (CN), $G_{i,j}$ is the conductance element between the nodes i and j, and I_i is the current imbalance at the node i. $G_{i,j}$ can take only three values: G_b, G_e or the contact conductance G_c. The exact value of G_c is unimportant for the measurements in the four-probe configuration and disappears and the end of the calculation. Note that I_i in Eq. 1.30 is defined by the boundary conditions, more specifically by the source and drain contacts. The I_i value is non-zero only if the node i is connected to an additional contact acting as a current source or drain. In the latter case, $I_i = G_c(V_i - V_c)$, V_c is the imposed voltage of the contact. The network is described by the set of coupled linear Eqs. 1.30 for the unknown V_i's. This problem can be solved numerically when the voltages of the source and drain contacts are imposed (*i.e.*, when the currents I_i are known).

When $n_L, n_W \to \infty$, the square network model becomes equivalent to the finite difference method for the resolution of the Laplace equation $\nabla^2 V = 0$. The voltages of the source and drain contacts are imposed, yielding Dirichlet boundary conditions. The boundary conditions imposed by the edge states are:

$$\sigma_{\text{edge}}\partial^2 V/\partial x^2 + \sigma_{\text{bulk}}\partial V/\partial y = 0. \tag{1.31}$$

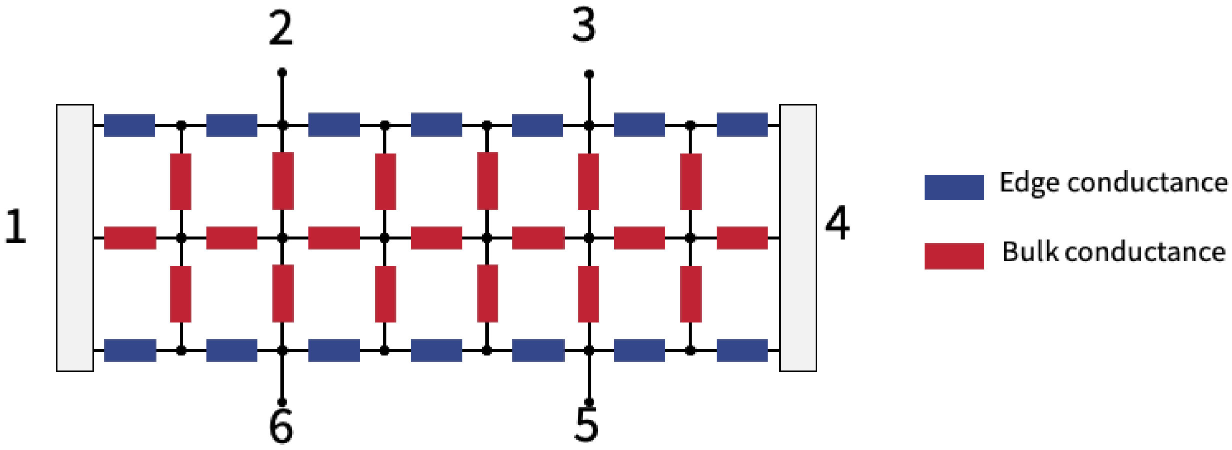

Figure 1.19: Sketch of a resistance square network for a given Hall bar geometry ($n_L = 7, n_W = 2$). The squares have a side length l_c. The red resistors represent the contribution of the 1D edge state. They have a resistance $G_1^{-1} = \sigma_{\text{edge}}^{-1} l_c$. The blue resistors model the 2D bulk and they have a resistance $G_2^{-1} = \sigma_{\text{bulk}}^{-1}/\square$.

Basic tests have been conducted to check the validity of this approach. For instance, we have checked that the model reproduces satisfactorily the expected non-local resistance $R_{25,34}$ of an homogeneous device (*i.e.* without edge conduction), when the size of the square mesh l_c tends to zero. Figure 1.20 shows the evolution of the ratio R_{NL}/R_L as a function of the geometric ratio l_p/W, l_p is the distance between the lateral probes; W is the Hall bar width. For the simulation, $n_W = 21$, and the number of nodes between the lateral probes n_p varies such that the geometric ratio evolves from $l_p/W = 0.5$ to 5. The model reproduces satisfactorily the well known formula for the current spreading:

$$R_{NL}^{\text{Ohmic}} = \frac{4}{\pi} R_L \frac{W}{l_p} \exp\left(-\pi \frac{l_p}{W}\right) \tag{1.32}$$

Figure 1.21 shows the current dissipation in the configuration R_{2635} calculated from three different cases: $G_{\text{edge}} = G_{\text{bulk}}/100$, $G_{\text{edge}} = G_{\text{bulk}}$, and $G_{\text{edge}} = 100 G_{\text{bulk}}$. For completeness, a simplified version of the python code that was developed for this figure is given in Annex.

Such a model can be used to extract both bulk and edge contribution. The procedure is as follows. Experimentally, for a given Hall bar of known geometry, for a given gate voltage, we measure two four-probes configurations. Usually, we measure the local resistance defined as$R_L = R_{14,23}$, and the nonlocal resistance, defined as $R_{NL} = R_{26,35}$. These two resistances can be fitted by a unique set of conductances (G_b, G_e) in the square lattice model. Therefore, the bulk and edge conductances can be estimated for each gate voltage.

Note that in Chapter 3, we compare the extracted bulk conductivity σ_{bulk} to the additional conductance of the "lateral" edge as $G_{\text{edge}} = (G_e - G_{\text{b}})\frac{l_c}{l_p}$ where l_p is the length between the lateral probes.

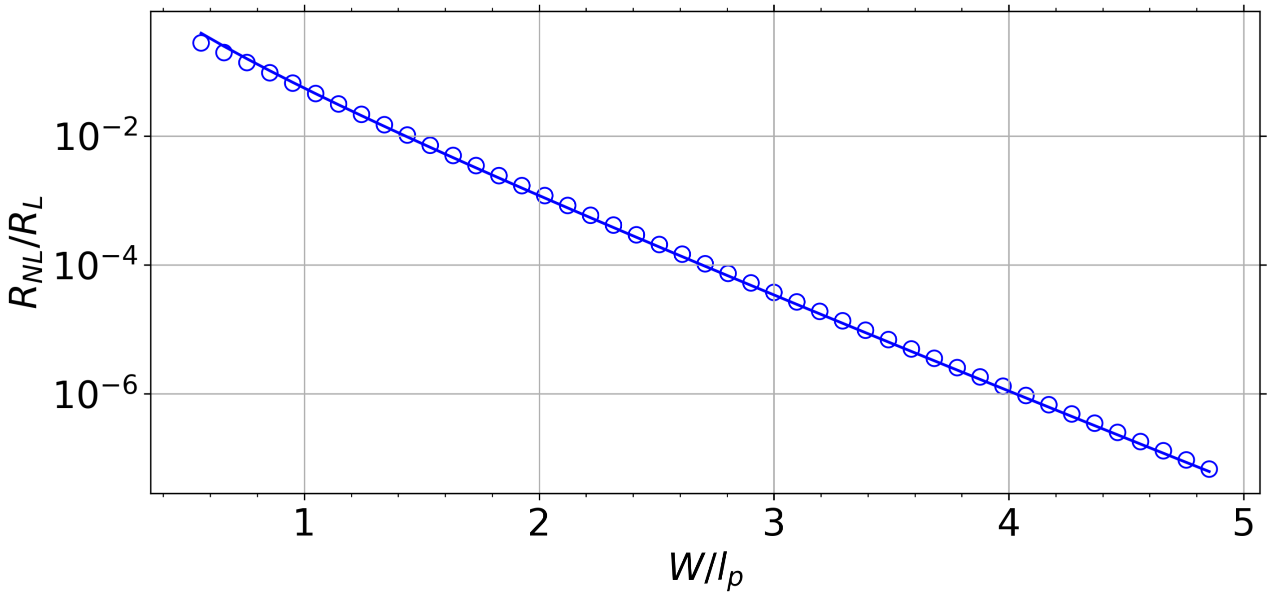

Figure 1.20: Comparison of the numerical estimate of the non-local resistance $R_{26,35}$ as given by the square network (blue circle symbols) and conventional formula $R_{NL}^{\text{Ohmic}} = (4/\pi)\ R_L(W/l_p)\exp(-\pi l_p/W)$. Here, l_p is the distance between the probes 2 and 3 while W is the Hall bar width.

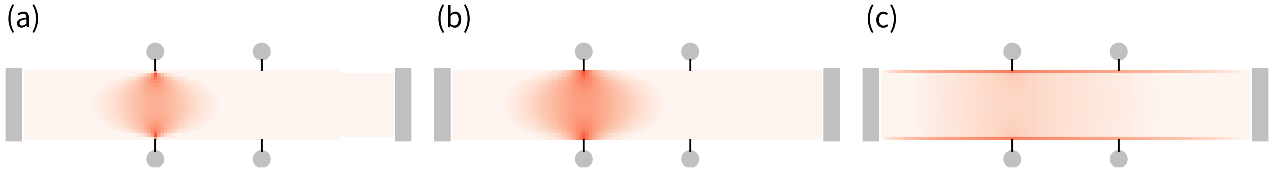

Figure 1.21: Current dissipation in a Hall bar geometry ($n_L = 111, n_W = 21$) in the non-local configuration. The calculation of the current dissipation is calculated for three different cases: (a) $G_{\text{edge}} = G_{\text{bulk}}/100$, (b) $G_{\text{edge}} = G_{\text{bulk}}$, and (c) $G_{\text{edge}} = 100G_{\text{bulk}}$.

Conclusion

In this chapter, we have detailed a state of the art focused on two dimensional topological insulators, as well as the theoretical concepts used for this study. It is important to note that the presentation of the topological insulators field is not intended to be exhaustive, because it is limited to 2D topological insulators on the one hand, and we do not detail all the candidate materials, such as those based on transition metal dichalcogenides [QLFL14, WFG+18]. Nevertheless, the path that led to the work presented in the following chapters has been presented.

CHAPTER 2

Fabrication of InAs/GaSb based devices and Experimental setups

This chapter focuses on the fabrication processes and characterisation methods of the devices under study. It is divided into three parts: the experimental setups and techniques used in these investigations, the growth of heterostructures based on InAs/GaSb and their characterization, and the fabrication process of the devices. The chapter provides details on each of these topics and presents the various devices that are part of this work.

2.1 Experimental setup

2.1.1 Cryogenics and magnetic field

Investigation of quantum Hall effects such as the QSHE requires to reach low temperatures down to the kelvin range. For this reason, both electrical and magneto-optic characterization of the grown heterostructures and transport measurements of various gated Hall bars were performed in a cryostat equipped either with a variable temperature insert (VTI) or with a ^{3}He insert for the temperatures below 1.7 K. The principle of these cooling systems have been nicely described for many years [Pob07, Zha16]. We still provide here their main details. Figure 2.1 displays both insert principles.

The ^{4}He dewar is made of an inner ^{4}He bath at 4.2 K isolated from room temperature by a vacuum jacketand a liquid Nitrogen jacket. The cryostat is equipped with a magnet insert from Cryogenics Limited that supports the magnet in the lower section of the helium reservoir. The superconducting magnet supplied in power by the Oxford Instruments Mercury IPS-M allows a vertical magnetic field up to 13 T. The ^{3}He insert allows reaching a temperature of 300 mK by pumping a liquid ^{3}He bath. The bath is isolated using a 1 K-pot in which a small volume of liquid ^{4}He is filled from the cryostat bath through a needle valve and pumped by an external pump at room temperature. The purpose of the 1 K-pot is also to cool down an internal adsorption pump made of charcoal on the ^{3}He line. The temperature of the sample can be varied from 300 mK to 2 K by the use of a heater thermally connected to the adsorption pump. To reach higher temperatures, all the liquid ^{3}He in the sample chamber is vaporised and pumped back to the ^{3}He reservoir, while a heater in the sample chamber allows the control of the temperature from 2 K to 200 K.

The principle of the VTI is similar to the 1 K-pot in the ^{3}He insert. A liquid bath of ^{4}He is filled by a capillary terminated by a needle valve from the main cryostat bath and pumped

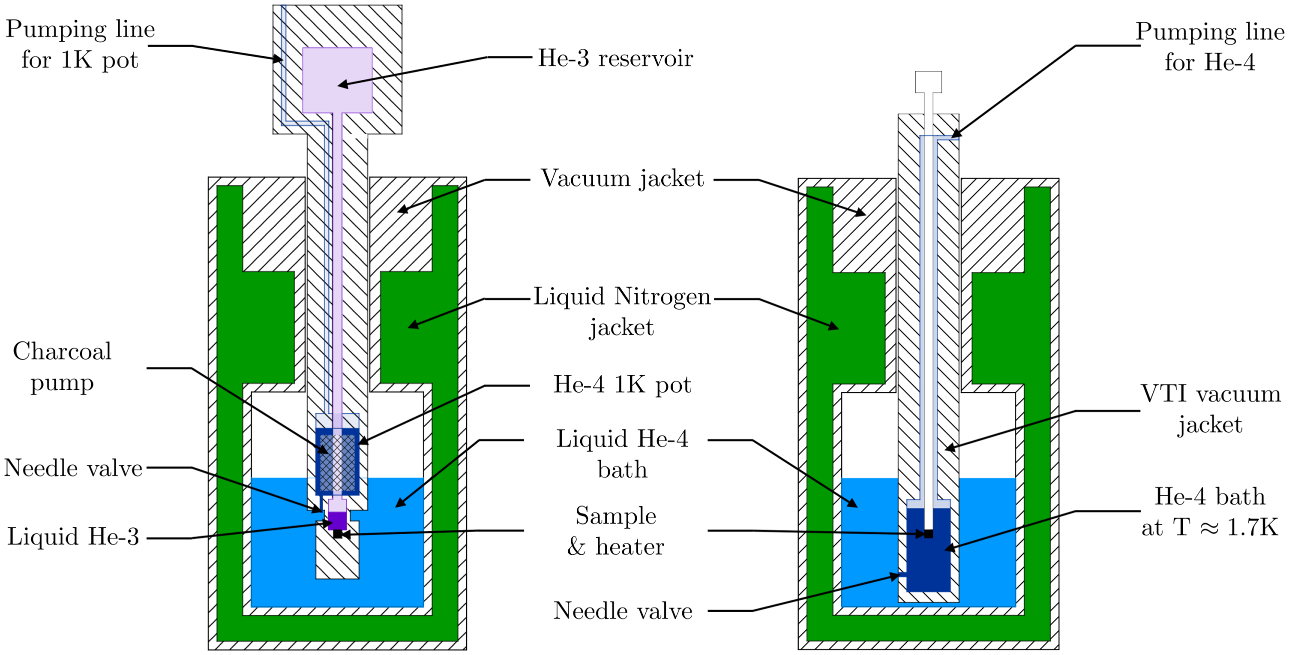

Figure 2.1: Schematics of the Helium-4 cryostat set up with Helium-3 Insert on the left and Variable Temperature Insert (VTI) on the right.

by an external pump, allowing to reach a minimal temperature of 1.7 K. The temperature is controled directly through a 100 Ω-resistive heater placed on the measurement probe. The main interest of the VTI is the timeliness of operation due to the 'top loading' of samples, compared to the ^{3}He insert.

2.1.2 Electronics

A low frequency ($f = 11$ Hz) electrical current is applied between the source and drain electrodes using the association of a voltage source at the output of a PerkinElmer **7225** lock-in amplifier and a high resistance of 10 or 100 MΩ. The resulting intensity is at maximum $I = 100$ nA in order to minimise the dissipated heat by the resistive devices. The current at the drain is measured in real-time using a current preamplifier and a lock-in. The different voltages between the other electrodes are measured with high-impedance 1 TΩ preamplifiers and lock-ins. A schematic of the standard measurement configuration of a gated Hall bar device is shown in Fig. 2.2. When a field-effect transistor configuration can be used to tune the Fermi level in the investigated 2DEG, a Source Measure Unit (SMU) Keithley **2602** is used to simultaneously apply a gate voltage V_g and measure the leak current I_{leak} between the 2DEG and the top gate.

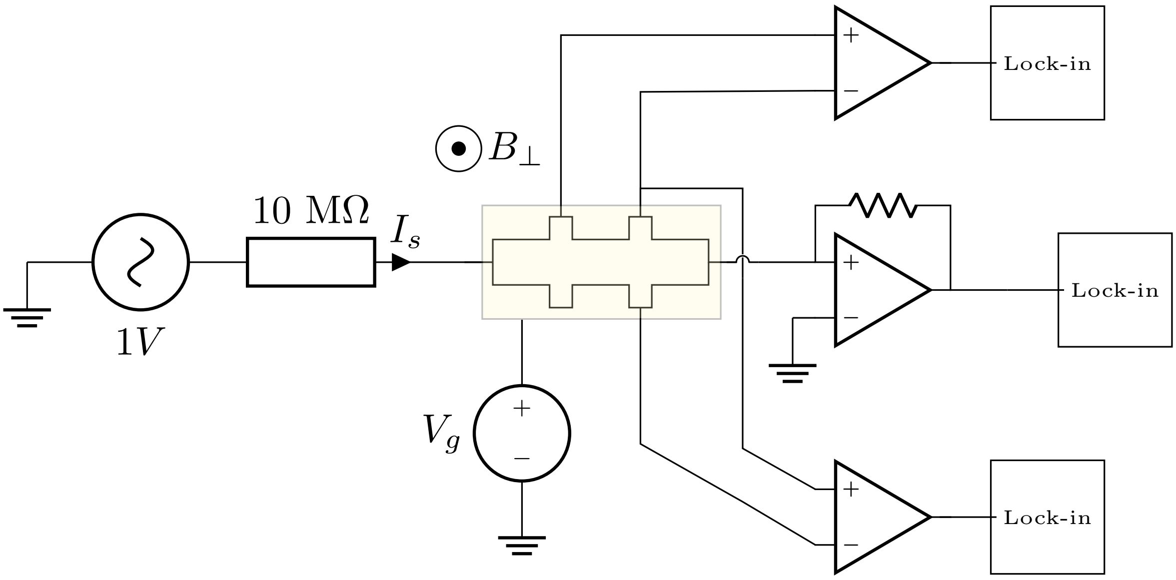

Figure 2.2: Schematic representation of the measurement setup for a Hall bar device. The current is applied from the source to the drain terminal and measured with the middle lock-in. Lateral probes allow the measurement of both longitudinal and transverse resistivities by the top and bottom lock-in respectively. The yellow frame represents the top gate of the HB device used to tune the Fermi level.

2.2 Growth of III-V materials

In the framework of this PhD thesis, the growth of InAs/GaSb materials stands on the shoulder of the Institut d'Électronique et Structure (IES[1]) and its long-expertise [RCC+05, SRT+07]. The studied samples were grown by molecular beam epitaxy (MBE) with the growth thickness controled by reflection high-energy electron diffraction (RHEED). In the following, we detail the several layers of the studied heterostructures shown in Fig. 2.3.

First of all, the growth is done on a substrate. Through the different growths, different substrates have been considered. The first one, corresponding to the S3052 and S3054 samples is a GaAs substrate. As it is transparent in the THz range, it was chosen to allow magneto-absorption measurements. It is also a fairly standard substrate for the growth of TIs such as InA/GaSb double wells. The second one is a GaSb substrate, more conventional for the growth of high-mobility 2DEG in InAs QW [SDP+16, THT+18], and corresponds to the S3198 sample.

The first epitaxied layers on the substrate are those forming the buffer. The purpose of these layers is to modify the strain in the QW layers induced by the difference of the lattices constants between the QW layers and the pseudomorphic buffer. [KRGP+19]. In S3054, it consists of a $\sim 1\,\mu$m-thick layer of GaSb in order to fully relax the strain in the QW as GaAs has initially a $\sim 8\%$ mismatch with respect to GaSb. The buffer is then followed by a superlattices of few nm-thick AlSb and GaSb layers. In S3052 and S3198, there is a metamorphic AlSb buffer, which has a $\sim 2\%$ lattice mismatch with respect to the $\mathrm{Ga_{0.65}In_{0.35}Sb}$ layer in the QW. Note that due to the GaAs substrate, the metamorphic AlSb buffer is a AlSbGaAs layer in S3052.

The active part corresponds to the quantum well layers $\mathrm{InAs/Ga_{1-x}In_xSb/InAs}$ confined by barriers of AlSb or $\mathrm{AlSb_{0.9}GaAs_{0.1}}$, depending on the substrate. The respective thicknesses

---

[1] Université de Montpellier, Institut d'Électronique et des Systèmes, 860 rue St Priest, 34095 Montpellier (cedex 5), France

d_1 and d_2 are chosen to match the theoretical position of a QSHI in the phase diagram shown in Section 1.2.5. The whole growth is covered by a cap layer of $In_{0.75}Ga_{0.25}As$ for S3054 and S3052, and GaSb for S3198 to protect the AlSb barrier from oxydation.

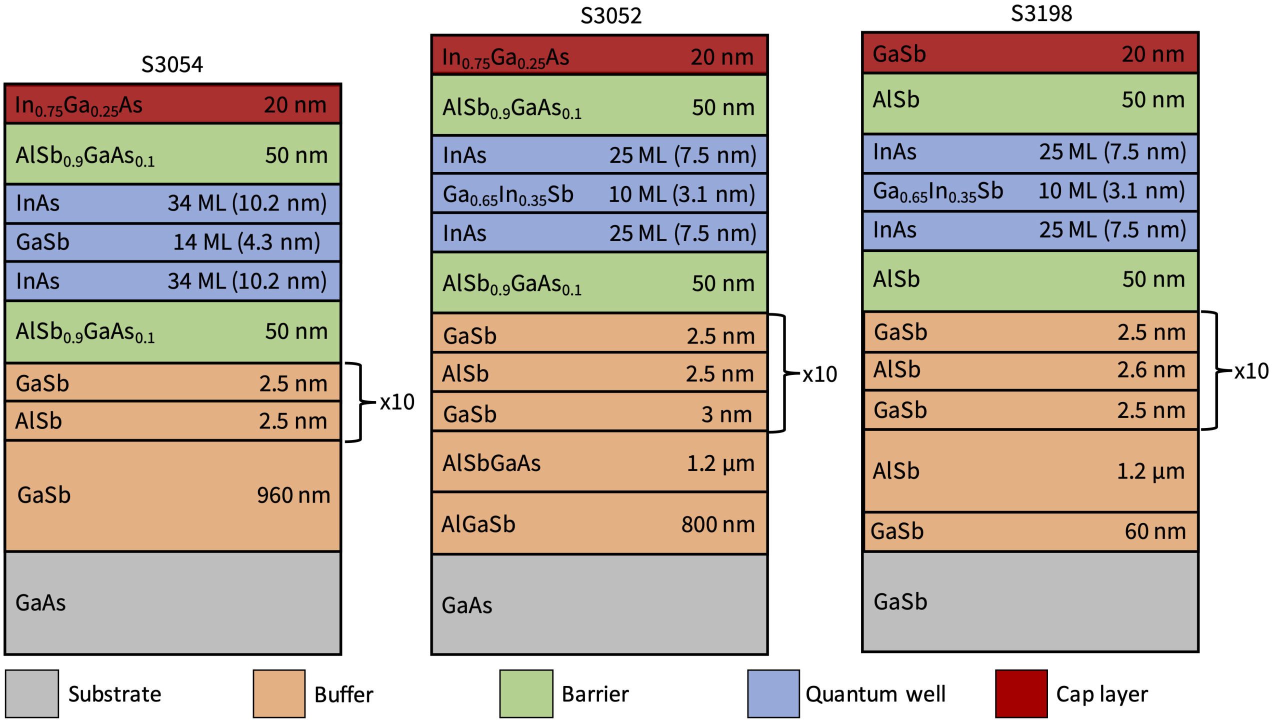

Figure 2.3: Schematic view of the layer structure for the S3054, S3052, and S3198 samples. The colors indicate the function associated with the layer.

Band structure calculations were performed by using the eight-band Kane model [KYB+16], which directly takes into account the interactions between Γ_6, Γ_8, and Γ_7 bands in bulk materials. This model well describes the electronic states in a wide range of narrow-gap semiconductor QWs, particularly in the broken-gap InAs/Ga(In)Sb quantum wells (QWs) [KRGP+18, KT18b, KRGP+19, KDS+19]. In the eight-band Kane Hamiltonian, we also took into account the terms, describing the strain effect arising because of the mismatch of lattice constants in the buffer, QW layers, and AlSb barriers. Parameters for the bulk materials and valence band offsets used in the eight-band Kane model are taken from Refs [VMRM01, KIM+12, KIO+15].

Figures 2.4(a), 2.5(a) and 2.6(a) show the band structure calculation for S3054, S3052 and S3198 samples respectively. All the samples have an inverted band structure with the hole-like $H1$ band lying above the electron-like $E1$ band. The calculated band-gap for the samples S3054, S3052 and S3198 is $\Delta \simeq 15\,\text{meV}$, $30\,\text{meV}$ and $45\,\text{meV}$ respectively. Note that the sample S3054 with the smaller gap is similar to the one studied in Ref. [KRGP+18], in which the inverted band structure was evidenced by magneto-absorption measurements. The carrier density is calculated assuming axial symmetry of the calculated band structure. To calculate LLs, we used the so-called axial approximation. Within this approximation, one keeps in-plane rotation symmetry by omitting the warping terms in the Hamiltonian. The calculations had been performed by expanding the eight-component envelope wave functions in the basis set of plane waves and by numerical solution of the eigenvalue problem.

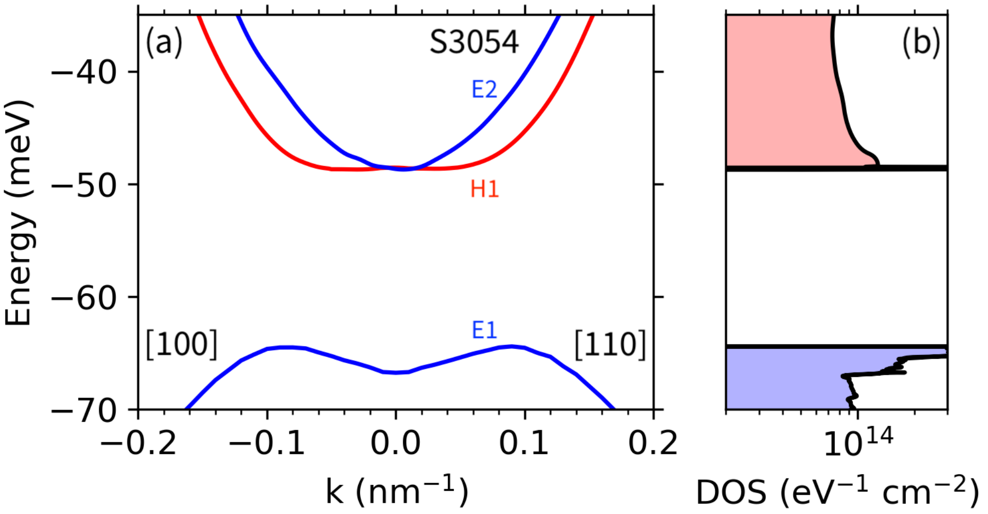

Figure 2.4: (a) Band structure, (b) density of states, and (c) Landau levels for growth S3054. The bandgap is between the E_1 and H_1 subbands with an energy gap $\Delta = 15\,\text{meV}$. The active part is a TQW of InAs/GaSb with $d_{\text{InAs}} = 34$ ML and $d_{\text{GaSb}} = 14$ ML. The theoretical critical magnetic field is $B_c = 10.6\,\text{T}$.

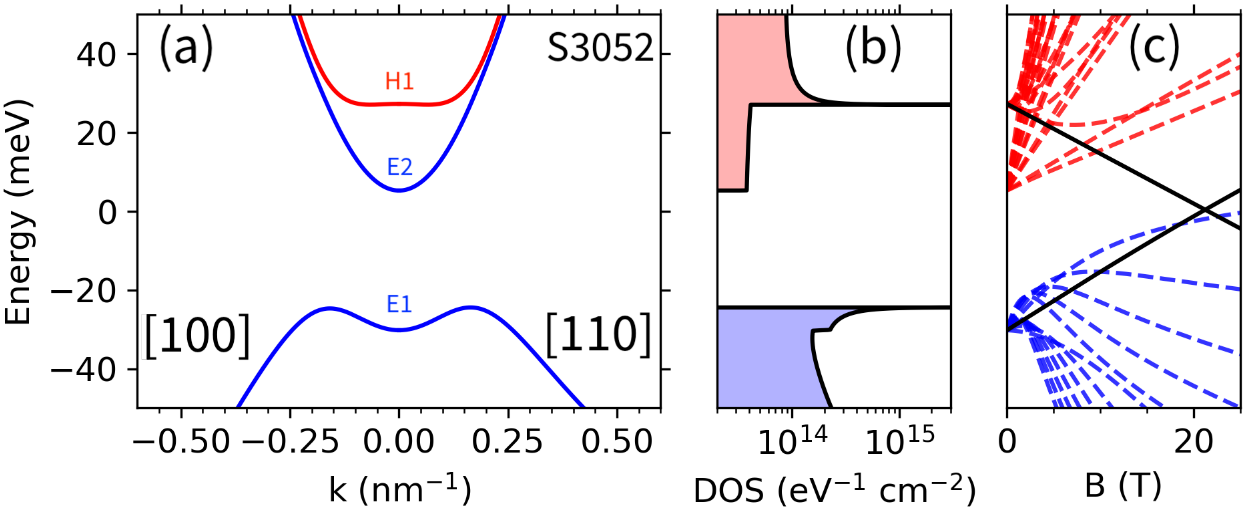

Figure 2.5: (a) Band structure, (b) density of states, and (c) Landau levels for growth S3052. The bandgap is between the E_1 and H_1 subbands with an energy gap $\Delta = 30\,\text{meV}$. The active part is a TQW of InAs/GaSb with $d_{\text{InAs}} = 25$ ML, $d_{\text{Ga}_{1-x}\text{In}_x\text{Sb}} = 10$ ML, and $x = 0.35$. The theoretical critical magnetic field is $B_c = 21.3\,\text{T}$.

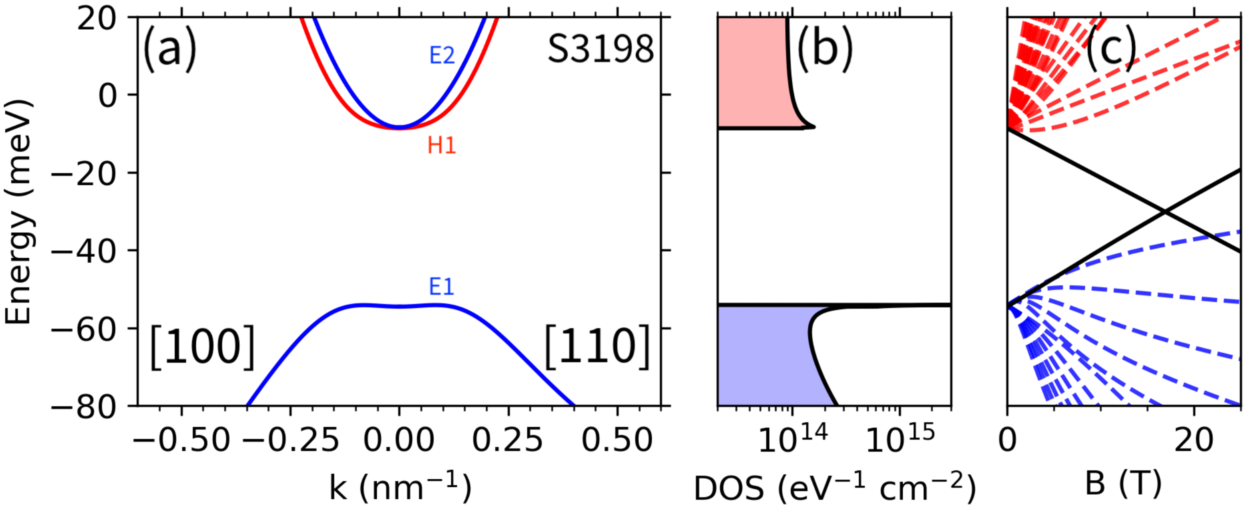

Figure 2.6: (a) Band structure, (b) density of states, and (c) Landau levels for growth S3198. The bandgap is between the E_1 and E_2 subbands with an energy gap $\Delta = 45\,\text{meV}$. The active part is a TQW of InAs/GaSb with $d_{\text{InAs}} = 25$ ML, $d_{\text{Ga}_{1-x}\text{In}_x\text{Sb}} = 10$ ML, and $x = 0.35$. The theoretical critical magnetic field is $B_c = 17.2\,\text{T}$.

2.3 Characterization of the growth structures

Before any sample fabrication from the previously introduced heterostructures, preliminary measurements of electrical transport and magneto-absorption have been performed.

2.3.1 Landau-level spectroscopy

A method for studying the band structure of 2D systems is the spectroscopy of allowed transitions between Landau levels. As formerly mentioned, the sample S3054 with the smaller gap is similar to the one studied by Krishtopenko *et al.* [KRGP+18] using this technique. Indeed, an incident photon is absorbed if its energy $\hbar\omega$ is equal to the energy difference between two Landau level. To be observed, the transitions from Landau levels below the Fermi level to empty states above the Fermi level must satisfy certain selection rules. However, in the situation of three subbands (H_1, E_1, E_2), the number of transitions satisfying the condition $\Delta n = \pm 1$, where n is the number of Landau levels in the classification of the eight-band Kane Hamiltonian, in the axial approximation, is extremely large. Here, we simply extrapolate linearly the evolution of these transitions in order to estimate the associated energy at zero magnetic field. A non-zero energy at zero magnetic field is interpreted as the inter-band transition signature. This energy is then associated with the energy gap.

We now present the experimental study of the magneto-absorption spectra of growth S3052. Figure 2.7 shows the experimental setup used for this measurement. The magneto-absorption spectra is carried out by Fourier transform spectroscopy in the Faraday configuration in magnetic fields up to 16 T at $T = 6\,\text{K}$. The sample is placed in liquid helium; radiation transmitted through the sample was detected by a composite bolometer, the signal from which was amplified and fed to the input of an analog-to-digital converter of the Fourier transform spectrometer.

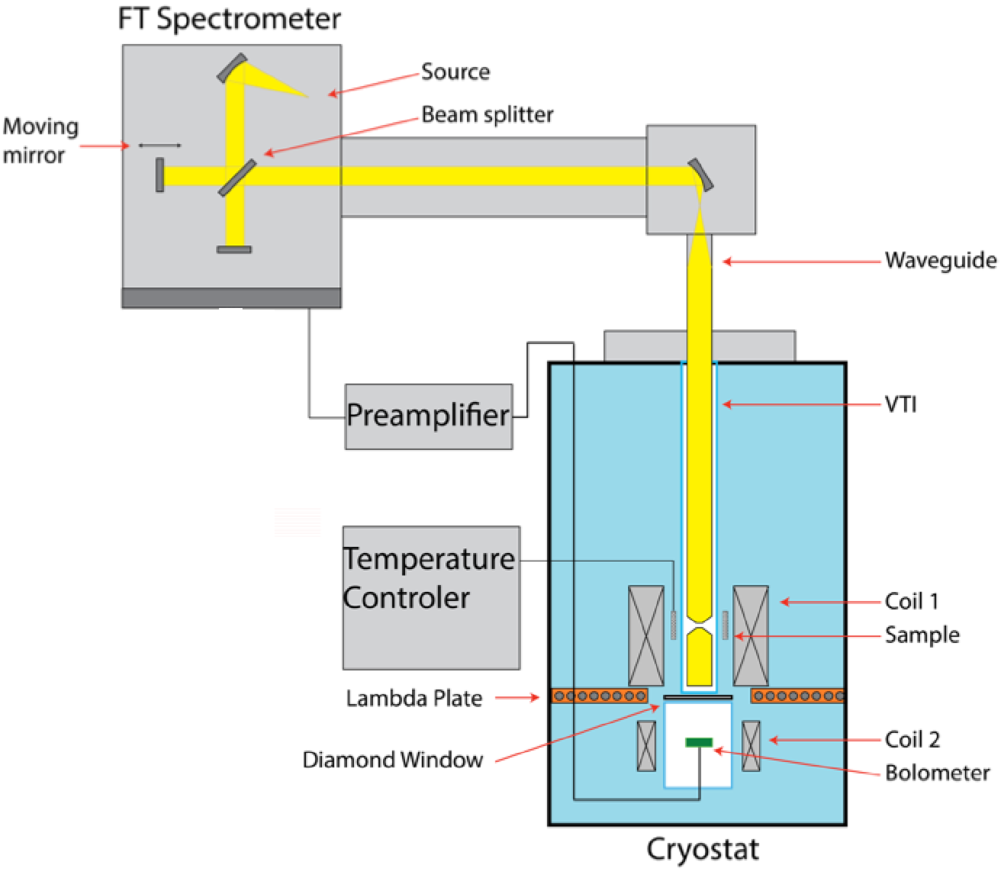

Figure 2.7: Schematic illustration of the terahertz magneto-spectroscopy setup. The first part is composed of a Fourier spectrometer following the principle of the Michelson interferometer principle. The superconducting coil (Coil 1) can provide magnetic field with inductance up to 16 T, while the compensating coil (Coil 2) keeps the overall magnetic field at zero in the vicinity of the bolometer. The bolometer is separated by a diamond window from the sample space (figure and caption adapted from [Mar17]).

Figure 2.8 shows the magneto-absorption spectra as a false color map. The yellow color correspond to maximum absorption intensity. Two absorption lines corresponding to interband transition are observed and are linearly interpolated at $B = 0\,\mathrm{T}$. The zero-magnetic field energy $\Delta \approx 300\,\mathrm{cm}^{-1} \approx 38\,\mathrm{meV}$ is obtained, which is quite large compared to the expected gap in S3052 $\Delta_{(th)} = 30\,\mathrm{meV}$. In addition, around $E \approx 550\,\mathrm{cm}^{-1}$ and $4\,\mathrm{T} < B < 12\,\mathrm{T}$, an absorption line independent of the magnetic field is observed and cannot be understood considering the Landau level structure shown in Fig. 2.5(c). A second absorption line indepdent of the magnetic field is observed at low energy ($E \approx 100\,\mathrm{cm}^{-1}$). Nevertheless the estimated gap value remains of the expected order of magnitude, which motivates further investigation of this sample by magneto-transport measurements.

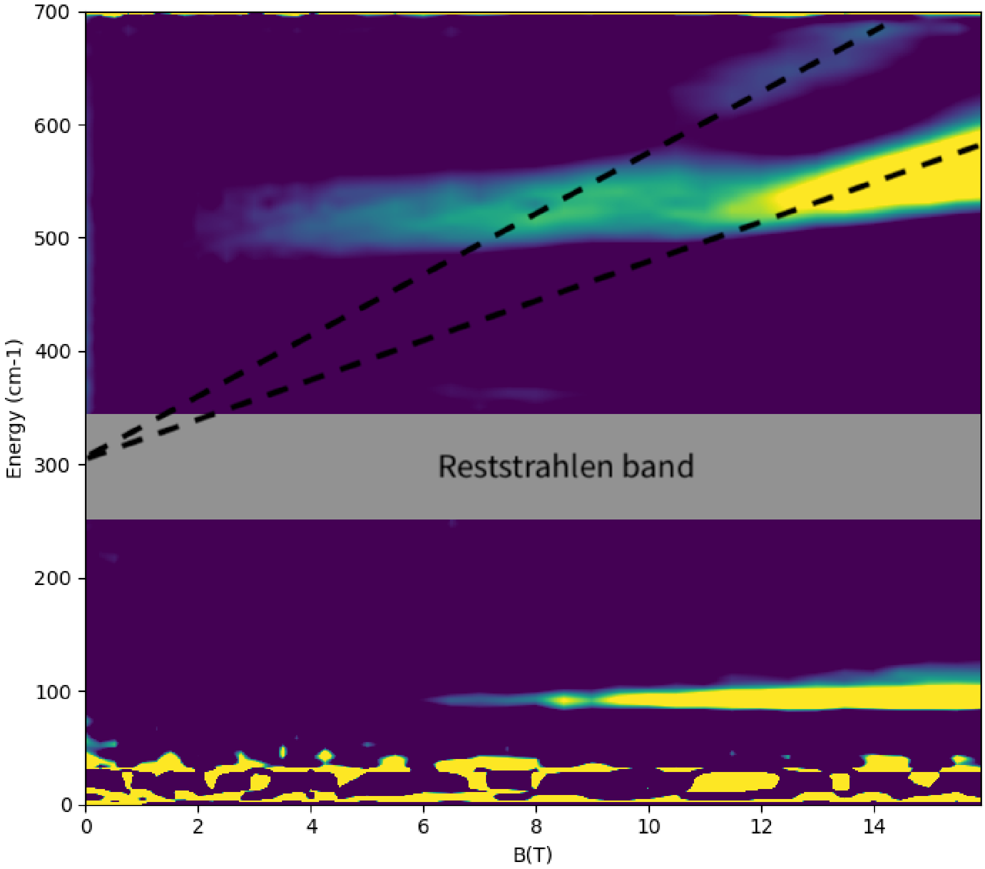

Figure 2.8: Magnetoabsorption spectra presented as a false color map for growth S3052. An increase in the absorption intensity corresponds to the color transition from blue to yellow. The gray band corresponds to the Reststrahlen region in the GaAs substrate. The black dashed lines highlight the observed absorption lines.

2.3.2 The van der Pauw method

One of the most common measurements of magneto-transport is the measurement of substrate resistivity as a function of magnetic field using the van der Pauw configuration (see Fig. 2.9). Its interest is also related to the ease of measurement because the preparation of the samples requires only to solder 4 contacts, (*e.g.*, by indium) to the four corners of a square sample. Note that the contact size must be small compared to the sample size. Moreover, the van der Pauw measurement of the resistivity requires samples which are homogeneous, isotropic and thin. This last condition is always verified for a 2DEG and note that we use in the following the notation ρ directly for the 2D resistivity $\rho_{2D} = \rho_{3D}/t$ where t is the thickness of the square sample. Van der Pauw showed that one can extract the resistivity ρ of a square sample by measuring the resistances $R_{AB,CD} = V_{CD}/I_{AB}$ and $R_{BC,DA} = V_{DA}/I_{BC}$, where V_{CD} is the voltage between the contact C and D, I_{AB} is the current applied between the contact A and B. The two resistances satisfy the relation:

$$\exp\left(\frac{\pi}{\rho} R_{AB,CD}\right) + \exp\left(\frac{\pi}{\rho} R_{BC,DA}\right) = 1. \tag{2.1}$$

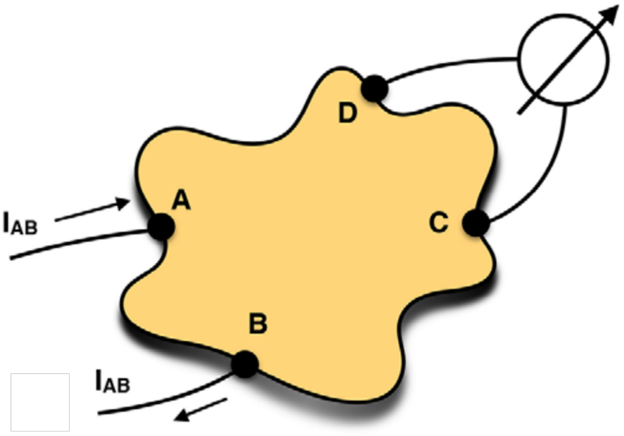

Figure 2.9: Typical van der Pauw arrangement of the 4P probes placed along the periphery of a thin and arbitrarily shaped sample (figure and caption adapted from [MEPT15]).

For a symmetric sample, such as a square, the reprocity theorem, one should verify $R_{AB,CD} = R_{BC,DA} = R$ and obtain:

$$\rho = \frac{\pi}{\ln 2} R. \tag{2.2}$$

However, it is worth mentioning that this method extends to non-symmetrical sample. The resistivity is then expressed as:

$$\rho = \frac{\pi}{\ln 2} \frac{R_{AB,CD} + R_{BC,DA}}{2} f, \tag{2.3}$$

where f is a form coefficient, function of the $R_{AB,CD}/R_{BC,DA}$ ratio and satisfies the condition

$$\cosh\left(\frac{\pi}{\ln 2} \frac{R_{AB,CD} + R_{BC,DA} - 1}{R_{AB,CD} + R_{BC,DA} + 1}\right) = \frac{1}{2} \exp\left(\frac{\ln 2}{f}\right). \tag{2.4}$$

2.3.3 The poor man's method: an extension of the van der Pauw method to anisotropic media

Initially, we performed van der Pauw measurements directly on some selected samples. For simplicity, all these samples had a square geometry, and the four contacts $1, 2, 3$ and 4 were placed clockwise on the four corners of the samples. Some samples exhibited a pronounced electrical anisotropy, with $R_{12,43} \gg R_{23,14}$. In the van der Pauw procedure, such an experimental anisotropy can *a priori* be cured by taking into account the f function, to extract the resistivity. However, we know that the original shape of the sample is a square, hence a large difference in the two van der Pauw resistances signals an isotropic conductivity, and the resistivity extracted by the usual van der Pauw procedure is incorrect. Another method has to be implemented.

Most 2D materials have an easy direction, in which the conductivity $\sigma_{\parallel}$ (the resistivity $\rho_{\parallel}$) is enhanced (reduced), and a perpendicular hard direction, in which the conductivity $\sigma_{\perp}$ (the resistivity $\rho_{\perp}$) is reduced (enhanced). These directions are sometimes determined by the crystal lattice. In our case, due to the cubic symmetry of the III-V semiconductor, the detected anisotropy cannot be attributed neither to the band structure nor the mass anisotropy. Anisotropic conductivity is sometimes observed in (In)GaAs channel heterostructures at low temperatures, and has been tentatively attributed to anisotropic interface roughness [TSTH92], cross-hatch

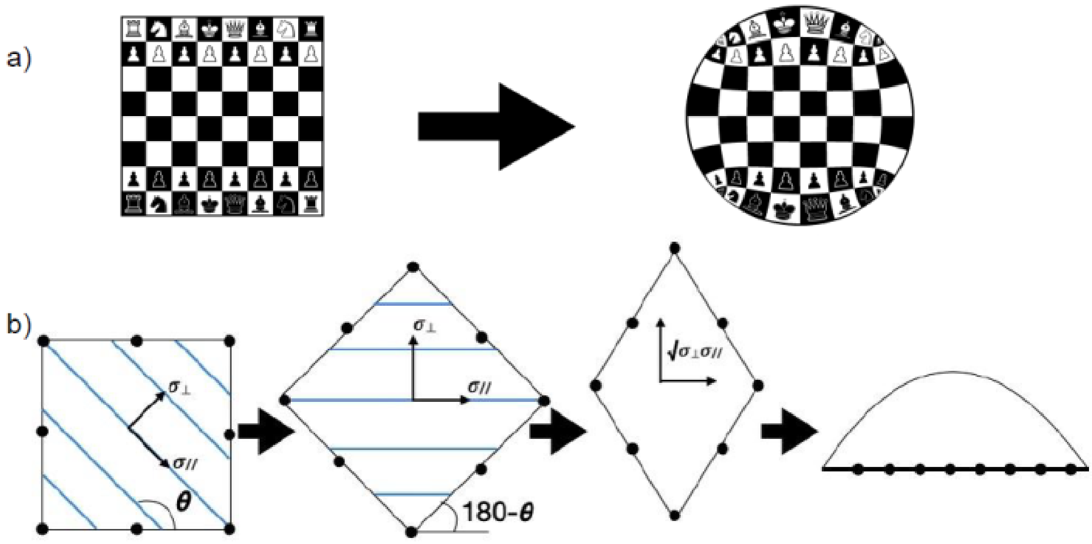

Figure 2.10: (a) Illustration of the Schwarz-Christoffel mapping on a chessboard. (b) Steps of the poor man's method for the determination of anisotropic conductivity. Mathematically, the sample is rotated, deformed and then mapped on a half-infinite plane.

morphology [LMV+03], lattice relaxation [GWK+94], dislocation distribution [MZN+10], composition modulation [EBC+08], and random piezoelectricity [LkS21]. More recently, a similar anisotropy has been observed in (Al,Ga)Sb/InAs two-dimensional electron gases epitaxied on GaAs (001) substrates, and attributed to piezoelectric scattering [WWZZ22]. This scattering originates from interface roughness, which can have different correlation lengths in the [110] and $[1\bar{1}0]$ directions, and gives rise to anisotropic piezoelectric field and scattering.

A precise determination of the anisotropy can be performed by using different kinds of devices (Hall bars of different orientations [LkS21], for instance, or a disk-shaped sample on which four probes can be positioned at the periphery [MEPT15]). In our case, we developped a poor man's method to rapidly characterize such a possible anisotropy. Let us assume that we have a 2D homogeneous sample in a plain domain G, whose electrical conductivity is defined by an anisotropic tensor σ. We assume that G is defined in local coordinate (x, y). The $\mathbf{x}$ and $\mathbf{y}$ axes do not necessarily coincide with the anisotropy axes $\mathbf{x}_{\|}$ and $\mathbf{y}_{\perp}$, and there is an angle θ between the two coordinate systems. Such a situation is depicted in Fig. 2.10(b). In the coordinates corresponding to the anisotropy axes, the conductivity tensor is simply

$$\sigma = \begin{bmatrix} \sigma_{\|} & 0 \\ 0 & \sigma_{\perp} \end{bmatrix}.$$

In the poor man's method we developed, as shown in Fig. 2.10b, G is a perfect square. The reason for this is that it is relatively easy to cleave square samples. The problem to solve is

$$\begin{cases} \nabla \cdot \mathbf{j} = 0, \forall (x, y) \in G, \\ \mathbf{j} = \sigma \nabla \varphi, \\ \phi|_{\kappa} = const, \\ (\sigma \nabla \varphi)_n |_{\Gamma \setminus \kappa} = 0. \end{cases} \tag{2.5}$$

Here, Γ is the contour of the domain G, κ is the part of the contour Γ that correspond to perfect ohmic contacts κ_1, κ_2, ... and n is the contour normal. We choose to have eight infinitely small ohmic contacts. Four contacts correspond to the corners of the square G. The four other contacts are placed in the middle of the four edges of the square, see Fig. 2.10(b).

The experimental procedure is relatively straightforward. We measure 16 different four probes configurations. If the contacts are labeled clockwise, as shown in Fig. 2.11, then the first four configurations are $R_{13,75}$, $R_{83,74}$, $R_{82,64}$, $R_{72,64}$. Then this pattern is repeated 4 times, increasing each contact number by two ($n \rightarrow (n+2 \mod 8)+1$). To evidence graphically the anisotropy, it is easier to label these 16 configurations $i = 1, 2...16$ by the angle φ_i between the **x** axis and the vector defined by the source and drain contacts ($\varphi_i = 0°, 26.5°, 45°, 63°, 90°, 116.5°..$). By doing so, the resistance can be graphically shown in a polar plot, and any anisotropy is easily evidenced. We can now detail the mathematical transformations corresponding to this poor man's method:

1. We initialize the problem by choosing some trial parameters $\sigma_\parallel$, $\sigma_\perp$, and θ.

2. We rotate the sample G, so as the anisotropy axes correspond to the axis **x** and **y** defined previously.

3. We change the variables in problem 2.5 by

$$\xi = x\sigma_\perp, \eta = y\sqrt{d},$$

   where $d = \sigma_\parallel\sigma_\perp$. This is depicted in Fig. 2.10 (b). The new domain is called $\hat{G}$. We then define a new problem as:

$$\begin{cases} \nabla \cdot \hat{\mathbf{j}} = 0, \forall(\xi,\eta) \in \hat{G}, \\ \hat{\mathbf{j}} = s\nabla\hat{\varphi}, \\ \hat{\varphi}|_{\hat{\kappa}} = const, \\ \dfrac{\partial\hat{\varphi}}{\partial\hat{n}}|_{\hat{\Gamma}\setminus\hat{\kappa}} = 0. \end{cases} \tag{2.6}$$

   Here $\hat{n}$ is the contour normal of $\hat{G}$, and $s = \sqrt{d}$. Kleiza *et* al. [KSK07] demonstrated that the problems 2.5 and 2.6 are equivalent. Remarkably the new problem is isotropic.

4. We can now apply a Schwarz-Christoffel (SC) transformation. A SC transformation, as shown in Fig. 2.10, map a given shape into another one, preserving all local angles. We map numerically the deformed, isotropic device $\hat{G}$ into the half-upper plane of the complex plane. We extract from this transformation the positions of the eight contacts along the real axis. This can be done easily by using some predefined numerical libraries [2].

5. We can now calculate in the half-upper plane the 16 resistances $R_{13,75}$, $R_{83,74}$, etc. using the method initially proposed by van der Pauw. The properties of the SC transformation combined with the equivalence of the problems 2.5 and 2.6, guarantees that these resistances equal the resistances that would be measured in the original, anisotropic sample shown in Fig. 2.10 (b).

6. We compare the numerical result with the experimental resistances which have been measured. We evaluate a residual error by using the method of the least squares. We then apply an optimization procedure based on the least-square method, we modify the trial parameters $\sigma_\parallel$, $\sigma_\perp$, and θ, until the final convergence, where the error cannot be reduced anymore.

---

[2] https://tobydriscoll.net/project/sc-toolbox/

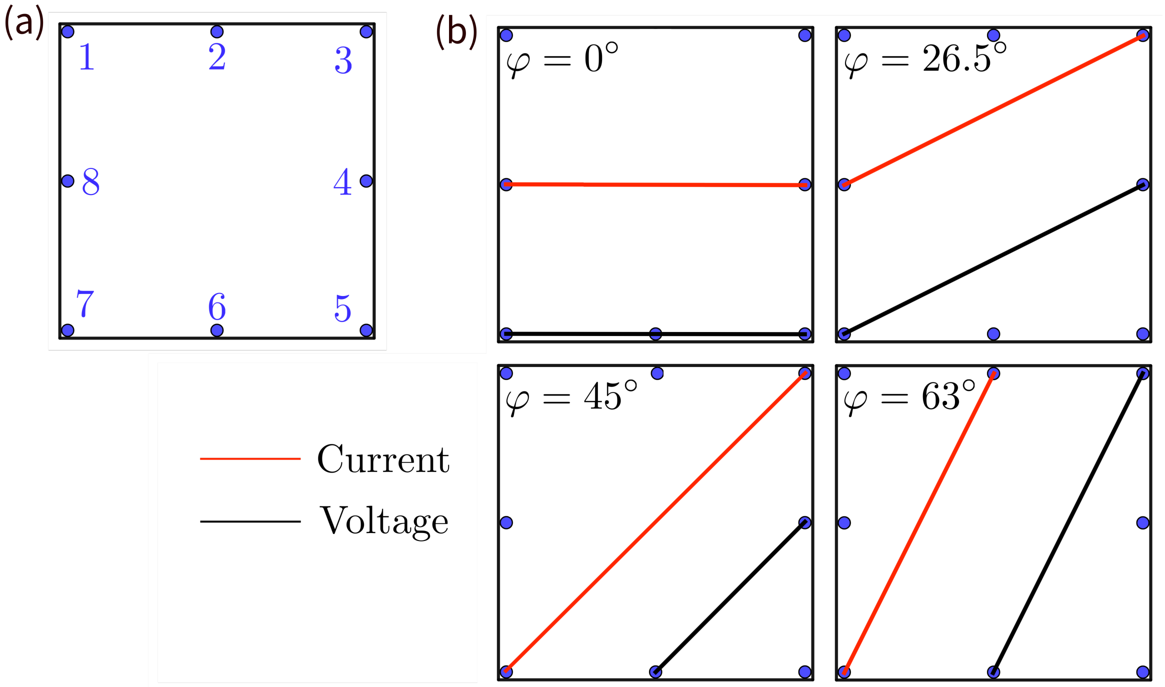

Figure 2.11: (a) Schematic representation of an anisotropic square sample with 8 contacts. (b) Schematic representations of different four-probes configurations for the measurement of electric anisotropy in a square sample with 8 contacts (blue circles). These configurations can be extended by 90° rotations to a total of 16 different resistivity directions φ.

The advantage of this method lies in its simplicity. Some parts of the grown samples are mechanically cut into square pieces (the axis will then correspond to the [110] and [1$\bar{1}$0] directions). Then, 8 contacts are deposited with indium, and the measurement are performed in a cryostat. The measurement of the different resistances is automatized by using mechanical switches (we used a Keithley **7001** switch system). The fitting procedure is implemented in a *MatLab* program. With this technique, only one device has to be measured. Moreover, the angle θ can be determined. We stress that with four probes only, it is usually not possible to determine the anisotropy, especially if θ is not known.

Let us now illustrate the sensitivity of this method. Let us call $R_i(\rho_\perp, \rho_\parallel, \theta)$, $i = 1, ...16$, the values of the 16 resistances calculated for a given anisotropic configuration $(\rho_\perp, \rho_\parallel, \theta)$. Figure 2.12 shows in a polar plot the 16 normalized resistances $R'_i(\rho_\perp, \rho_\parallel, \theta = 0)$, defined as

$$R'_i(\rho_\perp, \rho_\parallel, \theta) = \frac{R_i(\rho_\perp, \rho_\parallel, \theta)}{\min(R_i(\rho_\perp, \rho_\parallel, \theta))}.$$

Figure 2.12 (a) shows 6 different anisotropy factors corresponding to $\rho_\perp/\rho_\parallel = 1, 2, 3, 4, 5$ and 6. For $\rho_\perp/\rho_\parallel = 1$, R'_i gives a perfect circle in the polar coordinates. When the anisotropy increases, the circle develops progressively 2-nodes. The main axes of the butterfly-like pattern give the angle θ of the anisotropy. Figure 2.12 (b) demonstrates that this method is quite sensitive. Indeed, for $\rho_\perp/\rho_\parallel = 6$, the ratio $\max(R_i)/\min(R_i)$ is as large as 30.

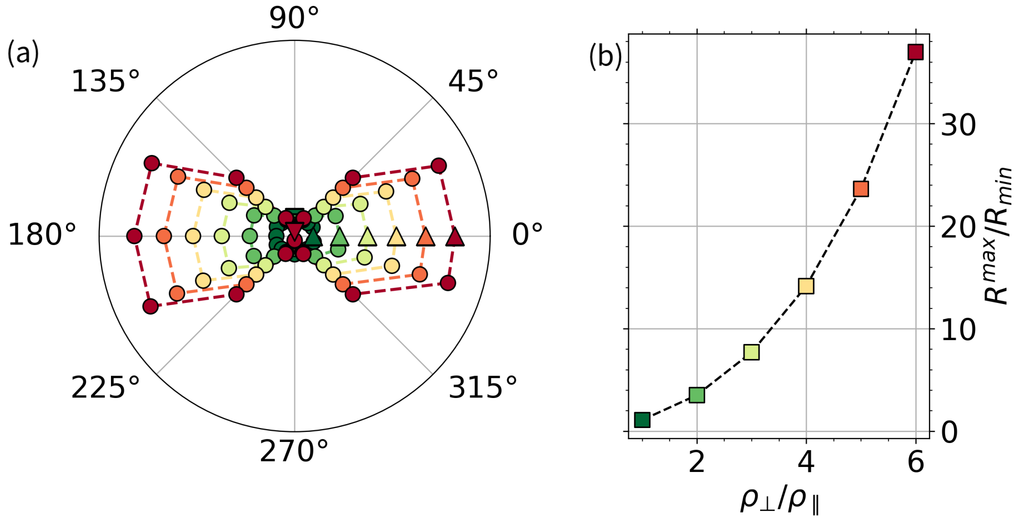

Figure 2.12: Sensitivity of the poor man's method. (a) Polar plot of the 16 normalized resistances R'_i (see main text) versus the angle φ_i for different anisotropy ratio $r = \rho_\perp/\rho_\parallel$. We have chosen $\theta = 0°$. (b) $\max(R_i)/\min(R_i)$ as a function of r. The colorscale is the same for both panels.

Let us show now experimental results. Figure 2.13(a) shows the 16 resistances arranged in polar coordinates for growth S3052. The resistances have been measured at seven different temperatures, from 300 K down to 10 K. The measurements were performed in a ^{4}He cryostat, under a low Helium pressure. It is obvious from the graph that the anisotropy increases when the temperature decreases. Also, is is clear that $\theta \simeq 0°$. Unfortunately, we could note discriminate the two [110] and [1$\bar{1}$0] axes when we cut the sample, but it is clear from the analysis that the anisotropy axes do correspond to these two crystallographic directions. Figure 2.13(b) shows the easy and hard resistivities $\rho_\perp$ and $\rho_\parallel$ extracted from the fit, as a function of T. It appears that $r = \rho_\perp/\rho_\parallel$ increases from $r = 1.6$ at $T = 300$ K to $r = 5$ at $T = 10$ K, corresponding to a resistance ratio $\max(R_i)/\min(R_i) = 2.7$ and $\max(R_i)/\min(R_i) = 20$ respectively.

Previous studies of anisotropic electron transport in InAs-based structures usually refer to mobility anisotropy [LMV$^+$03, GWK$^+$94, MZN$^+$10, EBC$^+$08]. Additional magneto-transport measurements should be considered to extract mobility as a function of contact configuration orientation. Figure 2.14 shows atomic force microscopy measurements of growth S3052 surface that reveals an anisotropic distribution of trenches on the cap layer surface. The cross-hatch morphology in III-V semiconductors is attributed to large lateral variations of the in-plane strain, due to the lack of inversion symmetry. The correlation between the anisotropic transport properties and the asymmetric cross-hatch morphology has already been reported in strained InAs channel grown on GaAs substrates [LMV$^+$03].

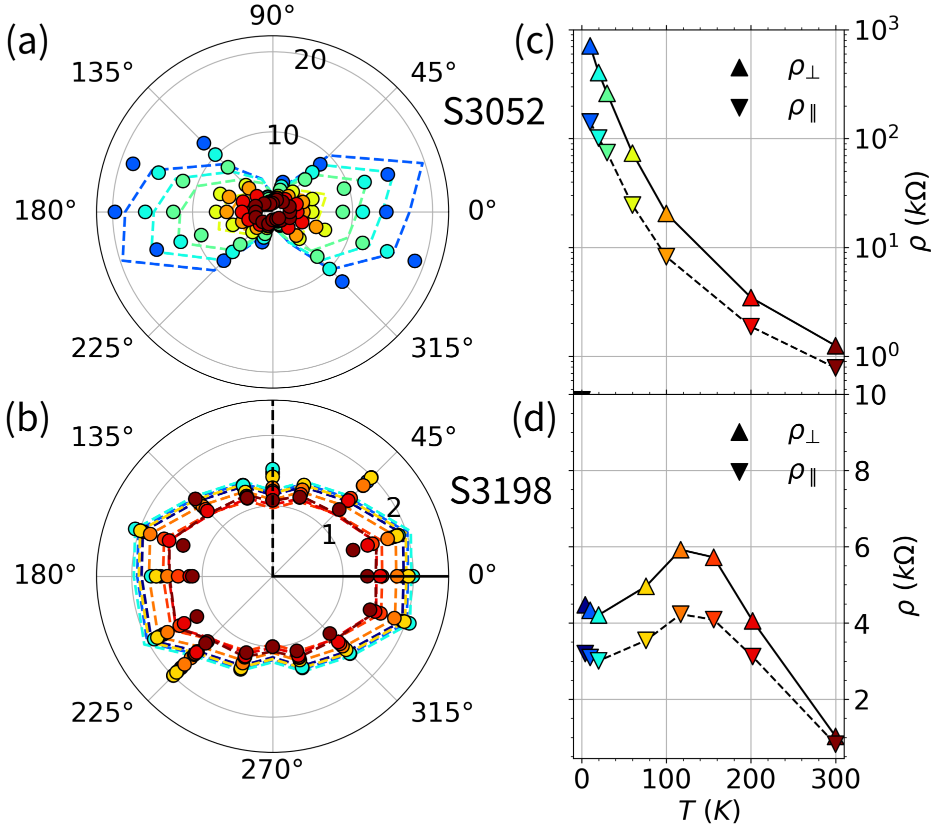

Figure 2.13: (a, b) Polar plot of the resistance ratio R'_i for different temperatures for S3052 (a) and S3198 (b). The symbols correspond to the experimental values, and the colored dashed lines correspond to the fits. The solid and dashed black lines highlight the two resistance directions shown in the (c, d) panels. (c, d) Temperature dependence of 2 specific resistivities directions $\rho_\perp$ (up triangle) and $\rho_\parallel$ (down triangle).

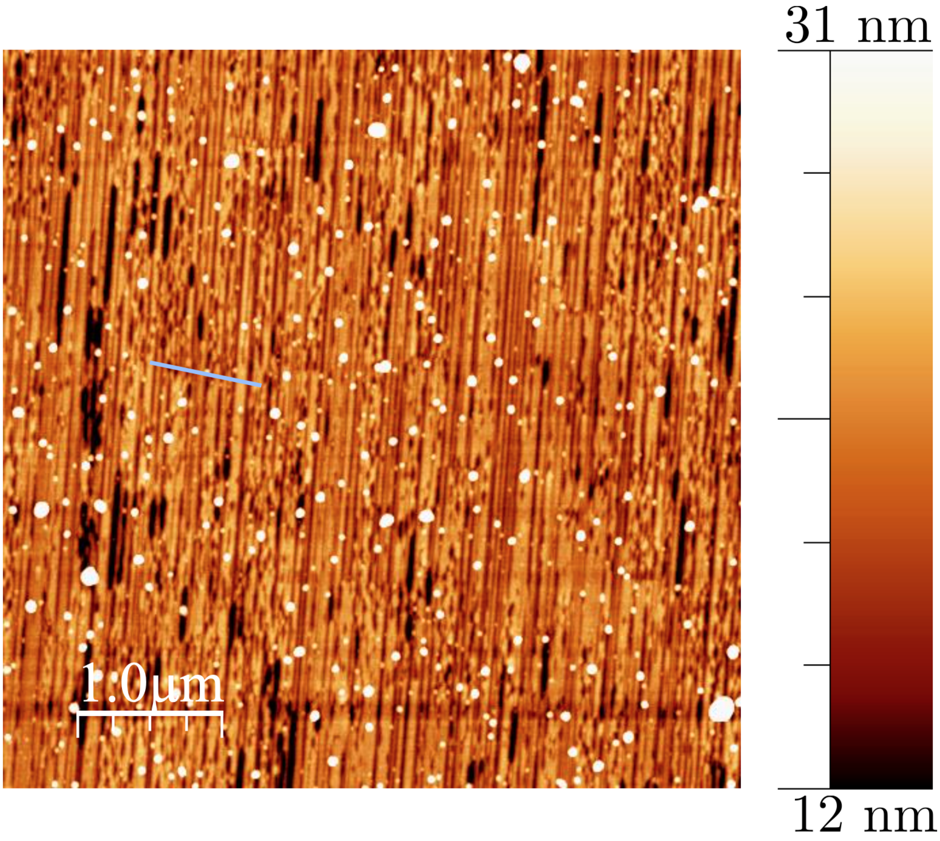

Figure 2.14: AFM image revealing the cross-hatch morphology of the surface for growth S3052.

2.4 Hall bars fabrication

The fabrication process of devices for magneto-transport measurements has been developed in the Centrale de Technologie en Microélectronique (CTM[3]). In addition, some samples grown in the IES were also sent to the Technische physik group (TEP[4]) for the fabrication of Hall bar devices. We will present here the process optimized at the CTM during my PhD; and devices obtained from both clean rooms in Chapter 2.5.

In order to fabricate Hall bar devices from the CTM lithography mask, the sample wafer were cleaved into 6 mm × 6 mm square piece along the (100) and (010) directions. Optical lithography was preferred to electron-beam lithography because of the large size of some devices. Different lithography mask were used for the realisation of Hall bars. The lithography mask used in CTM and the one used in TEP are presented in Figure 2.15 and Figure 2.16 respectively. The CTM lithography mask is designed for the fabrication of 6 mm × 6 mm square samples with 6 Hall bars of different sizes and the TEP one is an array of 16 Hall bars, all with the same sizes but different lengths between the lateral probes. More details are provided in Table 2.1.

Table 2.1: Hall bar dimensions for the (a) CTM and (b)TEP lithography mask.

(a)	L (µm)	W (µm)	l_p(µm)	l_1(µm)
CTM	400	100	100	120
	200	50	50	60
	40	10	10	12

(b)	L(µm)	W(µm)	l_p(µm)	l_1(µm)
TEP	110	20	70	10
			50	20
			30	30
			10	40

2.4.1 Alignment markers

The manufacture of Hall bar requires many steps of lithography, the first one being the fabrication of alignment marks. These markers allow us to align the lithography mask at all stages of the lithography. A 1.4 µm-thick layer of photoresist (AZ-5214) is made by spin-coating at 4000 rpm for 30 s and then dried after a post-deposition bake at 110 °C for 2 minutes. A first UV-exposition for 7 s with the lithography mask followed by a post-exposure bake at 110 °C for 2 minutes allows the inversion of the photoresist polarity. Initially, the photoresist has a positive polarity. It follows that the chemical development will dissolve the exposed photoresist. On the contrary for a negative photoresist, the areas exposed to UV-light are not opened after chemical development.

Figure 2.17(a) shows the pattern of the alignment marks (CTM), where the red areas are the opaque regions of the mask. After the first UV-exposure and post-exposure baking, the polarity of the photoresist is inverted. A second exposure under UV-light without mask followed by chemical development (in AZ-726 developper for 55 s) then opens the region initially under the opaque regions of the lithography mask. Once the pattern is developed from the photoresist, a metallic layer of Cr/Au (10/100 nm) is deposited on the sample by electron gun evaporation. The Cr layer ensures good adhesion and the gold layer keeps the markers clearly visible. The metallic layer deposited on photoresist is lifted-off by dissolving the photoresist with acetone. The device is cleaned in an acetone bath in an isopropanol (IPA) bath. Figure 2.17(b) is a microscope image of a sample after the fabrication of the markers and Table 2.2 summarizes the fabrication process of the markers.

---

[3] Université de Montpellier, Centrale de Technologie. en Micro et nanoélectronique, 860 rue St Priest, 34097 Montpellier (cedex 5), France

[4] Technische Physik, Physikalisches Institut, University Würzburg, Am Hubland, 97074 Würzburg, Germany

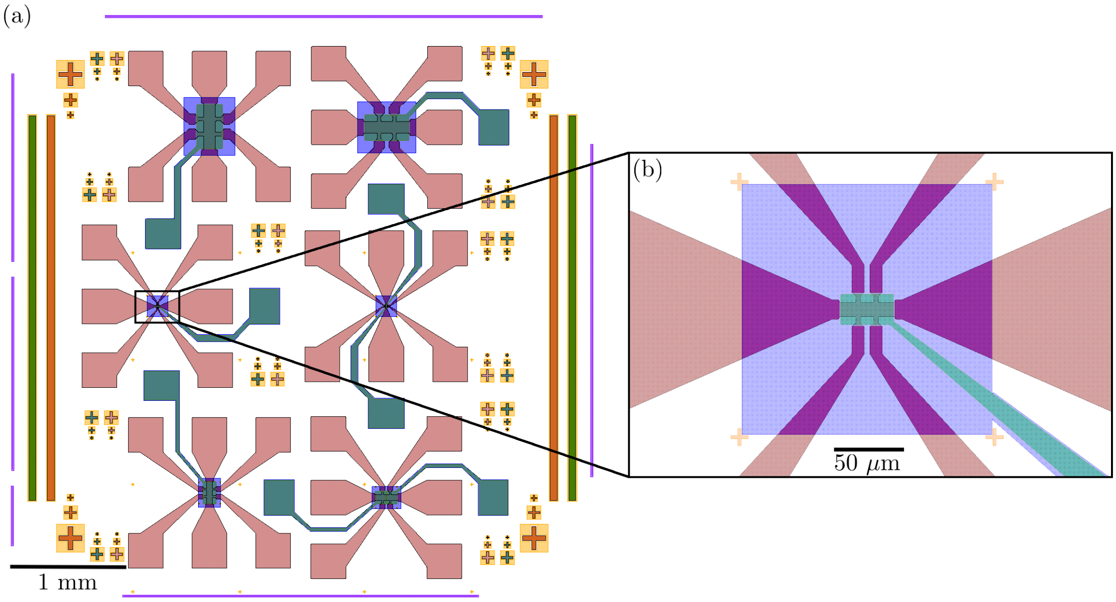

Figure 2.15: (a) Sketch of the 6 mm × 6 mm lithography mask combining 6 Hall bars (CTM) and (b) zoom on the smallest Hall bar. The yellow patterns correspond to the Alignment markers. The pink patterns correspond to the HB contacts and the blue patterns correspond to the dielectric layer. The green pattern corresponds to the layer of the gate.

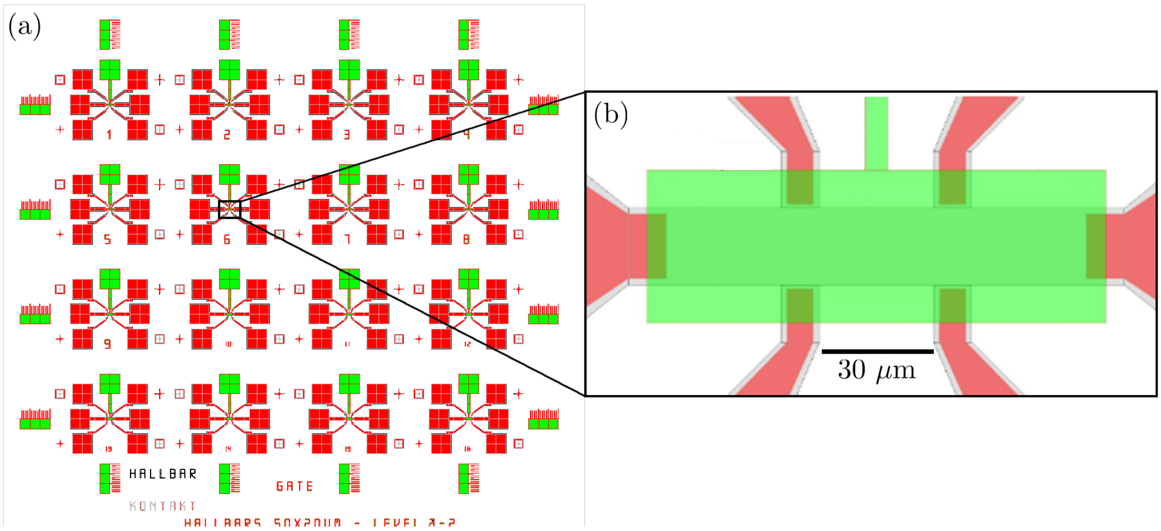

Figure 2.16: (a) Sketch of the Hall bar lithography mask for Würzburg devices (TEP) and (b) zoom on one Hall bar.

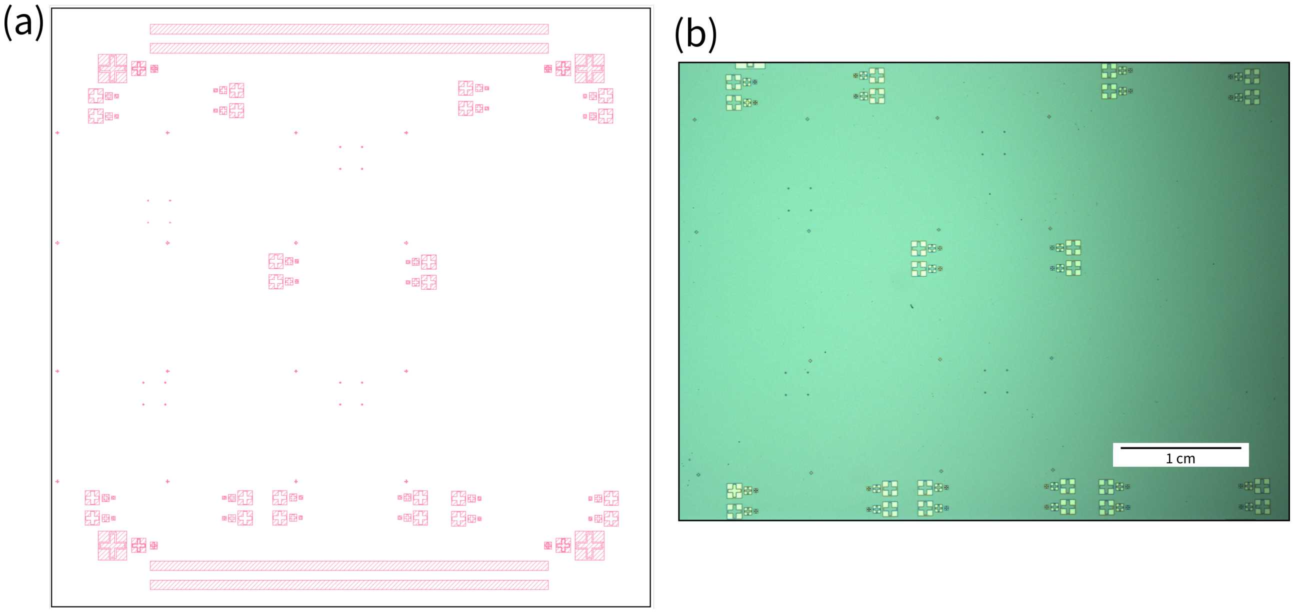

Figure 2.17: (a) Sketch of the marker layer from the CTM lithography mask. The red regions correspond to the opaque part of the mask. (b) Microscope image after fabrication of the markers. The green region corresponds to the cap-layer of the grown sample and the yellow patterns are the Cr/Au markers.

2.4.2 *Mesa* definition

After the markers, we isolate the active part of the heterostructure *i.e.*, the TQW and the AlSb barriers, in well-defined regions. These regions consist in the Hall bar region itself, as well as the part which will be metallized for the contacts (see Fig. 2.18(a)). The isolation is made by etching the active part outside these regions, which are then usually called *mesa*. It prevents the current to spread outside the Hall bar during transport measurements. There are different etching options, such as wet etching or dry etching. This step is not trivial because the size of the patterns can be relatively small, *i.e.*, on the order of magnitude of a few microns. Moreover, the etching method itself may influence the *mesa* flank properties and induces a non-topological conduction through the edges. Finally, a certain precision of the etched thickness is also expected, *i.e.*, of the order of a few nanometers. For these reasons of resolution and precision of etching depths, we preferred a dry etching rather than a wet etching based on phosphoric acid (3 mL), hydrogen peroxide (5 mL), citric acid (55 mL, 1:2) and water (220 mL).

The Hall-bar *mesa* was patterned using UV-light lithography with a resolution down to 1 µm. The positive photoresist AZ-1518 is spin-coated with parameters : 4000 rpm, 30 s. The 1.8 µm thick layer of photoresist is baked for 1 min at 110 °C and exposed to UV-light for 35 s. The exposed regions (transparent region in Fig 2.18(a)) are opened after the development performed using the AZ-726 developer for 25 s. InAs/GaSb based growths were etched by dry etching using an Inductive Coupled Plasma ICP based on Chlorine-containing gas. The sample is etched down to the superlattice of GaSb/AlSb. A schematized side-view of the *mesa* definition is shown in Fig. 2.19. For both wet and dry etching recipes, the etch rate can vary depending on the clean room condition and previous use. To ensure the precision of the etched thickness, a first test must be performed on a test sample for the same wafer. Figure 2.18(b) shows a microscope image of a device after defining the *mesa* and removing by an acetone bath the remaining photoresist above the protected regions. The *mesa* definition process is summarized in Table 2.3

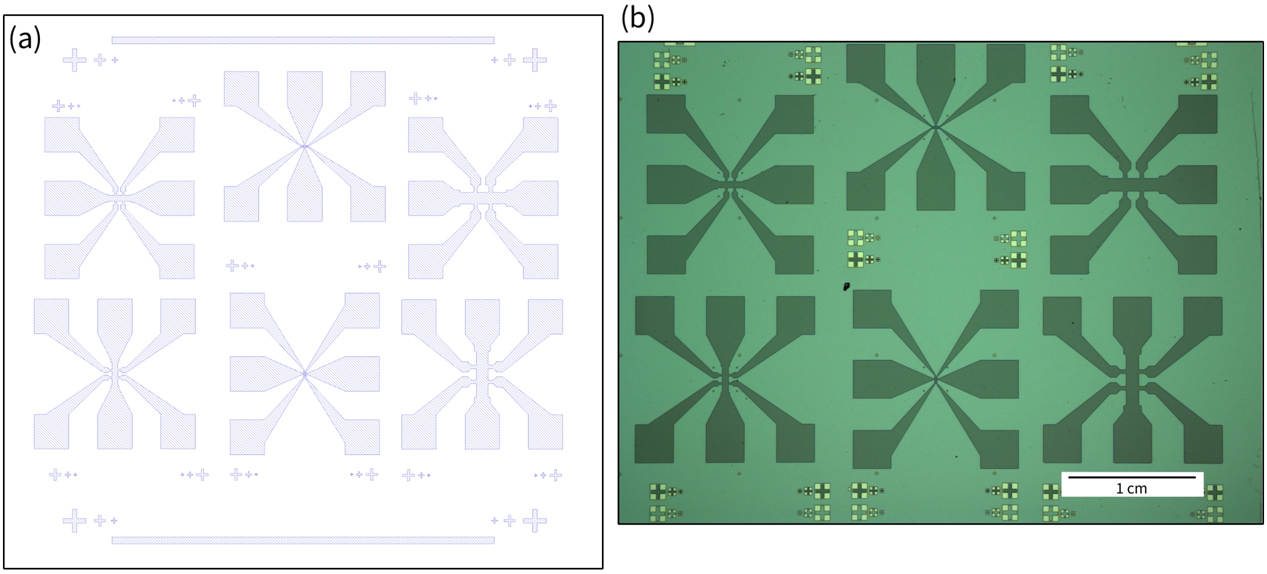

Figure 2.18: (a) Sketch of the *mesa* layer from the CTM lithography mask. The blue regions correspond to the opaque part of the mask. (b) Microscope image after the *mesa* pattern etching. The lighter green region corresponds to the etched one.

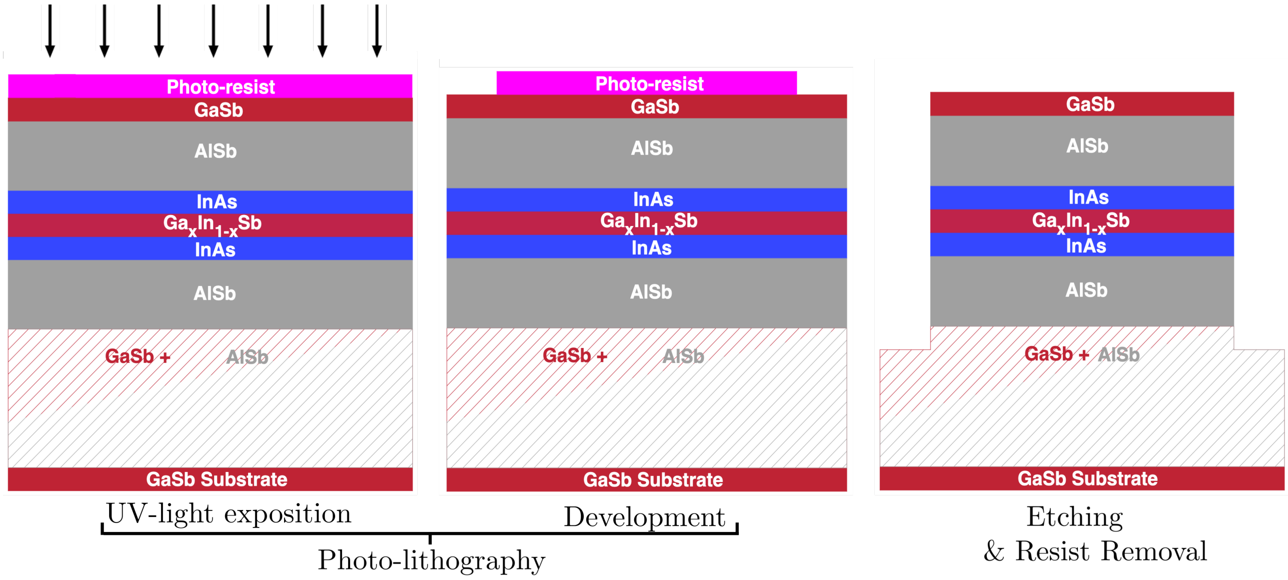

Figure 2.19: Steps for Hall-bar *mesa* etching.

2.4.3 Metallization

The metallization of the HB probes allows us to wire-bond any device to the device holder for transport measurement. The contact pads are designed large enough to connect the device by manual indium soldering. Even if this technique was prefered at the first stages of the HB fabrication, it can be time-consuming on the long run and makes it difficult to disconnect and reconnect another device from the same chip. Two different contact recipes for the metallic deposition were subsequently tested. Both are perfomed using UV-light photo-lithography, following the same lithography process as for the marks (see Section 2.4.1), using the contact layer of the lithography mask, shown in Fig. 2.20(a).

The first recipe is to etch the heterostructure to deposit the metal directly on the top InAs layer. For the same reasons of etched thickness and in-plane resolution mentioned in Section 2.4.2, ICP dry-etching was prefered to wet etching recipes. A Ti/Pt/Au (10/30/150 nm) electron gun evaporation is performed directly after the etching to prevent oxydation of the exposed InAs layer. Finally, the metal is lifted off in acetone. A schematized side-view of this metallization recipe is shown in Fig. 2.21

The second metallization recipe tested differs as it does not require etch the contact pads. A deposition by sputtering of AuGeNi/Au (70/150 nm) is directly performed after the lithography process. After a lift-off, the device is then annealed for 3 minutes at 380 °C under nitrogen atmosphere in order to vertically diffuse the AuGeNi though the heterostructure. However, this alternative was not chosen in spite of the ohmicity of the contacts due to an isotropic diffusion phenomena of the metal in the sample, which creates short-circuits between the contacts for the smallest Hall bars. In addition, it was observed that the wire bonding was easier on devices metallized following the first recipe. Both recipes are still summarized in Table 2.4.

The wire bonding was performed in the CTM by wedge bonding with aluminum wire. However a ball bonding with gold wire could be also used in L2C as a back-up in case of disconnection.

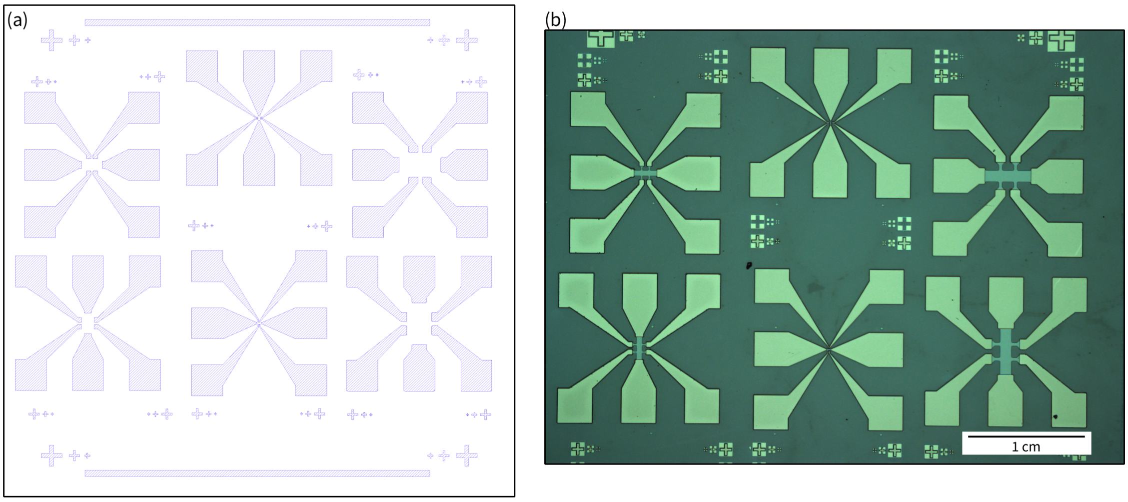

Figure 2.20: (a) Sketch of the contact layer from the CTM lithography mask. The blue regions correspond to the opaque part of the mask. (b) Microscope image after the metallization of the contacts (first recipe).

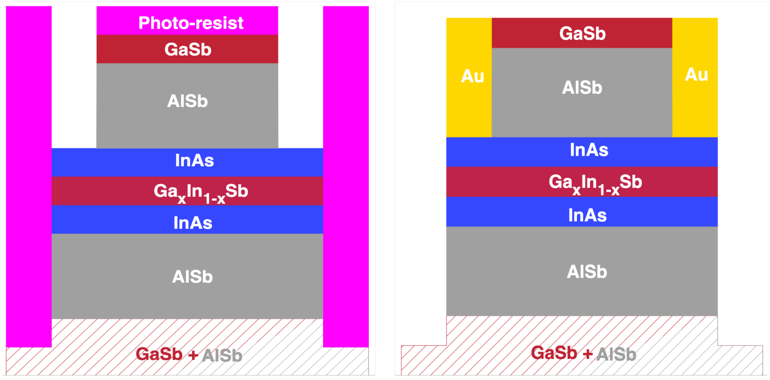

Photo-lithography

Metallization
& Lift off

Figure 2.21: Steps for metallic contact fabrication.

2.4.4 Estimation of the substrate resistivity

At this stage of fabrication, Hall bars could be tested and measured to improve the fabrication steps up to this point. In Section 2.4.2 we mentioned that the purpose of the *mesa*-etching is to design the Hall bar shapes and isolate the device. We investigate a possible contribution in the conduction through the substrate by using two Hall bars bonded from the same chip. Note that considering the etch depth, a conduction between 2 Hall bars can take place, in the substrate, or in the buffer. However, we compare in the following experimental results obtained from growths S3052 and S3198, both having a similar buffer structure but different substrates.

It is well known that the two-probe method is inappropriate for a correct determination of the resistivity of an infinite homogenous plane. Indeed, a point contact has no size and gives an infinite contribution to the resistance. However, if we measure the resistance between two Hall devices, the typical size of the contact resistance can be roughly approximated as the size of the Hall devices themselves. We could not find in the literature any formula giving the value of the resistance between two circular contacts of radius a, of zero resistance, separated by a distance d, and placed onto an infinite 2D plane of resistivity ρ. Therefore we solved this problem numerically, using a finite difference scheme. The code is given in the annex and the result in shown in Fig. 2.22. We find that for our geometries, where it is reasonable to take $d/a \simeq 3$–10, the two-probe resistance is of the same order of magnitude than the resistivity itself.

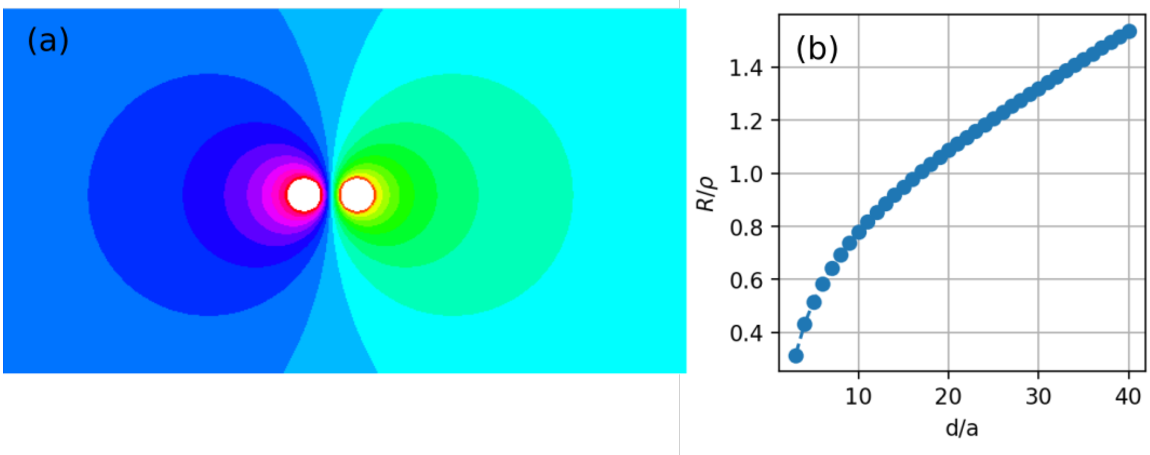

Figure 2.22: (a) Scheme of the equipotential lines in an infinite 2D plane when a current flows between two circular, perfect contacts of radius a, separated by a distance d between their centers. Here, $d/a = 3$. (b) Ratio of the measured resistance between the 2 contacts and the resistivity ρ of the 2D plane, as a function of d/a.

Figure 2.23 shows that both substrates from the S3052 and S3198 growths are conducting at room temperature. In the case of growth S3052 (GaAs substrate), the resistivity remains lower than 10 kΩ even at $T = 50$ K. We compare the rough estimation of substrate resistivity to the resistivity of the single Hall bar measured in the gap regime (see Chapter 3) for both S3052 and S3198 based devices.

To safely determine the resistivity in the Hall bar, we restricted the temperature ranges to temperatures where the resistivity of the devices is less than 1% of the measured resistances of the etched areas (e.g., $T < 25$ K for S3052). In the case of the growth S3198, the gap regime was not reached above 150 K (see Chapter 3). This being said, we still esteem that under temperature of 250 K, the GaSb substrate doesn't induce any parallel conduction, considering that the resistivity measured between two Hall bars is above 10 MΩ.

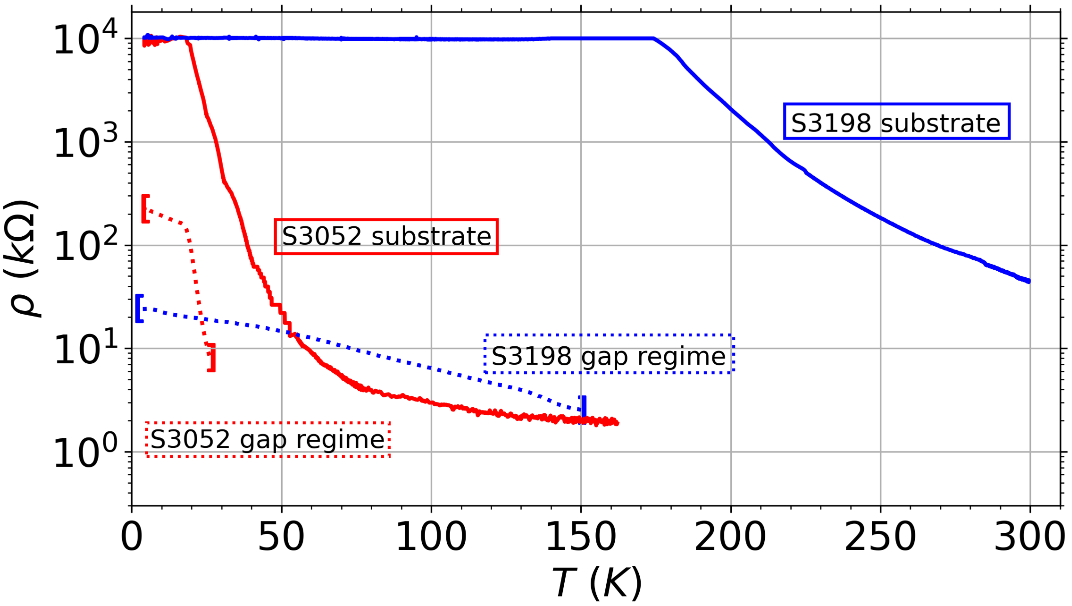

Figure 2.23: Temperature dependence of resistivities of the etched areas in growths S3052 (red) and S3198 (blue) respectively. The solid lines correspond to the resistivity of the substrate S3052 and S3198 growths. The dotted lines are the maximum of resistivity extracted in the gap regime for both structures. The saturation at 10 MΩ is an artifact due to the input impedance of the electronics - the real resistivity is much higher.

2.4.5 Dielectric Gate

The final step of the process is the fabrication of a top dielectric gate. The main purpose is to obtain a field-effect transistor configuration to tune the Fermi level. Besides, the dielectric layer also protects the flanks of the Hall bars from oxydation. In CTM, dielectric layers are deposited by Plasma-Enhanced Chemical Vapor Deposition (PECVD). Two different recipes of dielectric layer deposition were tested. The first one is a unique 300 nm thick layer of SiO_2 and the second one is a stack of $Si_3N_4/SiO_2/Si_3N_4$ (3SiX) of thickness 100 nm each. The main idea behind the second recipe is to reduce the leakage current of the dielectric gate thank to the mismatch between SiO_2 and Si_3N_4 defects. Note that for both dielectric deposition recipes, it was not possible to obtain a dielectric gate on a cm^2 surface scale without significative current leakage. This is most probably due to a too important defect density. As a consequence, it is difficult to make a generic characterization of the dielectric layers without the influence of the previous fabrication steps. For this reason, the behavior of the top gate is specific to each device and detailled in Section 2.5.

After the deposition, a new lithography step is done with positive resist as detailled in Section 2.4.2, using the blue pattern shown in Fig 2.24(a). The non-protected areas (transparent regions) are then etched by ICP based on Fluor gas. A second lithography process is done to deposit a Ti/Au (10 nm/200 nm) layer for the top gate, following the same procedure as for the alignement mark fabrication detailed in Section 2.4.1). Figure 2.24(b) shows a microscope image a device after the fabrication of the top gate. On the one hand it is quite complicated to realize dielectric gates on these structures (*cf.* the behavior of the different gates in Section 2.5), on the other hand, the pattern itself has an importance with respect to the distribution of the electric field induced by the top gate, in particular at the edges of the device. We have therefore opted for metallic gate patterns covering a larger area than the *mesa*. A schematized side-view of the top gate fabrication is shown in Fig. 2.25 and summarized in Table 2.5.

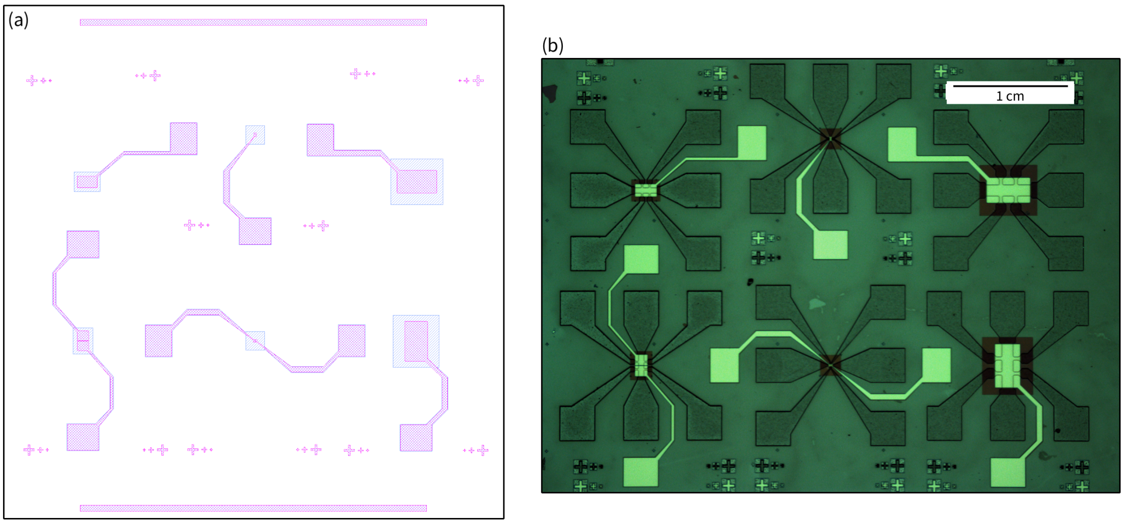

Figure 2.24: (a) Sketch of the top gate layer from the CTM lithography mask. The blue pattern corresponds to the dielectric and the purple one correponds to the metallic layer of the top gate. (b) Microscope image after the metallization of the contacts.

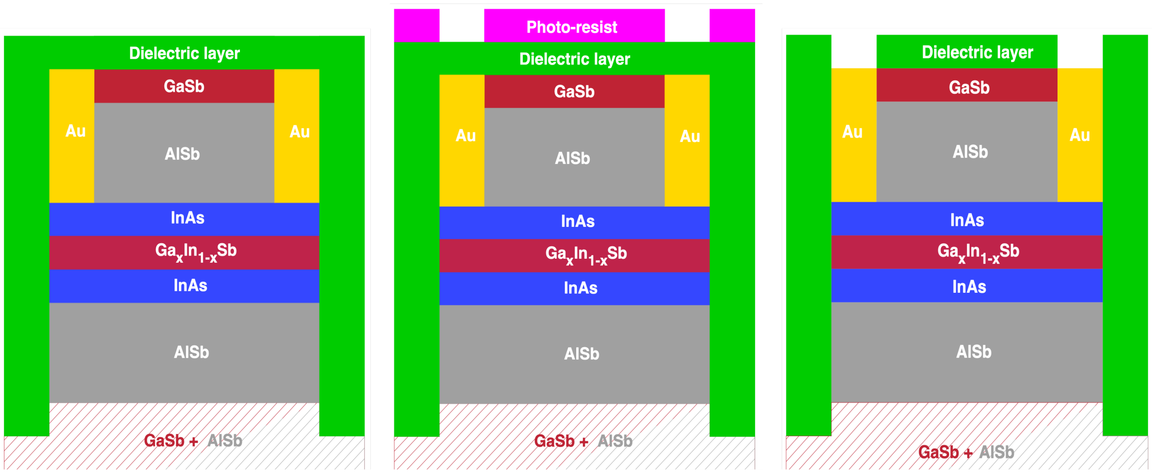

Dielectric deposition

Photo-lithography

Etching & Resist Removal

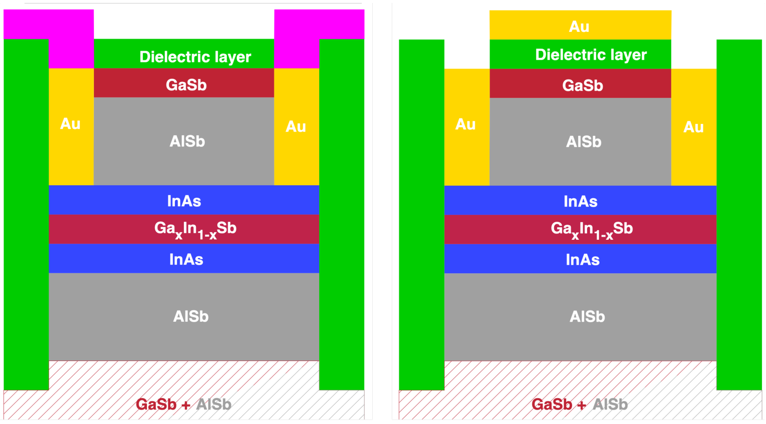

Photo-lithography

Metallization & Lift off

Figure 2.25: Steps for dielectric gate fabrication.

Hall bar fabrication process

Table 2.2: I. Alignment marks

Sample cleaning	Acetone bath Isopropanol bath
Lithography	Spin-coating of AZ-5214 (-) resist at 4000 rpm for 30 s First bake at 110 °C for 2 min First UV exposition with lithography mask for 7 s Second bake at 110 °C for 2 min Second UV exposition without lithography mask for 60 s Development in AZ-726 developer for 55 s
Metallic deposition	Cr/Au (10/100 nm)
Lift-off	Acetone bath Isopropanol bath

Table 2.3: II. *Mesa* definition

Sample cleaning	Acetone bath Isopropanol bath		
Lithography	Spin-coating of AZ-1518 (+) resist at 4000 rpm for 30 s Bake at 110 °C for 1 min UV exposition with lithography mask for 30 s Development in AZ-726 developper for 25 s		
Etching	Dry ecthing in ICP RIE Cl-gas Oxford plasmalab 100 down to the GaSb/AlSb superlattice	or	Wet etching in $H_2O/C_6H_8O_7/H_2O_2/H_3PO_4$ (220/55/5/3 mL) down to the GaSb/AlSb superlattice
Sample cleaning	Acetone bath Isopropanol bath		

Table 2.4: III. Metallization of the contact pads

<table>
<tr><td>Sample cleaning</td><td colspan="3">Acetone bath
Isopropanol bath</td></tr>
<tr><td>Lithography</td><td colspan="3">Spin-coating of AZ-5214 (-) resist at 4000 rpm for 30 s
First bake at 110 °C for 2 min
First UV exposition with lithography mask for 7 s
Second bake at 110 °C for 2 min
Second UV exposition without lithography mask for 60 s
Development in AZ-726 developper for 55 s</td></tr>
<tr><td>Etching</td><td>Dry ecthing using the ICP RIE Cl-gas Oxford plasmalab 100 down to the upper InAs layer</td><td colspan="2"></td></tr>
<tr><td>Metallic deposition</td><td>Ti/Pt/Au (10/30/150 nm) by electron gun evaporator using Univex 350</td><td>or</td><td>AuGeNi/Au (70/150 nm) by sputtering using Alcatel SCM 600</td></tr>
<tr><td>Lift-off</td><td>Acetone bath
Isopropanol bath</td><td></td><td>Acetone bath
Isopropanol bath</td></tr>
<tr><td>Rebake</td><td colspan="2"></td><td>Bake at 380 °C for 1 min
in Nitrogen atmosphere</td></tr>
</table>

Table 2.5: IV. Top gate

Sample cleaning	Acetone bath Isopropanol bath
Dielectric deposition	Deposition of SiO2 and Si3N4 by PECVD using the Corial D250
Lithography	Spin-coating of AZ-1518 (+) resist at 4000 rpm for 30 s Bake at 110 °C for 1 min UV exposition with lithography mask for 30 s Development in AZ-726 developper for 25 s
Etching	Dry etching using the ICP RIE F-gas Corial 200 IL down to the cap layer
Sample cleaning	Acetone bath Isopropanol bath
Lithography	Spin-coating of AZ-5214 (-) resist at 4000 rpm for 30 s First bake at 110 °C for 2 min First UV exposition with lithography mask for 7 s Second bake at 110 °C for 2 min Second UV exposition without lithography mask for 60 s Development in AZ-726 developper for 55 s
Metallic deposition	Ti/Au (10/200 nm)
Lift-off	Acetone bath Isopropanol bath

2.5 Device presentation

During this thesis, several samples with different expected gaps, different growth substates with the respective advantages of being THz transparent for GaAs and presenting a lower electrical anisotropy and leakage for GaSb were measured. The main devices analyzed in Chapter 3 are introduced here. Table 2.7 summarizes the characteristics of each devices detailled in the following.

2.5.1 Hall Bar 0 (HB0)

The Hall bar 0 (HB0) was fabricated in the CTM from growth S3054. The layer structure and the band structure of growth S3054 are given in Fig. 2.26(a). More detail on the energy dispersion calculation is provided in Chapter 1. In the case of this device, the Hall bar *mesa* is patterned by wet etching with a $H_3PO_4/C_6H_8O_7/H_2O_2/H_2O$ solution (see Section 2.4.2) down to and including the second barrier of AlGaAsSb.

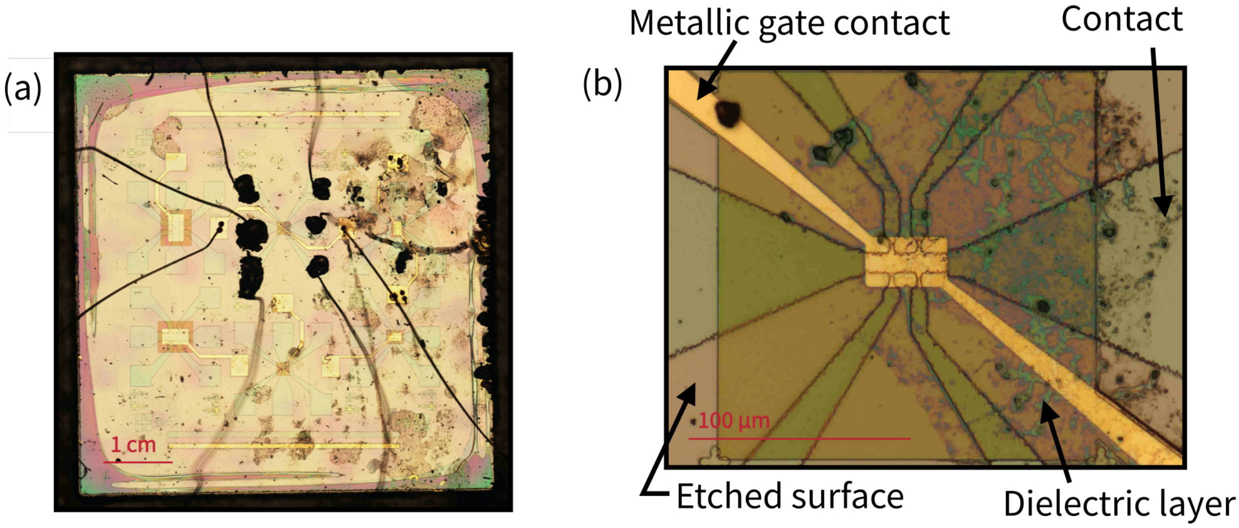

Figure 2.26: (a) Microscope image of the 6 mm × 6 mm chip made from growth S3054 and using the CTM lithography mask shown in Fig. 2.15. The chip has 6 Hall bars of different sizes. More details are provided in Table 2.1. The Hall bar connected in the center of the image corresponds to device HB0. (c) Microscope image of device HB0. The length L, the distance between the lateral probes l_p and the width W of the Hall bar are respectively 40 µm, 10 µm and 10 µm. The centered shape corresponds to the *mesa* of the Hall bar and the contacts. It is covered by a tri-layer of dielectric $Si_3N_4/SiO_2/Si_3N_4$(100/100/100 nm) patterned in a square shape above the Hall bar *mesa*. A metallic gate of rectangular shape, is patterned with 2 external contacts above the Hall bar *mesa*.

The device was covered by a tri-layer of dielectric $Si_3N_4/SiO_2/Si_3N_4$ (100/100/100 nm) deposited by PECVD. The dielectric layers were patterned by dry etching using the Corial Inductively coupled plasma (ICP) etcher. The gate was completed by a Ti/Au coating (10/150 nm). Note that no metallization was made on this first device as we planned to directly connect the contacts by indium soldering. From the 6 Hall bars fabricated, the one called HB0 bonded had the following dimensions : $L = 40$ µm, $W = 10$ µm and $l_p = 10$ µm. HB0 is shown in Fig. 2.26 (b). Although the indium soldering allowed us to avoid a metallization step, it is rather damaging for the chip. This choice was mainly motivated, at this stage of the thesis, to minimize the technological uncertainties for the realization of this first chip. Indeed there is a gate voltage hysteresis in this device.

Figure 2.27(a) shows the gate voltage ramp applied to tune the Fermi level in device HB0 at $T = 1.7\,\mathrm{K}$ and applying a bias current $I = 100\,\mathrm{nA}$. The resulting leakage current is shown in panel (b) of the same figure and its absolute value does not exceed $0.6\,\mathrm{nA}$. It is negligeable compared to the bias current I applied to measure the longitudinal resistance R_{xx} shown in panel (c). Although one direction of the gate voltage sweep is shown, R_{xx} is independent of the direction of variation of the gate voltage.

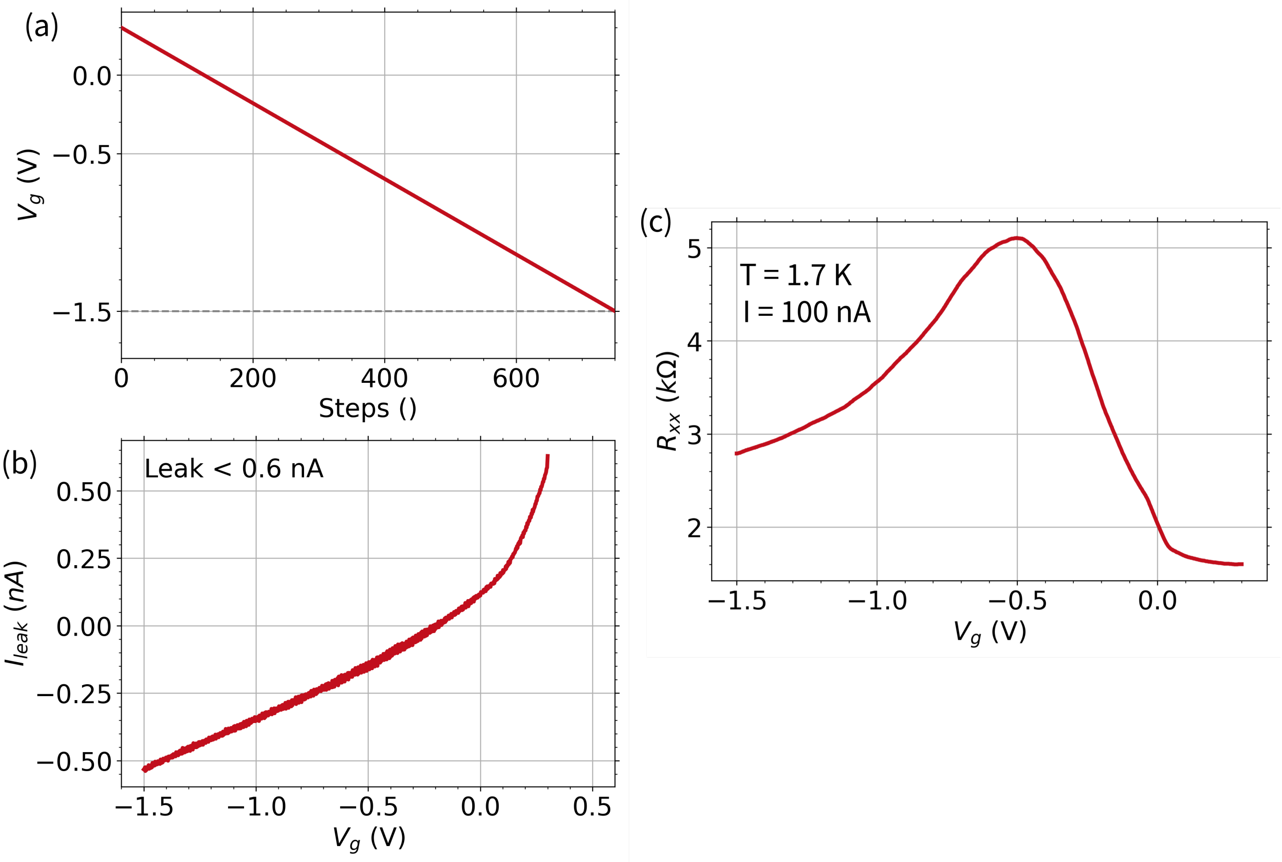

Figure 2.27: Gate control of device HB0. (a) Gate voltage sweep applied to device HB0. The sweep goes from $V_g = 0.3\,\mathrm{V}$ to $V_g = -1.5\,\mathrm{V}$ in 750 steps. (b) Leakage current I_{leak} induced by the sweep in V_g. (c) Longitudinal resistance R_{xx} as a function of the gate voltage measured at $T = 1.7\,\mathrm{K}$, applying a bias current $I = 100\,\mathrm{nA}$. In the three panels, colors highlight the different regions of the gate voltage sweep.

2.5.2 Hall Bar 1 (HB1)

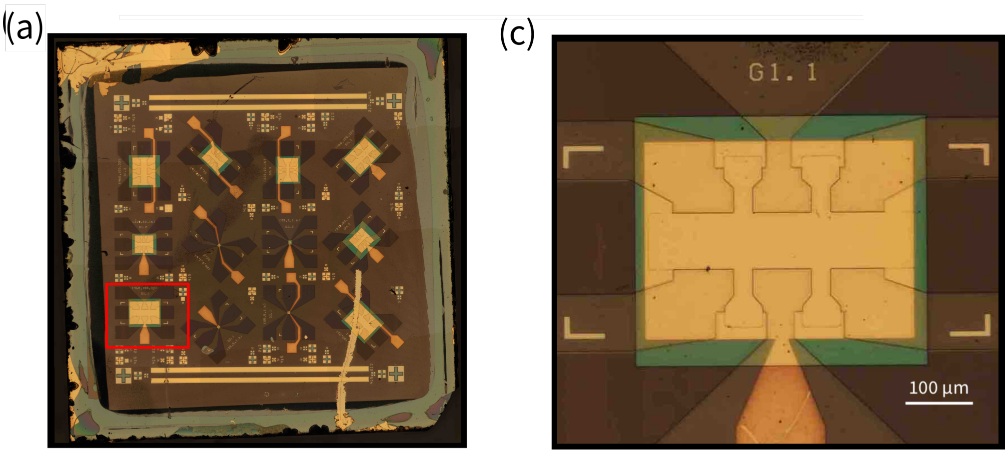

Figure 2.28: (a) Microscope image of the 6 mm × 6 mm chip made from growth S3052 using a CTM lithography mask similar to the one shown in Fig. 2.15. The device has 12 Hall bars of different sizes. The Hall bar evidenced by a red frame corresponds to device HB1. (c) Microscope image of device HB1. The length L, the distance between the lateral probes l_p and the width W of the Hall bar are respectively 400, 100 and 100 µm. The Hall bar is covered by a 300 nm-thick dielectric layer of SiO_2 patterned in a square shape above the Hall bar. A metallic gate is aso patterned above the dielectric layer in a reduced rectangular shape above the Hall bar *mesa*.

The Hall bar 1 (HB1) was fabricated in CTM from growth S3052. The mask used to manufacture device HB1 is not the same as the one used for the HB0. It is an old mask with more Hall bars, with dimensions similar to those of the mask shown in Fig. 2.16. Only the size of the contact pads differs. The layer structure and the band structure of growth S3052 are given in Fig. 2.3 and Fig. 2.5 respectively. More detail on the energy dispersion calculation is provided in Chapter 1. The Hall bar *mesa* is patterned by dry etching using chlorine gas in the Oxford ICP (see Section 2.4.2) down to and including the second barrier of AlGaAsSb. The device was covered by a 300 nm thick layer of SiO_2 as dielectric layer deposited by PECVD. The dielectric deposited is patterned by dry etching using the Corial Inductively coupled plasma (ICP) etcher (see Section 2.4.5). The gate is completed by a Ti/Au coating (10/150 nm). Note that no metallization has been done on this first sample as it was planned to directly connect the contacts by indium soldering. This choice was motivated at this stage of the thesis for the same reasons as previously mentioned (see Section 2.5.1). However, because of the reduced size for contact pads, only the four lateral probes could be connected. HB1 has the following dimensions : $L = 400\,\mu\text{m}$, $W = 100\,\mu\text{m}$ and $l_p = 100\,\mu\text{m}$. HB1 is shown in Fig. 2.28 (a, b). The gate voltage range applied is much larger than for device HB0 from growth S3054 as it consists of a sweep from $V_g = 0\,\text{V}$ to $V_g = -15\,\text{V}$, then to $V_g = 5\,\text{V}$ to $V_g = 0\,\text{V}$. The counter effect of such large gate voltage ramp is a significative hysteresis effect understood as the charge trapping between the insulator/semiconductor interface [MPK+15, LLE+19]. The parameters of the sweep have been chosen so that the observed resist peaks observed in Fig. 2.29 (c) are not shifted after several repetition of the gate voltage sweep. The measurement is performed at $T = 300\,\text{mK}$ and applying a bias AC $I = 100\,\text{nA}$. Moreover, it is not possible to work with a fixed gate voltage for this sample. Indeed, at fixed gate voltage the Fermi level is not constant over time. Figure 2.30(a) shows the evolution of V_g for a sweep from 0 to -5V with a speed rate of $4\,\text{mV}\,\text{s}^{-1}$. Panel (b) show the evolution of $R_{xx}(V_g)$, following these sweep parameters. It is clear that R_{xx} depends on the direction of variation of V_g. We show in the inset the time dependence of R_{xx} and we define $t = 0$ as the time when we stop scanning the gate voltage at a non-zero value, for different V_g. The time dependence of R_{xx} in the inset is normalized by the value at $t = 0$. The transient regime is all the more exacerbated as $|Vg|$ is high. For example, if we set $V_g = -4\,\mathrm{V}$ then $R_{xx}(t = 50s) = 0.95R_0$. It is estimated that we get rid of this effect by scanning fast enough and with limits such that the position of the peaks does not change between two sweeps. We have chosen to scan V_g quickly as shown in Fig. 2.29 (a) at the speed rate of 0.2 V/s. As a general rule, the larger the first $|V_g|$ bound value is (here $V_g^{min} = -15\,\mathrm{V}$), the more the second $|V_g|$ bound value must be artificially increased ($V_g^{max} = 6\,\mathrm{V}$) to compensate for the shift of the resistance peak on the V_g-axis.

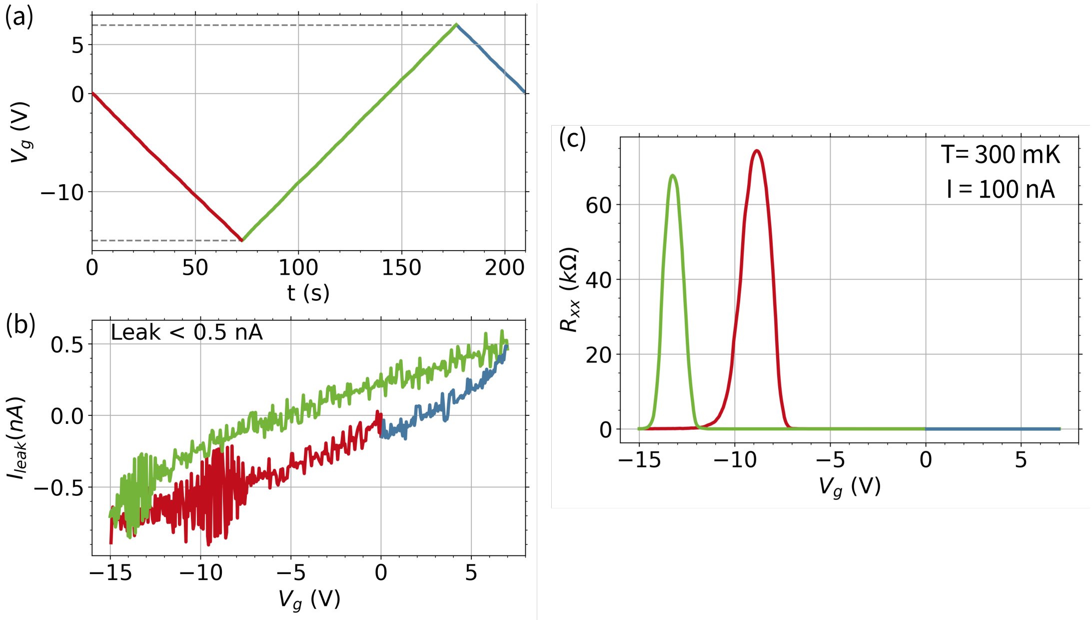

Figure 2.29: Gate control for device HB1. (a) Gate voltage sweep applied to device HB1. The scan is set such that $V_g = 0\,\mathrm{V} \rightarrow V_g = -15\,\mathrm{V} \rightarrow V_g = 6\,\mathrm{V} \rightarrow V_g = 0\,\mathrm{V}$ with $V_g^{step} = 0.05\,\mathrm{V}$ and $t^{step} = 0.25\,\mathrm{s}$. (b) Leakage current I_{leak} induced by the sweep in V_g. (c) Longitudinal resistance R_{xx} as a function of the gate voltage measured at $T = 300\,\mathrm{mK}$ and applying a bias current $I = 100\,\mathrm{nA}$. In the three panels, colors highlight the different regions of the gate voltage scan.

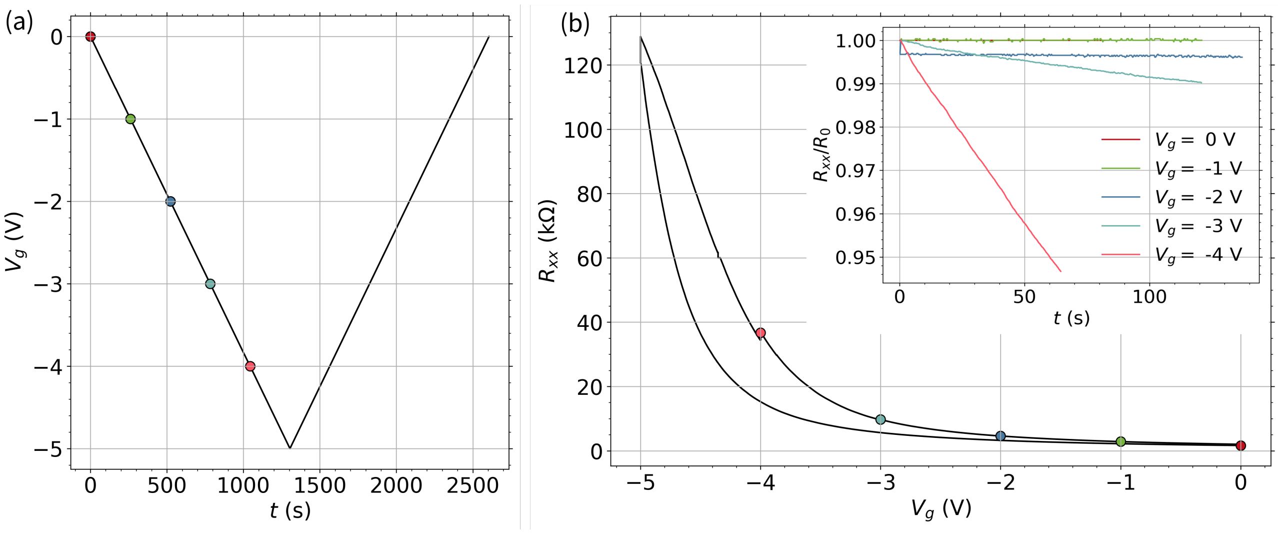

Figure 2.30: (a) Gate voltage sweep applied to device HB1. The scan is set such that $V_g = 0\,\mathrm{V} \rightarrow V_g = -5\,\mathrm{V} \rightarrow V_g = 0\,\mathrm{V}$ with $V_g^{step} = 0.001\,\mathrm{V}$ and $t^{step} = 0.25\,\mathrm{s}$. (b) Longitudinal resistance R_{xx}as a function of the gate voltage V_g. The inset show the time dependence of $R_{xx}(t)/R_{t\,=\,0}$ at fixed gate voltages. The color correspond to the different gate voltages. In panel (a, b) the circles highlight the V_g shown in the inset and corresponding $R_{xx}(t = 0)$ values.

2.5.3 S3198 based devices

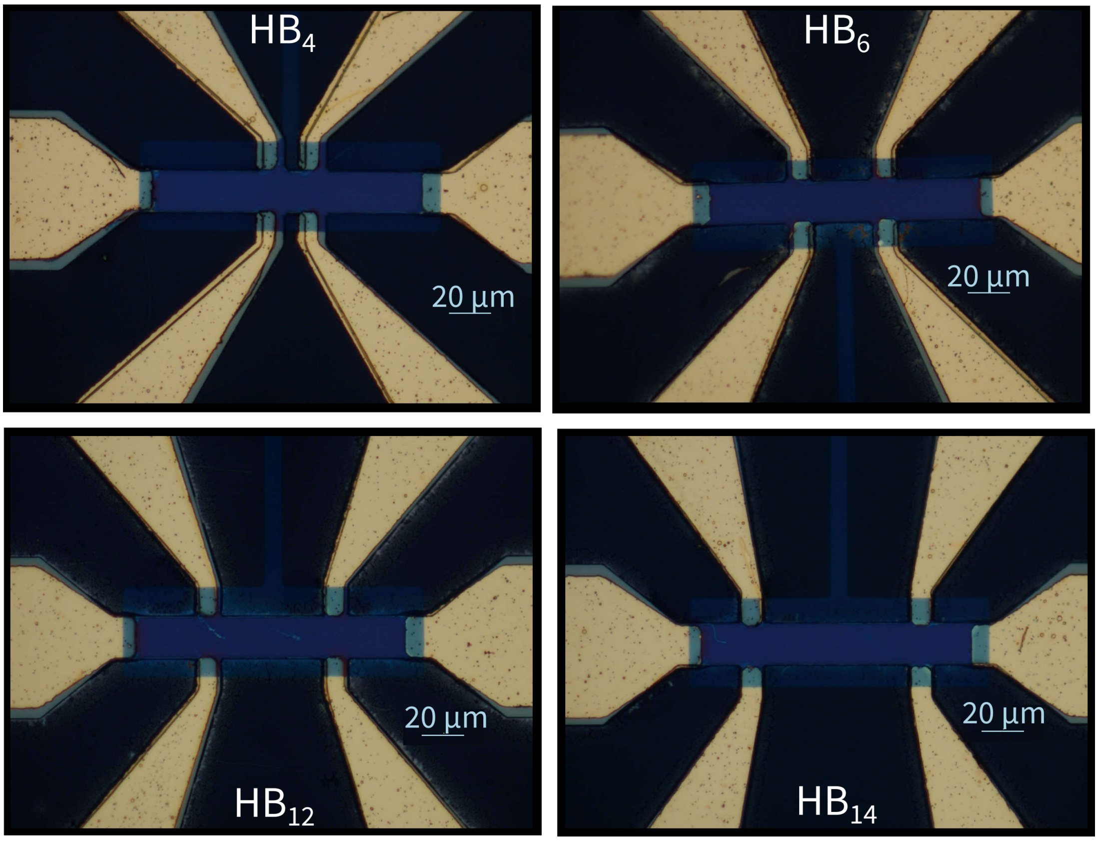

Figure 2.31: (a) Microscope image of the devices made from growth S3198 in TEP using the mask similar to the one shown in Fig. 2.16. The four Hall bars have the same dimensions $L = 100\,\mu\text{m}$ and $W = 20\,\mu\text{m}$ and only differ by the length between lateral probes l_p. More details are provided in Table. 2.1.

The four devices, shown in Fig. 2.31 were fabricated in Würzburg in the Technische Physik group (TEP). The details of the fabrication process is given in detail in [Geb22]. We provide some information on the fabrication process below:

- the devices are made by optical lithography from a single piece of growth S3198, and individually cleaved at the end of the process;
- the *mesa* are patterned and etched by two steps of etching. The first step is a dry etching in the Oxford ICP with a Chlorine-Argon mix down to the superlattice of GaSb/AlSb. The second is a wet etching in a solution based on phosphoric acid and citric acid to improve the quality of the side walls of the *mesa*;
- the dielectric layer is a superlattice of 10 repetitions of SiO_2/Si_3N_4 (10/10 nm) deposited on an other layer of Si_3N_4 (10 nm);
- the metallic contact are made by a deposition of Ti/Pt/Au following the same procedure as detailled in Section 2.4.3.

We now detail the gate voltage response for the four different Hall bar devices. As for device HB1, the range of gate voltage that has to be applied is rather large compared to device HB0. A transcient regime and a significative hysteresis are also exhibited. As for device HB1, we assume that if V_g is scanned quickly enough, if the limits of the V_g sweep are chosen so that the peak positions are reproductible, then one can consider that the proportionality between the total amount of charge n_{tot} and gate voltage V_g is verified by the relation:

$$\frac{C_g}{e}(V_g - V_g^{th}) \;=\; n_{tot}, \tag{2.7}$$

where C_g is the capacitance of the dielectric layer, V_g^{th} is the gate voltage at which the transition between electrons ($n_{tot} \;=\; n - p > 0$) and holes ($n_{tot} \;=\; n - p < 0$) takes place, and e is the electron charge.

Hall Bar 4 (HB4)

Device HB4 has been measured in two different campaigns and the effect of the gate voltage sweep was not the same during these two measurement campaigns. For this reason we show in Fig. 2.32 the two sweeps for the two campaigns. In both cases, both the scan rate and the bound values are determined in order to have the gate voltage position of the peaks unchanged between two sweeps. It is clear that during the second campaign the insulating dielectric layer is less efficient as before. First the second bound $|V_g|$ value has to be increased ($V_g^{max} = 12\,\mathrm{V} \rightarrow 15\,\mathrm{V}$) but also the scan rate is tripled ($V_g/t = 0.2\,\mathrm{V\,s^{-1}} \rightarrow 0.6\,\mathrm{V\,s^{-1}}$).

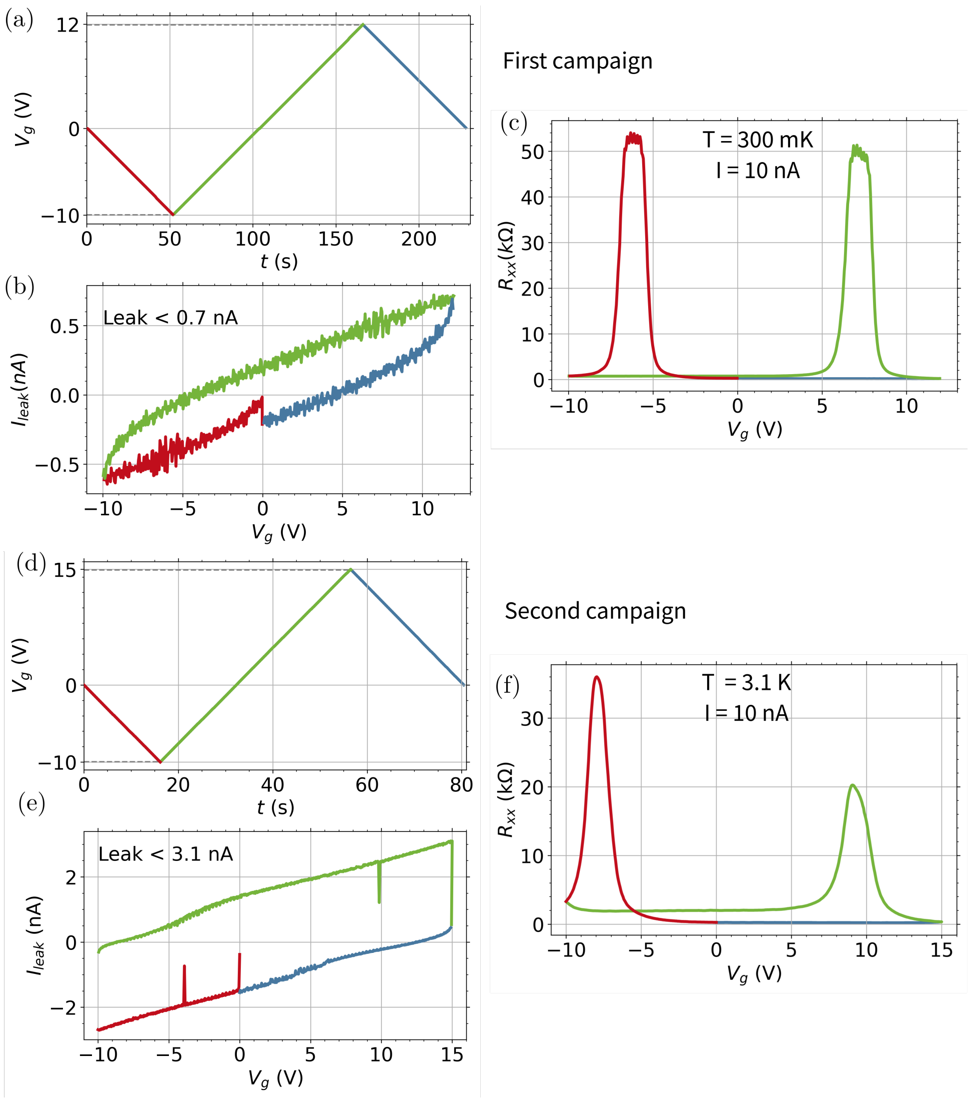

Figure 2.32: Gate control for device HB4. (a, d) Gate voltage sweep applied to device HB4. The scan of the first campaign is set such that $V_g = 0\,\mathrm{V} \rightarrow V_g = -10\,\mathrm{V} \rightarrow V_g = 12\,\mathrm{V} \rightarrow V_g = 0\,\mathrm{V}$ with $V_g^{step} = 0.05\,\mathrm{V}$ and $t^{step} = 0.25\,\mathrm{s}$. The scan of the first campaign is set such that $V_g = 0\,\mathrm{V} \rightarrow V_g = -10\,\mathrm{V} \rightarrow V_g = 15\,\mathrm{V} \rightarrow V_g = 0\,\mathrm{V}$ with $V_g^{step} = 0.06$ volt and $t^{step} = 0.1\,\mathrm{s}$. (b, e) Leakage current I_{leak} induced by the sweep in V_g. (c, f) Longitudinal resistance R_{xx} as a function of the V_g measured at $T = 300\,\mathrm{mK}$, and $T = 3\,\mathrm{K}$ respectively and applying a bias current $I = 10\,\mathrm{nA}$. In the six panels, colors highlight the different regions of the gate voltage scan.

Hall Bar 6 (HB6)

Device HB6 has also been measured during only one campaign. It was attempted to measure the device during a second campaign but the gate was too damaged to tune the Fermi level. Figure 2.33 shows the gate voltage scan for device HB6 at $T = 300\,\mathrm{mK}$ and applying a bias current $I = 10\,\mathrm{nA}$. The behavior observed for the longitudinal resistance shown in Fig. 2.33 (c) is very similar to the behavior of device HB4. The gate voltage bounds are $V_g^{min} = -10\,\mathrm{V}$ and $V_g^{max} = 10\,\mathrm{V}$ and the scan rate is $V_g/t = 0.2\,\mathrm{V\,s^{-1}}$.

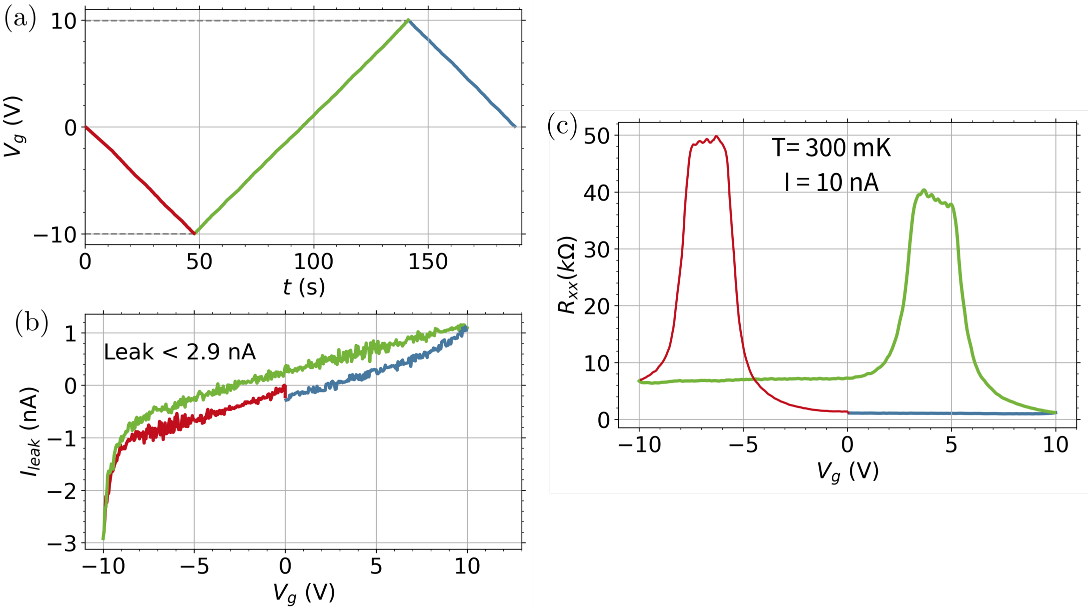

Figure 2.33: Gate control for device HB6 during the first campaign. (a) Gate voltage sweep applied to device HB6. The scan is set such that $V_g = 0\,\mathrm{V} \rightarrow V_g = -10\,\mathrm{V} \rightarrow V_g = 10\,\mathrm{V} \rightarrow V_g = 0\,\mathrm{V}$ with $V_g^{step} = 0.05\,\mathrm{V}$ and $t^{step} = 0.25\,\mathrm{s}$. (b) Leakage current I_{leak} induced by the sweep in V_g. (c) Longitudinal resistance R_{xx} as a function of V_g, measured at $T = 300\,\mathrm{mK}$, and applying a bias current $I = 10\,\mathrm{nA}$. In the three panels, colors highlight the different regions of the gate voltage scan.

Hall Bar 12 (HB12)

Device HB12 have been measured during a single campaign. Figure 2.34 shows the gate voltage scan for device HB12 at $T = 1.7\,\mathrm{K}$ and applying a bias current $I = 500\,\mathrm{nA}$. In the previous devices, the longitudinal resistance had a magnitude of $50\,\mathrm{k\Omega}$ or less. By comparison, R_{xx} can reach values as high as $130\,\mathrm{k\Omega}$, as shown in Fig. 2.34 (c). We determined that it was easier to get out of this insulating state by first applying a positive gate voltage. The parameters of gate voltage limits and scan speed have been determined to keep the position of these peaks between two scans and are $V_g^{max} = 15\,\mathrm{V}$, $V_g^{min} = -15\,\mathrm{V}$, and $V_g/t = 0.2\,\mathrm{V\,s^{-1}}$. Figure 2.34(a) shows that a mistake in the programmation of V_g sweeps was present during the measurements, and a jump from $V_g = -12\,\mathrm{V}$ to $V_g = -15\,\mathrm{V}$ occured between the lowering and the raising of the gate voltage. However, the behavior observed for R_{xx} shown in Fig. 2.34 (c) is very similar to the behavior in the previous devices.

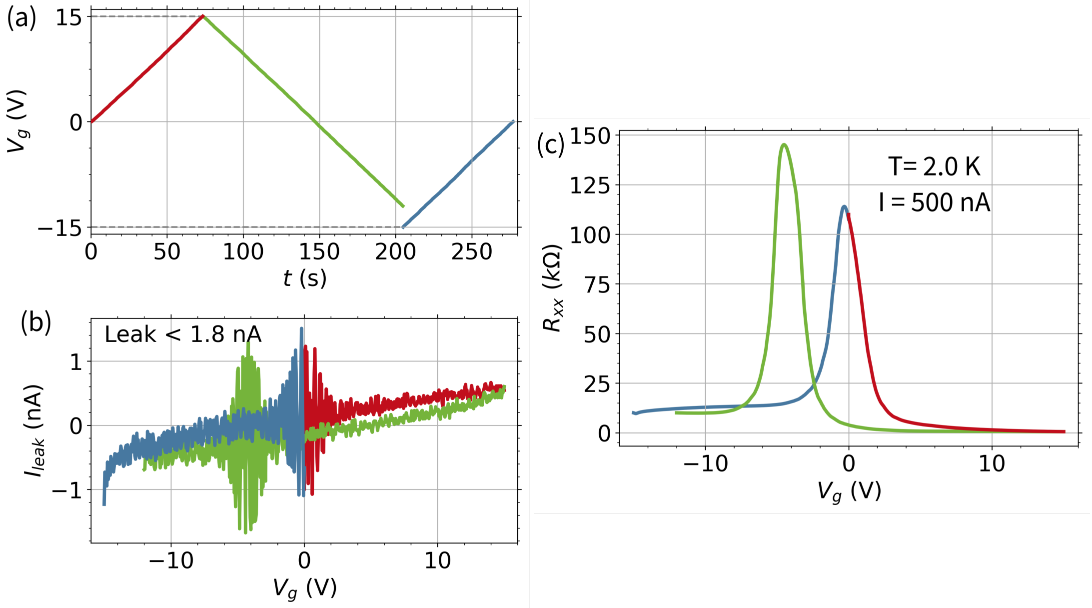

Figure 2.34: Gate control for device HB12. (a) Gate voltage sweep applied to device HB12. The scan is set such that $V_g = 0\,\mathrm{V} \rightarrow V_g = 15\,\mathrm{V} \rightarrow V_g = -15\,\mathrm{V} \rightarrow V_g = 0\,\mathrm{V}$ with $V_g^{step} = 0.05\,\mathrm{V}$ and $t^{step} = 0.25\,\mathrm{s}$. (b) Leakage current I_{leak} induced by the sweep in V_g. (c) Longitudinal resistance R_{xx} as a function of the gate voltage. In the three panels, colors highlight the different regions of the gate voltage scan.

Hall Bar 14 (HB14)

Device HB14 has been measured during a single campaign on the pulsed high magnetic field setup in the Laboratoire National des champs magnétiques intenses (LNCMI). The use of pulsed magnetic field with a pulse duration of 500 ms is an additional constraint on the determination of gate voltage scanning parameters. The time between two shots is more than one hour, so it is particularly important that R_{xx} is reproducible for each gate voltage cycle. Moreover, the scanning speed must be low enough so that the variation of the gate voltage is not too significant over the time of a single pulse. The scan is shown in Fig. 2.35. The V_g scan parameters chosen are $V_g^{max} = 10\,\mathrm{V}$, $V_g^{min} = -9\,\mathrm{V}$, and $V_g/t = 0.05\,\mathrm{V\,s^{-1}}$. The gate voltage variation during a single pulse of B is then $\delta V_g = 25\,\mathrm{mV}$.

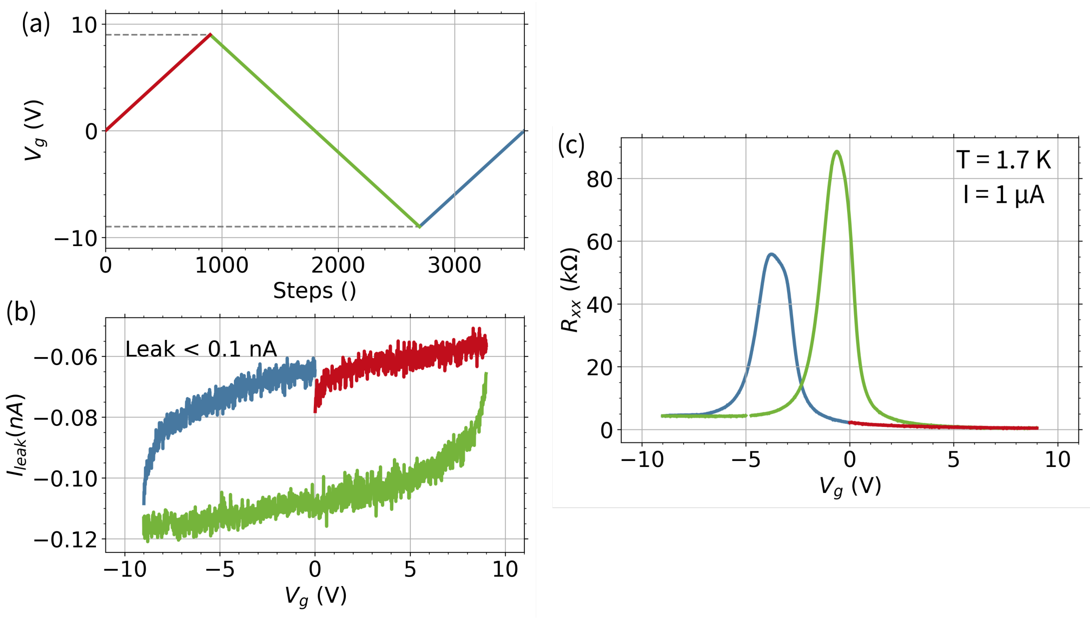

Figure 2.35: Gate control for device HB14. (a) Gate voltage sweep applied to device HB14. The scan is set such that $V_g = 0\,\mathrm{V} \rightarrow V_g = 10\,\mathrm{V} \rightarrow V_g = -9\,\mathrm{V} \rightarrow V_g = 0\,\mathrm{V}$ with $V_g^{step} = 0.01\,\mathrm{V}$ and $t^{step} = 0.2\,\mathrm{s}$. Gate voltage and leakage current I_{leak} (b) are respectively applied and measured by a single sourcemeter. (c) Longitudinal resistance R_{xx} as a function of the gate voltage. In the three panels, colors highlight the different regions of the gate voltage scan.

Conclusion

To conclude, we have presented a selection of devices, with which we could perform more detailed transport measurements, that we present in the next Chapter. Tables 2.6 and 2.7 summarize the main parameters of the three growths studied and the several devices affiliated.

Table 2.6: Growth parameters

Growth	Substrate	d_1 (InAs)	d_2($Ga_{1-x}In_xSb$)	x	ρ_1/ρ_2 ($T = 1.8$ K)	$\Delta_{(th)}$ (meV)
S3054	GaAs	34 ML	14 ML	0		15
S3052	GaAs	25 ML	10 ML	0.35	4	30
S3198	GaSb	25 ML	10 ML	0.35	1.2	45

Table 2.7: Devices parameters

Device	L (µm)	W (µm)	l_p (µm)	V_g cycle	V_g/t (V/s)	R_{max} or $R_{max}^{left}\|R_{max}^{right}$ (kΩ)	$\|I_{leak}^{max}\|$ (nA)
HB0	40	10	10	0.3 V → -1.5 V		5 kΩ (T = 1.7 K)	0.6 nA
HB1	400	100	100	0 V → -15 V -15 V → 6 V 6 V → 0V	0.2	70|80 kΩ (T = 300 mK)	0.5
HB4	110	20	10	0 V → -10 V -10 V → 12 V 12 V → 0V	0.2	52|50 kΩ (T = 300 mK)	0.7
				0 V → -10 V -10 V → 15 V 15 V → 0V	0.6	38|20 kΩ (T = 3.1 K)	3.1
HB6	110	20	30	0 V → -10 V -10 V → 10 V 10 V → 0V	0.2	50|40 kΩ (T = 300 mK)	2.9
HB12	110	20	50	0 V → 15 V 15 V → -15 V -15 V → 0V	0.2	145|115 kΩ (T = 2 K)	1.8
HB14	110	20	70	0 V → 10 V 10 V → -9 V -9 V → 0V	0.05	55|90 kΩ (T = 1.7 K)	0.1

CHAPTER 3

Experimental Results and analysis

The chapter is devoted to the presentation of the main experimental results accumulated during this thesis. We could only measure Hall bars, because unfortunately we did not have Corbino, TLM structures, H-bars,... at our disposal. Moreover, these Hall bars were relatively large, so the observation of a quantum topological effect was out of reach. In these conditions, the research on these devices followed three main axes: i) the determination of global band structures by Hall effect, magnetoresistance, Shubnikov–de Haas oscillations ; ii) the detection of possible edge conduction by local and non-local electrical measurements; iii) the determination of the energy gap by thermal activation.

This chapter in divided into three sections, which correspond to three different grown structures. In the first section, we present the results obtained with the Hall bar HB0, from growth S3054. This device has the smallest energy gap among all the studied devices. In the second section, we present the results from HB1, which is the only device where a detailed analysis of growth S3052 has been made. In the last part, we present a set of Hall bars made by the University of Würzburg, from growth S3198.

3.1 Hall bar HB0: the small inverted gap of S3054

Let us focus now on experimental results obtained with the Hall bar HB0 presented in Chapter 2. This device has been obtained from growth S3054. It is made of a 34/14/34 monolayer-thick quantum well of InAs/GaSb/InAs. From the band dispersion given in Chapter 2, we expect a inverted gap, with an energy gap of 15 meV. In this device, the ratio between the lateral probe distance l_p and the width W of the Hall bar is 1, so we identify the longitudinal resistivity ρ_{xx} to the longitudinal resistance $R_{xx} \simeq \rho_{xx}$.

Measurements were performed by imposing a fixed gate voltage V_g while the perpendicular magnetic field B was swept from 0 to 6T for both positive and negative orientations of the magnetic field. Both magnetoresistances are shown in Fig. 3.1 for different gate voltages, at a temperature of 1.7 K. For clarity, only magnetoresistances obtained from a reduced selection of gate voltages are shown in panels (a,b). The gate voltage dependence of the longitudinal resistivity at zero-magnetic field, $\rho_0(V_g)$, is extracted and displays a peak, indicating a gap opening, as shown in Fig. 3.1(c). Fig. 3.1 (d) shows the gate voltage dependence of the Hall coefficient $R_H = \rho_{xy}/B$ at $B = 1\,\text{T}$. The change of sign of R_H is related to a change of the carrier charge. These measurements evidence the ambipolarity of the device, and we define the voltage at the charge neutrality point (CNP) $V_{CNP} = -0.6\,\mathrm{V}$ as the gate voltage corresponding to $R_H \simeq 0\,\Omega$.

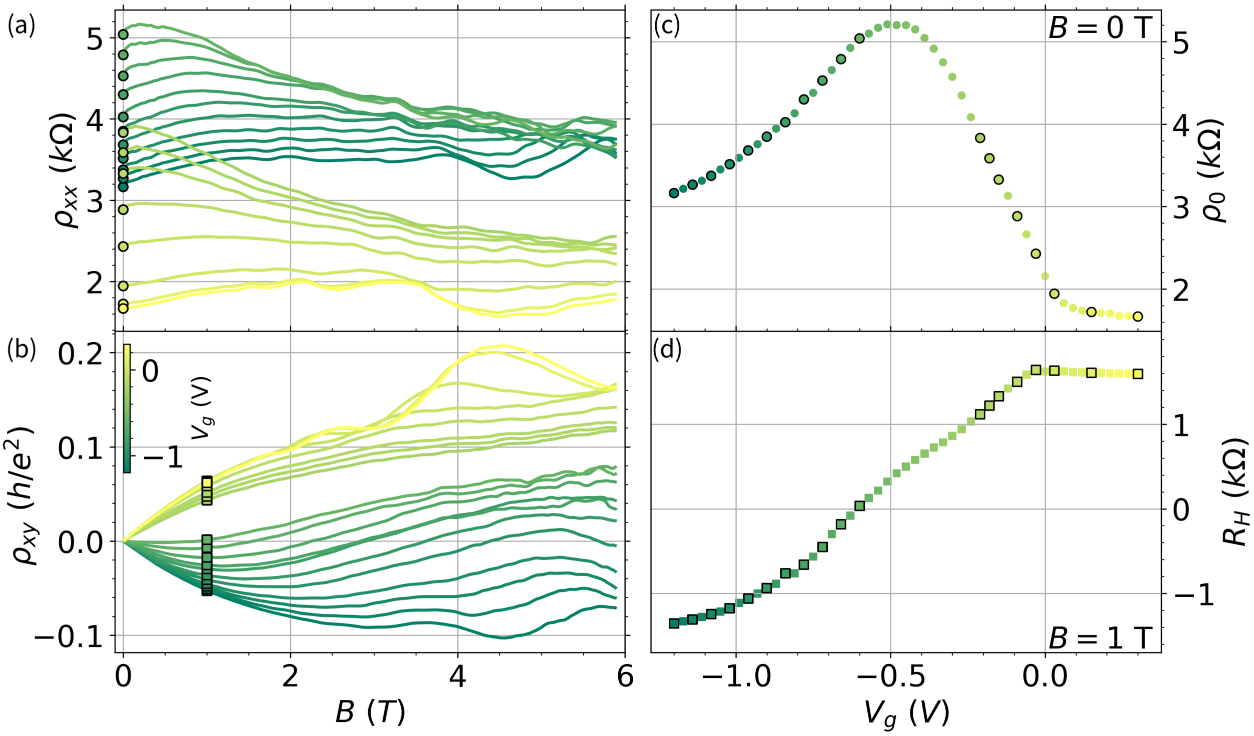

Figure 3.1: (a) Longitudinal resistivity ρ_{xx} and (b) transverse resistivity ρ_{xy} as a function of magnetic field B up to 6 T for a reduced selection of gate voltages. The color scale corresponds to the gate voltage and is given in panel (b). (c) Gate voltage dependence of the zero-field longitudinal resistivity ρ_0 extracted from the different magnetic field sweep. (d) Gate voltage dependence of the Hall coefficient R_H extracted at $B = 1\,\mathrm{T}$. In addition, in panel (a), the round symbols corresponds to the zero-magnetic field value of the resistivity reported and highlighted by a black frame in panel (c). The Hall resistivity extracted at $B = 1\,\mathrm{T}$ are shown as square symbols in panel (b) and reported with a black frame in panel (d). All magnetic field dependences of both resistivities components were measured in a liquid He^4 cryogenic system at a temperature $T = 1.7\,\mathrm{K}$ and with a bias current $I = 100\,\mathrm{nA}$.

3.1.1 Single carrier model

We first focus on the behavior of the resistivity components at low magnetic field, where there is no quantum effect such as Shubnikov-de Haas (SdH) oscillations or quantum Hall effect (QHE). Both longitudinal and transverse resistivities are shown in Fig. 3.2 with a zoom in the magnetic field range 0–1 T. These data are analyzed first within a single carrier approximation:

$$\rho_{xx}(B) = \frac{1}{en_H\mu} = \rho_0, \qquad \rho_{xy}(B) = \frac{B}{en_H} = BR_H,$$

where n_H is the Hall carrier density. Figure. 3.2(a,b) shows $\rho_{xy}(B)$ for two different gate voltage ranges. The expected linear Hall resistances corresponding to the R_H coefficients are also shown. It is obvious that the experimental $\rho_{xy}(B)$ is not perfectly linear. In addition, Figure. 3.2(c,d) shows $\rho_{xx}(B)$ at the same gate voltages. The constant solid lines, corresponding to $\rho_{xx}(B = 0)$, evidence that ρ_{xx} is not independent of B and even exhibits a positive magneto-resistance. A positive magneto-resistance can be due to weak antilocalization, or disorder. From all this, it seems that the single carrier model is not a very good assumption. This is confirmed in

Fig. 3.3(a), where the single carrier concentration n_H is extracted. From this figure, it is clear that the single carrier model is bad, because $n_H(V_G)$ is not linear and diverges at the CNP. Nevertheless, we calculate the single carrier mobility given by $n_H e\mu = 1/\rho_0$. The mobility shown in Fig. 3.3 (b) is valid only far from the V_{CNP}, in the regions I and II. The mobilities $\mu \approx 1\,\mathrm{m}^2\,\mathrm{V}^{-1}\,\mathrm{s}^{-1}$ are comparable to those reported in [KD11, IAC$^+$20] for InAs/GaSb structures on GaAs substrates.

In region III corresponding to gate voltage -0.84 V $< V_g <$ -0.21 V, both longitudinal and transverse resistances exhibit behaviors not corresponding to a single carrier model. Unfortunately, we could not fit both ρ_{xx} and ρ_{xy} simultaneously by a two carriers model. We believe that this issue is due to the importance of the disorder (and also possibly to weak localization and weak anti-localization).

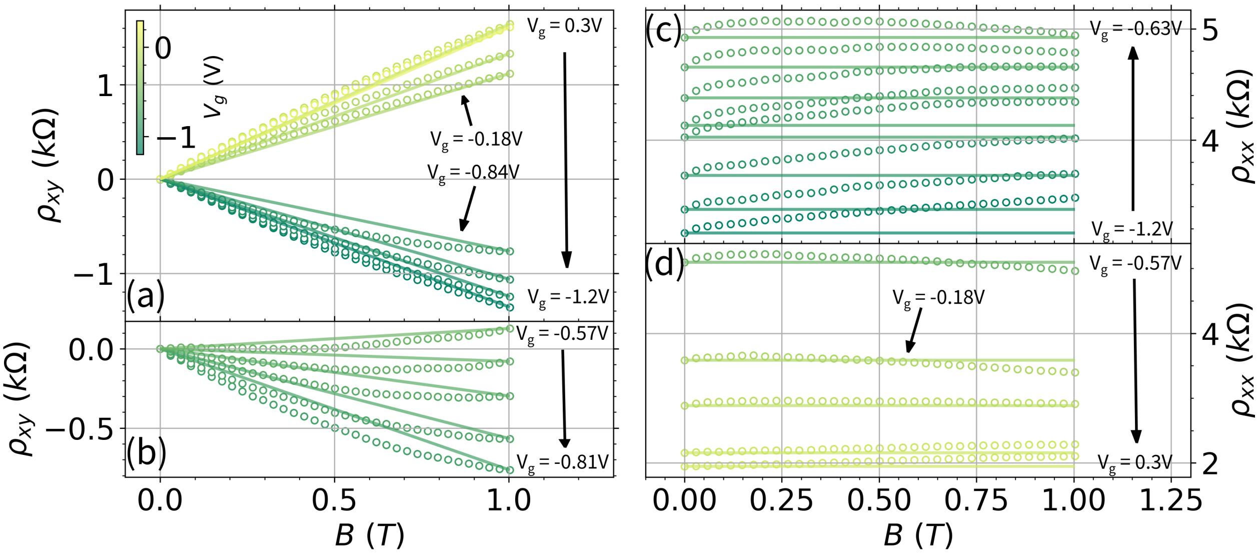

Figure 3.2: Zoom on the (a,b) transverse resistivity ρ_{xy} and (c,d) longitudinal resistivity ρ_{xx} as a function of magnetic field B up to 1 T for different gate voltages. The colorscale is given in panel (a) and is the same as the one in Fig. 3.1. In the four panels, the experimental data are indicated by open circles and fitted in the framework of a single carrier model. The resulting fit is shown by solid lines. The transverse resistivity is separated into panels (a) and (b) such as panel (a) shows gate voltages between $-0.18\,\mathrm{V}$ and $0.3\,\mathrm{V}$ (positive Hall effect in the conduction band) and V_g between $-1.2\,\mathrm{V}$ and $-0.84\,\mathrm{V}$ (negative Hall effect in the valence band). Panel (b) shows gate voltages between $-0.81\,\mathrm{V}$ and $0.57\,\mathrm{V}$. This corresponds to a third regime in the vicinity of the CNP. The longitudinal resistivity is also separated such as panels (c) and (d) show the longitudinal resistivity for gate voltages $V_g < V_{CNP}$ and $V_g > V_{CNP}$ respectively.

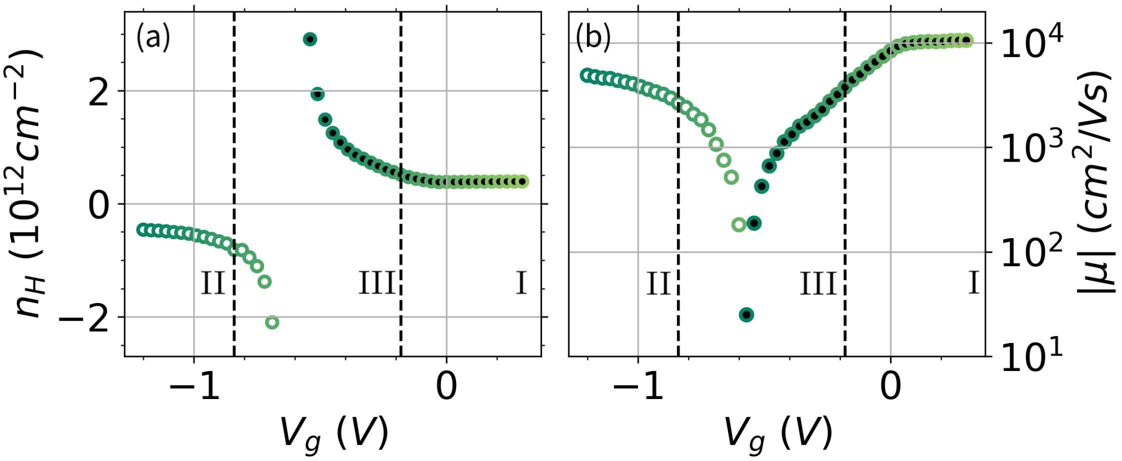

Figure 3.3: (a) Hall carrier concentration n_H and (b) associated mobility μ as a function of gate voltage V_g extracted from experimental data in the framework of a single carrier model. Filled and open symbols represent the concentration and mobility associated with electrons and holes respectively. The color scale corresponds to the gate voltage and is the same as in Fig. 3.1. The dashed lines separate in both panels three regimes: electrons (I), holes (II), and puddles (III).

3.1.2 High magnetic field measurements

SdH analysis

We now detail the magneto-transport measurements performed of the HB0 device at higher magnetic fields up to 6 T, and at a temperature of 1.7 K. At magnetic fields higher than 2 T, the classical model of transport no longer describes the magnetoresistances as Shubnikov–de Haas oscillations (SdHOs) emerge. Figure 3.1 (a, b) shows the evolution of the longitudinal magnetoresistivity $\rho_{xx}(B)$ and the transverse magnetoresistivity $\rho_{xy}(B)$ for different gate voltages. In the following we only consider the SdHOs measured at the extreme values of gate voltages $V_g = -1.2\,\mathrm{V}$ and $-1.05\,\mathrm{V}$ for the valence band and $V_g = -0.03\,\mathrm{V}, 0.18\,\mathrm{V}$ and $0.3\,\mathrm{V}$ for the conduction band, as the oscillations are less evident for intermediate gate voltages. The carrier concentration n_{SdH} is related to the SdHOs $1/B$ periodicity as $\Delta\left(1/B\right) = g_s g_v \times e/n_{SdH}h$, where g_s is the spin degeneracy and g_v is the band degeneracy. We manually extract in Fig. 3.4(a) the magnetic field values corresponding to the minima of the SdHOs and report them versus the Landau Level indexes in Fig. 3.4(b). In the conduction band, the Landau level indexes are extracted from the quantized values of the transverse resistivity. The corresponding carrier densities are reported in Fig. 3.4(c) as symbols and compared to the concentration extracted with the single carrier model. The concentrations calculated in both cases are the quite same, if we assume that $g_s = 2, g_v = 1$ in the valence band and $g_s = 2, g_v = 2$ in the conduction band.

Estimation of the energy gap

From the previous analysis, we infer that there is no real gap. The magnetoresistances evidence that both electrons and hole puddles exist and are always present, even at the CNP. The energy gap cannot be measured from thermal activation, because of the presence of these puddles. Nevertheless, we try to give an estimate of the energy gap below. These puddles modify the DoS $D_p(E)$ and $D_e(E)$ of both valence and conduction bands. In Fig. 3.5 we show the approximation made on $D_p(E)$ and $D_e(E)$ in the gap. We approximate the densities of states in the gap, for both electrons and holes, as a linear variation as a function of energy.

At $V_g = -1.05$ V and $V_g = 0.03$ V, we extract carrier densities $n^p_{SdH} = 4.62 \times 10^{11}\,\mathrm{cm}^{-2}$

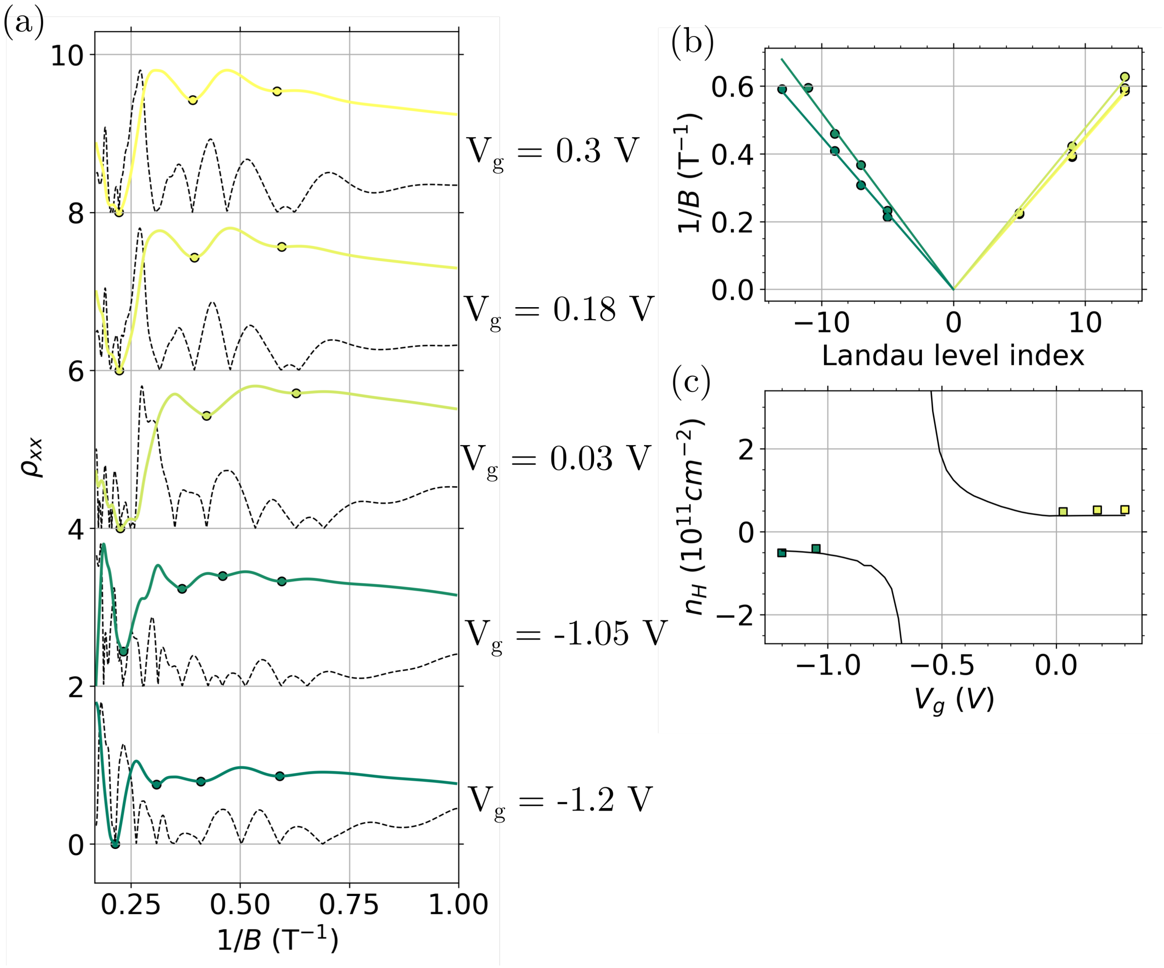

Figure 3.4: Carrier density extraction from SdH oscillations analysis. (a) Normalized longitudinal resistivity ρ_{xx} (coloured solid lines) and the absolute value of it first derivative $\frac{\partial \rho_{xx}}{\partial B}$ (black dashed lines) as a function magnetic field for different gate voltages. The colored solid lines correspond to ρ_{xx} and the superposed dashed lines to the derivative. The circle symbols corresponds to the extracted minima. The gate voltage values are provided on the right side of panel (a). We use the same color code to represent the gate voltage in the whole figure . (b) Position of the SdH minima $1/B$ as a function of the Landau level index for different gate voltages. Landau level indexes are determined by the quantized value of the Hall plateaus observed in the transverse resistivity ρ_{xy}. Circle symbols correspond to the extraction made from panel (a). Solid lines are the corresponding linear fits. The slope of the different fits is extracted to calculate the corresponding SdH concentrations. (c) Carrier concentrations n as a function of gate voltage V_g extracted from the experimental data. The black solid line corresponds to the concentration calculated from R_H.Circle symbols correspond to the concentrations extracted from the SdH oscillations. All extractions are made from magneto-transport measurements performed at $T = 1.7$ K and with a bias current $I = 100$ nA.

and $n^{e}_{SdH} = 5.07 \times 10^{11}\,\text{cm}^{-2}$ respectively. Hence, across the gap we measure from SdHO a variation of the carrier density $\Delta n = n^{p}_{SdH} + n^{e}_{SdH} = 9.7 \times 10^{11}\,\text{cm}^{-2}$. The gap Δ is linked to these carrier densities by the relations:

$$n^{p}_{SdH} = \int_{-\Delta/2}^{\Delta/2} D_p(E)dE = 2 \times \frac{m^*}{2\pi\hbar^2}\frac{\Delta}{2}, \tag{3.1}$$

$$n^{e}_{SdH} = \int_{-\Delta/2}^{\Delta/2} D_e(E)dE = 2 \times 2 \times \frac{m^*}{2\pi\hbar^2}\frac{\Delta}{2}, \tag{3.2}$$

where we assume that across the gap there is still a parabolic dispersion, with $m^* = 0.0434\, m_0$

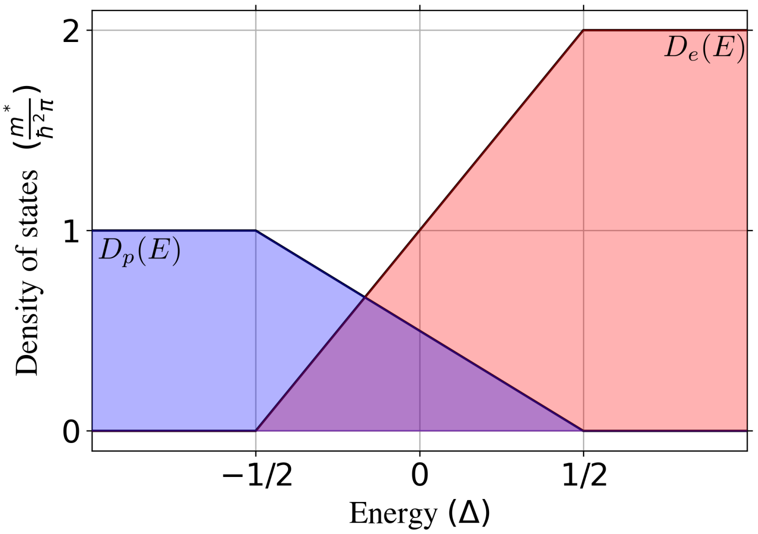

Figure 3.5: Schematic illustration of the density of states at the vicinity of the band gap in HB0 device for holes (blue) and electrons (red).

as it was measured in similar samples by magneto-spectroscopy measurements [KRGP+18]. This gives an energy variation $\Delta E_F = \Delta n \times 2\pi\hbar^2/3m^*$. The carrier concentrations are extracted not exactly at the gap edges, so the resulting energy difference is larger than Δ, and we get a upper estimate for the energy gap: $\Delta < \Delta E_F \approx 36$ meV. This result is coherent with the expected value of $\Delta = 15$ meV. Needless to say, this is a rough approximation.

3.1.3 Non-local measurements

Ballistic edge states model

So far we have evidenced the presence of puddles at the CNP. What about the possible survival of topological edge states in such a situation ? From Fig. 3.1(c) we already know that the resistivity peak maximum is $\rho_0 = 5.2\,\text{k}\Omega$ whereas a value of $h/2e^2 \approx 13\,\text{k}\Omega$ is expected if the conduction is driven by ballistic edge states. Therefore, we certainly do not have a ballistic topological device.

Ohmic model

Let us check now if the device can be considered as diffusive and homogeneous in the gap. In Fig. 3.6, we compare this peak resistance measured in the local configuration $R_L = R_{14,23}$ to the four probe resistance measured in a non-local configuration $R_{NL} = R_{26,35}$. In the case of an homogeneous, ohmic device, this non-local resistance can be derived directly from the local resistance using the formula:

$$R_{NL}^{\text{Ohmic}} = \frac{4}{\pi} R_L \frac{W}{l_p} \exp\left(-\pi \frac{l_p}{W}\right), \tag{3.3}$$

where $W = 10\,\mu\text{m}$, and $l_p = 10\,\mu\text{m}$ are respectively the width and the lateral probe distance of the Hall bar. Fig. 3.6 shows that close to the CNP, the measured R_{NL} is ten times higher than the expected value for an homogeneous device $R_{NL}^{\text{Ohmic}}(R_L)$. Therefore this model is not appropriate.

Diffusive edge states model

We test now a third model. We assume that conduction is driven by topological edge states, but the sample size L_{edge} is too large to allow for a ballistic regime: $L_{edge} \gg \lambda$, where λ is the inelastic mean free path of the edge states. The non-local resistance can again be derived only from the local resistance, using the equations:

$$R_L = \frac{h}{e^2} \frac{1}{\lambda} \frac{l_p}{2}, \qquad R_{NL} = \frac{h}{e^2} \frac{1}{\lambda} \frac{(2l_1)^2}{(4l_1 + 2l_p)}, \tag{3.4}$$

where l_1 is the distance between the source or drain contact and the closest lateral probe, l_p is the distance between two adjacent lateral probes. These two formula give two different values for λ: $\lambda = 35\,\mu\text{m}$ and $157\,\mu\text{m}$ for the local and non-local cases. Not only these values largely exceed the device dimensions, but these two estimates differ. Thus this last model given by Eq. 3.4 is also inadequate.

Coupled edge and bulk conduction model

We are left with a last possible model. We have seen in the previous chapters that a residual bulk conduction is often observed in devices with small energy gaps. Let us assume now that the conduction is not only carried by the edges but also by the bulk. We use our so-called square lattice model to evaluate the contribution of both edges and bulk in this device. The resistor network used to model device HB0 has node numbers $n_L = 201$, $n_W = 51$ and $n_c = 60$. This corresponds to the device HB0 size and geometry if we take a mesh length of 0.2 µm. Figure 3.7(a) shows that the square lattice method converges to a solution that exactly reproduces the experimental data. The corresponding bulk and edge conductivities $(\sigma_{\text{bulk}}, G_{\text{edge}})$ are shown in Fig. 3.7(b). It appears that close to the CNP, $G_{\text{edge}} > \sigma_{\text{bulk}}$, but σ_{bulk} is not negligible. Even more remarkably, the contribution of the edge G_{edge} does not vanish in both valence and conduction bands, and seems relatively independent of the gate voltage. This suggests that the edge conduction is not topological. Moreover, there is another simple argument against a topological origin of the edge conduction. At the CNP, $G_{\text{edge}} \simeq 2 \times 10^2$ µS $\simeq 5e^2/h$. This value exceeds the quantum of conductance, which is the maximal possible value for topological conductance. Thus, the edge conduction cannot be attributed to topological edge states only: additional parasitic edge conduction is at play. Different phenomena can induce trivial conduction through the edge. A first one can be of technological nature. Indeed, a redeposition of Sb during the etching of the AlSb barrier can make conductive the mesa flanks. Also, there could be a passivation of the dangling bonds after the exposure to air. Another possibility is due to charge accumulation at the etched edge of the samples induced by the InAs conduction band bending at the vacuum interface depending on the precise termination of the semiconductor crystal. This last phenomenon is more relevant as the energy gap is small, *i.e.* comparable to the energy gap of InAs/GaSb double quantum wells.

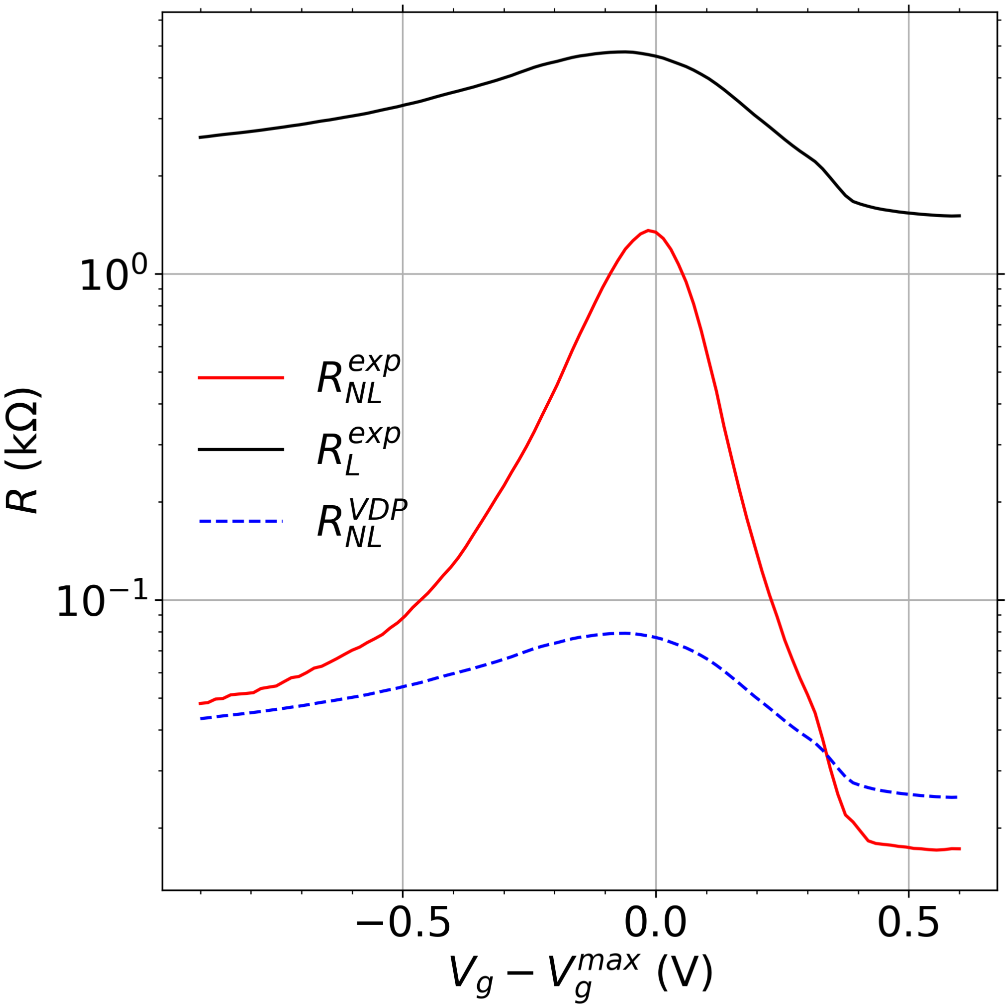

Figure 3.6: Non-local (red solid line) and local (black solid line) resistances as a function of the gate voltage at $T = 2$ K for device HB0. The blue dashed line corresponds to the non-local resistance calculated from the local resistance for a device of homogeneous resistivity. The gate voltage is rescaled to align the peak values of resistance on the position $V_g - V_g^{max} = 0\,\mathrm{V}$. The measurements were done at a temperature $T = 1.7$ K and with a bias current $I = 100$ nA.

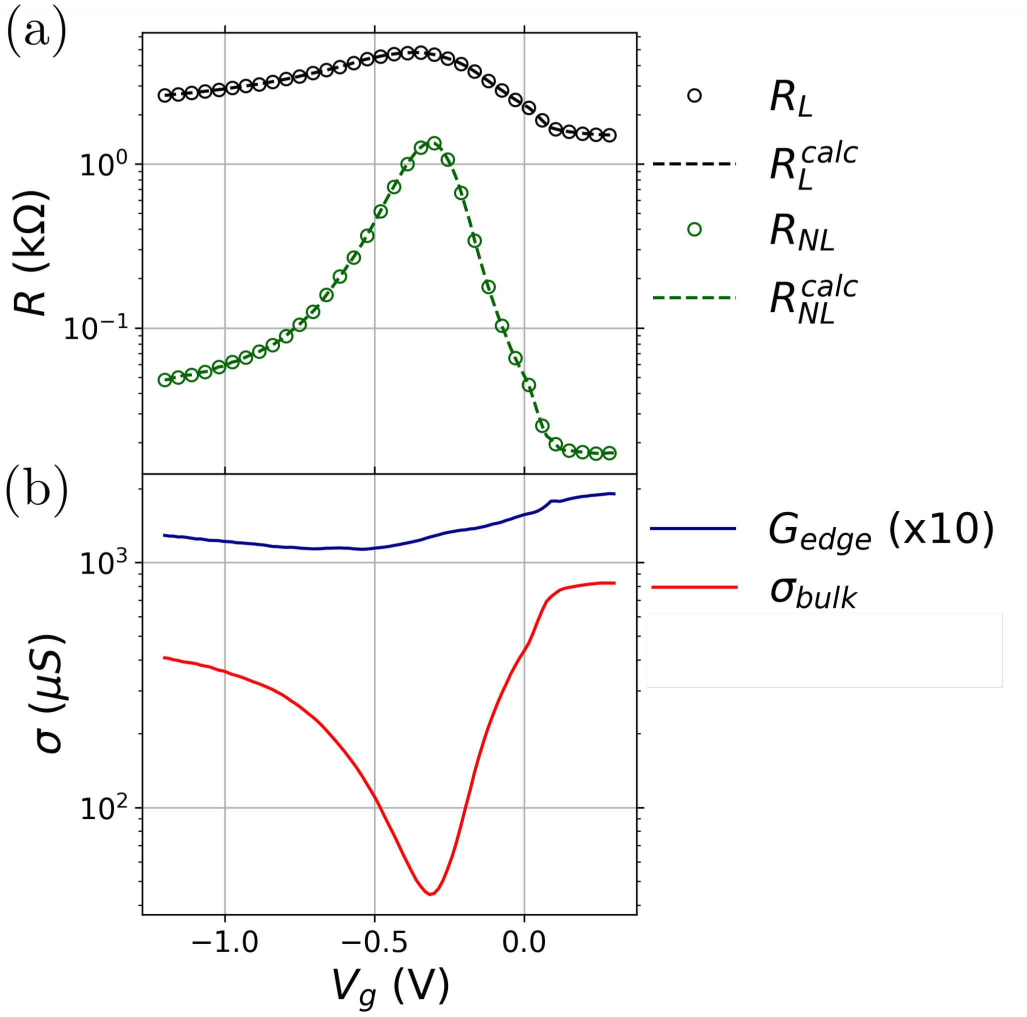

Figure 3.7: (a) Local resistance R_L and non-local resistance R_{NL} as a function of the gate voltage at respectively $T = 2\,\mathrm{K}$ for device HB0. The circle symbols correspond to the experimental data and the dashed lines to the resistances calculated using the square lattice model. (b) Bulk conductivity σ_{bulk} and edge conductance G_{edge} as a function of the gate voltage for respective devices. Both σ_{bulk} and G_{edge} are extracted from the square network of dimensions $n_L, n_W, n_C = 81, 21, 24$ (this corresponds to the geometry of HB0). The edge conductance G_{edge} is multiplied by a factor 10 in order to be compared to σ_{bulk} using the same y-scale.

3.1.4 Conclusion

To conclude, we have evidenced an ambipolar behavior in device HB0. A charge neutrality point separates valence and conduction bands. The gap is very disordered, with a probable presence of charge puddles. Indeed, our square lattice model suggests that bulk conduction persists even in the gap. Edge conduction is also detected. Remarkably this is a parasitic, non topological edge conduction which is evidenced in this device.

3.2 Hall bar HB1, structure S3052

We now present the experimental results obtained in device HB1, introduced in Chapter 2. The device was obtained from growth S3052, and the active part of the device consists of a 25/10/25 monolayer-thick InAs/GaInSb/InAs structure, corresponding to an theoretical energy gap of 30 meV.

We recall that only the four lateral contacts could be connected on this device. Moreover, the ratio between the lateral probe distance l_p and the width W of the Hall bar is $l_p/W = 1$. Thus, in the following, we identify the longitudinal and transverse resistivities ρ_{xx} and ρ_{xy} to the measured resistances $R_{14,23}$ and $R_{14,26}$ respectively. ρ_{xx} and ρ_{xy} have been symmetrized/antisymmetrized with respect to the magnetic field direction. Finally, as also detailed in Chapter 2, there is a sizable gate voltage hysteresis in HB1. To overcome this issue, we measured the device by continuously sweeping the gate voltage V_g at fixed magnetic field B, from 0 to 2 T for both positive and negative orientations of B.

3.2.1 Overview of the magnetoresistances

Figure 3.8 shows colormaps of the longitudinal and transverse resistivities ρ_{xx} and ρ_{xy}, as a function of V_g and B, at $T = 300\,\mathrm{mK}$. In panel (a), ρ_{xx} exhibits Shubnikov-de Haas (SdH) oscillations for $V_g > -11\,\mathrm{V}$, and a resistivity peak for $V_g < -11\,\mathrm{V}$. The linear interpolation of the SdH oscillations converge to a charge neutrality point (CNP) at $V_{CNP} = -13.3\,\mathrm{V}$ and $B = 0\,\mathrm{T}$. Panel (b) shows ρ_{xy} for $V_g > -10.4\,\mathrm{V}$. At lower V_g, ρ_{xy} varied rapidly and is not shown here. ρ_{xy} shows Hall plateaus corresponding to filling factor $\nu = 1, 2, 3, 4, 6$. The good agreement between SdH oscillations in ρ_{xx} and Hall plateaus in ρ_{xy} evidences the stability of the gate voltage sweeps.

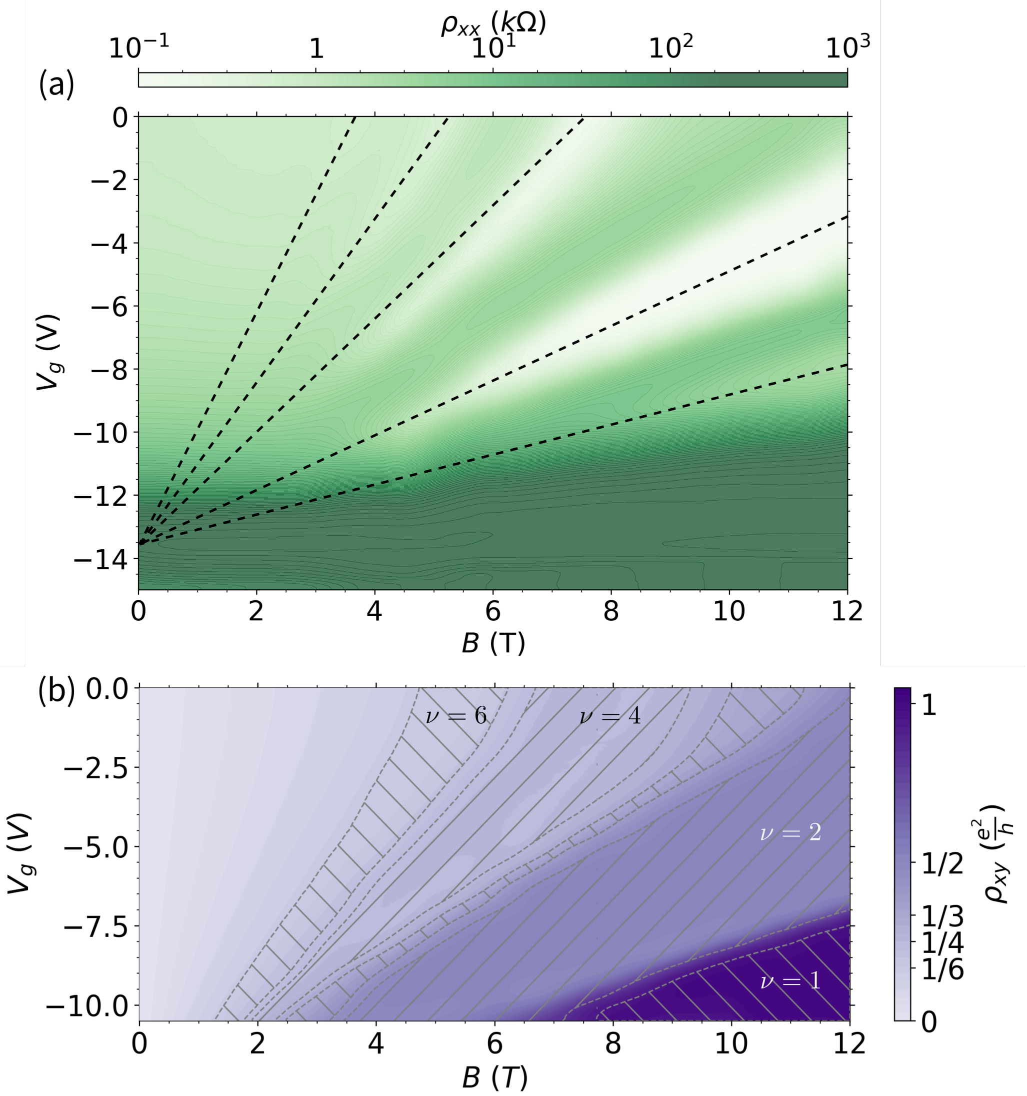

Figure 3.8: Magnetotransport measurements of device HB1. (a) Colormap of ρ_{xx} on a logarithmic scale, as a function of V_g and B. The black dashed lines are guidelines for the eyes to evidence ρ_{xx} minima associated to SdH oscillations. From $V_g = -11\,\mathrm{V}$ to $-15\,\mathrm{V}$, ρ_{xx} increases up to a peak value of $\rho_{xx} = 300\,\mathrm{k}\Omega$, attributed to the band gap. (b) Colormap of $\rho_{xy}(V_g, B)$. The hatched areas correspond to quantum Hall plateaus. The filing factor ν for some plateaus is reported on the colormap. The measurements were performed at $T = 300\,\mathrm{mK}$ with a bias current $I = 100\,\mathrm{nA}$.

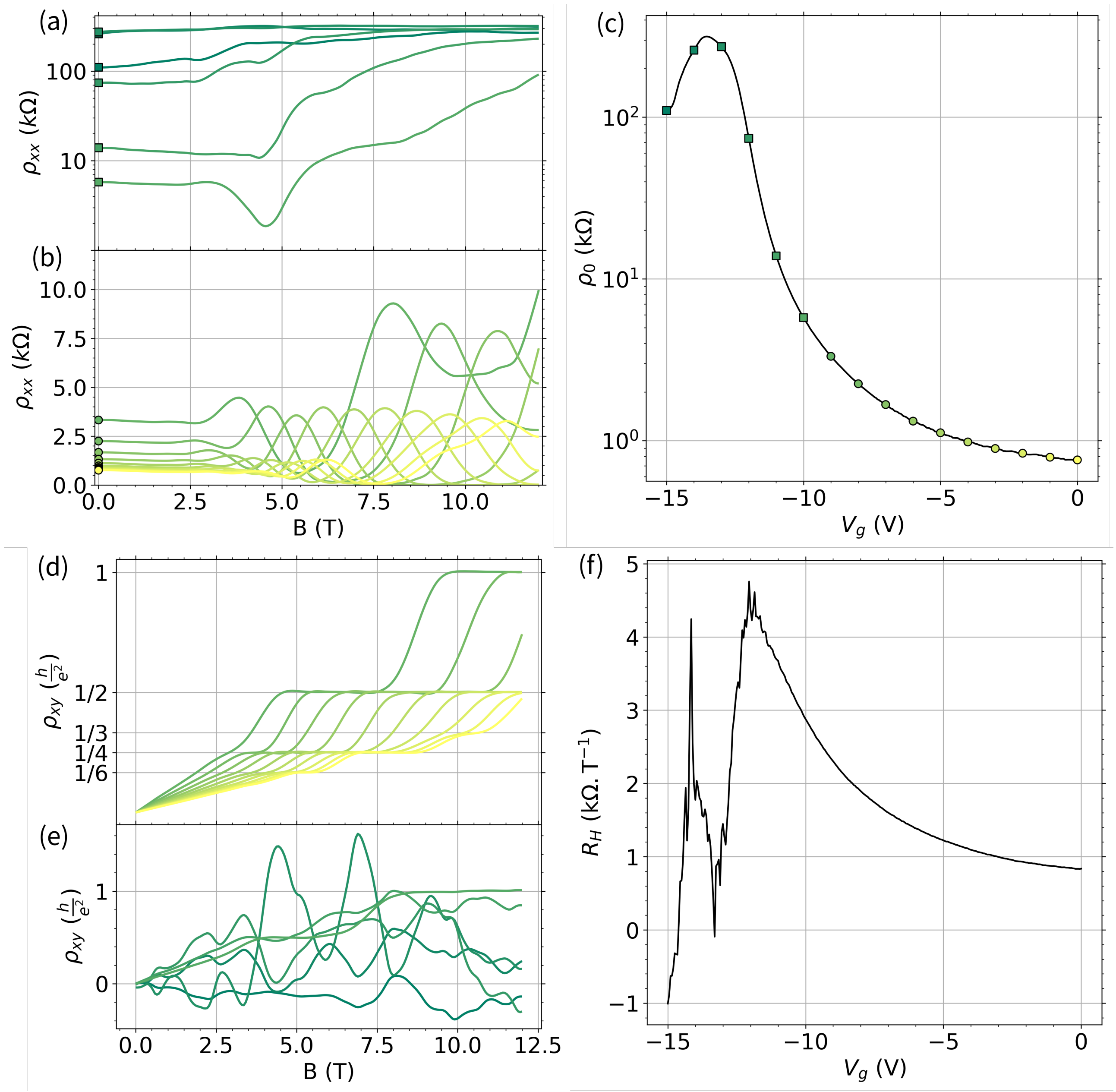

Figure 3.9: (a, b) Longitudinal resistivity ρ_{xx} as a function of magnetic field B up to 12 T for a reduced selection of gate voltages. (c) Gate voltage dependence of the zero-field longitudinal resistivity ρ_0 on a logarithmic scale. The black solid line corresponds to the experimental data and the symbols correspond to the specific values of gate voltage corresponding to the magnetic field dependences in panels (a, b, d, e). Distinction is made with square and round symbols to illustrate the separation between gate voltage values in panels (a, b) and (d, e) espectively. (d, e) Transverse resistivity ρ_{xy} as a function of magnetic field B for different gate voltages. The color of the lines corresponds to the gate voltage and is identical in (a, b, c, d, e) panels. (f) Gate voltage dependence of the Hall coefficient R_H extracted at $B = 1\,\mathrm{T}$. The measurements were performed at $T = 300\,\mathrm{mK}$ with a bias current $I = 100\,\mathrm{nA}$.

3.2.2 Single carrier model at low fields

We first analyze the behavior of device HB1 at low magnetic field. In Fig. 3.9(b,d), in the region $V_g > -11\,\mathrm{V}$ and $B < 2.5\,\mathrm{T}$, ρ_{xy} and ρ_{xx} are well described by a single carrier model as ρ_{xy} increases linearly with B and ρ_{xx} is constant. The increase of both zero-field resistivity and Hall coefficient as the gate voltage approaches the charge neutrality point V_{CNP} is the expected behavior for a single carrier model. The carrier concentration and average mobility extracted from the experimental data are reported in Fig. 3.10. There is a good agreement between the Hall carrier density and the expected carrier density given by $n = C/e(V - V_{CNP})$, where C is the capacitance per unit area of the gate. The extracted mobility strongly decreases as the Fermi energy approaches the gap, and lies in a range $0.1\,\mathrm{m^2\,V^{-1}\,s^{-1}}$ to $1\,\mathrm{m^2\,V^{-1}\,s^{-1}}$. This is coherent with mobility values previously observed in similar structures. This is also in rough agreement with the emergence of Hall plateaus and SdH oscillations at $B > 2.5\,\mathrm{T}$, where the condition $\mu B \geq 1$ is fulfilled.

For $V_g < -11\,\mathrm{V}$, the zero-field resistivity ρ_0 peaks up to $300\,\mathrm{k\Omega}$, as shown in Fig. 3.9(c). Moreover, as shown in Fig. 3.9(d), ρ_{xy} oscillates rapidly from positive to negative values. We interpret these oscillations of ρ_{xy} in the gap as a signature of the presence of both hole and electrons puddles. In this range of magnetic field, the single carrier model no longer describes the resistivity tensor, and the extracted carrier properties are no longer relevant. Note that ρ_{xy} at $V_g = -15\,\mathrm{V}$ is negative in all the magnetic field range from $0\,\mathrm{T}$ to $2.5\,\mathrm{T}$, evidencing a majority of hole-like carriers. Thus, we believe that the gap is almost entirely crossed from the top of the valence band ($V_g = -15\,\mathrm{V}$) to the bottom of the conduction band ($V_g = -11\,\mathrm{V}$).

3.2.3 High magnetic field behavior

Extraction of the carrier density from the SdH oscillations

We now analyze the magnetoresistances on the whole magnetic field range shown in Fig. 3.9(a,-b,d,e). We first extract the carrier density from the SdH oscillations. Figure 3.11(a) shows ρ_{xx} and the absolute value of its first derivative $|\partial\rho_{xx}/\partial B|$ as a function of $1/B$ for several gates voltages. The first derivative allows us to extract more precisely the inverse magnetic field values corresponding to the minima of the SdH oscillations. In Fig. 3.11(b), we report the extracted Landau level positions for the different gate voltage and calculate the related carrier concentration n_{SdH} by a simple linear fit as $1/B = \nu e/n_{\mathrm{SdH}}h$. The corresponding Landau levels indexes are extracted from the transverse resistivity quantized value $\rho_{xy} = \frac{e^2}{\nu h}$ at the same (B, V_g) coordinate in Fig. 3.9. The good agreement with the carrier densities extracted from Hall effect and SdH oscillations (see Fig. 3.11 (c)) indicates that only one band is populated. Coming back to the band structure presented in Chapter 2, this implies that the H1 band is never populated; only the E1 band is filled [MGR+13]. Using the formula $k = \sqrt{4\pi n_{\mathrm{SdH}}}$, we obtain $k_F = 0.3\,\mathrm{nm^{-1}}$ at $V_g = 0\,\mathrm{V}$. For such a large wave vector k_F, both E1 and H1 should be populated and the Fermi level should lie $20\,\mathrm{meV}$ above the bottom of the H1 band. Thus, the theoretical band structure underestimates the energy of the H1 band with respect to E1.

Extraction of the effective mass of carrier from the SdH oscillations

Considering the quality of the device and, by contrast to the previous device HB0, the possibility to use the top gate as we increase the temperature, we now investigate in more details the band structure by considering the temperature dependence of the SdH oscillations. We stress that the data set used for this analysis was obtained from another cooling cycle, and that there is a small shift of the carrier density with respect to the data presented in the previous section.

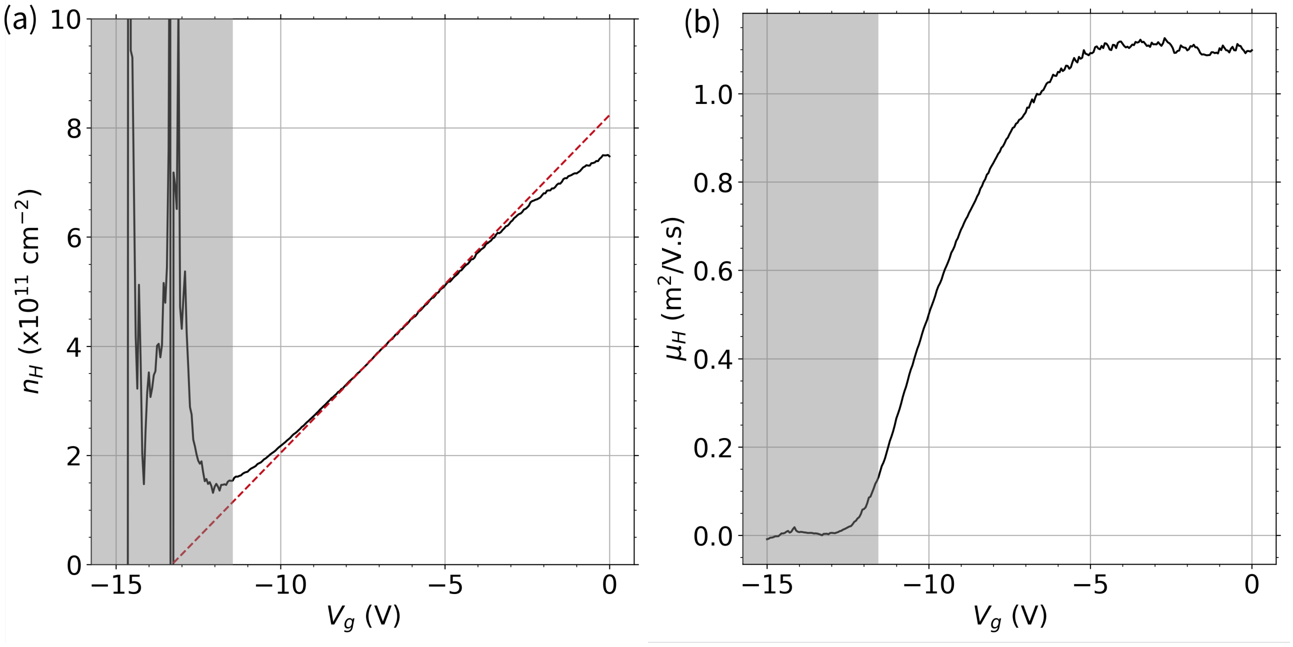

Figure 3.10: Carrier properties extracted from the single carrier model. (a) Hall carrier density n_H calculated from the Hall coefficient R_H as a function of the gate voltage V_g. The black solid line corresponds to the concentration calculated from R_H and the red dashed line corresponds to the linear evolution of concentration calculated from the gate capacitance per unit area $C = 9.9 \times 10\ \mu\mathrm{F\,cm^{-2}}$, assuming the charge neutrality point $V_{CNP} = 13.3\,\mathrm{V}$. (b) Hall mobility μ_H extracted from the zero-field longitudinal resistivity ρ_0 and Hall concentration n_H as a function of V_g. In both panels, the grey areas correspond to the gate voltage region in which the single carrier model is not valid. Carrier properties are calculated from data measured at $T = 300\,\mathrm{mK}$ with a bias current of $I = 100\,\mathrm{nA}$.

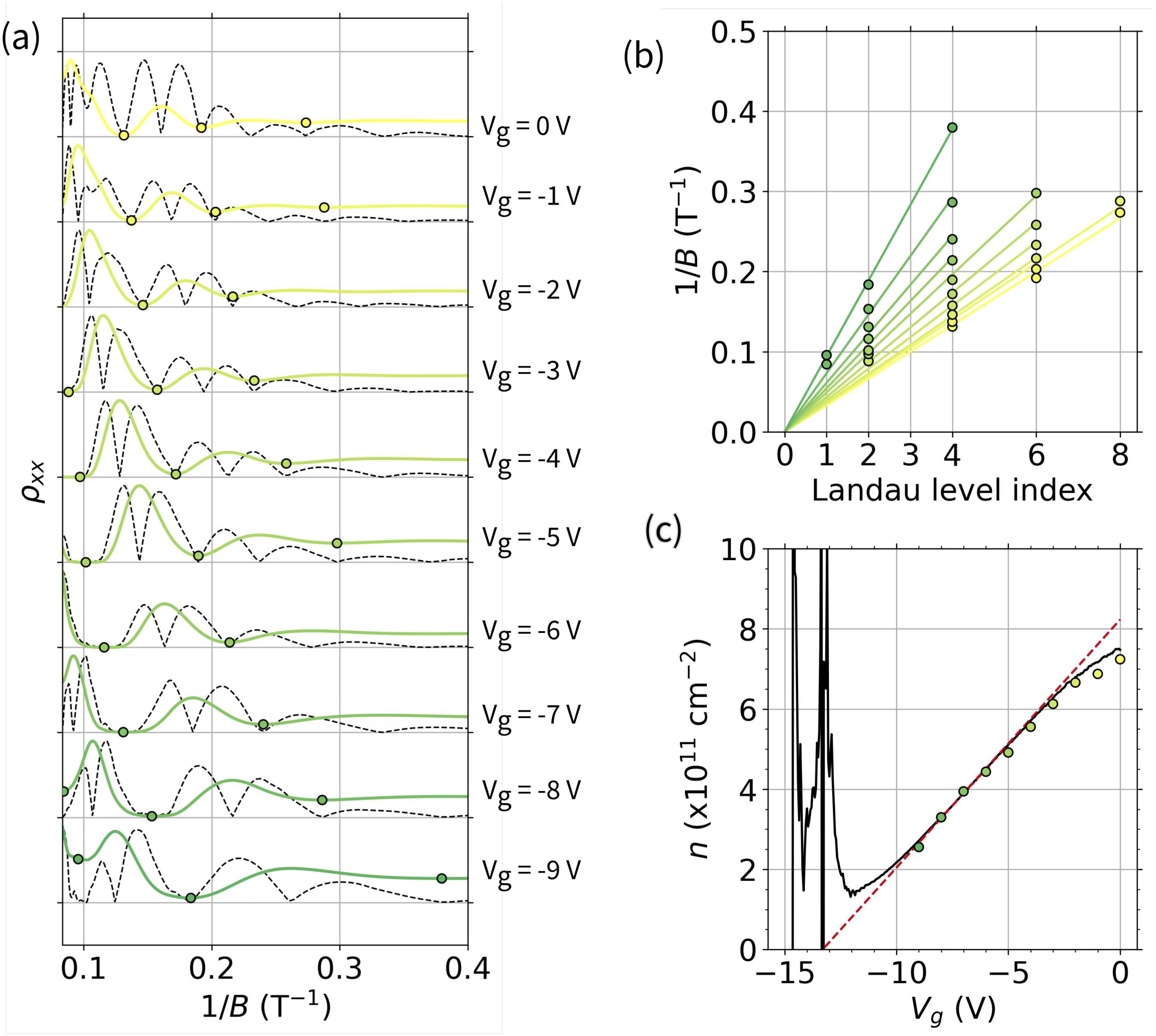

Figure 3.11: Carrier density extraction from SdH oscillations analysis. (a) Normalized longitudinal resistivity ρ_{xx} (colored solid lines) and the absolute value of it first derivative $\frac{\partial \rho_{xx}}{\partial B}$ (black dashed lines) as a function of B for different V_g. The colored solid lines correspond to ρ_{xx} and the superposed dashed lines to its derivative. The circles correspond to the extracted minima. The gate voltage values are provided on the right side of panel (a). We use the same color code to represent V_g in the whole figure. (b) Position of the SdH minima $1/B$ as a function of the Landau level index for different V_g. Landau level indexes are determined by the quantized value of the Hall plateaus observed in ρ_{xy}. The circles correspond to those shown in panel (a). Solid lines are linear fits. (c) Carrier densities n as a function of gate voltage V_g extracted from the experimental data. Black solid line: carrier density calculated from R_H; red dashed line: carrier density calculated from the gate capacitance per unit area $C = 9.9 \times 10\ \mu\mathrm{F\,cm^{-2}}$, assuming CNP at $V_g = 13.3\,\mathrm{V}$; circles: carrier density extracted from the SdH oscillations.

For this new data set, HB1 was first cooled down to $T = 300\,\mathrm{mK}$ and then warmed up until the SdH oscillations vanished.

We already detailed in Chapter 1 the expression of the SdH oscillations and we now investigate the temperature dependence of their envelope:

$$\Delta\rho_{xx}^{\mathrm{LK}}(B,T) = 4\rho_0 e^{-\pi/\omega_c\tau_q} \frac{2\pi^2 k_B T/\hbar\omega_c}{\sinh\left(2\pi^2 k_B T/\hbar\omega_c\right)}, \tag{3.5}$$

where $\omega_c = eB/m^*$ is the cyclotron frequency and τ_q is the quantum time. We have previously demonstrated that, if we note $\Delta\rho(B,T)$ the amplitude between two SdH extrema around an average magnetic field B and at a temperature T, then :

$$T \gg \frac{\hbar\omega_c}{2\pi^2 k_B} \Rightarrow \ln\left(\frac{\Delta\rho_{xx}(B,T)}{\Delta\rho_{xx}(B,T_{\mathrm{ref}})}\frac{T_{\mathrm{ref}}}{T}\right) \sim \alpha - \beta T, \tag{3.6}$$

with $\alpha = \ln\left(2\sinh\left(2\pi^2 k_B T_{\mathrm{ref}}\right)/(\hbar\omega_c)\right)$, $\beta = 2\pi^2 k_B/\hbar\omega_c$ and T_{ref} is a reference temperature. Equation 3.6 shows that for high temperature, $\ln(\Delta\rho_{xx}(B,T)/T)$ evolves linearly with T, with a slope directly proportional to the effective mass m^*.

Figure 3.12(a) shows the temperature evolution of ρ_{xx} at $V_g = 0$ V. As T increases, the positions of the SdH oscillations shift in magnetic field, leading to a change of carrier density. To overcome this issue, the carrier density is extracted at the lowest and highest temperatures and we determine an average carrier concentration $n_{\mathrm{SdH}} = (2.70 \pm 0.06) \times 10^{11}\,\mathrm{cm}^{-2}$. We define $\Delta\rho_{xx}(B_n,T)$ as the resistivity difference between two successive extrema of the oscillations. Here, B_n is the magnetic field at which a temperature-independent ρ_{xx} node between the two chosen extrema appears. Three values of B_n have been chosen for the analysis: $B_n = 3.3\,\mathrm{T}$, $4.4\,\mathrm{T}$ and $5.6\,\mathrm{T}$. These values are reported in Fig. 3.12(a) as vertical dashed lines. For the reference temperature T_{ref}, we have chosen $T_{\mathrm{ref}} = 0.3\,\mathrm{K}$, $0.3\,\mathrm{K}$ and $0.8\,\mathrm{K}$ for $B_n = 3.3\,\mathrm{T}$, $4.4\,\mathrm{T}$ and $5.6\,\mathrm{T}$ respectively. For $B_n = 5.6\,\mathrm{T}$, T_{ref} is higher, because at lower T quantum Hall effect is at play and the magnetoresistance goes to zero. For $B_n = 3.3\,\mathrm{T}$ and $4.4\,\mathrm{T}$, ΔR could not be estimated for $T > 20\,\mathrm{K}$, as the SdH oscillations disappear at these temperatures.

Figure 3.12(b) shows the temperature dependence of these three sets of $\Delta\rho_{xx}(B_n,T)$, and the corresponding fit. The 3 sets have been fitted together, with the same effective mass as a fit parameter. This gives $m^* = (0.046 \pm 0.004) \times m_0$, where m_0 is the electron mass. This value is in good agreement with previous estimates obtained in similar structures [KRGP+18].

From the theoretical band structure and the DoS presented in Chapter 2, we can calculate the effective mass as a function of the density. Indeed, the effective mass can be easily derived from the band structure as $m^* = \hbar/\Delta E_k$, where ΔE_k is the Laplacian of the energy dispersion. Figure 3.13 shows the theoretical effective mass of the E1 band, as a function of the carrier density. The effective mass which has been estimated from the data is also indicated as a blue symbol. It is clear that the measured effective mass is close to its expected value, providing confirmation of the energy dispersion for the E1 band.

In Fig. 3.13, the effective mass is divided by $m^*_{\mathrm{ref}} = 0.056 m_0$, which is the effective mass of electrons in a single 7.5 nm thick InAs quantum well [KDM+88]. This ratio m^*/m^*_{ref} is greater than one. This demonstrates that the electrons are not uniquely confined in the InAs quantum wells, and makes us confident that the device can host topological carriers.

Extraction the Landau Level broadening from the SdH oscillations

We can now evaluate the quantum time τ_q in the exponential term in Eq. 3.5. The quantum lifetime is directly related to the Landau Level broadening as $\Gamma = \hbar/2\tau_q$. Figure 3.14(a) shows the longitudinal resistivity as a function of the magnetic field, at $T = 300\,\mathrm{mK}$ and $V_g = 0\,\mathrm{V}$.

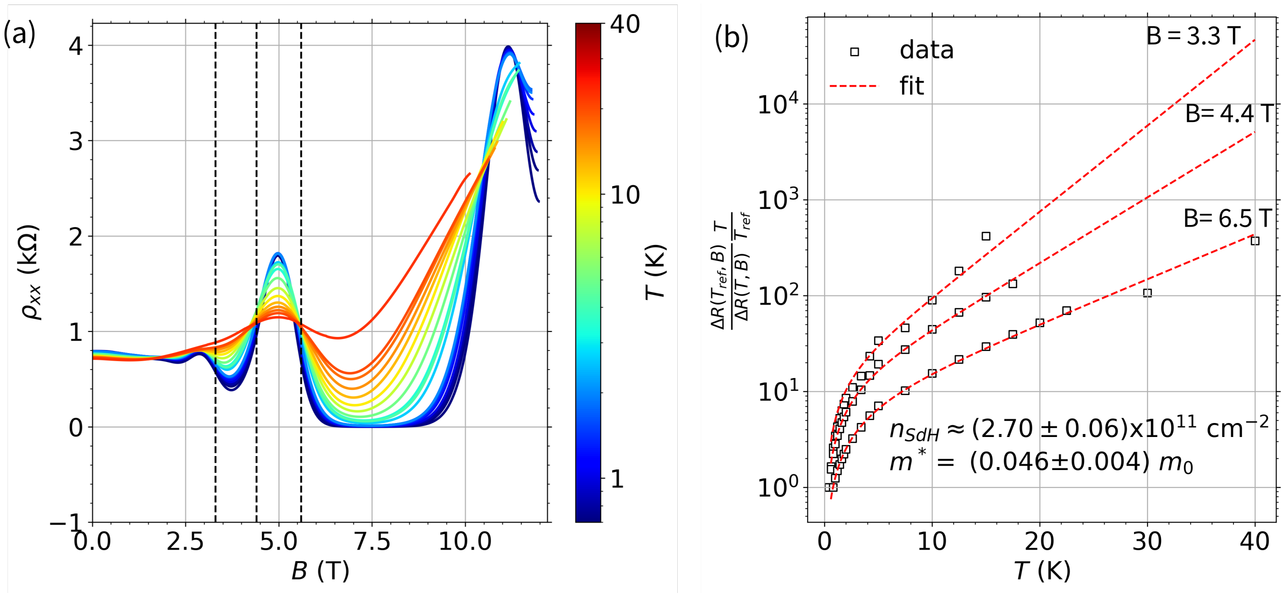

Figure 3.12: Effective mass obtained from SdH oscillations. (a) ρ_{xx} as a function of B for different temperatures. The color scale corresponds to a temperature range from $T = 300\,\mathrm{mK}$ to $T = 40\,\mathrm{K}$. The vertical dashed lines correspond to the positions $B_n = 3.3\,\mathrm{T},\ 4.4\,\mathrm{T}$ and $5.6\,\mathrm{T}$ of the three nodes of the SdH oscillations analyzed in panel (b). (b) $T/\Delta R(B_n, T)$ as a function of T for three magnetic fields B_n. The variation of $T/\Delta R(B_n, T)$ is normalized by taking a temperature reference T_{ref}. The experimental $T/\Delta R(B_n, T)$ are indicated by the black squares. The red dashed lines correspond to the fit. The fitting parameter m^* is the effective mass and is imposed to be identical for the three B_n.

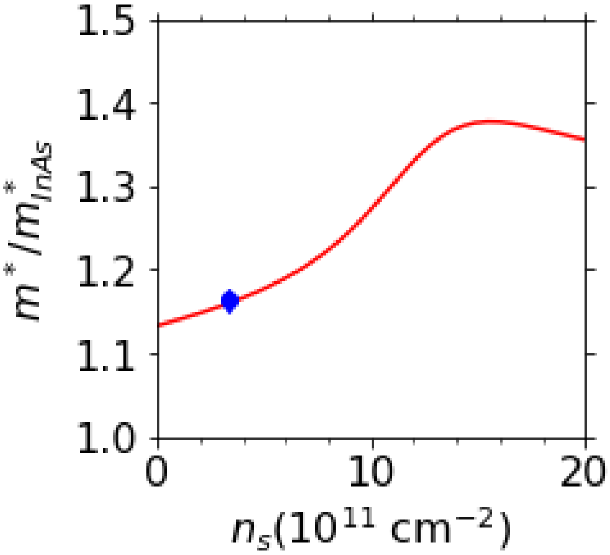

Figure 3.13: Red solid line: theoretical effective mass of the E1 band, extracted from the band dispersion as a function of the carrier density. Blue circle: effective mass extracted from the SdH analysis. The effective mass is normalized by the effective mass of electrons confined in a single 7.5 nm-thick InAs QW ($m^* = 0.056$).[KDM+88]

Note that the experimental data correspond to those presented for the determination of the effective electron mass. We extract the envelope of SdH oscillations ΔR_{xx} as a function of magnetic field. Indeed, one can rewrite Eq. 3.5 as:

$$\frac{\Delta R_{xx}}{4R_0} = R_T e^{-\pi/\omega_c \tau_q}, \tag{3.7}$$

where R_0 is the resistance at $B = 0\,\mathrm{T}$, R_T is a temperature dependent term given by

$$R_T = \frac{X}{\sinh X}$$

with

$$X = \frac{2\pi^2 k_B T}{\hbar \omega_c},$$

and $\omega_c = eB/m^*$ the cyclotron frequency. Here, as we work at $T = 300\,\mathrm{mK}$, $R_T \approx 1$. Figure 3.14(b) shows the evolution of the SdH amplitude as a function of the inverse magnetic field on a logarithmic scale. The quantum lifetime τ_q is calculated from the slope of the linear fit. The fit is not of very good quality. Nevertheless, we are confident that the data can be fitted, because we have i) a rough exponential dependence and ii) $\lim_{1/B \to 0} \Delta R_{xx}/4R_0 = 1$. A quantum lifetime $\tau_q = 0.05\,\mathrm{ps}$ is obtained, leading to a Landau Level broadening $\Gamma = 6\,\mathrm{meV}$. This value is quite comparable to what has been observed in similar InAs/GaSb TQWs [HZC86].

Estimation of the Fermi level

In order to find the position of the Fermi level E_F as a function of both V_g and B, we calculated the trajectories of $E_F(n)$ in the (B, E) plane for some fixed carrier density n, as shown in Fig. 3.16. For such an analysis it is necessary to know the density of states (DoS) as a function of B. The DoS was obtained from the theoretical LL dispersion reported in Chapter 2. We introduced for each LL a constant Lorentzian broadening $\Gamma = 6\,\mathrm{meV}$. Fig. 3.16 shows the iso-carrier density trajectories as colored dashed lines, labeled by the corresponding gate voltage V_g. We also show with solid lines the trajectories of integer values of $\nu = 1,\ 2,\ 3,\ 4,\ 5,\ 6,\ 7$ and 8. Without broadening, the trajectories of the integer values of ν matches the LLs trajectories as shown in Fig. 3.15(a). However, we represent in Fig. 3.15(b) the trajectories when considering Lorentzian broadening with $\Gamma = 6\,\mathrm{meV}$.

We can now compare this theoretical representation with the experimental results. We report on this graph the SdH minima previously indicated in Fig. 3.11. These minima appear at the coordinates $(B_{\text{min,i}}(n_{SdH}), E_F(n_{SdH}))$, where n_{SdH} is the carrier density extracted from the SdH oscillations, at a given V_g, and $B_{\text{min,i}}$, $i = 1, 2, \ldots$ are the magnetic fields at which these minima appear.

As expected, the SdH minima correspond to the positions of the integer filling factors. More remarkably, the model shows that E_F can be more than $25\,\mathrm{meV}$ above the bottom of the $E1$ band. By comparison, the theoretical calculation predicts that the $H1$ band has its minimum only $20\,\mathrm{meV}$ above the bottom of the $E1$ edge. This is another hint that the theoretical model underestimates the energy of the H1 band.

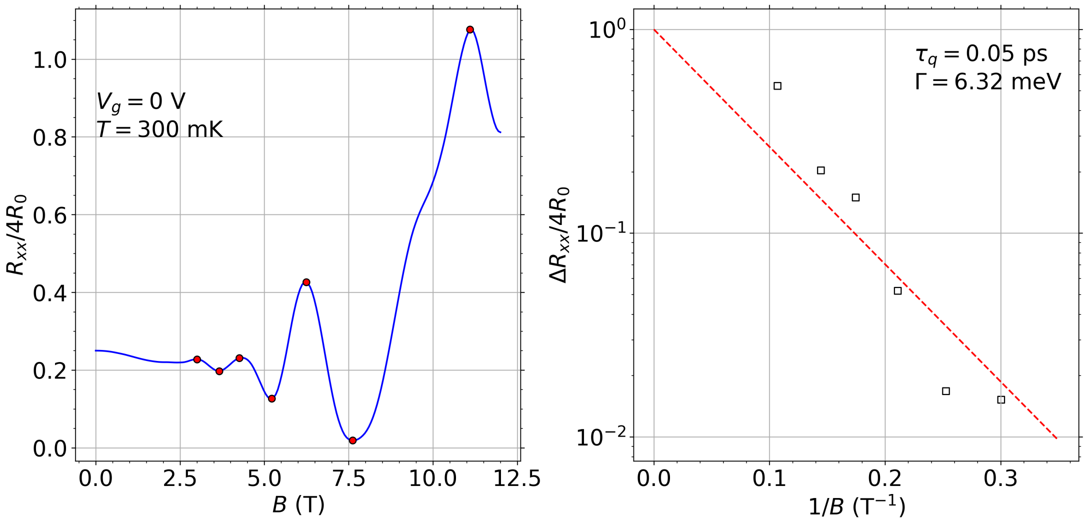

Figure 3.14: (a) Longitudinal resistance R_{xx} as a function of B for $V_g = 0\,\mathrm{V}$ and $T = 300\,\mathrm{mK}$. The red dots represent maxima and minima defining the SdH envelope function. The difference between an adjacent maximum and minimum gives ΔR_{xx}. (b) ΔR_{xx} normalized by the background $4R_0$ as a function of $1/B$. Black squares: data, red dashed line: linear fit.

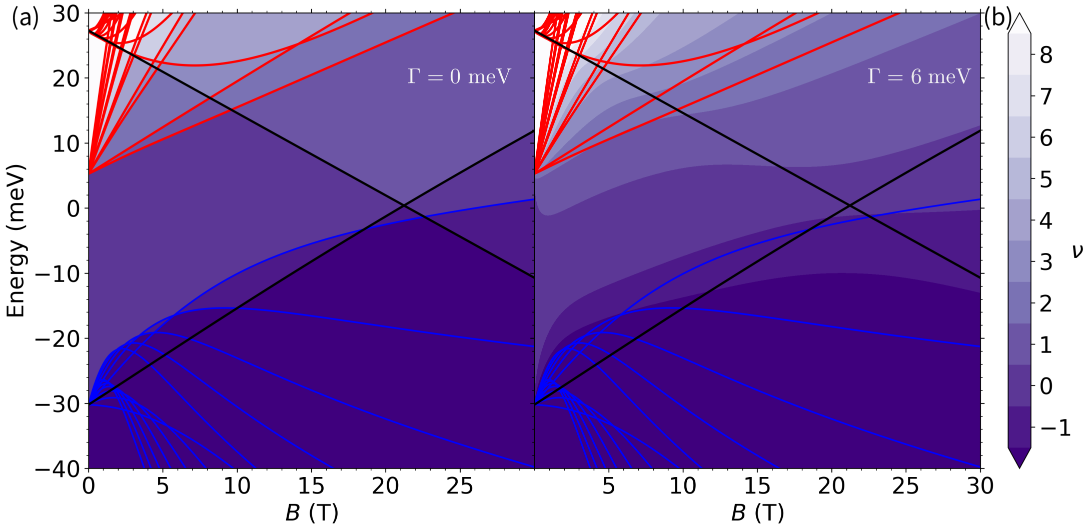

Figure 3.15: Color map of filling factor ν as a function of magnetic field and energy. The solid lines correspond to the trajectories of the Landau Levels. Panel (a) corresponds to the case without broadening and panel (b) to a LL broadening of $\Gamma = 6\,\mathrm{meV}$.

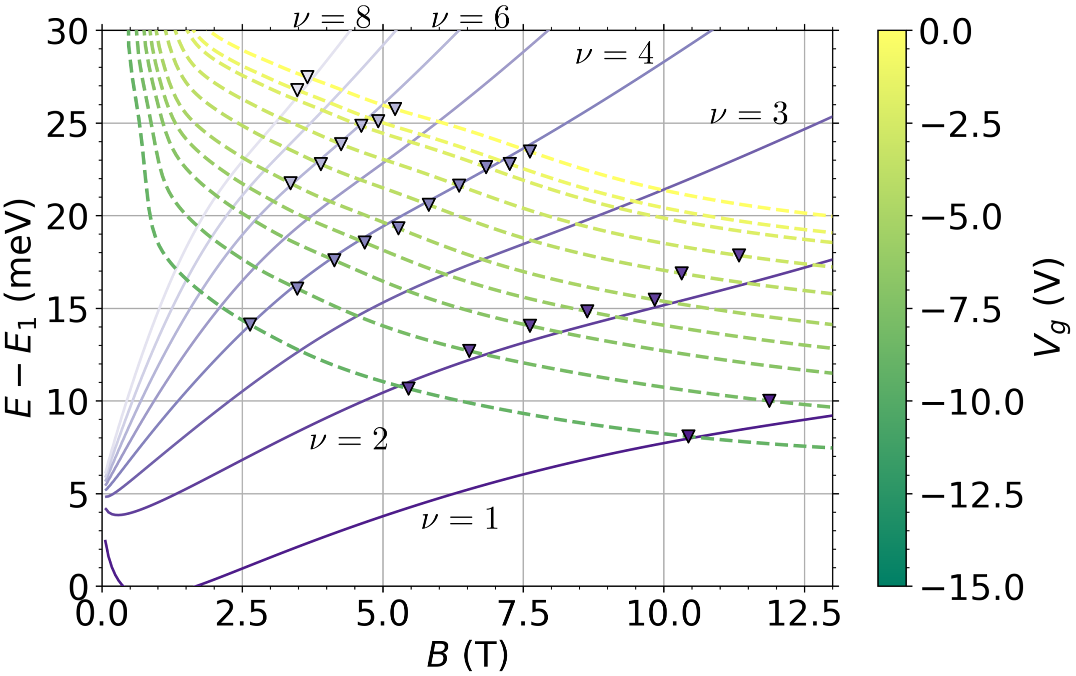

Figure 3.16: Effective fan-chart of filling factor ν as a function of magnetic field and energy. The energy reference is the bottom of the E1 band. The solid lines correspond to the trajectories of the integer value of ν derived from the Landau Levels, with a LL Broadening of $\Gamma = 6$ meV. The dashed lines correspond to Fermi Level trajectories at fixed concentrations. The Iso-carrier densities are calculated for DoS where the LLs have a Lorentzian distribution with a half width of $\Gamma/2$. Triangle symbols correspond to the experimental positions of the SdH minima extracted from Fig. 3.11 (a).

3.2.4 Activation energy

The magneto-transport measurements in the previous paragraphs provide a good description of the conduction band and the associated transport regime. They also indicate the presence of a gap. We now propose to evaluate the magnitude of the energy gap by thermal activation. Figure 3.17 (a) shows the longitudinal resistivity peak in the vicinity of the gap. We define $V_g^{\max}$ as the gate voltage position of the peak value of the resistivity. Note that this position is not the same as the temperature increases (see section 3.2.3) so the gate voltage dependence of ρ_{xx} is shown as a function of $V_g - V_g^{\max}(T)$. In addition, as we previously concluded that the contribution of the substrate conduction for temperatures $T > 25\,\mathrm{K}$ is not negligible, only data acquired at $T < 25\,\mathrm{K}$ were used to determinate the energy gap. In Fig. 3.17 (b) we report the peak values of the resistivity on a logarithmic scale as an inverse function of the temperature. The temperature dependence of the resistivity is fitted by a sum of three terms:

$$(\rho_{xx}^{\max})^{-1}(T) = \sigma_a(T) + \sigma_{loc}(T) + \sigma_0, \tag{3.8}$$

where

$$\sigma_a(T) = \sigma_a \exp\left(-\frac{\Delta}{2k_B T}\right)$$

is the thermal activation term,

$$\sigma_{loc}(T) = \sigma_{loc} \exp\left(-\frac{\Delta_{loc}}{k_B T}\right)$$

is the localization gap term induced by nearest neighbor hopping [IAC+20, DKSD15], and σ_0 is an additional term independent of the temperature. The three terms are represented independently by dashed lines in Fig. 3.17 (b). From the fit, we obtain an energy gap $\Delta = (30.0 \pm$

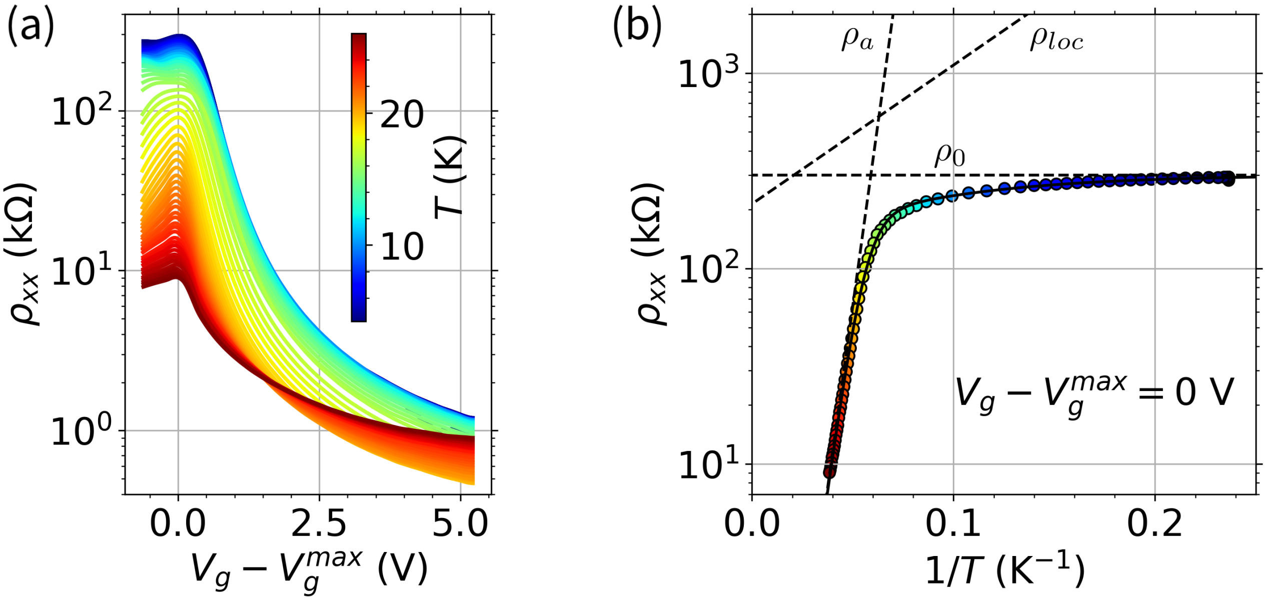

Figure 3.17: Extraction of the activation energy from the temperature dependence of the longitudinal resistance. (a) Longitudinal resistivity ρ_{xx} as a function of the gate voltage at different temperatures. The color scale corresponds to the temperature. The gate voltage is rescaled to be centered on the gate voltage position of the resistivity peak $V_g^{\max}(T)$. (b) Temperature dependence of the resistivity peak. The colored circle symbols correspond to the experimental resistivity peaks. The colors correspond to the temperature, with the same code as in panel (a). The solid line is the fit of the experimental data, and the dashed lines are the 3 contributions to the fit: ρ_a, ρ_{loc} and ρ_0, corresponding to the activation energy, localization gap and edge state terms respectively.

0.3) meV and $\Delta_{loc} = (1.3 \pm 0.1)$ meV. The dispersion of both calculated values only includes the standard deviation from the data fit. The measured energy gap nicely matches the theoretical band structure expectations $\Delta_{th} = 30$ meV. In the framework of nearest neighbor model, $\Delta_{loc} = (Da^2)^{-1}$, where D is the density of states inside the band gap, and a is the distance between nearest sites [QXW+13]. In Section 3.2.2, we argued that the band gap is in the range $-15\,\text{V} < V_g < -11\,\text{V}$. The D value is defined as:

$$D = \Delta V(C/e)/\Delta, \tag{3.9}$$

where $\Delta V = 4$ V is the difference of gate voltage values corresponding to the edges of valence and conduction band, $C = 9.9 \times 10^{10}\,\mu\text{F}\,\text{cm}^{-2}$ is the capacitance per unit area of the dielectric gate, and $\Delta = 30$ meV is the energy gap. We obtain $D = 8.25 \times 10^{12}\,\text{eV}\,\text{cm}^{-2}$ and $a = (97 \pm 3)$ nm,which is a rather large value. Finally, the last term σ_0 in Eq. 3.8 dominates at low temperature and prevents the divergence of the resistivity in the band gap. It is interpreted as the first hint of a possible contribution of edge states. We propose in the following to investigate this possible contribution through non-local measurements.

3.2.5 Non-local measurement

Landauer-Büttiker model

We now investigate the transport properties in the band gap by local and non-local measurements. Note that for this device, the local configuration does not correspond to the usual one. Schemes of the Hall bar in non-local and local measurement configuration are provided in Fig. 3.18(b) and (c) respectively. Figure 3.18(a) shows the resistance for both local R_L and

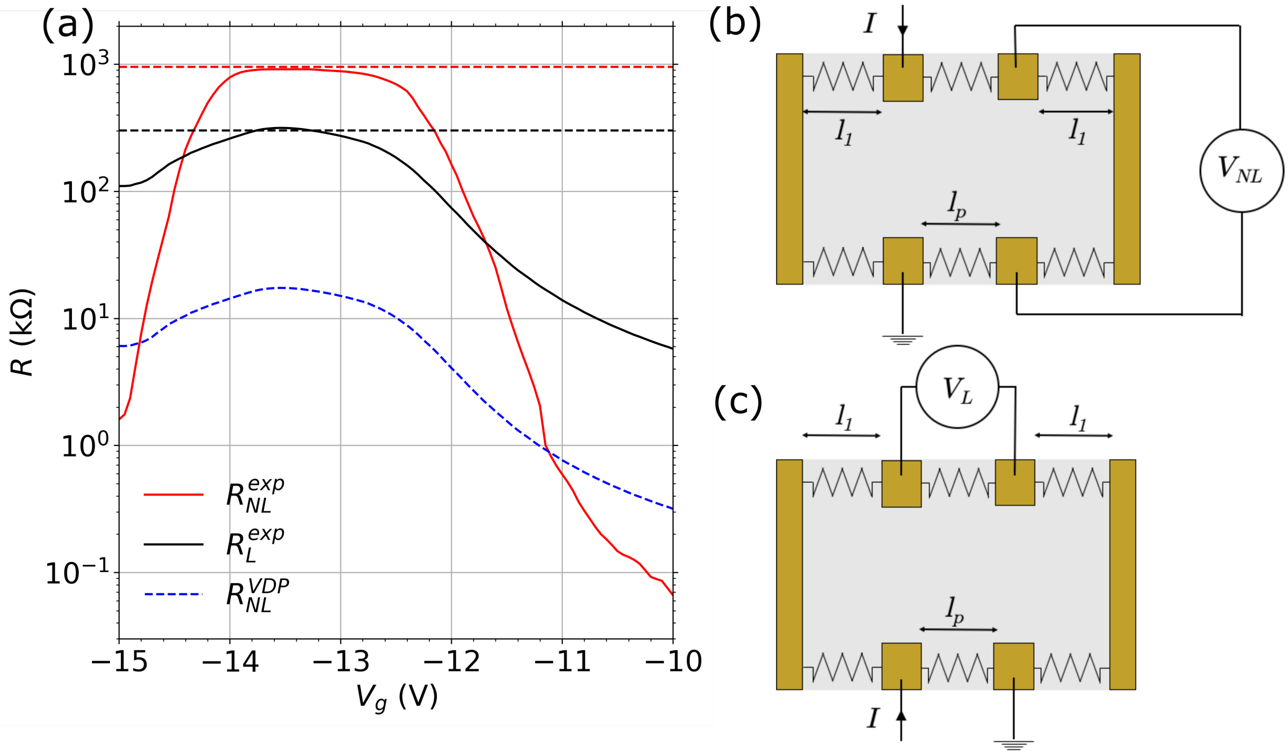

Figure 3.18: (a) Non-local (red solid line) and local (black solid line) resistances as a function of the gate voltage at $T = 300\,\mathrm{mK}$. The blue dashed line corresponds to the non-local resistance calculated from the local data for a device of a homogeneous, ohmic conduction. The dotted lines correspond to the expected peak resistances for local and non-local configurations assuming edge states only, with $\lambda = 2.0\,\mu\mathrm{m}$. The same color code is used to distinguish non-local and local configurations. (b) Scheme of device HB1 in the non-local configuration. (c) Scheme of device HB1 in the local configuration. In both (b,c) panels, the device in the band gap regime is modeled by taking only edge channels into account. The edges of the device are modeled as resistors with $R_{\mathrm{edge}} = (h/e^2)L_{\mathrm{edge}}/\lambda$.

non-local R_{NL} configurations at $B = 0\,\mathrm{T}$, as a function of V_g. The experimental non-local resistance is compared to the expected non-local resistance R_{NL}^{Ohmic} of an homogeneous device (*i.e.* without edge conduction) defined by the formula:

$$R_{NL}^{\mathrm{Ohmic}} = \frac{4}{\pi} R_L \frac{W}{l_p} \exp\left(-\pi \frac{l_p}{W}\right), \tag{3.10}$$

where $W = 100$ µm and $l_p = 100$ µm are respectively the width and the distance between the lateral probes of the Hall bar. It is clear from Fig. 3.18(a) that the non-local resistance peak of $R_{NL} = 1\,\mathrm{M\Omega}$ is far too large to be explained by current spreading in homogeneous device. We interpret this as due to an important contribution of edge conduction. However, in both local and non-local configurations, the resistance values largely exceeds the expected values for topological edge states in the ballistic regime, respectively $R_L = (1/2)h/e^2 \approx 13\,\mathrm{k\Omega}$ and $R_{NL} = (2/3)h/e^2 \approx 17\,\mathrm{k\Omega}$.

Considering the large dimensions of device HB1, the non-ballistic regime of topological edge states is not surprising and we propose a more relevant model of edge states in a diffusive regime. As shown in Fig. 3.18(b, c), we model the edges of the Hall bar as resistors. The resistance value R_{edge} of each edge is defined by taking into account its length:

$$R_{\mathrm{edge}} = \frac{h}{e^2}\left(1 + \frac{L_{\mathrm{edge}}}{\lambda}\right) \simeq \frac{h}{e^2}\frac{L_{\mathrm{edge}}}{\lambda},$$

where λ is the characteristic length at which the two counter-propagating edge states equilibrate. More details on both ballistic and diffusive regimes in the Landauer-Büttiker description of edge channels are provided in Chapter 1. From Fig. 3.18(b,c), one can demonstrate that

$$R_L = \frac{1}{\lambda}\frac{h}{e^2}\frac{l_p^2}{2(l_p + l_1)}$$

and

$$R_{NL} = \frac{1}{\lambda}\frac{h}{e^2}\frac{2l_1^2}{l_p + 2l_1}$$

with $l_p = 100\,\mathrm{\mu m}$ and $l_1 = 120\,\mathrm{\mu m}$. We obtain $\lambda = (2.0 \pm 0.1)\,\mathrm{\mu m}$ as the average of λ values calculated from the two different configurations. The resulting values of resistance in both measurement configurations are shown in Fig. 3.18(a) by horizontal dashed lines. The small error on λ (5%) demonstrates that the diffusive topological edge state model is coherent with the experiment. Nevertheless, we have assumed for the moment that only the edges contribute to the conduction in the band gap at low temperature. In particular, this simple model does not take into account bulk conduction. In order to be sure that the estimate of λ is not seriously perturbed by residual bulk conduction, we have done a more complete numerical analysis, as detailed below.

Square lattice model

We investigated further the bulk and edge contributions to the conduction in the band gap by using the square lattice model detailed in Chapter 2. The network of resistors used to model device HB1 has the dimensions: $n_L = 81$, $n_W = 21$ and $n_c = 24$. This corresponds to the size and geometry of HB1 if we take a mesh length of 5 µm. In Fig. 3.19(a,b), we show the experimental local and non-local resistances for different temperatures from $T = 1.7\,\mathrm{K}$ to $16\,\mathrm{K}$. Note that the experimental data were measured during a different campaign of measurements than those presented in the previous sections. As a comparison, the peak value of resistivity at

$T = 4.2\,\mathrm{K}$ was $\rho_{xx}^{\max} \simeq 300\,\mathrm{k\Omega}$ during the previous campaigns and $\rho_{xx}^{\max} \simeq 180\,\mathrm{k\Omega}$ in Fig. 3.19(a). During these last measurements, we also observed a jump of the non-local resistance peak, at low temperature, see Fig. 3.19(b), and R_{NL} jumped from $500\,\mathrm{k\Omega}$ to $300\,\mathrm{k\Omega}$ when T increased from $1.7\,\mathrm{K}$ to $3\,\mathrm{K}$. We attribute these effects to some instabilities of the electrostatic environment.

In Fig. 3.19(a,b), the fit of both R_N and R_{NL} are also reported, superimposed on the experimental data. The fits, indicated as solid lines, are perfectly superimposed on the experimental points, indicated by symbols. It is clear that the square lattice model precisely fits the experimental data for all temperatures and gate voltages.

In panel (c), the two parameters, the bulk conductivity σ_{bulk} and the edge conductance G_{edge}, obtained from the square lattice fit, are reported as a function of $V_g - V_g^{\max}$, for the different temperatures. We recall that G_{edge} is defined as $G_{\text{edge}} = (G_e - G_b)l_c/l_p$, where G_e (G_b) is the conductance of the resistors at the mesh edge (in the mesh interior), $(G_e - G_b)$ is the additional conductance at the edge which is due to the edge state only, l_p is the distance between the lateral probes, and l_c is the mesh size. The renormalization by the factor l_c/l_p is important. Indeed, G_e is physically ill-defined, because $\lim_{l_c \to 0} G_e = \infty$, but $\lim_{l_c \to 0} l_c G_e = \sigma_e$, where σ_e is the edge conduction, which is physically well defined, in meter per Ohm.

In the middle of the band gap (*i.e.*, close to $V_g - V_g^{\max} = 0\,\mathrm{V}$), a significant reduction of the bulk contribution compared to band gap edges is observed, associated with the emergence of edge conductance. This effect is enhanced as the temperature decreases. On the contrary, in the valence and conduction bands ($|V_g - V_g^{\max}| \geq 2\,\mathrm{V}$), the edge conductance goes to zero and only σ_{bulk} persists.

From the square lattice model, one can calculate λ, which is given in the diffusive regime by $\lambda = (e^2/h)(G_{\text{edge}}/l_p)$. From $G_{\text{edge}} \simeq 1\,\mathrm{\mu S}$ in the middle of the gap at $T = 1.7\,\mathrm{K}$, using $l_p = 100\,\mathrm{\mu m}$, we obtain $\lambda = 2\,\mathrm{\mu m}$. This is coherent with our previous estimation, where the bulk contribution was neglected. The negligible role of the bulk conduction at these low temperatures is confirmed in Fig. 3.19(c).

The evolution of σ_{bulk} in the gap shows also a clear insulating behavior, whereas G_{edge} is almost temperature independent. In fact, we would expect G_{edge} to have a metallic behavior, but this is not strictly the case, and we observe in Fig. 3.19(d) that G_{edge} in the middle of the gap has a weak increase when increasing the temperature. We still do not known if this behavior has a physical meaning.

The disappearance of G_{edge} outside the band gap suggests that topological conduction is at play. Indeed, one would expect edge conduction independent of the gate voltage, in the case of parasitic edge conduction.

The edge conductance peak observed at $V_g - V_g^{\max} = 1.8\,\mathrm{V}$ is more surprising. Initially, we interpreted it as experimental error propagation, since R_{NL} and R_L are not measured during the same gate voltage sweeps. A small gate offset between these sweeps could induce an unphysical peak at the band edges. However, we could not get rid of this peak even after introducing an artificial gate voltage offset. Moreover, we cannot attribute this phenomenon to possible inhomogeneities of device HB1, since a similar behavior is also reproduced in other devices like HB4 and HB6. Thus, we suggest that this peak could have some physical origin. For instance, there are some recent theoretical studies predicting the coexistence of edge and bulk states in complex valence bands of HgTe QWs [KT18a], and the bands of our 3L InAs/GaInSb QWs share similarities with those of HgTe QWs [KYB+16].

3.2.6 Conclusion on HB1

To conclude, the band structure of growth S3052 has been investigated in details in the conduction band and the band gap, using device HB1. In the conduction band, the experimental observations confirm the theoretical predictions concerning the E1 band, but no signature of the H1 band has been found. In the band gap, we have extracted an energy gap $\Delta = 30\,\mathrm{meV}$, which is in good agreement with the theoretical expectations. We have also demonstrated that at the lowest temperatures, the conduction is dominated by the contribution of the edges in the gap. This additional conduction is consistent with edge states in a diffusive regime, but the large size of the device compared to $\lambda = 2\,\mu\mathrm{m}$ does not allow to highlight the topological nature of these edge states. Nevertheless, compared to device HB0, a significant improvement in the reduction of the residual conductivity in the band gap suggests that S3052 is a promising QW structure to accommodate topological edge states.

In these investigations, we neglected the electrical anisotropy highlighted in Chapter 2. In the next section, we study devices fabricated from quantum wells grown on a GaSb substrate, where this anisotropy is small. Moreover, these devices are smaller in size, and can be considered in order to approach the ballistic regime of topological edge states.

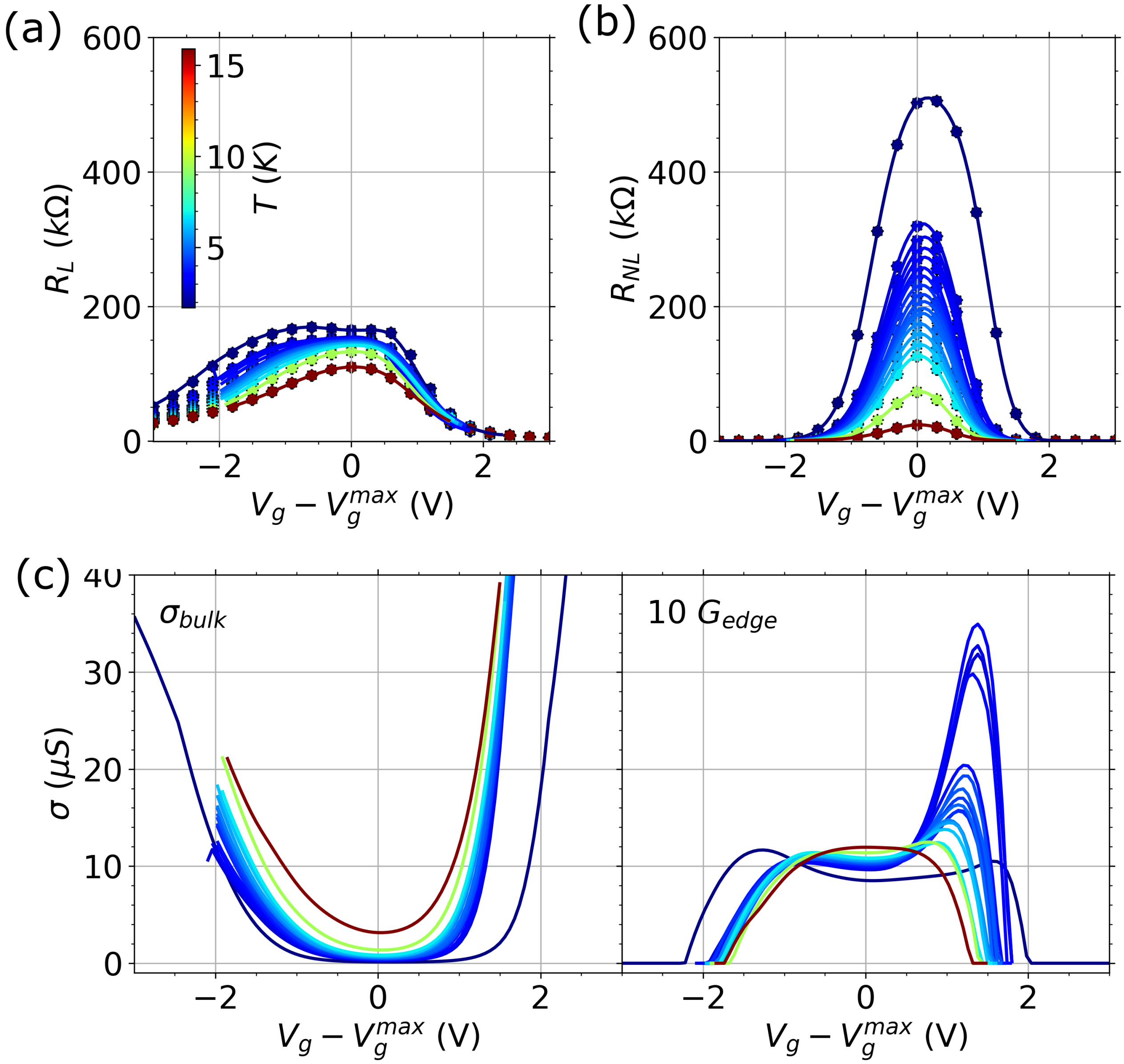

Figure 3.19: (a) Local resistance R_L and (b) non-local resistance R_{NL} as a function of V_g for different temperatures. In both panels, circle symbols correspond to the experimental data and the solid lines to the resistances calculated using the square lattice model. The gate voltage is rescaled to align the peak values of resistance on the position $V_g - V_g^{\max} = 0\,\mathrm{V}$. The same color scale corresponding to the temperature is used in panels (a,b,c) and is provided in panel (a). (c) Bulk conductivity σ_{bulk} (left panel) and edge conductance G_{edge} (right panel) as a function of V_g, for different temperatures. Both σ_{bulk} and G_{egde} are extracted from the square lattice model using a square network of dimensions $n_L, n_W, n_c = 81, 21, 24$ (this corresponds to the geometry of HB1). The edge conductance is multiplied by factor 10 in order to be compared to σ_{bulk} using the same y-scale.

3.3 Devices HB4, HB6, HB12 and HB14: (S3198)

We present in this section the experimental results obtained with a set of four Hall bar devices HB4, HB6, HB12 and HB14. All these devices have been already introduced in Chapter 2. The active part of the devices is a 25/10/25 monolayer-thick structure of InAs/GaInSb/InAs on a GaSb substrate. The band dispersion of the structure is shown in Chapter 2, and the expected energy gap is about 45 meV. Experimentally, the devices have been made from the same MBE growth S3198. As the devices are derived from the same growth and fabrication process, and differ only in the distance between the lateral contacts l_p, we group in this section the presentation of the experimental results obtained with these devices.

We stress that not all the following results were obtained during the same measurement campaigns. Notably, device HB14 was measured at the Laboratoire National des Champs Magnétiques Intenses (LNCMI) in Toulouse. This allowed us to measure this device under pulsed magnetic fields up to 55 T. We detail the results obtained on this device at the end of this chapter.

For these four devices, the carrier density modulation by the gate voltage is only transient with a characteristic time of approximately one minute. This behavior imposes to continuously sweep the gate voltage V_g. In the case of devices HB4, HB6 and HB12, the magneto-resistances were obtained following the same procedure as for device HB1. In the case of device HB14, during the 500 ms pulse duration, the variation of the gate voltage was $\delta V_g = 0.025\,\mathrm{V}$, so we assumed that the magneto-resistances were measured at a quasi-constant gate voltage.

Figure 3.20 shows the longitudinal resistivity at $B = 0\,\mathrm{T}$, named ρ_0, as a function of the gate voltage for devices HB4 and HB6. As for device HB1, a band gap is evidenced by the presence of a resistivity peak. We checked that this peak is associated with an inversion of the sign of the Hall effect.

The position $V_g^{\max}$ of the zero-field resistivity peak value $\rho_0^{\max}$ is not the same for the different devices, and is also very dependent of the parameters of the gate voltage sweep. Hence, for clarity, we often present in the following the gate voltage shifted by the position of the peak maxima $V_g^{\max}$.

3.3.1 Low magnetic field (single carrier model)

As for the previous devices HB0 and HB1, we start the analysis with a single carrier model. Figure. 3.21(a) shows the magnetic field dependence of the transverse resistivity of device HB6 at magnetic field B up to 12 T. In the region $V_g - V_g^{\max} > 1\,\mathrm{V}$, $B < 2\,\mathrm{T}$, the transverse resistivity increases linearly with respect to B. It evidences a single carrier transport. The same behavior is observed in the other devices. Near the band gap (*i.e.* $|V_g - V_g^{\max}| < 2\,\mathrm{V}$), the Hall effect is very disturbed and oscillates with respect to B as it can be seen at the bottom of panel 3.21(a). This is similar to what was observed in device HB1. Again, this effect is interpreted as due to the presence of both electron and hole puddles in the gap. In the valence band (VB), ρ_{xy} is bended below $B = 2\,\mathrm{T}$, evidencing the co-existence of different types of carriers. The magnetoresistances of the other devices are not presented here, but they are very similar to those of device HB6. The magnetoresistances of device HB14 are presented later (see Fig. 3.29).

Hall carrier density and Hall mobility for devices HB4, HB6 and HB14 are shown in Fig. 3.21(b,c). It is clear that these three devices are very similar. They have the same gate dependence, with respect to mobility and carrier density, and they have approximately the same mobility. The mobility for holes is not presented, because a model with only one carrier is not valid in the valence band.

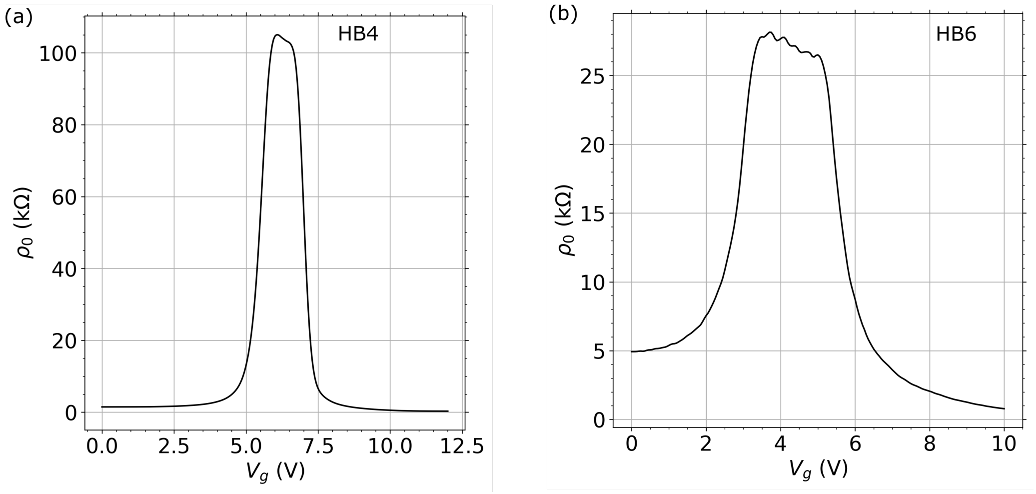

Figure 3.20: (a, b) Longitudinal resistivity ρ_0 as a function of gate voltage V_g from devices HB4 and HB6 respectively. Both measurements were performed in a He^3 insert at a temperature $T = 300\,\text{mK}$ and with a bias current $I = 10\,\text{nA}$.

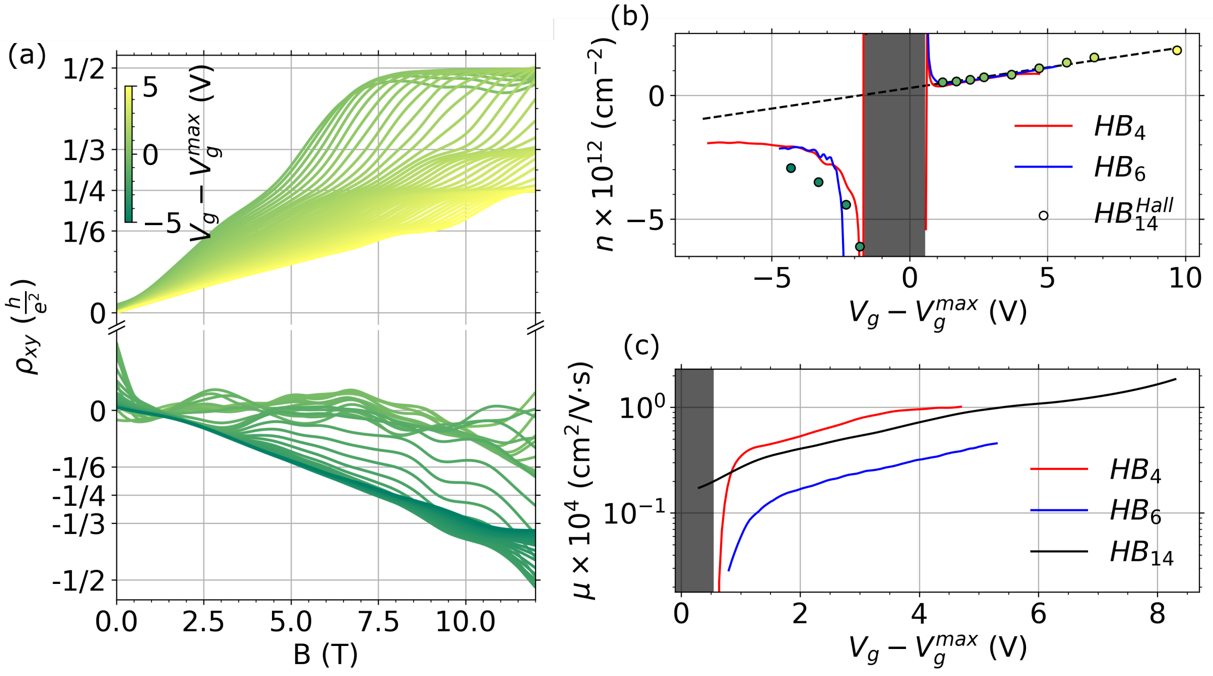

Figure 3.21: Carrier properties extracted from the single carrier model for device HB6. (a) Transverse resistivity ρ_{xy} of device HB6 as a function of magnetic field B for different gate voltages at $T = 300\,\text{mK}$. The color of the lines corresponds to the gate voltage and is provided in the upper left corner of the panel. (b) Hall carrier density n_H calculated from the Hall coefficient R_H as a function of the gate voltage V_g. R_H is defined as $\rho_{xy}(B = 1\,\text{T})$. The solid lines correspond to the concentration calculated from R_H for devices HB4 and HB6. Circle symbols correspond to the concentration extracted from the Hall coefficient for each magnetic pulse performed on HB14. The dashed line corresponds to the linear fit of the Hall concentration in HB14. Its slope corresponds to an effective gate voltage capacity $C_{\text{exp}} = 0.87 \times C_{th}$, where $C_{th} = 3 \times 10^2\,\mu\text{F}\,\text{m}^{-2}$, assuming a charge neutrality point $V_{\text{CNP}} = V_g^{\text{max}}$. The shadowed area corresponds to the band gap where the extracted Hall concentrations diverges. (c) Hall mobility μ_H extracted from the zero-field longitudinal resistivity ρ_0 and Hall concentration n_H as a function of gate voltage V_g. The gate voltage positions are restricted to the positive ones, corresponding to the conduction band. The data were measured at $T = 300\,\text{mK}$ with a bias current of $I = 10\,\text{nA}$ for devices HB4 and HB6. For device HB14, the measurements were done at $T = 1.7\,\text{K}$ and $I = 1\,\mu\text{A}$.

3.3.2 Activation energy

In this section, the magnitude of the energy gap is evaluated by thermal activation. Figure 3.22(a,b,c,d) shows the longitudinal resistivity peak $\rho_{xx}(V_g)$ in the vicinity of the gap for device HB4, HB6, HB12 and HB14 respectively. The measurements have been done at temperatures up to $T = 150\,\mathrm{K}$ for devices HB4 and HB6, and up to $T = 90\,\mathrm{K}$ only for devices HB12 and HB14. The maximum $\rho_{xx}^{\max}$ of the resistivity peak at $V_g = V_g^{\max}$ is extracted. It is shown as an inverse function of the temperature in Fig. 3.23 for the four Hall bar devices. The same temperature dependence is evidenced for all devices. When the temperature decreases from 80 K to 30 K, $\rho_{xx}^{\max}(T)$ increases exponentially. We attribute this exponential increase to thermal activation. Then, from $T = 30\,\mathrm{K}$ to 15 K, $\rho_{xx}^{\max}$ still increases a bit. Finally, at lower T, $\rho_{xx}^{\max}$ becomes constant. We attribute this last behavior to an additional edge conduction. We stress that devices HB12 and HB14 were not measured above $T = 90\,\mathrm{K}$, thus the extraction of the activation energy for these devices cannot be as precise as for devices HB4 and HB6.

The temperature evolution of $\rho_{xx}^{\max}$ is fitted by the same sum of three terms as for device HB1 in the previous section:

$$(\rho_{xx}^{\max})^{-1}(T) = \sigma_a(T) + \sigma_{\mathrm{loc}}(T) + \sigma_0, \tag{3.11}$$

where

$$\sigma_a(T) = \sigma_a^0 \exp\left(-\frac{\Delta}{2k_B T}\right)$$

is the thermal activation term,

$$\sigma_{\mathrm{loc}}(T) = \sigma_{\mathrm{loc}}^0 \exp\left(-\frac{\Delta_{\mathrm{loc}}}{k_B T}\right)$$

is the localization gap term induced by nearest neighbor hopping, and σ_0 is an additional term independent of temperature. The hopping term is introduced to get better fits around the transition from thermal activation to edge conduction. Without this term, the quality of the fits is significantly degraded. The five fit parameters are σ_0, σ_a^0, σ_{loc}^0, Δ, and Δ_{loc}.

The fits given by Eq. 3.11 are reported in Fig. 3.23. The fits for the four devices are all very good - hopefully, as we have five parameters. For device HB12, and only this device, the three terms of Eq. 3.11 are also reported separately by dashed lines in Fig 3.23. From these fits, we obtain energy gaps $\Delta = 35\,\mathrm{meV}$, $53\,\mathrm{meV}$, $36\,\mathrm{meV}$ and $39\,\mathrm{meV}$ for HB4, HB6, HB12 and HB14 respectively. These results give an average value $\Delta = (41 \pm 7)\,\mathrm{meV}$. The dispersion of Δ is due to the dispersion from device to device. We do not know the origin of this dispersion; possibly, strain relaxation could differ from one device to another. The most important result is that, as for device HB1, the measured energy gap matches the theoretical energy gap $\Delta_{th} = 45\,\mathrm{meV}$. Table 3.1 shows all the fitting parameters for the four devices.

	σ_a^0 (µS)	σ_{loc}^0 (µS)	σ_0 (µS)	Δ_{loc} (meV)	Δ (meV)
HB4	847	51	13	3.9	35
HB6	1725	59	46	5.0	53
HB12	642	11	21	1.6	36
HB14	771	19	15	3.6	39

Table 3.1: Fitting parameters for the four devices

Let us briefly comment what we can learn from the fitting of the hopping term. As for device HB1, we assume that $\Delta_{\mathrm{loc}} = (Da^2)^{-1}$, where D is the density of states inside the band gap,

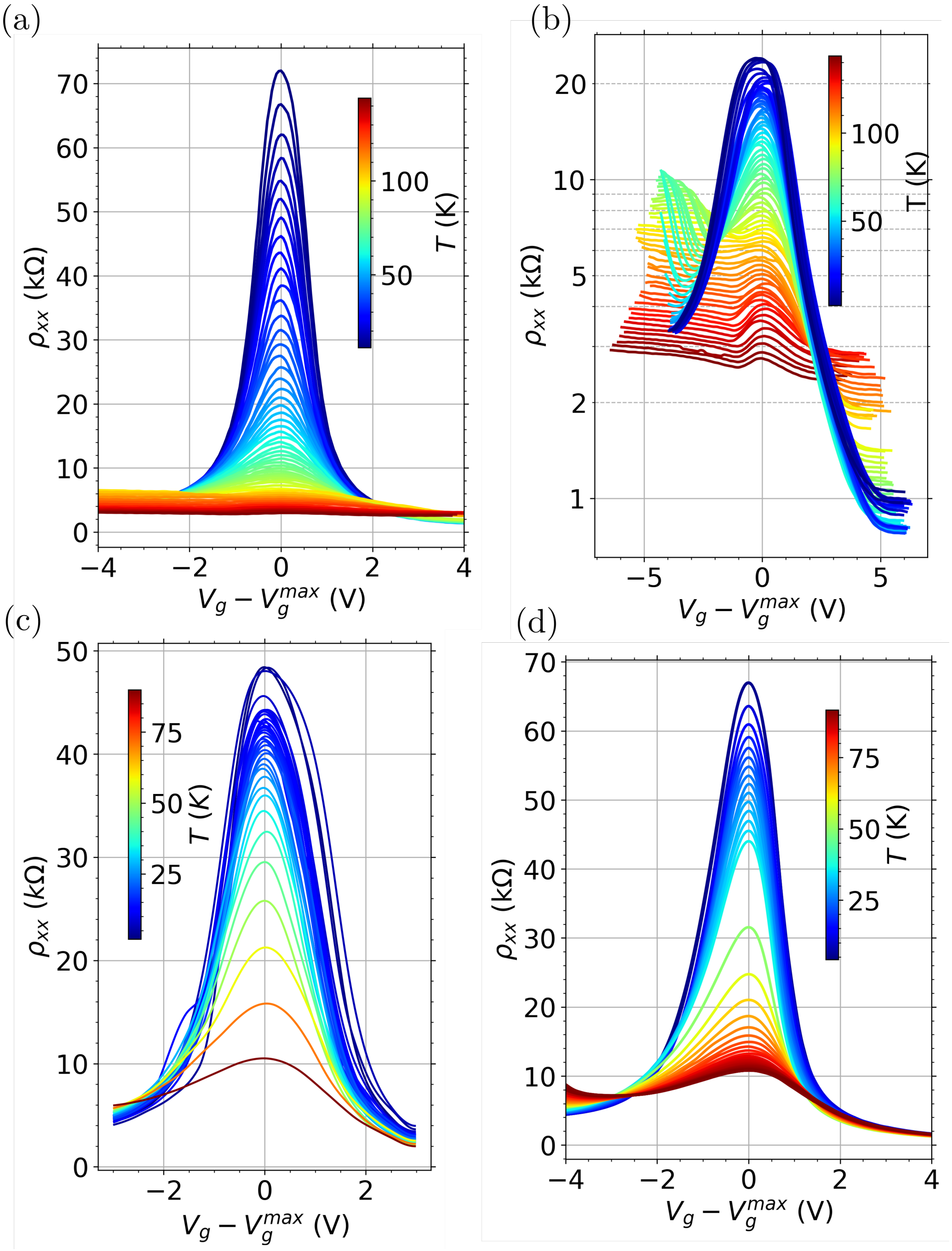

Figure 3.22: Longitudinal resistivity ρ_{xx} as a function of the gate voltage at different temperatures for devices HB4 (a), HB6 (b), HB12 (c) and HB14 (d). The color scales correspond to the temperature and is given for each device. The gate voltage is rescaled to be centered on the gate voltage position of the resistivity peak $V_g^{\max}(T)$.

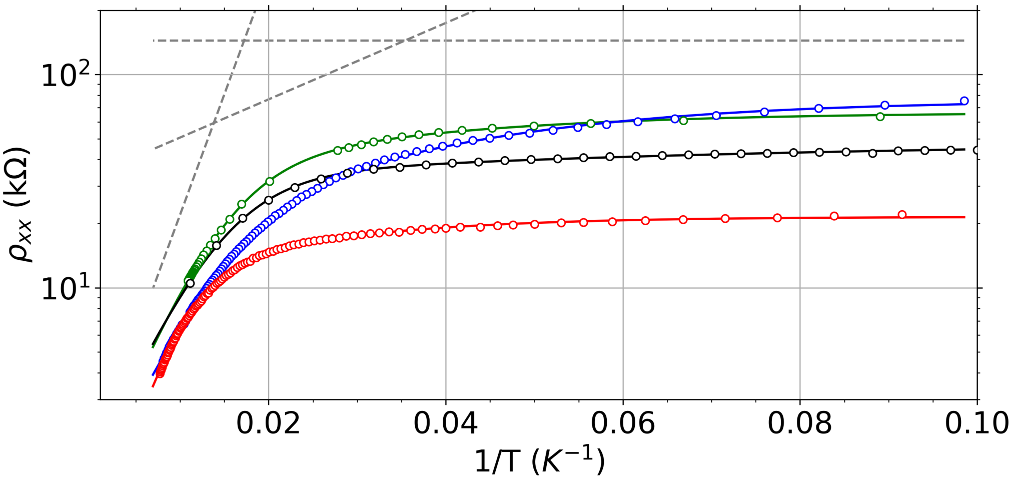

Figure 3.23: Extraction of the activation energy from the temperature dependence of the resistivity peak. The blue, red, black and green circles correspond to the experimental resistivity peak for devices HB4, HB6, HB12, HB14 respectively. The solid lines are the fits of the experimental data for the same four devices. For device HB12, the dashed lines also shows the 3 contributions to the total fit: $\rho_a^0 = 1/\sigma_a^0$, $\rho_{\mathrm{loc}}^0 = 1/\sigma_{\mathrm{loc}}^0$, and $\rho_0 = 1/\sigma^0$.

and a is the distance between the nearest hopping sites. From Section 3.3.1, we estimate that the gate voltage difference between the edges of valence and conduction bands is $\Delta V_g = 2\,\mathrm{V}$. We have:

$$D = \Delta V_g (C/e)/\Delta,$$

where $C = 0.3\,\mathrm{mF\,m^{-2}}$ is the capacitance per unit area of the gate, and $\Delta = 41\,\mathrm{meV}$ is the energy gap. We obtain $D = 8.8 \times 10^{12}\,\mathrm{eV\,cm^{-2}}$ and $a = (64 \pm 21)\,\mathrm{nm}$.These inter-site distances are rather large and correspond to a low density of hopping sites, $0.025 \times 10^{12}\,\mathrm{cm^{-2}}$. The same conclusion was obtained for device HB1. This suggests that the model of nearest neighbor hopping is not realistic. Variable range hopping could be a more adequate model, and gives also very good fits. In view of the data, as this additional, “hopping” term makes only a minor contribution to the overall fit, we cannot conclude.

3.3.3 Non-local measurements

Landauer-Büttiker model

We now investigate the transport properties in the band gap by local and non-local measurements. For the four different devices, the local and non-local resistances are defined as $R_L = R_{14,23} = V_{23}/I_{14}$ and $R_{NL} = R_{26,35} = V_{35}/I_{26}$. The numbering of contacts and the equivalent resistor network for a Hall bar device is provided in Chapter 1. Recall that contact 1 is one end of the Hall bar. From this end, the contacts are then indexed clockwise. Figure 3.24(a,b) shows both local R_L and non-local R_{NL} configurations around in the band gap for the four Hall bar devices, as a function of the gate voltage, at the temperature $T = 300\,\mathrm{mK}$.

First, the experimental non-local resistances are compared to the expected non-local resistance R_{NL}^{Ohmic} of an homogeneous device (*i.e.* without edge conduction) defined by the formula which we already used:

$$R_{NL}^{\mathrm{Ohmic}} = \frac{4}{\pi} R_L \frac{W}{l_p} \exp\left(-\pi \frac{l_p}{W}\right),$$

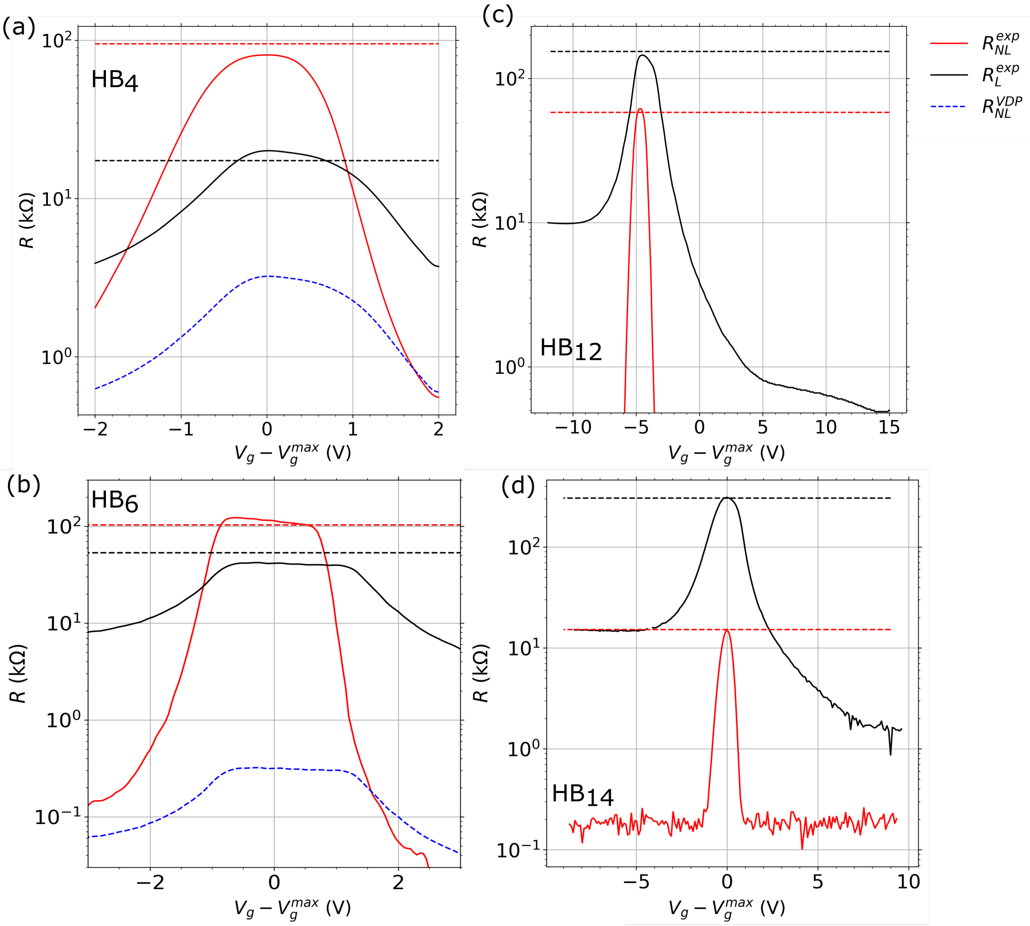

Figure 3.24: (a,b,c,d) Non-local (red solid line) and local (black solid line) resistances as a function of the gate voltage at $T = 300\,\mathrm{mK}$ for devices HB4, HB6, HB12, and HB14 respectively. The blue dashed lines in panels (a,b) panels correspond to the non-local resistance calculated from the local data for a device of homogeneous resistivity. Note that in the (c, d) panels, the non-local resistance calculated from the local data is not represented as its magnitude is negligible compared to both local and non-local resistances. The dotted lines correspond to the expected value of peak resistance for local and non-local configurations for diffusive edge state with an equilibration length $\lambda = 12\,\mu\mathrm{m},\ 7\,\mu\mathrm{m},\ 5\,\mu\mathrm{m}$ and $3\,\mu\mathrm{m}$ for devices HB4, HB6, HB12, HB14 respectively.

where W and l_p are the width of the Hall bar and the distance between the lateral contacts respectively.

For devices HB12 and HB14, the geometric ratio are $W/l_p \approx 1/3$ and $1/4$ respectively. Hence, the expected magnitudes for the ohmic non-local resistance R_{NL}^{Ohmic} are 10^5 and 10^6 times smaller than the local resistances R_L. From Fig. 3.24(c,d), it is clear that the experimental non-local resistances for devices HB12 and HB14 are several orders of magnitude higher than R_{NL}^{Ohmic} in the gap. This ohmic model completely fails. Note that for HB12 and HB14 devices, in both valence and conduction bands, the non-local resistance could not be measured; It dropped below the sensitivity of the lock-in in the former case and saturated due to the offset DC of the voltmeter in the latter case. This model also fails for devices HB4 and HB6, as shown in Fig. 3.24(a,b), where R_{NL}^{Ohmic} is indicated and again appears to be much lower than R_{NL}.

We assume now that the non-local peak is due to edge conduction and we fit R_L and R_{NL} in the band gap as

$$R_L = \frac{h}{e^2}\frac{1}{\lambda}\frac{l_p}{2}, \tag{3.12}$$

and

$$R_{NL} = \frac{h}{e^2}\frac{1}{\lambda}\frac{(2l_1)^2}{(4l_1 + 2l_p)}, \tag{3.13}$$

where λ is the length at which counter propagating edge channels equilibrate. In Fig. 3.24 we show the resistances calculated with the λ values obtained for each device, considering $l_p = 10\,\mu\text{m}$, $30\,\mu\text{m}$, $50\,\mu\text{m}$ and $70\,\mu\text{m}$ and $l_1 = 40\,\mu\text{m}$, $30\,\mu\text{m}$, $20\,\mu\text{m}$ and $10\,\mu\text{m}$ respectively. We obtain $\lambda = 12\,\mu\text{m}$, $7\,\mu\text{m}$, $5\,\mu\text{m}$ and $3\,\mu\text{m}$ for devices HB4, HB6, HB12, HB14 respectively. This gives an average value $\lambda = (6.8 \pm 3.3)\,\mu\text{m}$. Note that in the case of the HB4 device, λ slightly exceeds l_p, thus this result is inconsistent with a diffusive regime of topological edge state. We argue in what follows that this inconsistency is not due to parasitic trivial edge channels, and that it can be explained by taking into accound the residual bulk conduction in the gap.

Square lattice model

We investigated further the bulk and edge contributions to the conduction in the band gap using the square lattice model detailed in Chapter 2. The dimensions of the networks of resistors used to model the HB devices are provided in Table 3.2. In Fig. 3.25, we show the experimental local and non-local resistances at respectively $T = 300\,\text{mK}$ and $T = 2.0\,\text{K}$ for devices HB6 and HB14. In panels (a,c), it is clear that the square lattice model precisely fits the experimental data for all gate voltage values. In panels (b,d), we show both bulk conductivity σ_{bulk} and edge conductance G_{edge} obtained from the square lattice fit. We recall that G_{edge} is the conductivity of one edge, σ_{edge}, in meter per Ohm, divided by the distance between the lateral probes, l_p. Therefore, σ_{bulk} and G_{edge} are in the same units (in Siemens) and can be directly compared.

Table 3.2: Hall bar dimensions for the Hall bar devices and for the associated resistor network.

	L (µm)	W (µm)	l_p (µm)	l_1(µm)	mesh size (µm)	n_L	n_W	n_C
HB4	110	20	10	40	0.5	221	41	99
HB6	110	20	30	30	0.5	221	41	79
HB12	110	20	50	20	0.55	199	37	53
HB14	110	20	70	10	0.55	199	37	26

In the middle of the band gap (*i.e.* close to $V_g - V_g^{\max} = 0\,\text{V}$, a significant reduction of the bulk contribution compared to band gap edges is observed. For device HB6, we get $\sigma_{\text{bulk}} \simeq 2\,\mu\text{S}$ and $G_{\text{edge}} \simeq 15\,\mu\text{S}$. For device HB14, we get $\sigma_{\text{bulk}} \simeq 0.5\,\mu\text{S}$ and $G_{\text{edge}} \simeq 6.5\,\mu\text{S}$.

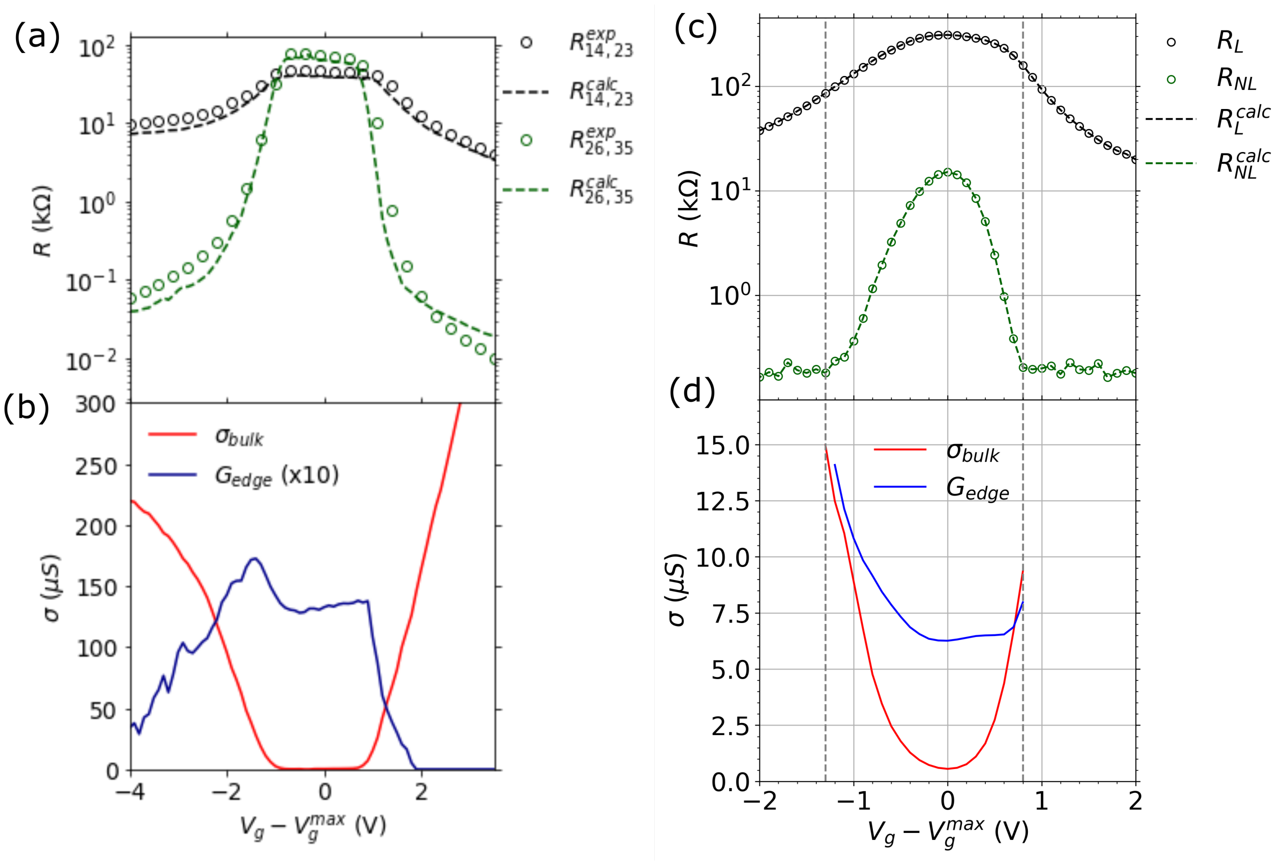

Figure 3.25: (a,c) Local resistance R_L and non-local resistance R_{NL} as a function of the gate voltage at respectively $T = 300\,\mathrm{mK}$ and $T = 2\,\mathrm{K}$ for the devices HB6 and HB14. In both panels, the circles correspond to experimental data and the dashed lines to the resistances calculated using the square lattice model. The gate voltage is rescaled to align the peak values of resistance on the position $V_g - V_g^{\mathrm{max}} = 0\,\mathrm{V}$. (b,d) Bulk conductivity σ_{bulk} and edge conductance G_{edge} as a function of the gate voltage for HB6 and HB14. Both σ_{bulk} and G_{edge} are extracted from the square network of dimensions given in Table 3.2. In panel (d), σ_{bulk} and G_{edge} are displayed only for a reduced gate voltage range indicated by vertical dashed lines. Outside this range the experimental R_{NL} is erroneous (lock-in offset).

For HB6, in the valence and conduction bands ($|V_g - V_g^{\mathrm{max}}| \geq 2\,\mathrm{V}$) the edge conductance is shunted by the dominating bulk conductivity σ_{bulk}. More precisely, $G_{\mathrm{edge}} = 0$ in the conduction band, and becomes small in the valence bands. In facts, a close inspection of Fig. 3.25(a) reveals that the fit of the non-local resistance is not perfect in the valence and conduction bands. We attribute this behavior to small differences between the actual geometry of the device, and the geometry used in the square lattice model. Indeed, the device is modeled by a perfect rectangle, with point-contact lateral probes.

For HB14, the situation is different. We cannot evaluate G_{edge} in the bands, because R_{NL} was not measured correctly in these regions. Therefore, Fig. 3.25(d) shows G_{edge} and σ_{bulk} in the band gap only.

Square lattice model: temperature

The local and the non-local resistances have been measured at a function of temperature for devices HB4 and HB6. Figure 3.26(a,b) shows the experimental R_N, R_{NL} as solid lines for device HB4. The temperature evolution of both resistances is striking. At low T, R_{NL} is much larger than R_N in the gap. When the temperature increases, both resistivity peaks decrease,

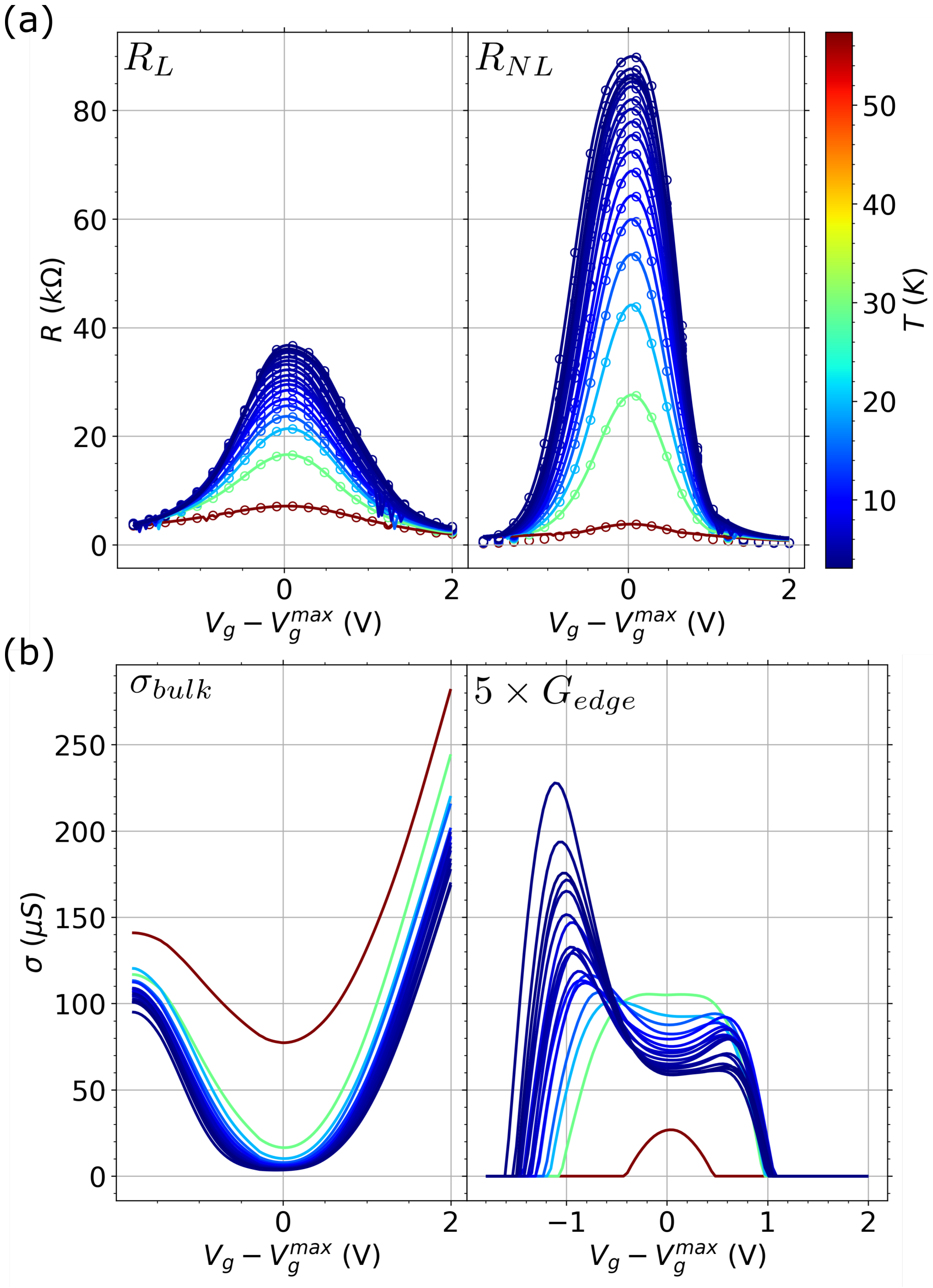

Figure 3.26: (a) Local resistance R_L and (b) non-local resistance R_{NL} as a function of the gate voltage at different temperatures for device HB4. In both panels, open circles correspond to the experimental data and the solid lines to the resistances calculated using the square lattice model. The gate voltage is rescaled to align the peak values of resistance on the position $V_g - V_g^{\max} = 0\,\mathrm{V}$. The same color scale corresponding to the temperature is used in panels (a,b,c) and is provided in panel (a). (c) Bulk conductivity σ_{bulk} (left panel) and edge conductance $5 \times G_{\text{edge}}$ (right panel) as a function of the gate voltage, for different temperatures. Both σ_{bulk} and G_{edge} are extracted from the square network whose dimensions are given in Table 3.2.

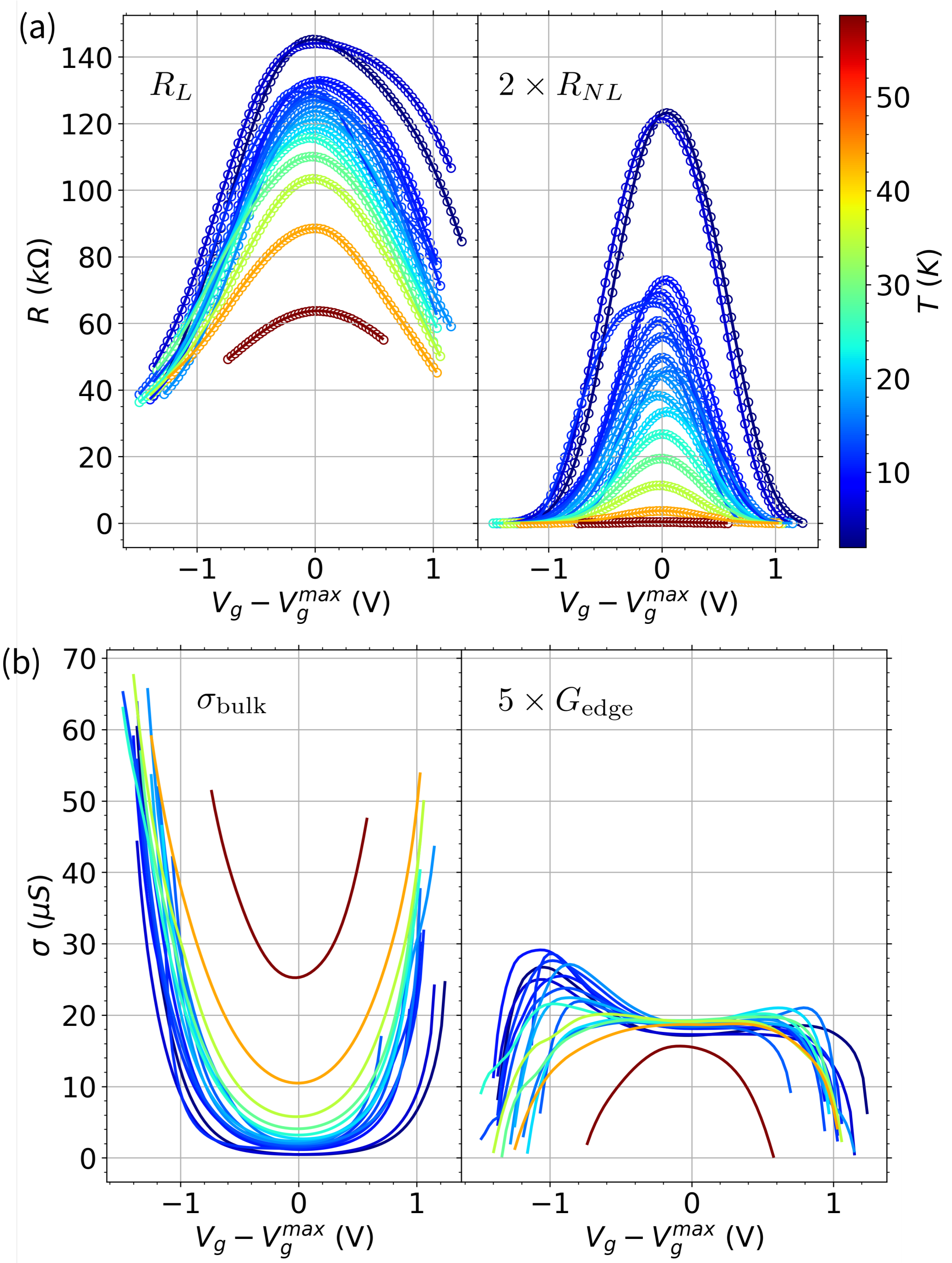

Figure 3.27: (a) Local resistance R_L and (b) non-local resistance $2 \times R_{NL}$ as a function of the gate voltage at different temperatures for the HB12 device. In both panels, circle symbols correspond to the experimental data and the solid lines to the resistances calculated using the square lattice model. The gate voltage is rescaled to align the peak values of resistance on the position $V_g - V_g^{\rm max} = 0\,{\rm V}$. The same colorscale corresponding to the temperature is used in panels (a,b,c) and is provided in panel (a). (c) Bulk conductivity $\sigma_{\rm bulk}$ (left panel) and edge conductance $5 \times G_{\rm edge}$ (right panel) as a function of the gate voltage, for different temperatures. Both $\sigma_{\rm bulk}$ and $G_{\rm edge}$ are extracted from the square lattice network whose dimensions are given in Table 3.2.

but the R_{NL} peak decreases faster. At $T = 50\,\mathrm{K}$, R_{NL} is smaller than R_N, for all gate voltages.

In the same panels, the results of the square lattice fit are also indicated with open circles. Again, this model fits quite perfectly the data. Fig. 3.26(c,d) shows σ_{bulk} and G_{edge}, as extracted from these fits. It appears that on the studied gate voltage range, σ_{bulk} is always insulating, as it increases with temperature. This indicates that the band edges have not been reached yet - this is confirmed by the direct analysis of the R_L data in Fig. 3.26(a). The edge conductance G_{edge} is non-zero in the gap only. There, it has a weak temperature dependence, suggesting a unexpected insulating behavior. There are two prominent peaks at the two edges of the band gap. These peaks are almost systematically observed for all devices. We have no definitive explanation for the origin of these peaks.

Finally, as for HB4 in Fig. 3.26, Fig. 3.27 shows the R_N and R_{NL} peaks for device HB12, and their analysis with the square lattice model. The edge of the valence band is well visible here, as there is a crossover from insulating to metallic behavior in both R_L and σ_{bulk} around $V_g - V_g^{\mathrm{max}} \simeq -1.5\,\mathrm{V}$. The fits have been done on a reduced range of gate voltages and focus on the band gap.

Figure 3.28(a) resumes the temperature dependence of σ_{bulk} and G_{edge} for both devices HB4 and HB12. The temperature dependence has been taken from the maximum of the resistivity peak, at $V_g = V_g^{\mathrm{max}}$. Some remarkable properties can be listed:

1. the temperature dependence of G_{edge} corresponds to a weak (HB4) or a very weak (HB12) insulating behavior. This seems to contradict the expectation that the edge states (at least if topological) should have a metallic behavior;

2. the edge conduction dominates over the bulk conduction up to $T \simeq 30\,\mathrm{K}$. Above this temperature, we observe a sudden collapse of G_{edge} that is probably an artifact of the numerical model;

3. σ_{bulk} has the expected temperature dependence (thermal activation) at high T. However, at low T, the temperature dependence of σ_{bulk} is much weaker. This could be a signature of variable range hopping. This point would deserve more attention, as the residual bulk conductivity is a problem in QSHI in general;

4. both devices have the same qualitative behavior. However, the overall conductivity of device HB12 is much smaller. There is no reason for this difference as both devices are from the same MBE growth, and the same lithography process.

Finally, Figure 3.28(b) summarizes the values of $(G_{\mathrm{edge}}, \sigma_{\mathrm{bulk}})$ at $V_g = V_g^{\mathrm{max}}$ for the four devices HB4, HB6, HB12 and HB14. The solid black line corresponds to the equation $\sigma_{\mathrm{bulk}} = G_{\mathrm{edge}}$. Above this line, the conduction is therefore dominated by the bulk conductivity. The vertical dashed line corresponds to $G_{\mathrm{edge}} = e^2/h$. This line corresponds to the case of perfect ballistic conduction. On the right side of this line the edge conduction is larger than the quantum of the conductance, and the edge conductance must have an additional parasitic component. On the left side of the same line, purely topological and ballistic edge conduction is possible. The main region of interest is the one painted in green, where purely topological edge conduction is possible, dominating the residual volume conductivity. It appears that at low temperatures, all four devices fall within this region of interest. When T increases, as shown by the temperature evolution of BH4 and HB12, the global conductivity increases and finally surpasses the contribution of the edge.

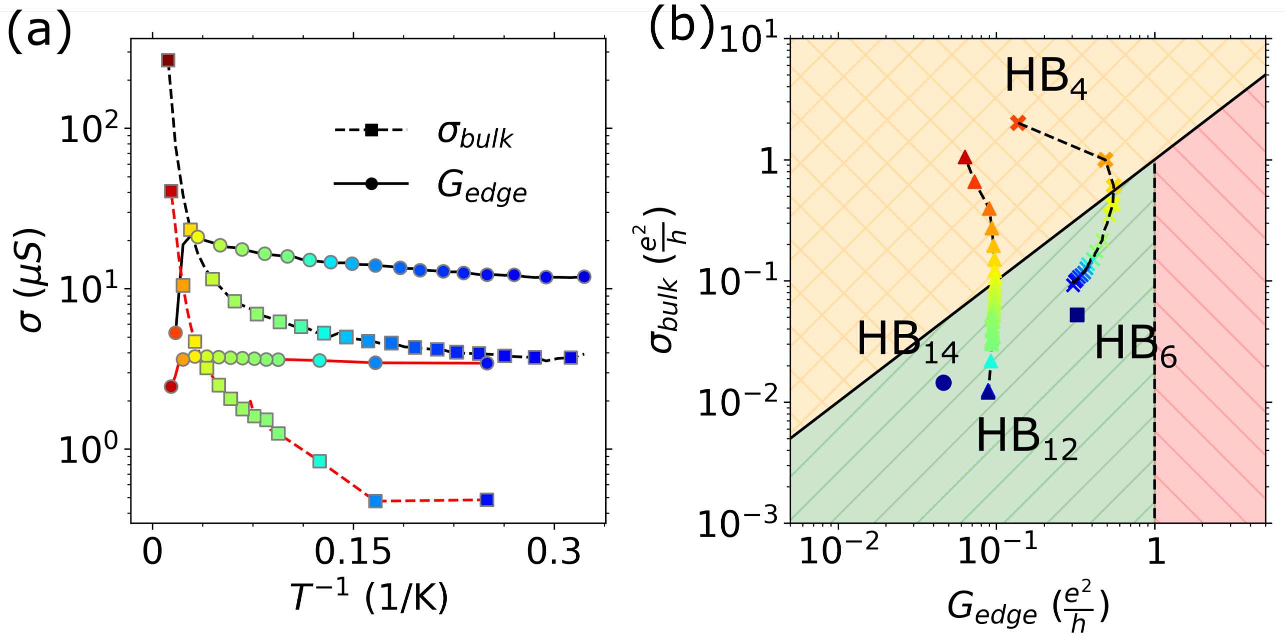

Figure 3.28: (a) Bulk conductivity $\sigma_{\rm bulk}$ and edge conductance $G_{\rm edge}$ as an inverse function of T at $V_g = V_g^{\rm max}$ for devices HB4 and HB12. The squares correspond to $\sigma_{\rm bulk}$ and the circles to $G_{\rm edge}$. The color of these symbols corresponds to the temperature. Distinction is made between the two devices by the color of both dashed and solid lines. The black lines correspond to device HB4, and the red lines to device HB6. (b) $G_{\rm edge}$ and $\sigma_{\rm bulk}$ for HB4 (cross), HB6 (square), HB12 (triangle) and HB14 (circle), at $V_g = V_g^{\rm max}$. The solid black line corresponds to the equation $\sigma_{\rm bulk} = G_{\rm edge}$ and the vertical dashed line to $G_{\rm edge} = \frac{e^2}{h}$ (ballistic edge conduction). Red region: additional parasitic edge conductivity is present. Green dashed region: diffusive edge conduction can be at play. The temperature dependence of $(G_{\rm edge}, \sigma_{\rm bulk})$ is indicated for HB4 and HB12 (up to $T = 57\,\mathrm{K}$) with the same color scale as in panel (a). The positions of HB6 and HB14 correspond to $T = 0.3\,\mathrm{K}$ and $2\,\mathrm{K}$ respectively.

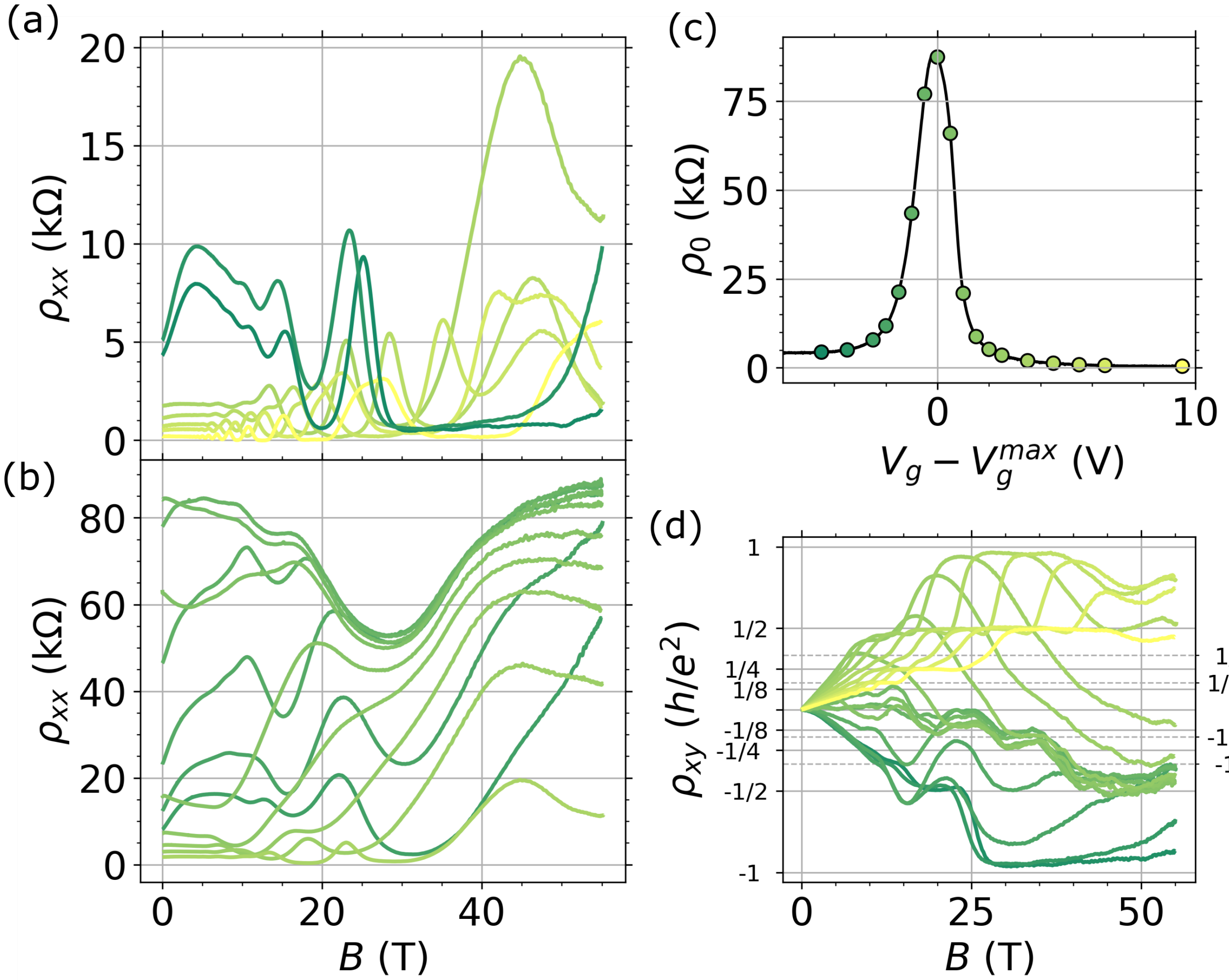

Figure 3.29: (a,b) Longitudinal resistivity ρ_{xx} of device HB14 as a function of B in the range 0 T to 55 T for a reduced selection of gate voltages highlighted in panel (c). (c) Gate voltage dependence of the zero-field longitudinal resistivity ρ_0. The black solid line corresponds to the experimental data and the symbols correspond to the specific values of gate voltage corresponding to the magnetic field dependence in (a,b,d) panels. (d) Transverse resistivity ρ_{xy} as a function of B for different V_g. The color of the lines corresponds to the gate voltage and is identical in panels (a,b,c,d). The measurements were done at $T = 1.7\,\text{K}$ with a bias current $I = 1\,\mu\text{A}$.

3.3.4 Device HB14 at very high magnetic fields

Because device HB14 was measured in pulsed magnetic field, it deserves a special attention and a dedicated section. Figure 3.29 shows the gate voltage and magnetic field dependencies of the longitudinal and transverse resistivities (ρ_{xx} and ρ_{xy}) for this device. Figure 3.29(a,b) shows the longitudinal resistivity ρ_{xx} for different gate voltages, and Figure 3.29(d) shows the transverse resistivity ρ_{xy}. SdH oscillations are clearly observed in ρ_{xx}, as well as quantized Hall plateaus in ρ_{xy}.The ambipolarity is clearly observed, and Fig. 3.29(c) also shows $\rho_0(V_g)$, which is the longitudinal resistivity at $B = 0\,\mathrm{T}$. There is an evident resistivity peak in the gap.

For clarity, the ρ_{xx} curves have been separated into two parts. Figure 3.29(a) shows ρ_{xx} when the Fermi level lies in the valence or conduction band. Note that the colors of the solid lines refer to the gate voltage positions and are provided by the color of the circle symbols in Fig. 3.29(c). In the conduction band, ρ_{xx} is almost constant at low B, as expected if only one carrier is present. By contrast, in the valence band, ρ_{xx} exhibits a strong positive magnetoresistance at low fields ($B < 5\,\mathrm{T}$), which we attribute to the coexistence of two carriers. This is in agreement with the curvature of the $\rho_{xy}(B)$ curve observed on the hole side, see Fig. 3.29(d). All these phenomena were already observed previously, see *e.g.* Fig. 3.21.

Fig. 3.29(b) only shows ρ_{xx} when the Fermi level is in the gap or close to the gap. The situation is quite remarkable here: a large resistivity dip persists, whatever the gate voltage. It culminates around $V_g \simeq 0\,\mathrm{V}$, at $B \simeq 30\,\mathrm{T}$, $\rho_{xx} \simeq 50\,\mathrm{k}\Omega$. Some additional oscillations are visible, that are quite similar to SdH oscillations. In the following, we will try to determine if this dip can be a signature of topological effects.

SdH regime

Let us first analyze shortly the SdH oscillations that are visible in device HB14, far from the gap. Figure 3.30 shows the longitudinal resistivity ρ_{xx} and the absolute value of its first derivative $|\partial\rho_{xx}/\partial B|$ as a function of the inverse magnetic field for several gates voltages. In Fig. 3.30(b), we report the extracted Landau level positions for the different gate voltages and calculate the related carrier concentration, as we did before for device HB1. The corresponding Landau levels indexes are extracted from the transverse resistivity quantized values $\rho_{xy} = e^2/\nu h$ at the same (B, V_g) coordinate in Fig. 3.29.

Figure 3.30(c) shows the carrier density extracted from both Hall effect (n_H) and SdH oscillations (n_{SdH}). Let us first consider the conduction band. As for device HB1, the good agreement between n_H and n_{SdH} indicates that there is only one kind of carrier. The situation is different in the valence band. The carrier density n_{SdH} is quite close to what is expected, with the correct slope. Therefore, we can determine that n_{SdH} is related to holes. The Hall concentration is obviously wrong. There must be another kind of carriers, probably electron-like, to compensate for the too high value of $|n_{\mathrm{SdH}}|$.

We believe that the presence of two different carriers in the valence band is an indirect signature of the inverted gap. If this is true, a high magnetic field analysis can bring us another critical hint. Indeed, at some magnetic field, one expect the crossing of the zero mode LLs.

Model of conductance

We are now in position to estimate the conductivity as a function of gate voltage and magnetic field. As shown in Chapter 2, we have already calculated the LL dispersion by the $k \cdot p$ method up to 25 T. As the $k \cdot p$ calculation is quite cumbersome, we fit the $k \cdot p$ result by the simpler BHZ model. Within the representation defined by the basis states $|E1, +i\rangle$, $|H1, +i\rangle$, $|E1, -i\rangle$

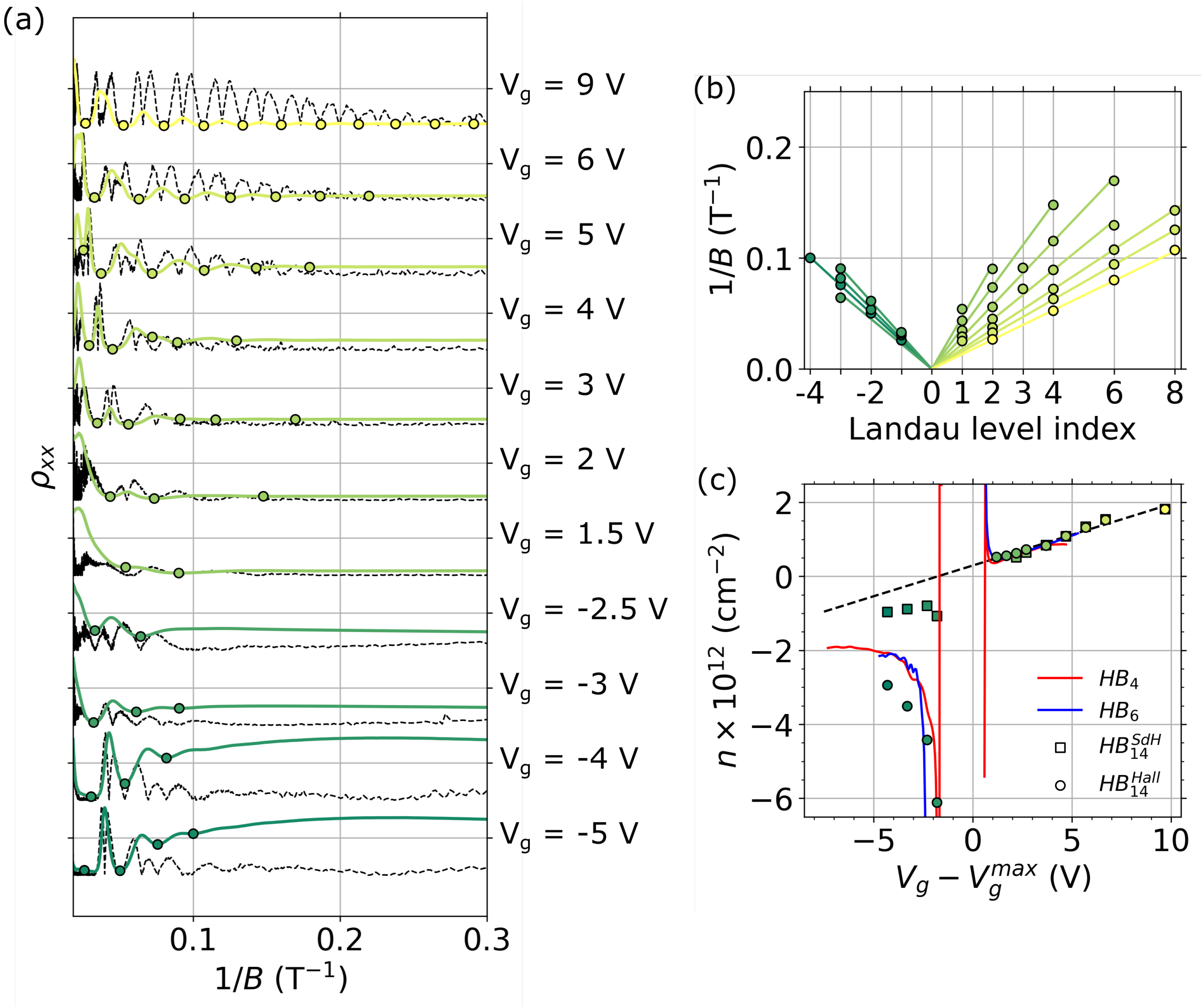

Figure 3.30: Carrier density extraction from SdH oscillations analysis for HB14. (a) Normalized longitudinal resistivity ρ_{xx} (coloured solid lines) and the absolute value of it first derivative $\frac{\partial \rho_{xx}}{\partial B}$ (black dashed lines) as a function magnetic field for different gate voltages. The colored solid lines correspond to ρ_{xx} and the superposed dashed lines to the derivative. The circle symbols correspond to the extracted minima. The gate voltage values are provided on the sides of panel (a). We use the same color code to represent the gate voltage in the whole figure . (b) Position of the SdH minima $1/B$ as a function of the Landau level index for different gate voltages. Landau level indexes are determined by the quantized value of the Hall plateaus observed in the transverse resistivity ρ_{xy}. Circle symbols correspond to the extraction made from panel (a). Solid lines are the corresponding linear fits. The slope of the different fits is extracted to calculate the corresponding SdH concentrations. (c) Carrier concentrations n as a function of gate voltage V_g extracted from the experimental data. The black dashed line corresponds to the linear evolution of the concentration calculated from R_H. Circle symbols correspond to the concentrations extracted from the Hall effect and square symbols correspond to the SdH oscillations analysis. All extractions are made from magneto-transport measurements performed at $T = 1.7$ K with a bias current of $I = 1$ µA.

$|H1,-i\rangle$, the effective 2D Hamiltonian has the form:

$$H_{2D}(\mathbf{k}) = \begin{pmatrix} H_{\mathrm{BHZ}}(\mathbf{k}) & 0 \\ 0 & H^{*}_{\mathrm{BHZ}}(-\mathbf{k}) \end{pmatrix}, \tag{3.14}$$

where asterisk stands for complex conjugation, $\mathbf{k} = (k_x, k_y)$ is the momentum in the QW plane, and H_{BHZ} is the 2×2 BHZ Hamiltonian defined in the introduction. To calculate LLs in the presence of an external magnetic field B oriented perpendicular to the QW plane, one should make the Peierls substitution. Additionally, we add the Zeeman term in the Hamiltonian

$$H_Z = \frac{1}{2}\mu_B B \begin{pmatrix} g_e & 0 & 0 & 0 \\ 0 & g_h & 0 & 0 \\ 0 & 0 & -g_e & 0 \\ 0 & 0 & 0 & -g_h \end{pmatrix}, \tag{3.15}$$

where $\mu_B B$ is the Bohr magneton, g_e and g_h are the effective (out-of-plane) g-factors of the $E1$ and $H1$ subbands, respectively. Solving the eigenvalue problem, the LL dispersion in the BHZ model is given by:

$$E_n^{(+)} = \mathcal{C} - \frac{2\mathcal{D}n + \mathcal{B}}{a_B^2} + \frac{g_e + g_h}{4}\mu_B B \pm \sqrt{\frac{2n\mathcal{A}^2}{a_B^2} + \left(\mathcal{M} - \frac{2\mathcal{B}n + \mathcal{D}}{a_B^2} + \frac{g_e - g_h}{4}\mu_B B\right)^2} \quad \text{for } n > 0, \tag{3.16}$$

$$E_0^{(+)} = \mathcal{C} + \mathcal{M} - \frac{\mathcal{D} + \mathcal{B}}{a_B^2} + \frac{g_e}{2}\mu_B B \qquad \text{for } n = 0, \tag{3.17}$$

$$E_n^{(-)} = \mathcal{C} - \frac{2\mathcal{D}n - \mathcal{B}}{a_B^2} - \frac{g_e + g_h}{4}\mu_B B \pm \sqrt{\frac{2n\mathcal{A}^2}{a_B^2} + \left(\mathcal{M} - \frac{2\mathcal{B}n + \mathcal{D}}{a_B^2} - \frac{g_e - g_h}{4}\mu_B B\right)^2} \quad \text{for } n > 0 \tag{3.18}$$

$$E_0^{(-)} = \mathcal{C} - \mathcal{M} - \frac{\mathcal{D} - \mathcal{B}}{a_B^2} - \frac{g_h}{2}\mu_B B \qquad \text{for } n = 0, \tag{3.19}$$

where B is the magnetic field, n is the index of the Landau level, $(+)/(-)$ designates the upper/lower block of the H_{2D} Hamiltonian, and $\mathcal{A}$, $\mathcal{B}$, $\mathcal{C}$, $\mathcal{D}$,$\mathcal{M}$ are the BHZ parameters that are to be adjusted, so that the dispersion of the BHZ LLs fit with those calculated by the $k \cdot p$ method. We can get a reasonable fit with the parameters $\mathcal{A} = 2.3\,\mathrm{eV\,Å}$, $\mathcal{B} = -40\,\mathrm{eV\,Å}^2$, $\mathcal{C} = -0.035\,\mathrm{eV}$, $\mathcal{D} = -18\,\mathrm{eV\,Å}^2$, $\mathcal{M} = -0.022\,\mathrm{eV}$, $g_e = 0.5$ and $g_h = 15$. However, of course, the critical magnetic field B_c at which the zero-mode LLs cross is still $B_c \simeq 17\,\mathrm{T}$, as given by the $k \cdot p$ method.

If we assume that the dip at $B = 27\,\mathrm{T}$ corresponds to the crossing of the zero-mode LLs, then, we have to dilate the magnetic field, as $B \to 1.6B$. How to justify such a renormalization? In both type I and type II quantum wells, it has been found that short-range disorder increases the characteristic field B_c [PHM+14]. However, this is a consequence of the same mechanism that operates in topological Anderson insulators: a disorder-induced renormalization of the band gap. Since it seems that the theoretical band gap (without disorder) corresponds to the experimental one, one cannot simply justify an increase of B_c by short range disorder. This kind of disorder should also increase the energy gap. We speculate, however, that long-range disorder may affect the energy gap and B_c differently, because typically such disorder should leave the energy gap at $k = 0$ unmodified, while the band dispersion (and thus the LL dispersion, following the Onsager semi-classical quantization approach) should be affected. We extracted both Hall mobility and quantum mobility from device HB14. The quantum mobility is defined by the quantum time τ_q, extracted from the damping of the SdH oscillations:

$\mu_q = e\tau_q/m^*$. We obtained $\mu = 5\,\mathrm{m^2\,V^{-1}\,s^{-1}}$, $7.5\,\mathrm{m^2\,V^{-1}\,s^{-1}}$, $9\,\mathrm{m^2\,V^{-1}\,s^{-1}}$ and $20\,\mathrm{m^2\,V^{-1}\,s^{-1}}$ (see Fig. 3.21), and $\mu_q = 0.8\,\mathrm{m^2\,V^{-1}\,s^{-1}}$, $1.1\,\mathrm{m^2\,V^{-1}\,s^{-1}}$, $1.2\,\mathrm{m^2\,V^{-1}\,s^{-1}}$ and $1.5\,\mathrm{m^2\,V^{-1}\,s^{-1}}$ at $V_g = 3\,\mathrm{V}$, $5\,\mathrm{V}$, $6\,\mathrm{V}$ and $9\,\mathrm{V}$ respectively. This yields $\mu/\mu_q \simeq 5$–15, in the conduction band. Therefore, the disorder is long-range, and our hypothesis is plausible. Of course, we still lack a more quantitative analysis to validate this model. For now, we simply assume that we can somehow justify the magnetic field expansion, and our last task is to mimic the overall behavior of the magnetoresistance.

Without disorder, the density of states D_{2D} is a sum of δ-functions centered on the energy E_N of the LLs:

$$D_{2D}(E) = \frac{eB}{h}\sum_N \delta(E - E_N), \tag{3.20}$$

where e is the elementary charge, h is the Planck constant, N is a global index over the LLs $E^{(+)}$, $E^{(-)}$, $E_0^{(+)}$, $E_0^{(-)}$. The factor eB/h is the degeneracy of each Landau level. Because of the finite value of τ_q, each LL is in fact broadened. We have chosen arbitrarily a Gaussian broadening of width at half maximum Γ, related to the mean time of diffusion of the carriers by $\Gamma = \hbar/\tau_q$. The density of state becomes:

$$D_{2D}(E) = \frac{eB}{h}\sum_N A(E - E_N), \tag{3.21}$$

$$A(E) = \frac{1}{\sqrt{2\pi}\Gamma}\exp\left(\frac{E^2}{2\Gamma^2}\right). \tag{3.22}$$

The density of states thus presents peaks, which are at the origin of the Shubnikov–de Haas oscillations. It is now necessary to fill the Landau levels with holes or electrons. The filling factor is given by the formula below:

$$\nu(E) = \frac{h}{eB}\int_{-\infty}^{E} D_{2D}(E)dE = \frac{1}{2}\sum_N\left(1 + \mathrm{erf}\left(\frac{E - E_N}{\sqrt{2}\Gamma}\right)\right) + C_{\mathrm{offset}}. \tag{3.23}$$

The offset term is a numerical artifact necessary to correctly fill the Landau levels. It is determined so that $\nu = 0$ when the energy E is in the gap. Once this offset is set, we can calculate the Fermi level for a given carrier density, fixed by the gate voltage. To calculate the Fermi level, we just have to find the zero of the following quantity:

$$f(E) = n_{\mathrm{exp}} - n(E) = n_{\mathrm{exp}} - \frac{eB}{h}\nu(E) \tag{3.24}$$

where n_{exp} is the experimental electron density, imposed by the gate voltage value. By doing this calculation for each value of magnetic field, we obtain the evolution of the Fermi level. At low field, we populate Landau levels up to a large index because of their low degeneracy. When we increase the magnetic field, the degeneracy of each Landau level increases and, as the number of electrons is fixed, we depopulate levels of high index to populate levels of low index. The Fermi level thus falls progressively towards the lowest Landau levels. The disorder influences the way, abrupt or smooth, in which the Fermi energy goes from one Landau level to another. The more important the disorder is, the wider the levels are and the more easily the Fermi energy will be stabilized between two neighboring Landau levels.

The last step is to calculate the conductivity from the density of state evaluated at the Fermi level. The calculation of the conductivity is not obvious and a number of models exist. We used a formula originally proposed by Gerhardts [Ger08].The conductivity is given by:

$$\sigma_{xx} = \sum_N\left(N + \frac{1}{2}\right)\sigma_0(E_F - E_N), \tag{3.25}$$

$$\sigma_0(E) = \frac{e^2}{h}\left[\sqrt{2\pi}\Gamma A(E)\right]^2. \tag{3.26}$$

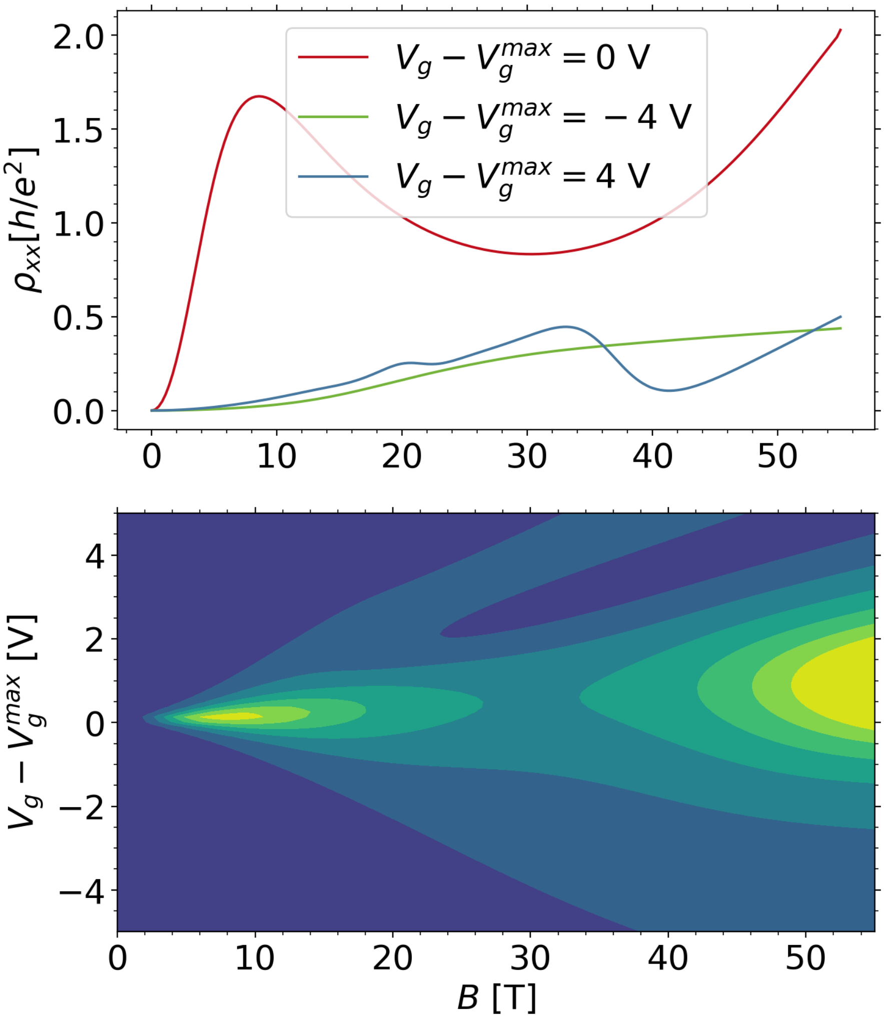

Figure 3.31: (a) Magnetoresistances ρ_{xx} at $V_g - V_g^{\max} = 0\,\mathrm{V}$, $-4\,\mathrm{V}$ and $4\,\mathrm{V}$ as calculated by the model. (b) Colormap of the longitudinal magnetoresistance, as a function of B and $V_g - V_g^{\max}$.

The transverse conductivity for one LL, $\sigma_{xy,N}$ is given by the semicircle relation $\sigma_{xx,N}^2 + \sigma_{xy,N}^2 = 1$.

The results of the simulation are reported in Fig. 3.31. Figure 3.31(a) shows only three magnetoresistances at three different voltages: one in the gap, one in the valence band, and the last one in the conduction band. The dramatic increase of the magnetoresistance when the Fermi energy lies in the gap is obvious. The dip around $B \simeq 30\,\mathrm{T}$ is well reproduced, and its overall amplitude is of the same order of magnitude, although twice as small as the experimental dip ($20\,\mathrm{k}\Omega$ *versus* $50\,\mathrm{k}\Omega$). The SdH oscillations are well reproduced in the conduction band. For the chosen LL broadening, no SdH oscillations are visible in the valence band. For completeness, a color map of the calculated magnetoresistance is shown in Fig. 3.31(b). Also, Fig. 3.32 compares both experimental and numerical magnetoresistances, as a function of gate voltage and magnetic field, evidencing the overall good agreement between the model and the experiment.

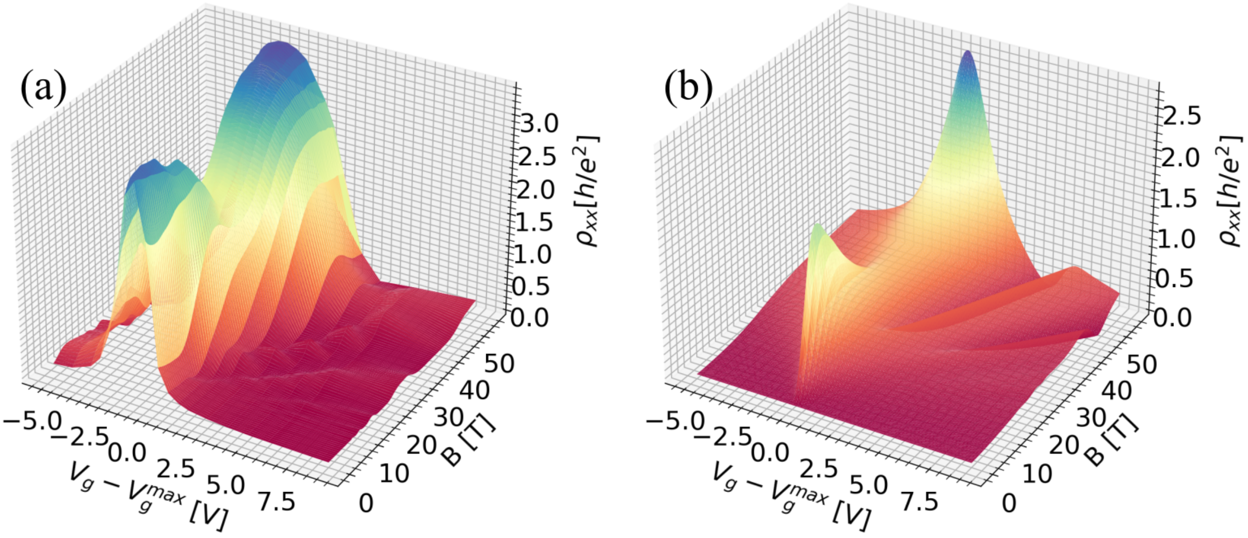

Figure 3.32: Three dimensional artistic view of the longitudinal magnetoresistance, as a function of B and $V_g - V_g^{\mathrm{max}}$, for (a) device HB14 and (b) the simuation.

Conclusion

The aim of this thesis was to emphasize the potential of InAs/GaSb based structures for the observation of the quantum spin Hall effect at higher temperatures. The idea at the origin of this work was to restore the inversion symmetry of the structure of the composite quantum well of InAs/GaSb, so as to amplify the energy of the topological gap in these structures to values greater than thermal energy at room temperature. Our strategy was the addition of a GaSb layer in the active part confined between the AlSb barriers. This wider gap gives hope to observe edge states with quantized conductance in the quantum spin Hall regime at temperatures higher than the tens of mK needed in II-VI structures. Of course, the first steps consisted in fabricating Hall bar devices from these specific quantum wells and characterizing their band structure by magneto-transport measurements, before attempting to measure the conductance of their edge states. The final objective was to demonstrate the quantum spin Hall effect in these new structures, through edge state studies using a non-local electronic transport technique. We therefore first presented the samples whose growth was performed to restore the inversion symmetry of the quantum well structure. We have seen that each layer is important until even the choice of the substrate. Indeed, the characterization of the growths made on GaAs subtrates revealed a strong electrical anisotropy, as well as a conduction in layers below those of the TQWs. A simple method has been proposed to rapidly evaluate the anisotropy from a 8-contact square sample.

Numerous devices were fabricated from these growths to finely probe the low temperature transport properties of these structures. In the second chapter, I emphasize the fact that an important part has been devoted to the development of the fabrication process of these devices. Still, a better control of the steps of etching and deposition of dielectric is necessary for the reduction of the size of the devices. We have limited ourselves in this work to the realization of Hall bar devices with relatively standard geometries. The fabricated devices have nevertheless allowed the study of these devices via magneto-transport measurements. We have demonstrated the expected gap widening, up to 45 meV, by thermal activation measurements of this gap. For comparison, a similar gap size has been measured in topological insulators based on WTe_2 [WFG+18] and has recently allowed the observation of the QSHE up to 100 K. In general, we have confirmed the validity of the theoretical calculations on which this work is based. Similarly, the magnetic field measurements have allowed us to reconstruct the expected structure for the Landau levels and demonstrate the band inversion. The last results obtained during the measurements under intense pulsed magnetic field motivate the continuation of these measurements for a finer and quantitative description of the role of the long-range disorder in the position of the B_c value, corresponding to a topological phase transition.

Finally, we have highlighted the presence of edge conduction which dominates in the gap. This was made possible by the use of a numerical model, developed for the occasion, to analyse both local and non-local transport results. This model, which consists of a 2D square lattice network of resistors, allows us to discriminate the resistivity of the bulk to the additional conduction along the edges. If the too large size of our devices does not allow us to observe the expected quantization for topological edge states, we were able to extract systematically an inelastic mean free path λ of the order of a few microns. Although the reduction in size of devices raises issues of technological realization, a resolution of less than a few microns is a very reasonable and attainable goal in the short run. For such a perspective, it is quite logical to consider devices of smaller sizes and other geometries, such as H-bars for the study of edge states, or L-shape Hall bars to evaluate locally the electrical anisotropy, and Corbino to focus on the contribution of the bulk in the conduction bands.

Appendix

Code for computing the resistance on an infinite 2D plane between 2 circular probes

This code has been developed for the FreeFem++ software.

```
//2D resistance between two circular perfect contacts.
real sc=1;  //scale for testing
real a= 1*sc;
{
ofstream file("2p_v2.txt");
for (real d=3.0;d< 41; d=d+1.0)
{

real f= 100.0*sc;
// A and B are perfect contacts (circles)
border A(t=0, 2*pi){x=a*cos(t)-d/2; y=a*sin(t);}
border B(t=0, 2*pi){x=a*cos(t)+d/2; y=a*sin(t);}
//E0 to impose a finer mesh close to the contacts
border E0(t=0, 2*pi){x=f*cos(t); y=f*sin(t);}
//E1= end of the world
border E1(t=0, 2*pi){x=d*cos(t); y=d*sin(t);}
mesh Th=buildmesh(A(-20) + B(-20) + E0(40)+E1(200));
//plot(Th,wait=1);

fespace Vh (Th, P2);
Vh u,v,dxu,dyu,dj; // u: voltage
real sigma=1;  // sigma is introduced for clarity only

problem croix(u,v)= int2d(Th)
( sigma*dx(u)*dx(v)   +sigma * dy(u)*dy(v))
    + on(A,u=1)+ on(B,u=-1)+on (E0,u=0);

croix;
//plot the solution
//plot (u, fill=1, value=1, wait=1);

//extract nabla u #electric field
dxu= dx(u);

// integrate the current along the y axis, x=0.
real res=0.0;
real ni= 1200;
for (int nc=0;nc< ni; nc++)
```

```
{
  real t= nc/ni;
    y = -f*(1-t) + f*t;
  res = res- dxu(0,y)*(2*f)/ni;
}
cout << "current = " <<  res << " a.u., " ;
cout << "R = " <<  2/ res << " rho [Ohms] " << endl;

file << a << ", " << d << ", " << 2/res << endl;
}
cout << "the end" << endl;
}
```

Code of the square lattice model

Below we provide a simplified version of the python code based on the square lattice model. This code can calculate numerically the non-local resistance:

$$R_{NL}^{\text{Ohmic}} = \frac{4}{\pi} R_L \exp\left(-\pi \frac{l_p}{W}\right), \tag{3.27}$$

where l_p is the distance between the lateral probes, and W is the Hall bar width.

```
#square lattice of resistors, following the idea of Nichele et al.

import numpy as np
from scipy.sparse import lil_matrix
from scipy.sparse.linalg import spsolve
from matplotlib import pyplot as plt

#defines the source and drain contacts
#with some contact conductance Gc
#for internal calculation, a voltage +/- 1 V is applied on source and drain
class DEVconnection:
    def __init__(self,nijkl, V0=-1,V1=1,Gc=100.0):
        self.V0=V0
        self.V1=V1
        self.Gc= Gc
        self.nijkl=nijkl
        self.source= nijkl[0]
        self.drain=  nijkl[1]

#class for a Hall bar of given geometry
#L : total length (int, arb. unit (eg um))
#W: total width (int)
#Lc: distance between the lateral probes and the closed source/drain contact (int)
#sca: scale of the square nerwork same unit as L,W, Lc
class HBtopol:
    def __init__(self, L=110, W=20, Lc=40,sca=1):

        self.n_L = (L)*sca//5 -1 # or +1 if GT 18*sca-1
        self.n_W = W*sca//5+1
        self.n_c = (Lc)*sca//5-1
        self.ntot= self.n_L * self.n_W +2
        self.sca= sca
        self.lcarre= 5/sca # size of the resistor square
        self.lclp= self.lcarre/ (L-Lc-Lc)
```

```

        self.tcontacts= [self.n_L*self.n_W,
                         self.n_c,
                         self.n_L-self.n_c-1,
                         self.n_L*self.n_W+1,
                         -self.n_c-1-2,
                         -self.n_L+self.n_c-2]
        self.Mb= self.G_matrix_setup(0,1, 0)
        self.Me= self.G_matrix_setup(1,0, 0)
        #MT= f_M_square_lattice(0,0, 1, n_L, n_W, n_c)

        self.R1423= DEVconnection([0,3, 1, 2])
        self.R2635= DEVconnection([1,5, 2, 4])

        self.DEVconn_setup(self.R1423) #local configuration
        self.DEVconn_setup(self.R2635) #non local configuration

    #for a given configuration c, defines the B vector (out/out currents)
    def DEVconn_setup(self,c) : #Gc, V1,V0, nijkl):
        source= c.nijkl[0]
        drain=  c.nijkl[1]
        #tcontacts lists the position of the 6 contacts

        #add a Gc conductance for the source and drain
        Mc=  lil_matrix((self.ntot,self.ntot))
        Mc[self.tcontacts[source],self.tcontacts[source]] += -c.Gc
        Mc[self.tcontacts[drain], self.tcontacts[drain]]  += -c.Gc
        c.Mc= Mc.tocsc()
        #contact vector
        c.Vc= [0]* (self.ntot)
        c.Vc[self.tcontacts[source]] += -c.V1* c.Gc
        c.Vc[self.tcontacts[drain]]  += -c.V0*c.Gc

    def G_matrix_setup(self,Ge,Gb, GT):
        A=  lil_matrix((self.ntot,self.ntot))
        d1= [Ge for _ in range(self.n_L-1)]+ [0]
        d2= [Gb for _ in range (self.n_L-1)]+[0]
        d3= [Gb for _ in range((self.n_W-1)*self.n_L)]
        d= [*d1, *d2*(self.n_W-2), *d1]
        A.setdiag(d, 1)
        A.setdiag(d,-1)
        A.setdiag(d3,self.n_L)
        A.setdiag(d3,-self.n_L)
        #charge transfer length for the contacts can be defined
        GeT=Ge
        GbT=Gb
        #contact 0
        d1= [GeT]+ [0]*(self.n_L-1)  #  GeT= Ge
        d2= [GbT]+ [0]*(self.n_L-1)  #  GbT= Gb
        d3= [*d1, *d2* (self.n_W-2), *d1, *[0, 0]]
        A[-2,:]=d3
        A[:,-2]=[[x] for x in d3]
        #contact 3
        d1=  [0]*(self.n_L-1)+[GeT]
        d2=  [0]*(self.n_L-1)+[GbT]
        d3= [*d1, *d2*(self.n_W-2), *d1, *[0, 0]]
        A[-1,:]=d3
        A[:,-1]=[[x] for x in d3]
        #diagonal terms
```

```
        d1= [-GeT-Ge-Gb, *[-2*Ge-Gb]*(self.n_L-2), -GeT-Ge-Gb]
        d2= [-GbT-3*Gb,   *[-4*Gb   ]*(self.n_L-2), -GbT-3*Gb]   * (self.n_W-2)
        d= [*d1, *d2, *d1, *[-2*GeT-GbT*(self.n_W-2), -2*GeT-GbT*(self.n_W-2)]]
        A.setdiag(d,0)
        return(A.tocsc())

    #calculate a four probe resistance for a Hall bar
    #Ge conductance at the edge
    #Gb bulk conductance
    #c four probe configuration
    def resistance_solver(self,Ge,Gb, c): #Gc, V0, V1, n_L, n_W, n_c, offc, Rijkl,Mco,Vc):
        M1= spsolve(Ge*self.Me+ Gb*self.Mb  + c.Mc, c.Vc)
        Isource= c.Gc* (c.V1-M1[self.tcontacts[c.source]])
        Idrain=  c.Gc* (M1[self.tcontacts[c.drain]]-c.V0)
        current= (Isource+Idrain)/2.0
        V= M1[self.tcontacts[c.nijkl[2]]]- M1[self.tcontacts[c.nijkl[3]]]
        R= V/current
        return (R)

def f_r_estim(L, W):
    return (4 / np.pi * np.exp(-np.pi * L / W))

tW= np.array([5,6,7,8,10,15,20,25,30,40])
t1= np.zeros(len(tW))
t1e=np.zeros(len(tW))
Lp=20  # distance between the lateral probes
for n, W1 in enumerate(tW):
    HB= HBtopol(sca=30, L=120,W=W1,Lc=int((120-Lp)/2.0))
    Rnl= HB.resistance_solver(1,1, HB.R2635)
    t1[n]= Rnl
    t1e[n]= f_r_estim(20, W1)
    print(Rnl, f_r_estim(20, W1))

plt.figure(figsize=(4,3))
plt.clf()
plt.semilogy(Lp/tW, t1,’o’, Lp/tW, t1e,’c--’)
plt.legend([’model’, ’theory’])
plt.xlabel(r’$L_p/W$’)
plt.ylabel(r’$R_{NL}/\rho$’)
plt.show()
```

Bibliography

[ACI$^+$16] T. Akiho, F. Couëdo, H. Irie, K. Suzuki, K. Onomitsu, and K. Muraki. Engineering quantum spin hall insulators by strained-layer heterostructures. *Applied Physics Letters*, 109(19):192105, November 2016.

[ANZ$^+$07] Dmitry A. Abanin, Kostya S. Novoselov, Uli Zeitler, Patrick A. Lee, A. K. Geim, and L. S. Levitov. Dissipative quantum hall effect in graphene near the dirac point. *Physical Review Letters*, 98(19):196806, may 2007.

[Beu16] A.J.A. Beukman. *Topology in two-dimensional systems.* PhD thesis, 2016.

[BHZ06] B. A. Bernevig, T. L. Hughes, and S.-C. Zhang. Quantum spin hall effect and topological phase transition in hgte quantum wells. *Science*, 314(5806):1757–1761, December 2006.

[BMC$^+$22] C. Bray, K. Maussang, C. Consejo, J. A. Delgado-Notario, S. Krishtopenko, I. Yahniuk, S. Gebert, S. Ruffenach, K. Dinar, E. Moench, J. Eroms, K. Indykiewicz, B. Jouault, J. Torres, Y. M. Meziani, W. Knap, A. Yurgens, S. D. Ganichev, and F. Teppe. Temperature-dependent zero-field splittings in graphene. *Physical Review B*, 106(24):245141, December 2022.

[BSH$^+$18] Kalle Bendias, Saquib Shamim, Oliver Herrmann, Andreas Budewitz, Pragya Shekhar, Philipp Leubner, Johannes Kleinlein, Erwann Bocquillon, Hartmut Buhmann, and Laurens W. Molenkamp. High mobility HgTe microstructures for quantum spin Hall studies. *Nano Lett.*, 18(8):4831, 2018.

[Büt86] M. Büttiker. Four-terminal phase-coherent conductance. *Physical Review Letters*, 57(14):1761–1764, October 1986.

[Büt88] M. Büttiker. Absence of backscattering in the quantum hall effect in multiprobe conductors. *Physical Review B*, 38(14):9375–9389, November 1988.

[CFR$^+$13] Christophe Charpentier, Stefan Fält, Christian Reichl, Fabrizio Nichele, Atindra Nath Pal, Patrick Pietsch, Thomas Ihn, Klaus Ensslin, and Werner Wegscheider. Suppression of bulk conductivity in InAs/GaSb broken gap composite quantum wells. *Appl. Phys. Lett.*, 103(11):112102, September 2013.

[DKSD15] Lingjie Du, Ivan Knez, Gerard Sullivan, and Rui-Rui Du. Robust helical edge transport in gated InAs/GaSb bilayers. *Phys. Rev. Lett.*, 114(9):096802, March 2015.

[EBC+08] Daniele Ercolani, Giorgio Biasiol, Emiliano Cancellieri, Marcello Rosini, Carlo Jacoboni, Franco Carillo, Stefan Heun, Lucia Sorba, and Frithjof Nolting. Transport anisotropy in $In_{0.75}Ga_{0.25}As$ two-dimensional electron gases induced by indium concentration modulation. *Physical Review B*, 77(23):235307, June 2008.

[Geb22] Sebastian Gebert. *Spectroscopie Térahertz de Matériaux de Dirac par Émission Cyclotron et Magnéto-Absorption.* PhD thesis, 2022.

[Ger08] Rolf R. Gerhardts. The effect of screening on current distribution and conductance quantisation in narrow quantum hall systems. *physica status solidi (b)*, 245(2):378–392, February 2008.

[GWK+94] R. S. Goldman, H. H. Wieder, K. L. Kavanagh, K. Rammohan, and D. H. Rich. Anisotropic structural, electronic, and optical properties of InGaAs grown by molecular beam epitaxy on misoriented substrates. *Applied Physics Letters*, 65(11):1424–1426, September 1994.

[HZC86] D. Heitman, M. Ziesmann, and L. L. Chang. Cyclotron-resonance oscillations in InAs quantum wells. *Physical Review B*, 34(10):7463–7466, nov 1986.

[IAC+20] H. Irie, T. Akiho, F. Couedo, K. Suzuki, K. Onomitsu, and K. Muraki. Energy gap tuning and gate-controlled topological phase transition in inas/ingasb composite quantum wells. *Physical Review Materials*, 4(10):104201, October 2020.

[IKD+16] A. V. Ikonnikov, S. S. Krishtopenko, O. Drachenko, M. Goiran, M. S. Zholudev, V. V. Platonov, Yu. B. Kudasov, A. S. Korshunov, D. A. Maslov, I. V. Makarov, O. M. Surdin, A. V. Philippov, M. Marcinkiewicz, S. Ruffenach, F. Teppe, W. Knap, N. N. Mikhailov, S. A. Dvoretsky, and V. I. Gavrilenko. Temperature-dependent magnetospectroscopy of HgTe quantum wells. *Phys. Rev. B*, 94:155421, October 2016.

[JC07] Arden Sher Junhao Chu. *Physics and Properties of Narrow Gap Semiconductors.* SPRINGER NATURE, November 2007.

[KD11] Ivan Knez and Rui-Rui Du. Quantum spin hall effect in inverted InAs/GaSb quantum wells. *Frontiers of Physics*, 7(2):200–207, September 2011.

[KDM+88] L.S Kim, H.D Drew, H Munekata, L.L Chang, and L Esaki. Electron and hole cyclotron resonance in semimetallic GaSb/InAs/GaSb quantum wells. *Solid State Communications*, 66(8):873–876, may 1988.

[KDS10] Ivan Knez, R. R. Du, and Gerard Sullivan. Finite conductivity in mesoscopic hall bars of inverted InAs/GaSb quantum wells. *Physical Review B*, 81(20):201301, May 2010.

[KDS+19] S. S. Krishtopenko, W. Desrat, K. E. Spirin, C. Consejo, S. Ruffenach, F. Gonzalez-Posada, B. Jouault, W. Knap, K. V. Maremyanin, V. I. Gavrilenko, G. Boissier, J. Torres, M. Zaknoune, E. Tournié, and F. Teppe. Massless dirac fermions in III-v semiconductor quantum wells. *Physical Review B*, 99(12):121405, March 2019.

[KIM$^+$12] S. S. Krishtopenko, A. V. Ikonnikov, A. V. Maremyanin, K. E. Spirin, V. I. Gavrilenko, Yu. G. Sadofyev, M. Goiran, M. Sadowsky, and Yu. B. Vasilyev. Cyclotron resonance study in InAs/AlSb quantum well heterostructures with two occupied electronic subbands. *Journal of Applied Physics*, 111(9):093711, May 2012.

[KIM$^+$17] S. S. Krishtopenko, A. V. Ikonnikov, K. V. Maremyanin, L. S. Bovkun, K. E. Spirin, A. M. Kadykov, M. Marcinkiewicz, S. Ruffenach, C. Consejo, F. Teppe, W. Knap, B. R. Semyagin, M. A. Putyato, E. A. Emelyanov, V. V. Preobrazhenskii, and V. I. Gavrilenko. Cyclotron resonance of dirac fermions in InAs/GaSb/InAs quantum wells. *Semiconductors*, 51(1):38–42, January 2017.

[KIO$^+$15] S. S. Krishtopenko, A. V. Ikonnikov, M. Orlita, Yu. G. Sadofyev, M. Goiran, F. Teppe, W. Knap, and V. I. Gavrilenko. Effect of electron-electron interaction on cyclotron resonance in high-mobility InAs/AlSb quantum wells. *Journal of Applied Physics*, 117(11):112813, March 2015.

[KKJ$^+$18] A. M. Kadykov, S. S. Krishtopenko, B. Jouault, W. Desrat, W. Knap, S. Ruffenach, C. Consejo, J. Torres, S. V. Morozov, N. N. Mikhailov, S. A. Dvoretskii, and F. Teppe. Temperature-induced topological phase transition in HgTe quantum wells. *Phys. Rev. Lett.*, 120:086401, February 2018.

[KM05] C. L. Kane and E. J. Mele. Quantum spin hall effect in graphene. *Physical Review Letters*, 95(22):226801, November 2005.

[KRGP$^+$18] S. S. Krishtopenko, S. Ruffenach, F. Gonzalez-Posada, G. Boissier, M. Marcinkiewicz, M. A. Fadeev, A. M. Kadykov, V. V. Rumyantsev, S. V. Morozov, V. I. Gavrilenko, C. Consejo, W. Desrat, B. Jouault, W. Knap, E. Tournié, and F. Teppe. Temperature-dependent terahertz spectroscopy of inverted-band three-layer inas/gasb/inas quantum well. *Physical Review B*, 97(24):245419, June 2018.

[KRGP$^+$19] S. S. Krishtopenko, S. Ruffenach, F. Gonzalez-Posada, C. Consejo, W. Desrat, B. Jouault, W. Knap, M. A. Fadeev, A. M. Kadykov, V. V. Rumyantsev, S. V. Morozov, G. Boissier, E. Tournié, V. I. Gavrilenko, and F. Teppe. Terahertz spectroscopy of two-dimensional semimetal in three-layer inas/gasb/inas quantum well. *JETP Letters*, 109(2):96–101, January 2019.

[KRY$^+$14] Ivan Knez, Charles T. Rettner, See-Hun Yang, Stuart S. P. Parkin, Lingjie Du, Rui-Rui Du, and Gerard Sullivan. Observation of edge transport in the disordered regime of topologically insulating InAs/GaSb quantum wells. *Phys. Rev. Lett.*, 112(2):026602, January 2014.

[KSK07] Jonas Kleiza, Mifodijus Sapagovas, and Vytautas Kleiza. The extension of the van der pauw method to anisotropic media. *Informatica*, 18(2):253–266, jan 2007.

[KT18a] S. S. Krishtopenko and F. Teppe. Realistic picture of helical edge states in hgte quantum wells. *Physical Review B*, 97(16):165408, April 2018.

[KT18b] Sergey S. Krishtopenko and Frédéric Teppe. Quantum spin hall insulator with a large bandgap, dirac fermions, and bilayer graphene analog. *Science Advances*, 4(4):eaap7529, April 2018.

[KWB+07] M. Konig, S. Wiedmann, C. Brune, A. Roth, H. Buhmann, L. W. Molenkamp, X.-L. Qi, and S.-C. Zhang. Quantum spin hall insulator state in hgte quantum wells. *Science*, 318(5851):766–770, November 2007.

[KYB+16] S. S. Krishtopenko, I. Yahniuk, D. B. But, V. I. Gavrilenko, W. Knap, and F. Teppe. Pressure- and temperature-driven phase transitions in HgTe quantum wells. *Phys. Rev. B*, 94(24):245402, December 2016.

[Lan57] R. Landauer. Spatial variation of currents and fields due to localized scatterers in metallic conduction. *IBM Journal of Research and Development*, 1(3):223–231, July 1957.

[Lan70] Rolf Landauer. Electrical resistance of disordered one-dimensional lattices. *Philosophical Magazine*, 21(172):863–867, April 1970.

[LHQ+08] Chaoxing Liu, Taylor L. Hughes, Xiao-Liang Qi, Kang Wang, and Shou-Cheng Zhang. Quantum spin hall effect in inverted type-ii semiconductors. *Physical Review Letters*, 100(23):236601, June 2008.

[LkS21] Son Phuong Le and Toshi kazu Suzuki. Electron mobility anisotropy in InAs/-GaAs(001) heterostructures. *Applied Physics Letters*, 118(18):182101, May 2021.

[LLB+16] Philipp Leubner, Lukas Lunczer, Christoph Brüne, Hartmut Buhmann, and Laurens W. Molenkamp. strain engineering of the band gap of HgTe quantum wells using superlattice virtual substrates. *Phys. Rev. Lett.*, 117:086403, August 2016.

[LLE+19] Lukas Lunczer, Philipp Leubner, Martin Endres, Valentin L. Müller, Christoph Brüne, Hartmut Buhmann, and Laurens W. Molenkamp. Approaching quantization in macroscopic quantum spin hall devices through gate training. *Physical Review Letters*, 123(4):047701, July 2019.

[LMV+03] S. Löhr, S. Mendach, T. Vonau, Ch. Heyn, and W. Hansen. Highly anisotropic electron transport in shallow InGaAs heterostructures. *Physical Review B*, 67(4):045309, January 2003.

[Mar17] Michal Marcinkiewicz. *Terahertz Spectroscopy of Topological Phase Transitions in HgCdTe-based systems.* Theses, Université Montpellier, July 2017.

[MEPT15] I. Miccoli, F. Edler, H. Pfnür, and C. Tegenkamp. The 100th anniversary of the four-point probe technique: the role of probe geometries in isotropic and anisotropic systems. *Journal of Physics: Condensed Matter*, 27(22):223201, May 2015.

[MGR+13] G. M. Minkov, A. V. Germanenko, O. E. Rut, A. A. Sherstobitov, S. A. Dvoretski, and N. N. Mikhailov. Two-dimensional semimetal in a wide hgte quantum well: Magnetotransport and energy spectrum. *Physical Review B*, 88(15):155306, October 2013.

[MPK+15] Susanne Mueller, Atindra Nath Pal, Matija Karalic, Thomas Tschirky, Christophe Charpentier, Werner Wegscheider, Klaus Ensslin, and Thomas Ihn. Nonlocal transport via edge states in InAs/GaSb coupled quantum wells. *Physical Review B*, 92(8):081303, August 2015.

[MRK$^+$17] M. Marcinkiewicz, S. Ruffenach, S. S. Krishtopenko, A. M. Kadykov, C. Consejo, D. B. But, W. Desrat, W. Knap, J. Torres, A. V. Ikonnikov, K. E. Spirin, S. V. Morozov, V. I. Gavrilenko, N. N. Mikhailov, S. A. Dvoretskii, and F. Teppe. Temperature-driven single-valley Dirac fermions in HgTe quantum wells. *Phys. Rev. B*, 96:035405, July 2017.

[MZN$^+$10] G. Moschetti, H. Zhao, P.-Å. Nilsson, S. Wang, A. Kalabukhov, G. Dambrine, S. Bollaert, L. Desplanque, X. Wallart, and J. Grahn. Anisotropic transport properties in InAs/AlSb heterostructures. *Applied Physics Letters*, 97(24):243510, December 2010.

[NGP$^+$09] A. H. Castro Neto, F. Guinea, N. M. R. Peres, K. S. Novoselov, and A. K. Geim. The electronic properties of graphene. *Reviews of Modern Physics*, 81(1):109–162, January 2009.

[NL01] Y. Naveh and B. Laikhtman. Magnetotransport of coupled electron-holes. *Europhys. Lett. (EPL)*, 55(4):545–551, August 2001.

[NPP$^+$14] Fabrizio Nichele, Atindra Nath Pal, Patrick Pietsch, Thomas Ihn, Klaus Ensslin, Christophe Charpentier, and Werner Wegscheider. Insulating state and giant nonlocal response in anInAs/GaSbQuantum well in the quantum hall regime. *Physical Review Letters*, 112(3):036802, January 2014.

[PHM$^+$14] D. I. Pikulin, T. Hyart, Shuo Mi, J. Tworzydło, M. Wimmer, and C. W. J. Beenakker. Disorder and magnetic-field-induced breakdown of helical edge conduction in an inverted electron-hole bilayer. *Physical Review B*, 89(16):161403, April 2014.

[Pob07] Frank Pobell. *Matter and Methods at Low Temperatures*. Springer-Verlag GmbH, February 2007.

[QLFL14] Xiaofeng Qian, Junwei Liu, Liang Fu, and Ju Li. Quantum spin hall effect in two-dimensional transition metal dichalcogenides. *Science*, 346(6215):1344–1347, dec 2014.

[QXW$^+$13] Hao Qiu, Tao Xu, Zilu Wang, Wei Ren, Haiyan Nan, Zhenhua Ni, Qian Chen, Shijun Yuan, Feng Miao, Fengqi Song, Gen Long, Yi Shi, Litao Sun, Jinlan Wang, and Xinran Wang. Hopping transport through defect-induced localized states in molybdenum disulphide. *Nature Communications*, 4(1), oct 2013.

[QZ10] Xiao-Liang Qi and Shou-Cheng Zhang. The quantum spin hall effect and topological insulators. *Physics Today*, 63(1):33–38, January 2010.

[QZ11] Xiao-Liang Qi and Shou-Cheng Zhang. Topological insulators and superconductors. *Reviews of Modern Physics*, 83(4):1057–1110, October 2011.

[RCC$^+$05] J.B. Rodriguez, P. Christol, L. Cerutti, F. Chevrier, and A. Joullié. MBE growth and characterization of type-II InAs/GaSb superlattices for mid-infrared detection. *Journal of Crystal Growth*, 274(1-2):6–13, January 2005.

[RKB$^+$17] S. Ruffenach, S. S. Krishtopenko, L. S. Bovkun, A. V. Ikonnikov, M. Marcinkiewicz, C. Consejo, M. Potemski, B. Piot, M. Orlita, B. R. Semyagin,

M. A. Putyato, E. A. Emel'yanov, V. V. Preobrazhenskii, W. Knap, F. Gonzalez-Posada, G. Boissier, E. Tournié, F. Teppe, and V. I. Gavrilenko. Magnetoabsorption of Dirac fermions in InAs/GaSb/InAs "three-layer" gapless quantum wells. *JETP Lett.*, 106(12):727–732, December 2017.

[SDP+16] B. Shojaei, A. C. C. Drachmann, M. Pendharkar, D. J. Pennachio, M. P. Echlin, P. G. Callahan, S. Kraemer, T. M. Pollock, C. M. Marcus, and C. J. Palmstrøm. Limits to mobility in InAs quantum wells with nearly lattice-matched barriers. *Physical Review B*, 94(24):245306, December 2016.

[SPAW18] Rafal Skolasinski, Dmitry I. Pikulin, Jason Alicea, and Michael Wimmer. Robust helical edge transport in quantum spin hall quantum wells. *Physical Review B*, 98(20):201404, November 2018.

[SRT+07] B. Satpati, J.B. Rodriguez, A. Trampert, E. Tournié, A. Joullié, and P. Christol. Interface analysis of InAs/GaSb superlattice grown by MBE. *Journal of Crystal Growth*, 301-302:889–892, April 2007.

[THT+18] C. Thomas, A. T. Hatke, A. Tuaz, R. Kallaher, T. Wu, T. Wang, R. E. Diaz, G. C. Gardner, M. A. Capano, and M. J. Manfra. High-mobility InAs 2degs on GaSb substrates: A platform for mesoscopic quantum transport. *Physical Review Materials*, 2(10):104602, October 2018.

[TMK+16] F. Teppe, M. Marcinkiewicz, S. S. Krishtopenko, S. Ruffenach, C. Consejo, A. M. Kadykov, W. Desrat, D. But, W. Knap, J. Ludwig, S. Moon, D. Smirnov, M. Orlita, Z. Jiang, S. V. Morozov, V. I. Gavrilenko, N. N. Mikhailov, and S. A. Dvoretskii. Temperature-driven massless Kane fermions in HgCdTe crystals. *Nat. Commun.*, 7:12576, 2016.

[TSTH92] Y. Tokura, T. Saku, S. Tarucha, and Y. Horikoshi. Anisotropic roughness scattering at a heterostructure interface. *Physical Review B*, 46(23):15558–15561, December 1992.

[vKDP80] K. v. Klitzing, G. Dorda, and M. Pepper. New method for high-accuracy determination of the fine-structure constant based on quantized hall resistance. *Physical Review Letters*, 45(6):494–497, August 1980.

[VMRM01] I. Vurgaftman, J. R. Meyer, and L. R. Ram-Mohan. Band parameters for III–v compound semiconductors and their alloys. *Journal of Applied Physics*, 89(11):5815–5875, June 2001.

[WFG+18] Sanfeng Wu, Valla Fatemi, Quinn D. Gibson, Kenji Watanabe, Takashi Taniguchi, Robert J. Cava, and Pablo Jarillo-Herrero. Observation of the quantum spin hall effect up to 100 kelvin in a monolayer crystal. *Science*, 359(6371):76–79, jan 2018.

[WWZZ22] Qiqi Wei, Hailong Wang, Xupeng Zhao, and Jianhua Zhao. Electron mobility anisotropy in (al,ga)sb/InAs two-dimensional electron gases epitaxied on GaAs (001) substrates. *Journal of Semiconductors*, 43(7):072101, July 2022.

[Zha16] Jinsong Zhang. *Transport Studies of the Electrical, Magnetic and Thermoelectric properties of Topological Insulator Thin Films*. Springer-Verlag GmbH, April 2016.